

Submarine landslides in active margin environments

-

**Slope stability vs. neotectonic activity on the northeastern margin of Crete,
eastern Mediterranean**

Dissertation

**Zur Erlangung des Doktorgrades der Naturwissenschaften am Fachbereich Geowissenschaften
der Universität Bremen**

**Submitted for the doctoral degree in natural sciences at the Faculty of Geosciences of Bremen
University**

By

Frank Strozyk

Bremen, 2009



Abstract

This thesis is a study of the processes and factors that may govern submarine slope destabilization and mass movement as well as a slope's resistance to failure in submarine active margin environments. Prior studies on this topic in active margin settings (e.g., western North America) have shown that their slopes can be peculiar, poorly understood systems with a low recurrence of slope collapse despite the 'paradigm' of extensive, diffuse, and widespread mass movement generally associated with the tectonic activity. The focus of this study is the active margin present along the northeast margin of Crete in the Hellenic subduction zone of the eastern Mediterranean. The previously unknown distribution and recurrence rate of landslides, their failure and transport kinematics, as well as the trigger mechanisms required for sediment instability along the northeast Cretan margin are thus investigated and reconstructed. Such data help answer the open questions related to such active margin settings.

As a starting point, several mass-transport deposits (MTDs) and their source scars are mapped and investigated from bathymetric charts and multi-channel seismic profiles. As a result, three different mass-movement patterns sourced from the NE Cretan margin are identified for the first time: (1) large major MTDs representing debrites of $\sim 30\text{-}50\text{ km}^3$ in the Kamilonisi Basin - the NE foot region of the Cretan slope, (2) midsize MTDs from translational, coherent landslides as well as debris-flows with volumes of $0.5\text{-}2.5\text{ km}^3$ in the Malia Basin and on the mid-slope close to the Bay of Mirabello, and (3) small sediment dislocations of cm- to dm-thicknesses in cores from foot regions of exposed steep slope parts (e.g. headwalls, Kamlinois Basin flank and Malia Basin flank).

Ages and recurrence rates of these patterns are back-calculated from background sediment thicknesses draping MTDs using sediment accumulation rates of approximately 7.8 cm/ka obtained from dated marker horizons in shallower gravity cores: (1) major slope collapses occur at 250 ka ($\pm 70\text{ ka}$) intervals with the youngest event occurring some $192\text{-}250\text{ ka B.P.}$ ($\pm 50\text{ ka B.P.}$); (2) midsize events occur at a $34\text{-}125\text{ ka}$ frequency (youngest event in the Malia Basin: $\sim 25\text{ ka B.P.}$ ($12.6\text{-}33\text{ ka}$)), but can also occur as locally restricted, single events (e.g. in the Bay of Mirabello with an age of $\sim 192\text{ ka B.P.}$ ($\pm 50\text{ ka B.P.}$)), and (3) small-scale sediment dislocations occur in intervals of approximately $3\text{-}25\text{ ka}$ depending on the local steepness of the relief. Given that no intermediate mass-movement patterns can be observed in the data, this recurrence rate of slope failure is low, and the Cretan margin mass movement is dominated by large, but only occasional events. This characterises the northern Cretan slope as a 'cohesive slope'. Further, attributes of a 'cohesive slope' are reinforced by morphometric measurements of MTDs, their scars, and the adjacent slope, implying failure and transport geometries that are typical for such cohesive slopes.

Given that seismicity in the Hellenic forearc is much above the average in Europe, frequent impacts from earthquakes in terms of maximum peak ground acceleration (PGA) are favoured trigger

mechanisms for slope failure on the northeastern Cretan slope. To quantify those local impacts, 1-D, infinite slope models are employed to back-analyse slope stability versus instability under pseudo-static and also static conditions. Results imply that the high shear strength (S_u) of the sediment (i.e. >5.0 up to 8.75 kPa/m S_u -vs.-depth-gradients) requires high PGAs of >29 and up to 42%g to cause failure at the scale of the detected midsize and major MTDs. The repetition-time of these PGAs, and thus also of earthquakes that may cause these PGAs, is hence suggested to be as low as that of at least major slope collapses (i.e., ~250 ka). Lower PGAs are considered to do not affect the slope catastrophically, while they may cause smaller sediment failures as well as creeping and de-watering of mid-slope MTDs. Moreover, these seismic loadings are suggested to strengthen the sediment column through development of excess pore-water pressures and subsequent drainage.

Amongst the impacts from regional seismicity, the high impacts of tectonic movements and resulting sediment truncations and offsets from faults along the Cretan margin are important in slope instability development. This is indicated by two studies on (1) structural interpretations of fault patterns and the overall slope architecture of the northeast Cretan slope compared to the distribution of landslides, and (2) numerical modelling of the kinematic behaviour of cohesive sediments during deformation to oversteepening slopes, indicating the significance of sediment properties and tectonics in slope-failure development. Hence, both studies imply that the Cretan slope sediment plays a key role in the observed tectonic deformation, which in turn is important for the pre-conditioning of sediment for failure. In contrast, slope stability analyses have shown that the relative importance of the tectonic deformation to the seismic triggers is low. However, volumetric proportions and failure kinematics of the cohesive landslides, as well as their further transport and disintegration to mass-flows afterwards are governed by the Cretan margin basin flank tectonics.

Overall, the results imply that (1) an infrequent recurrence of landslides along active margin slopes can be caused by a high shear strength of the slope sediment cover requiring an accordingly high (seismic) trigger, (2) the only occasional occurrence of nearby earthquakes that generate PGAs sufficient to cause instability in cohesive sediments, (3) a frequent seismic background tremor that mostly prevails in such active margin settings is noncritical in terms of larger destabilization in cohesive sediment, while it may rather cause a dynamic compaction and thus a higher stability of strata, and (4) large-scale tectonic movements along basin flanks and associated fault kinematics as well as localized steepening of a slope govern a local restriction also of sediment collapses.

Zusammenfassung

Diese Arbeit ist eine Studie über die bisher nur wenig bekannten Prozesse und Faktoren, die ein Destabilisieren und Rutschen, aber auch ein mögliche Verstärkung von Sedimente an submarinen Hängen entlang aktiver Kontinentalränder verursachen können. Frühere Studien an aktiven Rändern (z.B. westliches Nordamerika) haben gezeigt, dass einige dieser Hänge verhältnismäßig geringe Wiederkehraten von Rutschungen aufweisen. Dies widerspricht der allgemeinen Erwartung vieler, kleinerer und regional weit verstreuter Rutschungen, die durch eine hohe neotektonische Aktivität bedingt werden könnten. Solch eine Erwartungshaltung existierte ebenfalls für den nordöstlichen Hanges der Insel Kreta im Zentrum der tektonisch hoch aktiven Hellenischen Subduktionszone im östlichen Mittelmeer. Die bisher weitestgehend unerforschte Anzahl, Verteilung und Wiederkehrate von gravitativem Sedimenttransport, aber auch die Kinematik und Mechanik einzelner Rutschungen sowie ihre möglichen Auslösemechanismen entlang des submarinen Nordrandes Kretas werden in dieser Studie deshalb untersucht und rekonstruiert. Die Ergebnisse werden dann in Hinblick auf offene Fragen bezüglich der Rutschungsaktivität entlang dieses und vergleichbarer aktiver Ränder diskutiert.

Mit Hilfe bathymetrischer Karten und seismischer Profile, die während der Poseidon Ausfahrt P336 im Frühjahr 2006 gewonnen wurden, konnten mehrere Rutschungsablagerungen und die mit ihnen assoziierten Abbruchkanten am Hang kartiert und ihr chronologischer und kinematischer Ablauf rekonstruiert werden. Es konnten drei verschiedenen Größen-Klassen an Rutschungen identifiziert werden: (1) große, teilweise tief im Sediment lagernde Rutschungsablagerungen mit ca. 30-50 km³ Volumen im Kamilonisi Becken am nordöstlichen Hangfuß Kretas, (2) Ablagerungen „mittlerer“ Größen-Klasse im sogenannten Malia Becken und am mittleren Hang nahe der Bucht von Mirabello, die auf kompakte, planparallele Rutschungen und Debris Flows mit Volumen von 0.5-2.5 km³ zurückzuführen sind, und (3) kleinste Sedimentumlagerungen, die als Zentimeter bis Dezimeter mächtige Lagen in Schwerelot-Kernen (P-336) von Fußbereichen steilster Hangabschnitte (z.B. an Abbruchkanten und die Flanken des Malia und Kamilonisi Beckens) erkannt werden konnten.

Das Alter und die Wiederkehraten dieser drei Größen-Klassen von Massenumlagerungen wurde mit Hilfe von deren Mächtigkeiten und den durchschnittlichen Akkumulationsraten (ca. 7.8 cm/ ka) von jüngeren Hintergrund-Sedimenten, die auf den Rutschungsablagerungen aufliegen, bestimmt. Dabei hat sich gezeigt, dass (1) die größten Rutschungen etwa alle 250 ka (\pm 70 ka) auftreten, wobei das jüngste dieser Ereignisse ein Alter von etwa 192 - 250 ka (\pm 50 ka) aufweist; (2) sich mittelgroße Rutschungen etwa alle 34 - 125 ka wiederholen (jüngste Ereignisse im Malia Becken haben ein Alter von ca. 25 ka (12.6 - 33 ka)), wobei diese auch als örtlich begrenzte Einzelereignisse auftreten können (z.B. am mittleren Hang nahe der Bucht von Mirabello, wo mehrere Rutschungen einen Komplex mit einem Alter von etwa 192 ka (\pm 50 ka) bilden); (3) die kleinsten Sedimentumlagerungen in Abhängigkeit von der Steilheit des Reliefs etwa alle 3-25 ka auftreten (höchste Frequenz am Hangfuß

des Kamilonisi Beckens). Da sich die Rutschungsaktivität den vorliegenden Daten nach hauptsächlich auf die hier klassifizierten Größen beschränkt, und die größten, aber seltensten Rutschungen dabei den Großteil der umgelagerten Sedimentmasse darstellen, ist die durchschnittliche Wiederholungsrate von markanten Hangrutschungen am Nordost-Rand Kretas als relativ niedrig einzustufen. Die begrenzte Verteilung und geringe Wiederholungsrate von Rutschungen charakterisiert den untersuchten Nordost-Rand Kretas zudem als „kohäsiven Hang“. Dies wurde durch morphometrische Vermessungen der Rutschungsablagerungen, der assoziierten Abbruchkanten und der Geometrie des umliegenden Hanges sowie den geotechnischen Eigenschaften der beprobten Sedimente bestätigt.

Die Seismizität der Hellenischen Subduktionszone ist für europäische Verhältnisse ungewöhnlich hoch, und demnach ein wahrscheinlicher Auslösemechanismus für submarine Hangrutschungen in dieser Region. Um die Auswirkungen von Scherkräften durch Erdbeben induzierte Bodenbeschleunigungen auf die Hangsedimente zu quantifizieren, wurden infinite 1-D Modelle des Kretischen Hanges unter solch pseudo-statischen, aber auch statischen Bedingungen getestet. Die Ergebnisse dieser Tests verdeutlichen, dass die hohe Scherfestigkeit der kohäsiven Hangsedimente (Gradient der Scherfestigkeitszunahmen >5.0 bis 8.75 kPa/m) dafür verantwortlich ist, dass starke Beschleunigungen von >29 %g bis 42 %g für das Auslösen mittlerer beziehungsweise großer Rutschungen benötigt werden. Die Wiederkehrrate solch hoher Beschleunigungen liegt höchstwahrscheinlich in der Größenordnung der Frequenz der kartierten Rutschungen. Beschleunigungen geringerer Intensität treten in deutlich höheren Frequenzen auf, haben aber anscheinend kaum Auswirkungen auf die Stabilität der Sedimente am Hang und verursachen maximal kleinste Massenbewegungen entlang steilerer Hangbereichen. Zudem wird ein Zusammenhang hochfrequenter Beschleunigungen mit einem „Kriechen“ und Entwässern bereits vorhandener Rutschungsablagerungen am Hang vermutet. Darüber hinaus besteht die Möglichkeit, dass lokale Bodenbeschleunigungen unterhalb kritischer Grenzwerte die Hangsedimente zusätzlich verfestigen. Hierbei bauen sich kurzzeitig für ein Abrutschen der Sedimente unkritische Porendrucke auf, die die intakten Hangsedimente nach Abbau des Porendrucks entwässern können und die Sedimente so letztendlich stärker konsolidieren.

Neben diesen Auswirkungen seismischer Aktivität auf die Hangsedimente spielen großtektonische Bewegungen des aktiven Kontinentalrands und die resultierende, lokale Störungsaktivität eine wichtige Rolle bei der Destabilisierung. Dies konnte anhand (1) struktureller Interpretationen der Störungen sowie der generellen Entwicklung des Kretischen Hanges im Vergleich zur Verteilung und Wiederkehrrate von Rutschungen, und (2) numerischen Modellen des kinematischen Verhaltens kohäsiver Sedimente während ihres Versteilens entlang solcher Beckenflanken verdeutlicht werden. Die Studien implizieren, dass sich die mechanischen Eigenschaften der Sedimente entscheidend auf die tektonische Entwicklung des Hanges auswirken, die wiederum ein wichtiges Kriterium für die

Ausbildung von Rutschungsereignissen ist. Die Hangstabilitäts-Analysen (s.o.) zeigen jedoch, dass die Wichtigkeit der tektonischen Deformation auf das eigentliche von Rutschungen gegenüber den seismischen Scherkräften relativ gering ist. Nichtsdestotrotz sind die Störungstektonik und das damit einhergehende Versteilen des Kretischen Hanges mitverantwortlich für die Lokationen, Proportionen und die Kinematik von Rutschungen am Norostrand Kretas. Generell treten Rutschungen dann als kompakte, kohäsiven Sedimentkörper auf, die im sich während ihres möglichen weiteren Transports zu Debris Flows umwandeln können, und so letztendlich am Hangfuß (Malia Becken, Kamilonisi Becken) ablagern.

Zusammenfassend und übergreifend implizieren die Ergebnisse dieser Studie, dass (1) eine geringe Wiederkehrrate von Rutschungen entlang aktiver Ränder (wie am Beispiel des Nordrand Kretas) durch eine hohe Scherfestigkeit der Hangsedimente und entsprechend starke Anforderungen an einen Auslösemechanismus zurückgeführt werden können, (2) ein nur gelegentliches Auftreten starker, Erdbeben induzierter Bodenbeschleunigungen in der näheren Umgebung möglicherweise die benötigten Scherkräfte am Hang produzieren kann um größere Rutschungen in den kohäsiven Sedimenten zu initialisieren, (3) der die an aktiven Rändern typische, hochfrequente Erdbebenaktivität nur selten Scherkräfte produziert, die größere Rutschungen in kohäsiven Sedimenten auslösen können, und (4) die zunehmende Versteilen von submarinen Hängen und assoziierte Störungen das Vorkommen von Rutschungen auf bestimmte Bereiche kohäsiver Sedimentpakete beschränken können.

Table of contents

1. INTRODUCTION	11
1.1 Motivation	11
Submarine landslides and geohazards	11
Triggers of submarine landslides	11
Environmental reconstructions from landslide deposits.....	14
Landslides classification and global distribution	15
1.2. The eastern Mediterranean case study.....	19
1.3 Outline of the thesis.....	22
2. REGIONAL SETTINGS	25
2.1. The Hellenic subduction zone	25
2.3 Regional seismicity and seismic hazard risk	27
2.2. Setting in the southern Hellenic forearc basin (Cretan Sea).....	30
3. APPLIED METHODS	35
3.1 Preparation and application of acoustic data	35
3.2 Sediment attributes and slope stability assessment	37
3.3 Design and performances of numerical models	37
4. NEW EVIDENCE FOR MASSIVE GRAVITATIONAL MASS-TRANSPORT DEPOSITS IN THE SOUTHERN CRETAN SEA, EASTERN MEDITERRANEAN	39
4.1. Introduction	39
4.2. Geological setting along the Hellenic subduction zone	40
4.3. Methods	43
4.4. Observations & Results	44
4.4.1 Bathymetric data.....	44
4.4.2 Seismic reflection data:	45
4.4.3 Core data	50
4.5. Interpretations.....	51
4.5.1 Seismic units and seafloor textures	51
4.5.2 Age control from core and seismic data	53
4.6. Discussion	53
4.6.1 Conceptual model.....	53
4.6.2. Trigger mechanisms	55
4.7. Summary & Conclusions.....	56
4.8. Acknowledgments	56

References	57
5. RECONSTRUCTION OF RETREATING MASS WASTING FROM PROGRESSIVE SLOPE STEEPENING OF THE NORTHEASTERN CRETAN MARGIN, EASTERN MEDITERRANEAN	61
5.1. Introduction	62
5.2. Regional settings	63
5.3. Data and methods	64
5.3.1. Multibeam bathymetric data	64
5.3.2. Seismic data	64
5.4. Observations from acoustic data	65
5.4.1. Relief and seafloor morphology from bathymetric data	65
5.4.2. Seismic characterization of sediments	66
5.5. Interpretations	72
5.5.1. Timing and evolution of slope failure and mass-movements	72
5.5.2. Identification of mass-movement types	76
5.6. Discussion and Conclusions	76
Acknowledgements	79
References	79
6. SLOPE FAILURE REPETITION IN ACTIVE MARGIN ENVIRONMENTS – CONSTRAINTS FROM SUBMARINE LANDSLIDES IN THE HELLENIC FOREARC, EASTERN MEDITERRANEAN	81
6.1. Introduction	81
6.2. Tectonical setting	83
6.3. Data and methods	85
6.3.1 Acoustic data	85
6.3.2 Sediment physical properties data	85
6.3.3 One-dimensional, undrained, infinite slope stability analysis	86
6.4. Results	87
6.4.1 Geophysics, lithology, and geotechnical testing	87
6.4.2. Slope stability analyses and trigger evaluation	92
6.5. Conclusions and general implications	94
Acknowledgements	96
References	96
7. OVERSTEEPENING AS A KEY FACTOR FOR GRAVITATIONAL MASS MOVEMENT COMPARING COHESIVE AND NON-COHESIVE SLOPES UTILIZING DISCRETE-ELEMENT MODELS	101
Abstract	101

7.1. Introduction	101
7.2. Methods	103
7.2.1 The Discrete Element Method.....	103
7.2.2 Model configuration - 2D numerical biaxial tests.....	104
7.2.3 Model configuration - extensional basin flank.....	106
Limitation and capabilities of this model	107
7.2.4. Interpretation techniques	108
7.3. Model results	109
7.3.1 Cohesive slope ‘sediments’ - model A.....	110
7.3.2. Non-cohesive slope ‘sediments’ - model B.....	113
7.4. Interpretation & Discussion.....	116
7.5. Conclusion.....	119
8. SYNTHESIS: CONCLUSIONS AND OUTLOOK.....	125
8.1. The northeast Cretan margin mass-movement patterns	125
8.2. Triggers and pre-conditioning factors	126
8.3 General implications.....	128
8.4 Future perspectives & outlook	129
9. ACKNOWLEDGEMENTS AND REFERENCES.....	131
Acknowledgements	131
References	131

1. Introduction

1.1 Motivation

Submarine landslides and geohazards

The study of submarine landslides has grown since the pioneer studies of the Grand Banks landslides and tsunami that occurred in 1929 (Heezen and Ewing, 1952; Heezen et al., 1954). Given that about 60% of the world's population is settled in coastal areas, and thus in range of oceanic geohazards such as landslide-induced tsunamis, the socio-economic interest in causes and consequences of submarine landslides strongly increased (e.g. Masson et al., 2006). According to the high advancement of submarine acquisition techniques, the quality of data improved enabled deeper insights into processes and conditions that may cause landsliding as well as landslide tsunami initiation (Locat and Mienert, 2003; Camerlenghi et al., 2007; Cochonat et al., 2007). Much of what is known today about submarine mass movement has been established from the increasing number of case studies (e.g., Canals et al., 2004), which are often also combined to international campaigns (e.g., the Costa-project, Mienert et al., 2004; Canals et al., 2004, and references therein). Well known example are e.g. the Storegga Slide and the related tsunami offshore central Norway (e.g., Harbitz, 1992; Bondevik et al., 2005), the Mauna Loa, Hawaii, flank collapse and tsunami (Morgan et al., 2007), and the Nice Airport landslide and tsunami recorded in 1979 in the northwestern Mediterranean Sea (e.g., Mulder et al., 1997; Savoye et al., 2005). Many of these examples have already proven the destructive capacity of submarine landslides. But they have also shown that a landslide tsunami risk for a particular region is defined by the landslide recurrence rate, the totally displaced sediment volume, its transport dynamic, and the total runout distance of sliding masses (e.g. Synolakis et al., 2002; Bardet et al., 2003; Nadim, 2006). Consequently, more and more examples of landslide deposits are investigated in case studies for reconstructions of landslide failure and transport kinematics as well as slide mechanics to gain deeper insights in their geohazard potential (Bardet et al., 2003; Bradshaw et al., 2007). From the various environmental processes that may govern the initiation of landslides some can be geohazardous processes as well, e.g. earthquakes, storm waves, tsunamis or volcanic eruptions (e.g. Sultan et al., 2004; Mienert, 2007). This implies that impacts from both the landslide and the trigger can potentate a region's immanent geohazard risk (e.g., Tinti and Maramai, 1999). However, in many cases the particular factors and processes leading to landslides and their consequences are still poorly understood (e.g., Camerlenghi et al., 2007; Cochonat et al., 2007). Study on submarine landslides is thus of high priority to shed light on their trigger mechanisms as well as their consequences for the vulnerable coastal areas worldwide (e.g., Masson et al., 2006; Mienert, 2007).

Triggers of submarine landslides

In principal, a pure inclination causing gravitational driving stresses downslope that exceed the shear-resistance of a sediment column is required for its destabilisation and initiation of mass movement (e.g. Lee et al., 2007). The sediment's resistance (Eq. 1) against gravitational shear forces (Eq. 2) is

mainly defined by cohesion and friction defining a critical angle of response. A definition of a sediment's shear strength is principally given by its Mohr-Coulomb failure criterion (Coulomb, 1776), which represents a linear envelope obtained from the shear strength versus the applied normal stress. This relation is expressed as

$$[1] T_f = C' + (\sigma_n - u) \tan \phi,$$

where T_f is the shear stress at failure (or the material's shear strength S_u), C' is the effective cohesion, $\tan \phi$ is the friction angle, σ_n is the gravitational stress acting normal to the failure surface, and u is the pore water pressure ($\sigma_n - u$ then is the effective normal stress (σ_n')).

For the case that only gravitational loads act on a slope, the shear stress (T_s) for an infinite surface acting downslope is given by

$$[2] T_s = \gamma' z \sin \alpha,$$

where γ' is the submerged density of the sediment (total sediment density minus the density of seawater), z the depth below seafloor, and α the slope inclination (Fig. 1A).

As a consequence of that, a failure of a sediment load may occur when the downslope driving stress (T_s) exceeds the sediment's shear strength (T_f ; Fig. 1A). This ratio is expressed in a *Factor of Safety* ($FS = T_f / T_s$; Morgenstern and Price, 1965; Fig. 1A), which indicates either sediment stability ($FS > 1$) or sediment failure ($FS \leq 1$ or $T_f \leq T_s$; see also Chapter 6.3.3). Furthermore, the occurrence of sedimentary units that are mechanically weaker than the ambient sediment, e.g. clayey layers, may reduce the shear resistance of the entire sediment column (e.g., Huhn et al., 2006; Kock and Huhn, 2007). Such 'weak layers' are thus hypothesized to play a key role in landsliding (e.g., Loseth, 1999; Mienert et al., 2005).

Nevertheless, in many cases of submarine landsliding slope angles were reconstructed to have been much below a critical inclination depending on the sediment attributes, and their initiation required an additional stimulus (e.g., Hampton et al., 1996; Sultan et al., 2004; Lee et al., 2007; Shanmugam, 2009). Today, many long-term as well as instantaneous processes are known to can facilitate sediment failure by either a decrease of sediment strength (affecting T_f ; Equation 1) due to transient excess pore pressure, additional shear forces increasing the downward driving stresses (affecting T_s ; Equation 2), or a combination of both (e.g., Pestana et al., 2000; Stegmann et al., 2007; Sultan et al., 2004; Lee et al., 2007; Fig. 1B). Many of such trigger mechanisms are well-known today, and the most favoured are seismic shaking (e.g. Leynoud et al., 2009; Table 1), high fluid flow (e.g. groundwater seepage), gas charging, and gas hydrate dissociation (e.g. Loseth, 1999; Mienert et al., 2005; Behrmann et al., 2006; Table 1), as well as sealevel changes, tidal changes, wave activity, diapirism, rapid sediment

accumulation and under-consolidation, as well as erosional processes (Posamentier and Vail, 1988; Kayen and Lee; 1991; Hampton et al., 1996; Lee et al., 2007; Dan et al. 2007; Mienert, 2007; Lee, 2008; Shanmugam, 2009; Table 1; Fig. 1B). In addition to these natural processes, today's strong increase in on- and offshore exploration and property built-up is recognized to can also trigger landslides. Here, transients in excess pore pressures may occur from e.g. the additional loads of property build-up (Seed et al., 1988; L'Heureux et al., 2007) and dynamic loads from e.g. explosions (e.g., L'Heureux et al., 2007). Consequently, major efforts on the knowledge of causes of slope failures are also aimed in parallel with the exploration and exploitation of offshore industries (Barley, 1999).

Table 1) Examples of submarine landsliding and the here determined or suggested trigger mechanism(s) indicating the broad range of causes for submarine slope failure development

Documented trigger	Example	Reference
Earthquake	Grand Banks, west coast US	<i>Fine et al. (2005), Locat and Lee (2002), McAdoo et al. (2004)</i>
Hurricanes/ cyclic loading	Mississippi Delta	<i>Prior and Coleman (1982)</i>
Oversteepening/ loading	Nice, Canary Islands	<i>Assier-Rzadkiewicz et al. (2000)</i>
Underconsolidation	Mississippi Delta	<i>Prior and Coleman (1982)</i>
'Weak layers'	east coast US, Storegga, west coast Africa	<i>Longva et al., 1996</i>
Gas hydrate dissociation	east coast US, Storegga	suggested by <i>Sultan et al. (2003)</i>
Sea-level changes	Madeira Abyssal Pain	suggested by <i>Weaver and Kuijpers (1983)</i>
Volcanic activity	Hawaii, Canary Islands	<i>Moore et al. (1989), Masson et al. (2002)</i>

From the numerous triggers known for submarine landslides, seismicity or seismic loading is favoured in many cases, because earthquake shakings occur from a variety of source mechanisms in many different environments, e.g. active margin subduction earthquakes, passive margin glacial loading rebound, thermal adjustments, regional compression earthquakes, and volcanic eruption seismicity (see summary in Leynaud et al, 2009). It has been shown that these regions are often characterized by frequent instability of their submarine slopes (e.g., Locat and Lee, 2002; Lee et al., 2007). Consequently, seismicity is hypothesized to be one of the most important and frequent trigger mechanisms in landslide initiation (e.g. Lambe & Whitman, 1969; Lee, 1985; Locat and Lee, 2002; Sultan et al., 2004; Masson et al., 2006). As earthquakes produce loading stresses from ground accelerations in the sediment column that decrease with distance to the hypocentre (e.g. Main and Burton, 1989), the location of a target area relative to the earthquake source as well as the dynamic behaviour of the sediment column play key roles in slope instability development (e.g. Biscontin and Pestana, 2006). The allocation of earthquakes and their impacts as ground acceleration, producing either high shear stresses (e.g., Hampton et al., 1996), a degradation of the sediment (e.g., Pestana et

al., 2000) or both, are thus important for a trigger evaluation of sediment failure development along natural slopes (e.g., Sultan et al., 2004).

As shown in equation 1, each particular sediment (or sediment composition) will have its characteristic physical attributes causing either a high or a low initial resistance against sliding (see above). The quantitative requirements for a trigger causing failure are then accordingly high or low (Hampton et al., 1996; McAdoo et al., 2000; Shanmugam, 2000; Lee et al., 2007). But the temporal and spatial variability of landslides in terms of sediment attributes vs. quantitative trigger requirements is, however, not totally understood for many cases. Hence, today's research on causes of submarine landslides aims on a confrontation of the mechanical sediment strength against the quantity of potential trigger mechanism exerted by the environment (Locat and Lee, 2002; Biscontin et al., 2004; Biscontin and Pestana, 2006; Masson et al., 2006). Furthermore, the broad spectrum of environmental processes and conditions that are known to may cause sediment instability often lead to speculations about the type and the relative importance of a trigger (e.g. Lee et al., 2007; Leynoud et al., 2009). Quantitative approaches on slope stability and instability scenarios regarding sediment attributes, the regional framework of pre-conditioning factors, and most likely triggers are still major research targets.

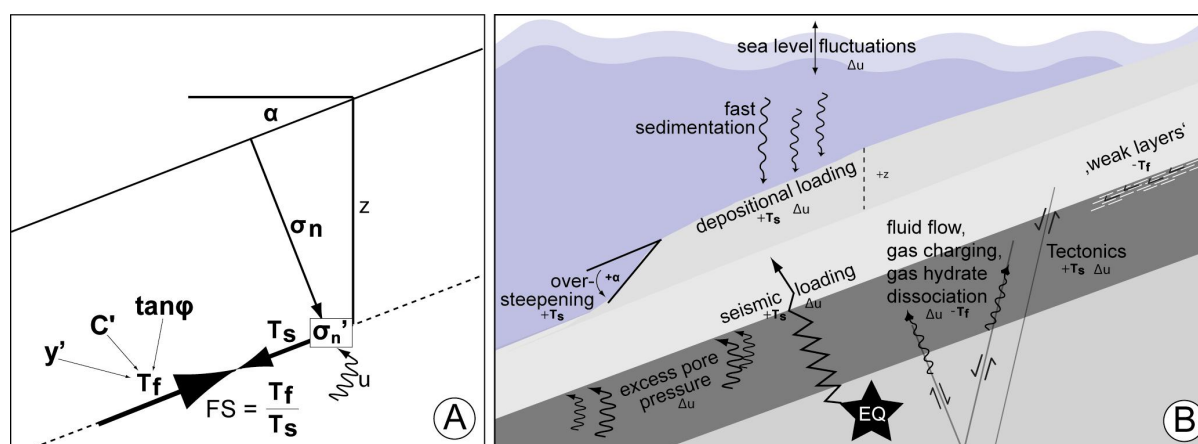


Fig. 1 **A:** Simplified sketch of forces acting on an inclined (α), submarine slope along an infinite surface in a distinct depth (z). The Factor of Safety (FS) displays the ratio of gravitational shear forces acting downslope (T_s) to resisting forces (T_f) that depend on the sediment attributes (cohesion (C'), friction ($\tan\phi$), and submerged density (γ')); **B:** Sketch of geological and climate-driven processes and how they may attend in sediment instability (not to scale). Note that these processes can cause transients in excess pore pressure and weakening of the sediment in depth or provide direct shear stress on the slope body.

Environmental reconstructions using landslide deposits

Due to the fact that mass-movement deposits are often preserved in the sedimentary record they can be used for reconstruction of environmental changes and conditions associated to sediment failures. It has also been shown that landslides can (i) affect the further evolution of sedimentary systems, e.g. by modifying the distribution pattern of submarine channels (e.g., Lastras et al., 2004), (ii) change slope architecture (e.g., O'Grady et al., 2001; Hutton and Syvitski, 2004), and (iii) be associated with

particular environmental conditions, processes, and changes, that are expressed in the recurrence, scale, and class of the mass-movement deposits (e.g. Coleman and Prior, 1988; Shanmugam, 2000; Mienert, 2007; Lee et al., 2007).

Such reconstructions of environmental changes associated with occurrences of mass movements were done, for example, by Hanebuth and Henrich (2008), who reconstructed a joint mechanism of turbidite activity and Sahara dust import to the Mauritanian shelf using the regular frequency of mass-transport deposits. Another example is given in Kayen & Lee (1991), who reconstructed the last eustatic sealevel fall to be expressed in a landsliding generation on the continental slope of the Beaufort Sea, and further suggest that this process probably operated at many other locations in the world's oceans at the same time.

Landslides have also been successfully used for paleo-seismicity reconstructions, e.g. for dating and localization of major subduction zone earthquakes along the western North America Cascadian margin (e.g., Goldfinger et al., 2003; McAdoo et al., 2004), major earthquakes in the Switzerland from Lake Lucerne landslide deposits (e.g., Strasser et al., 2006), or dyke intrusions and related seismic activity during caldera-forming on the western Canary volcanic island from associated landslides (Masson et al., 2002). But today there are still many environmental settings and regions where accurate landslide deposit examination and a reconstruction of their cause and effects may shed light on the open questions regarding processes and changes in the broad range of tectono-sedimentary systems (as proposed in e.g. Canals et al. (2004)).

Landslides classification and global distribution

Owing to the broad range of sedimentary settings where landslides occurred (e.g. Coleman and Prior, 1988; Mienert, 2007; Cochonat et al., 2007; Shanmugam, 2009; Table 1), mass movements have been classified in terms of their failure and transport mechanics as well as kinematics, their transport velocities, the runout distances, and their geometry and degree of deformation during transport and after deposition (Table 2).

Table 2) Basic terminology of mass movements recommended by Varnes (1958), Lee et al. (2007), and Shanmugam (2009)

Mass movements ^[1]	Slide	Slump	Creeping	Debris or mass flow	Turbidite
<i>Failure-plane geometry</i>	planar	concave	-	-	-
<i>Mass-movement geometry</i>	coherent, blocky ^[2]	coherent, blocky ^[2]	coherent, blocky ^[2]	clasts in fine grained matrix, coherent body	suspension, incoherent body
<i>Deformation degree</i>	low to intermediate	low to intermediate	low	Intermediate to high	high
<i>Transport</i>	translational	rotational	-	laminar	turbulent

<i>Velocity</i>	slow to fast	slow to fast	very slow	slow to fast	fast
<i>Runout</i>	short ^[3]	short ^[3]	(very) short	large	large

[1] Note that the use of the terms ‘landslide’ and ‘mass movement’ as well as ‘slope failure’ and ‘slope collapse’ is unbiased throughout this thesis

[2] Disintegrated, larger slides of rapid movement are referred to as ‘debris avalanches’ (Lee et al., 2007)

[3] Runout distance of slides and slumps can be large in terms of disintegration to ‘mass-flows’

Studies comparing the different mass-movement types in various sedimentary settings have shown that mass-flows and turbidites are more typical for slopes bearing non-cohesive sediments (e.g. terrigenous clastics), while compact slumps and slides preferentially occur along slopes dominated by cohesive sediments (e.g. hemipelagic muds) (e.g., Lee et al., 2007; McAdoo et al., 2000; 2004; Shanmugam, 2000; 2009; Table 3). Consequently, the global distribution of submarine mass movement as well as the distribution of the different mass movement classes is not uniformly (e.g., Mulder and Cochonat, 1996; Lee et al., 2007; Tables 2 and 3). Furthermore, the different classes of submarine mass movements and their distribution in environments typical for slope failure indicate that landslides tend to occur commonly often where (i) thick bodies of the respective sediments can be found (i.e. cohesive and non-cohesive), (ii) the slopes are steep, and (iii) the loads exerted by the environment are high (Lee et al., 2007). Regions where these conditions often met are fjords (e.g. Karlsrud and Edgers, 1982; Locat et al., 2003), active river deltas (e.g. Piper et al., 1982), submarine canyon-fan systems (e.g. McAdoo et al., 2000), volcanic island slopes (e.g. Masson, 2002; Morgan et al., 2007) and the open continental slopes that provide almost 50% of the currently known landslides (e.g., Canals et al., 2004; Lee et al., 2007).

Table 3) Compilation of some prominent mass-movements or mass-movement assemblages in active and passive margin settings as well as on volcanic island flanks.

Name	Location	Mass movement	Age	Volume [km ³]	Thickness [m]	Reference
<i>Active margins</i>						
Heceta Slide - Coos Basin Slide - Blanco Slide	Cascadian, W coast USA, Oregon	Debris flows	110, 450, 1210 ka	75.6	30-400	<i>Goldfinger et al., 2000; McAdoo et al., 2000</i>
Cascadian slumps	Cascadian, W coast USA, Oregon	Slumps, slides	110, 450, 1210 ka	0.5-40	10-90	<i>McAdoo et al., 2000 ; 2004</i>
Cadeb	Central Adriatic deformation Belt	Creeping, end-term slide	11.5 ka BP	38.5	<15	<i>Lee et al., 2002</i>
Palos Verdes	W coast USA, L.A., N27°W	Debris avalanche	7.5 ka BP	0.34-0.72	10-12	<i>Locat et al., 2004</i>

<i>Passive margins</i>						
BIG'95	E coast Spain, Mediterranean	Debris flow	11.5 ka BP	26	35	<i>Casas et al., 2002; Canals et al., 2002</i>
Storegga Slide	NW Norway	Debris flow, turbidites	6 -50 ka BP	~3.500	30	<i>Haflidason et al., 2004</i>
Afen Slide	NW Shetland Islands	Landslide	5.8 ka BP	1000	20	<i>Wilson et al., 2003</i>
Amazon Fan	NW Brazil	Debris flow	100 ka BP	1000	50-100	<i>Piper et al., 1997</i>
Gulf of Mexico	S coast USA	Debris flows, slumps	-	(5-150) 687	50-300	<i>McAdoo et al., 2000</i>
<i>Volcanic island flanks</i>						
Canary; San Andres, El Golfo, El Julan, Las Playas	Spain, Canary Islands; 200 km ESE of the Madeira Abyssal Plain	Slide, debris flow; debris flow, slump	10-17 ka; 10-545 ka	400; <30-180	10; 200-300	<i>Masson et al., 1998; Masson et al., 2002</i>
Mauna Loa landslide; Hilina Slump	Mauna Loa, Hawaii	Landslide, debris flows, slump	1.5 Ma; 120 ka; 1868	~3000 (in total)	≤ 500	<i>Morgan et al., 2007; Okubo, 2004</i>

In closer inspection of mass movements along passive margins, they often occur as single, large debris flows and turbidites of low recurrence rate (Table 3), which is often associated with the low tectonic activity in literature (e.g., Booth et al., 1993; Halifladson et al., 2003; Wilson et al., 2003). In contrast, the higher tectonic activity in active margin systems is hypothesized leading to a higher frequency in slope failure and a higher number of mass-movement events, often occurring as smaller and compact slides and slumps (e.g., Coleman and Prior, 1988; Hampton et al., 1996; McAdoo et al., 2004; Shanmugam, 2009; Table 3).

But recent studies have shown that there are also some contrary cases of only fewer landslides along present-day tectonically active margins, e.g. the western North America accretionary margin, especially along the Cascadian (Goldfinger et al., 2003; McAdoo et al., 2000; 2004) and the Eel margin (e.g., Nittrouer, 1999). The high shear strength caused by over-consolidation of accreted sediments is suggested as the key factor limiting the frequency of slope failure events in such settings. Hence, it could have been shown that also active margin environments can exhibit only infrequent sediment failures despite a general expectation of high-frequent landsliding in settings, where the load of trigger mechanisms exerted by the environment is high. But the conditions and processes leading to such peculiar settings in the many different tectono-sedimentary active margin environments are not completely understood.

Owing to these many open questions addressing submarine landslide research, this thesis focuses on the following general research target:

- 1) Why does a high neotectonic activity in active margin environments not necessarily fulfil the 'paradigm' of extensive, diffuse mass movement?**

- 2) What is the role of tectonic movements and seismicity in settings of only infrequent slope failure events? What other factors play a role in long-term slope stability?**

- 3) According to that, what quantities of ground acceleration exerted by seismicity (i) can be observed in the target areas and (ii) are sufficient for slope destabilization?**

- 4) What sediment compositions can be identified, and what is their role in (i) slope stability vs. instability, (ii) quantitative trigger requirements, and (iii) tectonic deformation?**

1.2. The eastern Mediterranean case study

The broad spectrum of tectono-sedimentary systems in the Mediterranean Sea - active and passive margins as well as volcanic island flanks, and therewith associated earthquakes, volcanic eruptions, landslides as well as about 10% of the worldwide reconstructed and recorded tsunami events make this region the most geohazardous one in Europe (see data in e.g. Galanopoulos et al., 1964; Papadopoulos and Chalkis, 1984; Tinti and Maramai, 1999; Yalciner et al., 2002; Fig. 2).

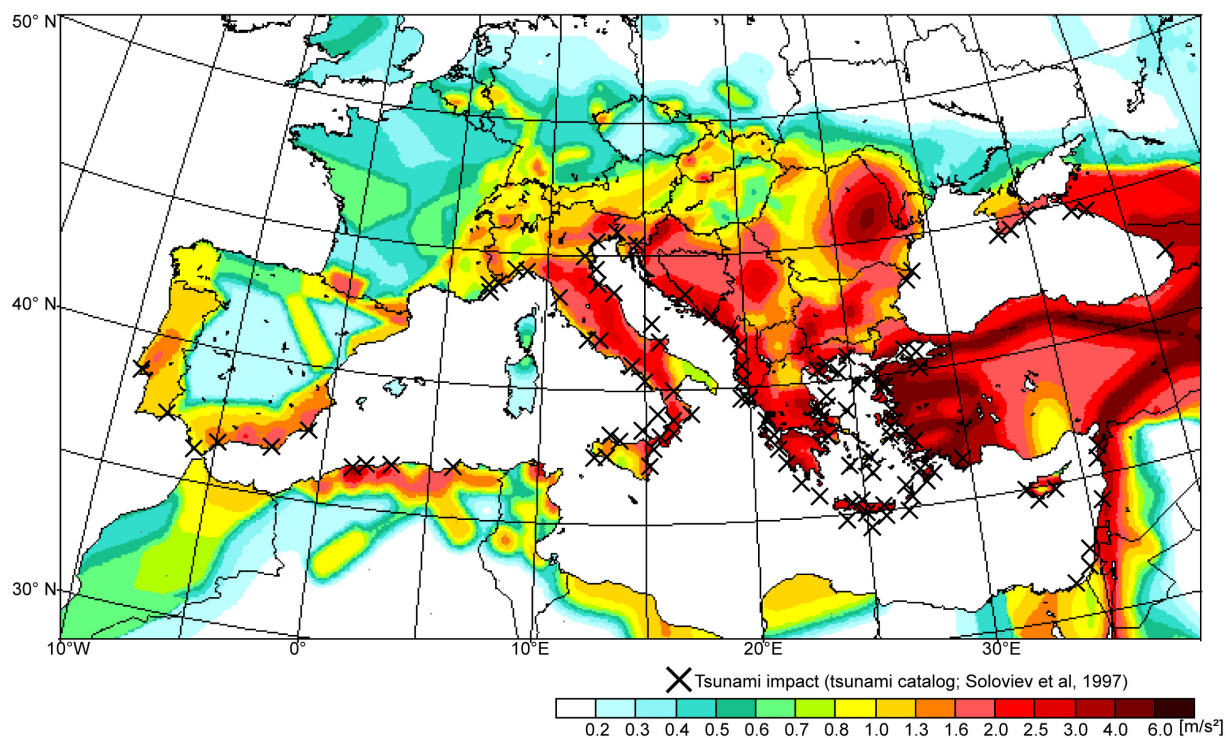


Fig. 2) Seismic hazard map of the European-Mediterranean region, coloured in terms of peak ground acceleration (PGA) at a 10% probability of exceedance in 50 years for stiff soil conditions, published in 2003 under the auspices of the European Seismological Commission (GSHAP global seismic hazard map (Giardini, 1999); modified after Grünthal et al., 1999). Crosses mark some of the more than 250 detected tsunami impacts in the Mediterranean region from 1500 to 1990 (tsunami catalog; modified after Soloviev et al., 2000).

As it was already shown that particular tectono-sedimentary settings generally tend to characteristical mass-movement patterns, the broad range of environments in the Mediterranean Sea provides inventories for a respective variation in patterns of landslides and triggers (e.g. Dominey-Howes et al., 2000; Canals et al., 2004; Camerlenghi et al., 2009; Morgan et al., 2009). A recently assembled catalogue of the in total 232 detected mass-movement events/ deposits in this region (Camerlenghi et al., 2009; Fig. 3) indicates the high variability in mass movement: most frequent and largest deposits are megaturbidites and mass-/debris-flows (i.e. unusually large turbidity currents) found in the deeper abyssal plains and sourced from the southern and western passive margins, e.g. the Nile deep sea fan (e.g., Garziglia et al., 2008; Fig. 3) or the Ebro continental slope, respectively (Lastras et al., 2004; 2006; Casas et al., 2003; Fig. 3). Compact slides and slumps are only barely found, mainly in the in

the eastern Mediterranean active margin system as volcanic islands flank collapses (e.g. the Santorini flank collapse, Dominey-Howes et al., 2000; Fig. 3), single, smaller events in the western Aegean Sea (Fig. 3), and along the western Grecian coast (Lykousis et al., 2004; Fig. 3). Further, ‘mass wasting’ events along the eastern Mediterranean Ridge (e.g., Zitter et al., 2003; 2005; Lykousis et al., 2004) are dominant in the southern part of the eastern Mediterranean Sea. Single slide deposits are further known from the southern margin of the island of Crete (e.g. the Lithonian Slide (Huisson and Fortuin, 1974); Fig. 3).

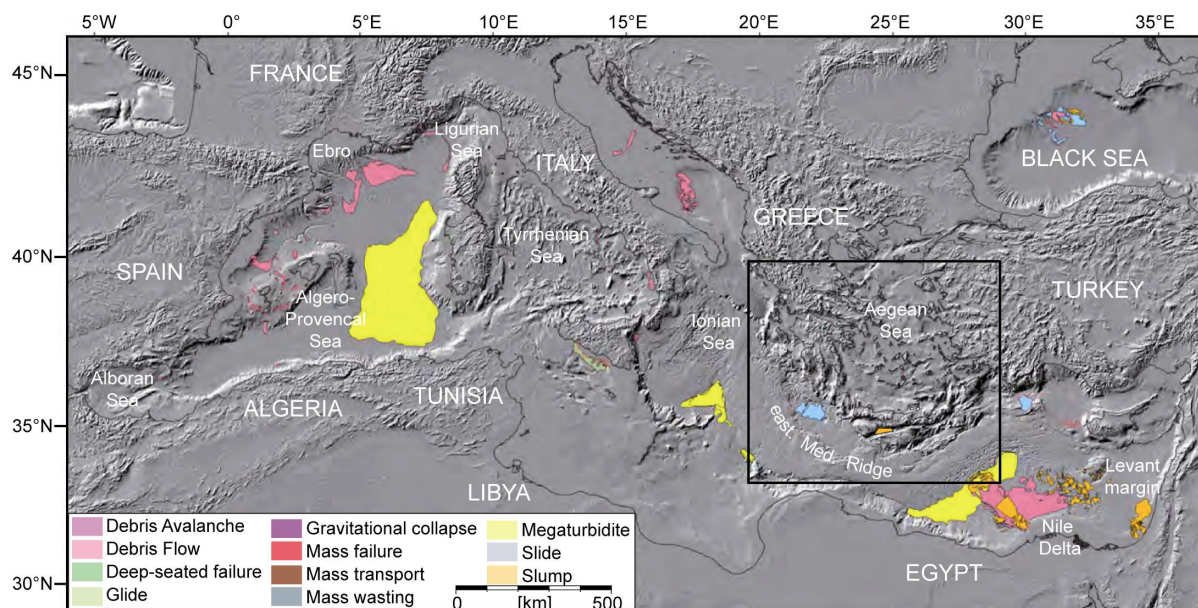


Fig. 3 Chart of submarine mass-movement deposits (MTDs) in the Mediterranean Sea and surroundings, superimposed to a shaded relief map of regional bathymetry (modified after Camerlenghi et al., 2009). Note that the MTD classification refers to various manuscripts and does not follow a uniform nomenclature (see Camerlenghi et al. (2009) and references therein). The black box indicates the area of interest in the eastern Mediterranean active margin system (Fig. 4A).

Numerous of the Mediterranean Sea landslides are known to have played a role in tsunami initiation, often associated with earthquakes (e.g. Papazachos et al., 1986; Soloviev, 1990; Salamon et al., 2007; Papadopoulos and Fokaefs, 2005). For example, the large and highly destructive *Amorgos Bain* landslide and tsunami in 1956 in the south Aegean Sea (Fig. 3) are associated with an M_s 7.5 earthquake localized in the eastern Cyclade islands (Papazachos et al., 1982; Fig. 4A). Due to a high number of recently recorded landslide tsunami events, e.g. the 1979-Nice Airport landslide and tsunami (Mulder et al., 1997; Savoye et al., 2005), the small dimension of the Mediterranean Sea and the close proximity of such hazard sources to coastal target areas are responsible for this region’s high vulnerability compared to others in Europe (e.g., Papadopoulos et al., 1995; Tinti and Maramai, 1999; Camerlenghi et al., 2009; see also Fig. 2). Hence, more than 250 tsunami impacts were recorded in the last 200 years (Soloviev et al, 2000; see Fig. 2), resulting in a frequency about one tsunami every 8 years (Soloviev, 1990; GITEC-TWO, 1999). This frequency confronts the today’s densely-populated Mediterranean coastline with a high probability for damage in infrastructure and casualties of human

lives (Tinti and Maramai, 1999; Camerlenghi et al., 2009). As publicly proposed (e.g. Barcelona, 2006, IODP Submarine Landslides Workshop; IODP Geohazards WS Portland, 2007; Magellan workshop ‘Ocean Drilling for Seismic Hazard in European Geosystems’ Luleå, 2008), the landslide and landslide-to-tsunami activity in large parts of the eastern Mediterranean region is still insufficiently understood, although there is a high socio-economic necessity for studies on the local landslide and landslide-tsunami activity (see e.g., IODP proposal #715 ‘MEDSLIDES’ by Camerlenghi et al., 2007).

Literature shows that previous studies on Mediterranean Sea active margin landslides focused on volcanic arc island flank collapses in the northern Cretan Sea as well as tectonic impacts on the sediment along the eastern Mediterranean Ridge (Fig. 4A). In contrast, the landslide activity in the forearc region in-between the ridge and the volcanic arc is still less explored although this region’s high seismicity and large tectonic movements provide a solid framework for frequent slope instability. In consequence of these shortcomings, a detailed investigation of the landslide activity in this region focused on (i) the occurrence of landslide deposits, (ii) ages and recurrences of reconstructed slope failure events, (iii) the impact of neotectonic activity on slope stability, and (iv) assessment of trigger mechanisms and pre-conditioning factors leading to landslides is the key target of the here presented studies.

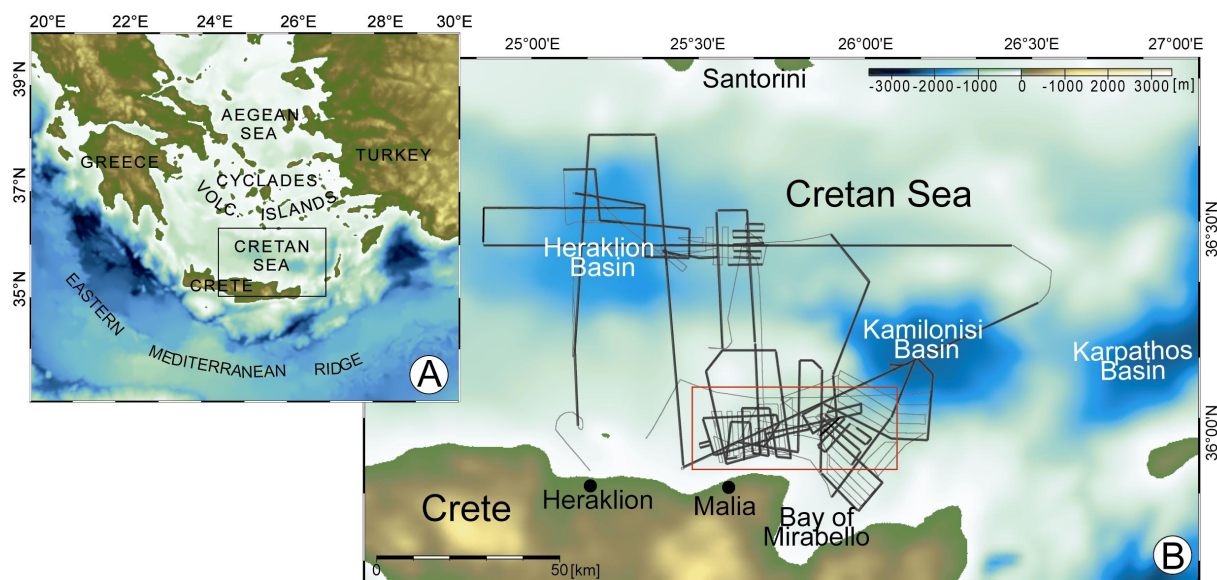


Fig. 4) A: Map of the eastern Mediterranean region and the location of the area surveyed during the CRESTS cruise north of Crete in the southern and central Cretan Sea (see Fig. 2B); **B:** Commercial bathymetric chart of the area surveyed during the CRESTS cruise P-336 (Kopf et al., 2006). Thin black lines indicate total cruise tracks, comprising continuous multibeam bathymetry mapping and partially 3.5 kHz as well as multi-channel reflection seismics acquisition (thick black lines). The red box indicates the location of the study areas investigated for this Ph.D. project (see Fig. 10)

Consequently, this thesis is a deeper insight into mass-movement occurrence and development along the northeastern margin of Crete and the adjacent southern Cretan Sea. Multi-methodological data sets

recovered during the CRESTS (Cretan Sea Tectonics and Sedimentology) research cruise with R/V Poseidon (P-336) in this region in spring 2006 (Kopf et al. (2006); Fig. 4B) are investigated and analyzed. Seismic units of chaotic reflection patterns as typical for submarine landslide deposits have already been detected on pre-stacked seismic profiles onboard (Kopf et al., 2006; 2007). These units provide a solid fundament for the closer inspection of the northern Cretan margin mass-movement activity. The results will address the open questions regarding slope-failure development here as well as in comparable active margin settings in a more general context (see chapter 1.3).

1.3 Outline of the thesis

According to the general research targets (see Chapter 1.1) and the open questions concerning the landslide activity in the southern Cretan Sea and along the northern margin of Crete (see Chapter 1.2), the following description of published or submitted manuscripts (Chapters 4-7) that make up the core chapters of this thesis will briefly commit on how these issues are addressed.

[1] **Chapter 4** (published in *Marine Geology*) deals with a first closer view on landslides characteristics for the northeast Cretan slope. The starting point is a detailed description of youngest mass-transport deposits (MTDs) in the Malia Basin located in the mid-slope region. A reconstruction of mass-movement transport paths, transport distances, failure and transport kinematics as well as mechanics is carried out. Further, MTD ages are assessed from a combination of marker horizon age-dating, local sediment accumulation rate estimates, and drape thickness measuring on top of MTDs. Measured variations in the slope gradients, interpreted faults in the areas of landslide source scars, and regional seismicity are here firstly hypothesized to have played a key role in slope failure development.

[2] **Chapter 5** (submitted to *Marine Geology*) deals with additional findings of landslide deposits also in a mid-slope position approximately 10 km east of the Malia Basin. The kinematical reconstruction of these slides to a retrogressive landslide complex is used to determine slope angles providing critical threshold values for slope stability and destabilization, and thus a discussion on the role of slope architecture sediment failure development. Except this complex, the adjacent slope shows still stable sediment cover or is devoid of both intact sediments or MTDs. Based on that, the long-term NE Cretan slope mass-wasting history is reconstructed and discussed. Furthermore, the found number of such MTDs is rated to be relatively low.

[3] In **chapter 6** (submitted to *Journal of Geophysical Research - Solid Earth*) the type and quantity of seismic triggers for the detected mid-slope landslides as well as for newly discovered large-scale MTDs in the adjacent Kamilonisi Basin are assessed. Therefore, sediment properties provided by Annika Förster (MARUM) and the cruise report (Kopf et al., 2006) are utilized to characterize Cretan slope sediment mechanics and the quantity of an earthquake trigger required for failure using slope

stability analysis. The low repetition-time of major Kamilonisi Basin MTDs is then confronted to the recurrence of earthquake-induced peak ground acceleration from a seismic hazard risk catalog (EPPO). The results are then discussed in terms of infrequent, large-scale slope collapses in active margin environments depending on recurrence rates of their seismic triggers vs. slope sediment strength.

[4] **Chapter 7** deals with the impact of large and long-term tectonic movements and fault kinematics associated to distinct sediment mechanics on the occurrence, dimension and recurrence rate of mass movements on extensional basin flanks. Therefore, near-surface mass movements are investigated from 2-D numerical Discrete Element models. Large assemblages of two granular materials, representing (i) muddy cohesive and (ii) sandy non-cohesive sediments are designed and deformed to steep inclined slopes. Model results are used to determine characteristic recurrences and dimensions of mass movements due to the deformational behaviour and critical inclination of the cohesive vs. non-cohesive sediments during large-scale and long-term extensional basin flank movement. Given active basin subsidence and incremental oversteepening of a slope as essential for slope failure, model results can also be compared to the similar tectonic setting of the northern margin of Crete as well as other environments.

2. Regional settings

2.1. The Hellenic subduction zone

The eastern Mediterranean region represents the boundary zone of the African, the Eurasian, the Aegean and the Anatolian plates (Fig. 5A). The central region (Fig. 5B) is dominated by the convergence of the subducting African and the overriding Aegean lithospheric plates (Fig. 5A). These tectonic movements still occur today as indicated by recent records of subduction seismicity (e.g., Meier et al., 2004; 2006), volcanic activity (e.g., Bohnhoff et al., 2006), and GPS plate motion records (e.g., Reilinger et al., 2006). Hence, the plate convergence is still proceeding as well as it was reconstructed to be active since the last 35 million years at minimum (e.g. McKenzie, 1978; Mercier et al., 1979). Thereby, dominant large-scale geodynamic processes of this retreating system are slab subduction, sediment accretion, arc magmatism, and back-stop exhumation in the forearc, as well as fore- and backarc extension (see summary in e.g. Thomson et al., 1998; McClusky et al., 2000; Fig. 5B and 6). Consequently, the entire region contains different tectono-sedimentary settings, including (from south to north) (i) slab subduction and the subduction trench, (ii) the Mediterranean Ridge accretionary complex, (iii) the Cretan island forearc high, (iv) the Cretan Sea forearc basin, (v) the volcanic island arc, and (vi) the Aegean Sea backarc basin (see Figs. 5 and 6).

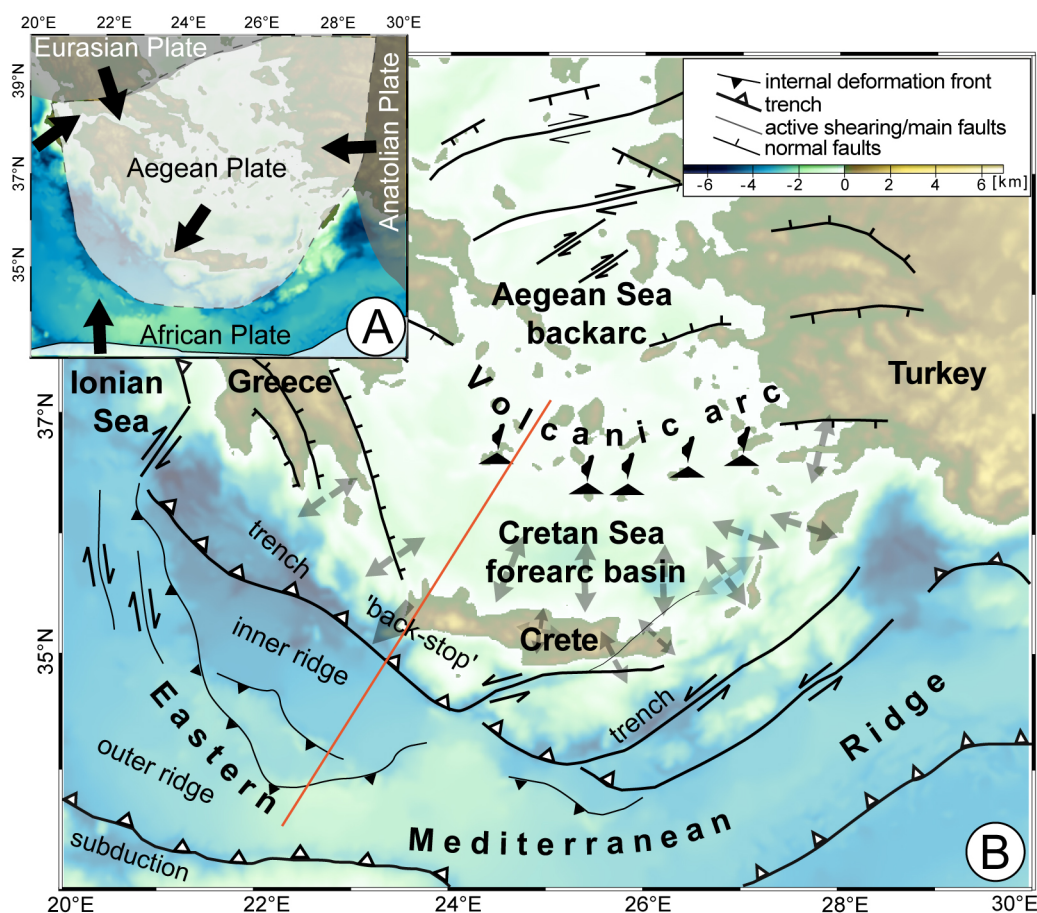


Fig. 5 **A:** Simplified sketch of eastern Mediterranean plate boundaries. Arrows indicate the convergent motion directions of the African, Aegean, Eurasian, and Anatolian plates; **B:** Generalized setup of the

Hellenic subduction zone resulting from the plate convergences. Arrows indicate the trends of extension in the forearc region. The red line refers to the cross-section shown in Fig. 6.

Thicknesses, dips, and dynamics of the African and the Aegean plate, as well as the depth of their boundary were interpreted from receiver functions, surface waves, and microseismicity provided by on- and offshore seismic networks (e.g., Meier et al., 2004). As a result, the convergence between the African and the Aegean plate was reconstructed to proceed with a mean speed of 3 cm per year (African plate ~ 1 cm/a, Aegean plate ~ 4 cm/a; Fig. 6), back-calculated to a total slab subduction of about 1200 km (e.g., Papazachos et al., 1992). Further, the present day African slab, which can be traced into 200-250 km depth, is interpreted to have an average low dip angle of 15-20° that increases from the west to the east (Meier et al., 2004; Ganas and Parsons, 2009). Hence, the slab is steeper towards the east and resulting dip gradients beneath the central Aegean plate region are determined to 30-40° in up to 180 km depth (e.g., Papazachos et al., 1995; Ganas and Parsons, 2009). In addition to varying slab dips, the African plate is subducted, or the up to 35 km thick Eurasian plate is overriding at different velocities (e.g., Robertson and Mountrakis, 2006). In account for the plate thicknesses, the relatively low dip and the lower subduction velocity of the African slab in the west, both lithospheric plates are here stacked one on top of the other, and only a thin asthenosphere is predicted in between (e.g. Meier et al., 2004).

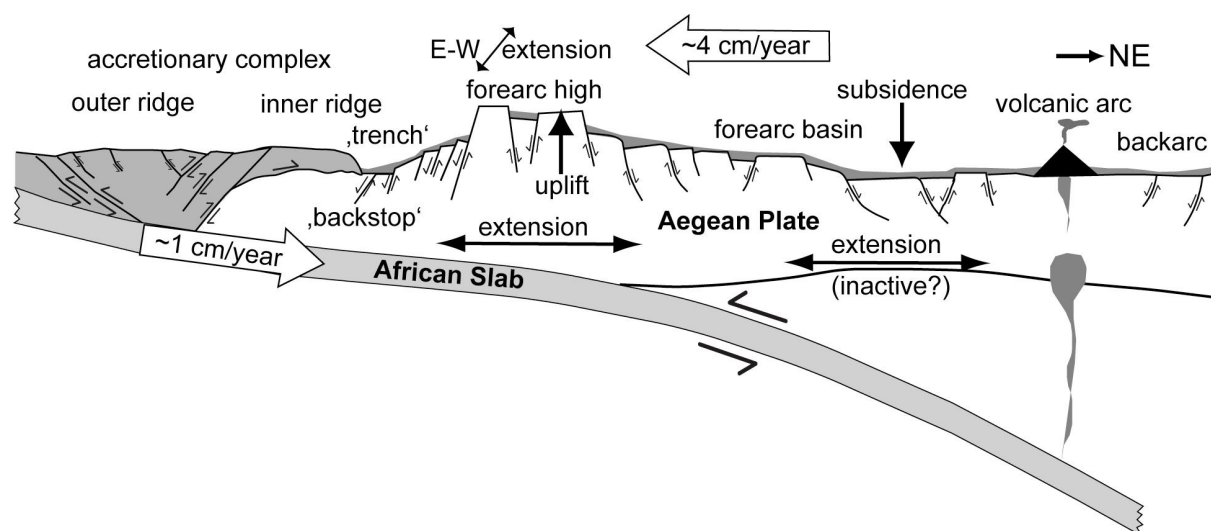


Fig. 6 SW-NE cross-section through the Hellenic subduction zone (not to scale) showing the overall geodynamic situation compiled and modified after Kopf et al. (2003; 2006), Meier et al. (2004) and Fassoulas (2001). For location see Fig. 5.

Owing to the maturity of this plate convergence, the African plate's sedimentary cover was continuously accreted to the eastern Mediterranean ridge south of Crete (McKenzie, 1978; Thomson et al., 1998; Fassoulas et al., 1994). The result is a large accretionary complex of approximately 1500 km in E-W- and about 250 km in N-S-extent today (Camerlenghi et al., 1995; Chaumillon and Mascle, 1997; Kopf et al., 2003). This complex comprises a southern outer ridge, which is about ~ 100 -120 km in N-S-extent, underplated by the African lithosphere from south, and a northern inner ridge of ~ 80

km N-S-extent, which is thrust towards the southern margin of Crete to the north (Polonia et al., 2002; Figs. 5 and 6). The inner ridge and the island of Crete thereby function as a backstop for the entire accretionary complex (Kopf et al.; 2003; Le Pichon et al., 2002; Figs. 5 and 6). Backthrusting of the accretionary wedge over the inner ridge further resulted in the development of several arc-parallel depressions, described as ‘trenches’ south of Crete (Camerlenghi et al., 1992; Chaumillon and Mascle, 1997; Fig. 6). As the Aegean plate continuously rides up the African slab, this backstop is permanently uplifted as exemplified by formation of the island of Crete, which continues to rise at rates about 6 mm/a (e.g., Ganas and Parsons, 2009). Hence, the island of Crete represents a horst structure (e.g., Pirazolli, 1982; Fig. 6) of stacked thrust nappes that exhumed since a slap break-off at approximately ~19 Ma B.P. (Bonneau 1984; Fassoulas et al., 1994). But its today’s tectonic setting of an uplift pattern is seen to more closely resemble a continental thrust in some places than a typical oceanic subduction zone (Ganas and Parsons, 2009).

North of Crete, the Cretan Sea forearc basin, the Aegean Sea backarc basin, and the volcanic arc between (e.g. Aksu et al., 1995; Dominey-Howes et al., 2000; Giresse et al., 2003) are suggested to have developed in the last 24 Ma (e.g. McKenzie, 1978; Mascle & Martin, 1990), while the main basin creation phase was reconstructed to occurred between the Late Miocene and Pliocene (Mascle & Martin, 1990). The opening from N-S- as well as E-W-extension resulting in subsidence to these large depressions is kinematically interpreted to occur from the faster south-westward advancement of the Aegean plate over the African plate (Mercier et al., 1979; Le Pichon & Angelier, 1979; Ganas & Parsons, 2009). This motion is suggested to be much slower in the eastern part in the boundary area to the Anatolian plate (see boundary in Fig. 5A). Here, the west-southwest movement of the Anatolian plate due to northward movement and collision of the Arabian plate with the Eurasian plate also affects Aegean plate deformation (e.g. McKenzie, 1978; Thomson et al., 1998; Sato et al., 2004). As a consequence, subsidence rates at least in the Cretan Sea increase from west to east, and several complex tectonic features established through time (Le Pichon 1983; Hatzfeld et al., 1993; Dilek, 2006, and references therein; see also section 2.1.3). Postma et al. (1993) summarized the forearc basin as an asymmetric south-facing graben, controlled by large-scaled detachment faulting (Vandenberg and Lister; 1996; Fig. 7B; see section 2.1.3. for further details).

2.3 Regional seismicity and seismic hazard risk

The effect of local ground acceleration caused by active margin earthquake activity has already been hypothesized playing a key role in eastern Mediterranean slope instability development (e.g. Chronis et al., 2000; Kopf et al., 2007). The seismicity is much above European average in both intensity and frequency (Figs. 2 and 7) by reason that more than 4000 earthquakes of $M_s \geq 4$ were recorded in the last 45 years throughout the Hellenic subduction zone (ISC catalog; Papazachos et al., 2000b; Fig. 9A). Thereof, the largest recent earthquakes had magnitudes of $M_s = 7.3$ (Ambraseys, 2001). A

maximum magnitude back-calculation from ISC catalog data suggests $M_s = 7.8 \pm 0.4$ for the Hellenic forearc region (Hamouda, 2006). Furthermore, historical and archaeological studies suggest that earthquakes that occurred near Crete in 365 A.D. (e.g., Stiros, 2001) and 1303 A.D. (e.g., Guidoboni and Comastri, 1997) have been in the order of $M_s > 8$, and thus have been much larger than earthquakes recorded in recent times.

Major earthquake source mechanisms in the Hellenic subduction zone have been classified to four zones, whereof (i) in the outer accretionary ridge (see section 2.1.1) earthquakes are mainly caused by NW-SE compressional movements in less than 50 km mean depth, (ii) the inner ridge is dominated by thrust- and reverse faulting earthquakes in 50-70 km depth, (iii) in the arc region, including the island of Crete, the southern to central Cretan Sea and the larger part of the Grecian peninsula earthquakes are sourced by E-W-extensional as well as Hellenic Arc uplift tectonics in 70-100 km depth, and (iv) in the central to northern Aegean Sea earthquakes occur in 100-160 km depth from N-S backarc extension (Papazachos et al., 2000a; Bonhoff, 2001; 2006; Meier et al., 2004; 2007; Fig. 7A).

The most active earthquake epicentres concentrate in three clusters along the Hellenic arc (e.g., Pirazolli et al., 1996; Meier et al., 2004; Becker et al., 2006; Hamouda, 2006; Fig. 7A). The first of these clusters was correlated to interface-seismicity between the Aegean and the African plates and concentrated at 20 and 40 km depth and about 40-100 km in lateral width. Its N-S-extent is known to decrease to the east as the African slab dips steeper in this region (Meier et al., 2004; see also section 2.1.1). The second cluster is detected in the upper crustal levels of the Aegean lithosphere south of Crete (Fig. 1), while the third cluster is located in the upper 20 km beneath Crete, where a dense accumulation of hypocentres was also used to identify the uplifting character of the Cretan island and its interpretation to a horst structure (see e.g. Meier et al., 2007). In closer inspection, the coastline of Crete mimics the shape of a microseismically relatively quiet realm in the Aegean lithosphere at 20-40 km depth, suggesting a relation between active processes at this depth range and the horst structure uplift (Meier et al., 2007).

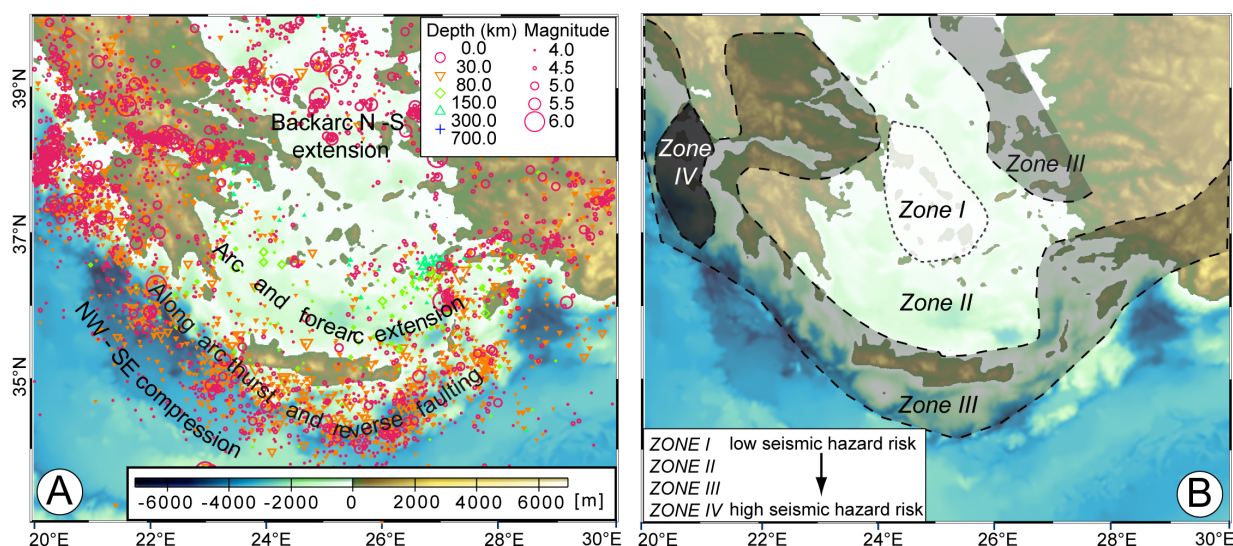


Fig. 7 **A:** Seismicity (ISC (International Seismology Centre) catalogue data 1964-2004; see also Manakou et al. (2000) and Bohnhoff et al. (2001)) and the major source mechanisms on a shaded relief bathymetry map of the Hellenic subduction zone and surrounding; **B:** seismic hazard risk zones for the Aegean plate (after EPPO (1992)).

Based on an approach of Aegean plate rheology and a uniformly dynamic behaviour of earthquake-induced ground acceleration, a formula that estimates local maximum peak ground accelerations (PGAs) depending on the epicentre and the magnitude of earthquakes was developed by Theodulidis (1991). The relation was inferred to be used for calculations of PGAs in target areas for known distance to the earthquakes magnitudes and epicentres, given by

$$[3] \log a = 1.77 + 0.49 M_s - 1.65 \log (D + 15),$$

where a [cm/s^2] is the PGA, D [km] is the distance to the epicentre, and M_s , the earthquake magnitude. Today it is known that such approaches disregard numerous possible source and side effects governing earthquake magnitudes to distant PGAs in accordance to e.g. seismic wave propagation and development, accumulation of plastic strains, or shear-induced excess pore water pressures with increasing number of loading cycles (see data in e.g. Sultan et al., 2004; Biscontin et al., 2001; Biscontin et al., 2004). A high inaccuracy for this approach in the Aegean region was exemplarily shown by Perissoratis and Papadopoulos (1999) for the Amorgos Bay earthquake and landslide (see section 1.2).

However, to shed light on the recurrence and intensity of local PGAs, the concept of ‘seismic hazard risk zones’ compiled by the EPPO (Earthquake Planning and Projection Organization of Greece, 1992; see e.g. in Papazachos et al., 1993) is considered. This approach indicates values of most probable maximum PGAs in four zones of the Aegean plate as a function of their mean repeat-time T_m (see also Perissoratis and Papadopoulos (1999)). The risk zone boundaries approximately correlate to the distribution of earthquake clusters (see above; compare Figs. 9A and 9B). *Risk Zone IV* (Fig. 7B)

represents highest risk for a frequent repetition of high ground acceleration and is located in the westernmost Hellenic subduction zone. *Risk Zone III* (Fig. 7B) with an approximately 500-years repetition of 29%g comprises most of the previously described earthquake clusters along the eastern Mediterranean Ridge, the trench system and western and central Greece. *Risk Zone II* (Fig. 7B) comprises the Cretan Sea, parts of southern Greece, a large part of the Aegean backarc, and can show about 22%g with $T_m=500$ years in a very high probability, whereas *Risk Zone I* (Fig. 7B) in the central Aegean region shows the lowest seismic hazard risk of about 14%g in a $T_m\sim 500$ -year repetition (Papazachos et al., 1993). The currently available hazard risk catalog data is based on today's earthquake records (ISC catalogue), whereof the zone boundaries as well as the predictable PGAs and their recurrence times in risk zones may be revised according to the increasing number of regional earthquake records (Papazachos et al., 1993).

2.2. Setting in the southern Hellenic forearc basin (Cretan Sea)

The tectonic setting in the investigated area and surrounding areas in the southernmost Cretan Sea and the northern margin of Crete (Figs. 4B and 8A) is dominated by (i) almost N-S basin extension (e.g., Le Pichon and Angelier, 1979; Ring et al., 2001; Fig. 8B), (ii) high subsidence rates in the central deeper depressions (e.g., the Heraklion Basin and the Kamilonisi Basin; Fassoulas et al., 1994; Stavrakakis et al., 2000; Fig. 8C), and (iii) tectonic movements along the surrounding, well-developed continental slopes, especially along the northern margin of the uplifting island of Crete (e.g., Mercier et al., 1979). Stratigraphic work of e.g. Drooger and Meulenkaamp (1973) showed that this part of the forearc mainly formed at 12 Ma B.P. and extension was accommodated along a series of large-scale, north-south-facing normal to strike-slip faults reaching up to 8-12 km depth (see also e.g., Chamot-Rooke et al., 2005; Ring et al., 2009 Fig. 8B). These low-angle detachment faults developed almost in parallel with the fault pattern onshore Crete (e.g., Fassoulas et al., 1994) and thus correlate to the south-north- to southeast-northwest-trend of the Cretan Sea extension relative to the arc (e.g., Mascle and Martin, 1990; Angelier et al., 1981). Mascle and Martin (1990) and Ring et al. (2001) figured out that a subordinated crustal block tilting (Figs. 8B and C) and a formation of half-grabens occurred (Figs. 8C). Opposite, it is still controversially discussed whether this graben formation is due to transpression or extension (Ring et al., 2001). However, according to the shape of the Hellenic arc at same longitudes, the axes of main structural elements that build-up the irregular and partially steep relief in the southern Cretan Sea (e.g., Fig. 8D) trend approximately southwest-northeast (McKenzie, 1978; Mascle and Martin, 1990).

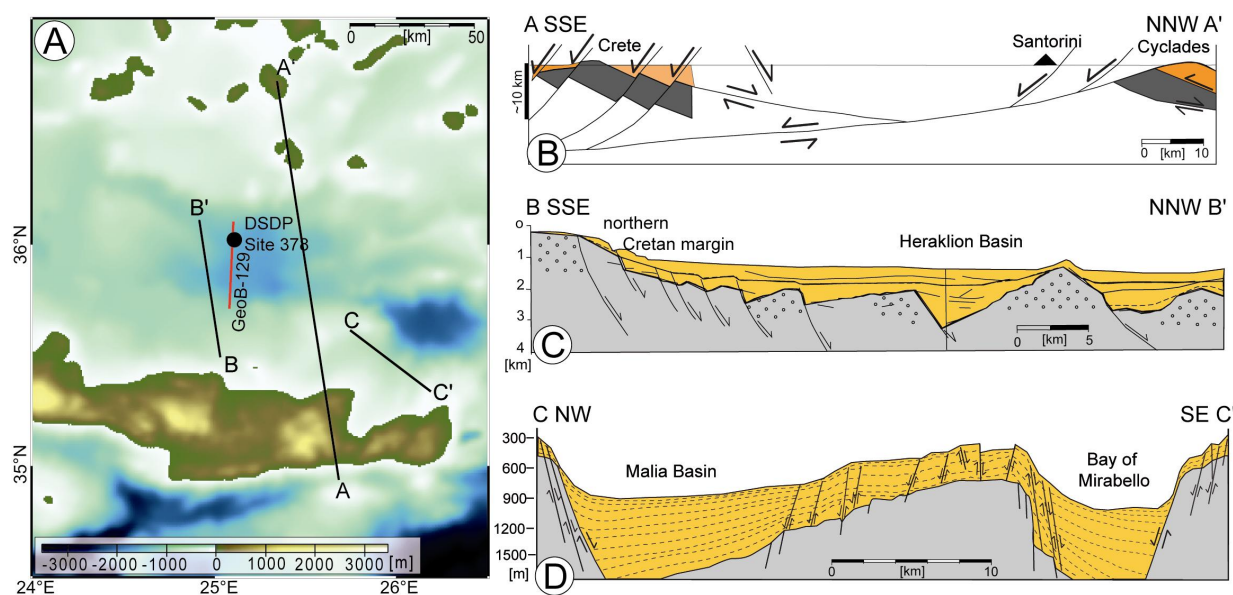


Fig. 8 A: relief map-plot of the central Cretan Sea. Black lines indicate the locations of profiles B-D showing the structural setup of the Cretan Sea in direction of main basin extension (red line and black dot show location of the seismic profile and DSDP core in Fig. 8); B: profile A-A' shows a generalized, conceptual cross-section model after Ring et al. (2001), indicating the Cretan nappes pile and probable relation of south-dipping high-angle normal faults to north-dipping Cretan detachment and south-dipping cross-cutting detachment (after Lister and Forster, 1996); C: profile B-B' traces northern margin of Crete and the southern margin of the Heraklion Basin cut at depth by normal faulting, interpreted from MCS seismic sections (the grey-yellow-boundary is interpreted as Messinian-Pliocene-boundary; after Mascle and Martin, 1990); D: profile C-C' shows the interpreted setup at the eastern study site (see chapters 5 and 6) based on a structural interpretation of Mascle and Martin (1990; see profile B-B'). Note that the acoustic basement (grey-yellow-boundary) may represent the Messinian-Pliocene-boundary similar to the latter profile (compare also to Fig. 8).

Furthermore, series of smaller, more localized faults strike approximately north-south and northwest-southeast and were traced back to (i) the sinistral basin transpression during incremental curvature of the entire Hellenic forearc (Fortuin and Peters, 1984), (ii) high subsidence of Cretan Sea sub-basins, e.g. the rhombohedral Kamilonisi Basin (Mascle and Martin, 1990), and (iii) the uplift of the Cretan island, and the consequent steepening of the northern Cretan slope (Fortuin, 1978; Mascle and Martin, 1990; Ring et al., 2001).

Therefore, the investigated area is dominated by southwest-northeast as well as southeast-northwest trends of faults and structural elements. The resulting irregular relief is an undulating system of morphological heights (i.e. block tilting) and lows (i.e. half-graben basins; Figs. 8C and D). However, despite studies on Cretan Sea tectonics, only little is known about the details of geometry and types of tectonic features which have been and are still active in the Cretan Sea (e.g., Mascle and Martin, Ring et al., 2001).

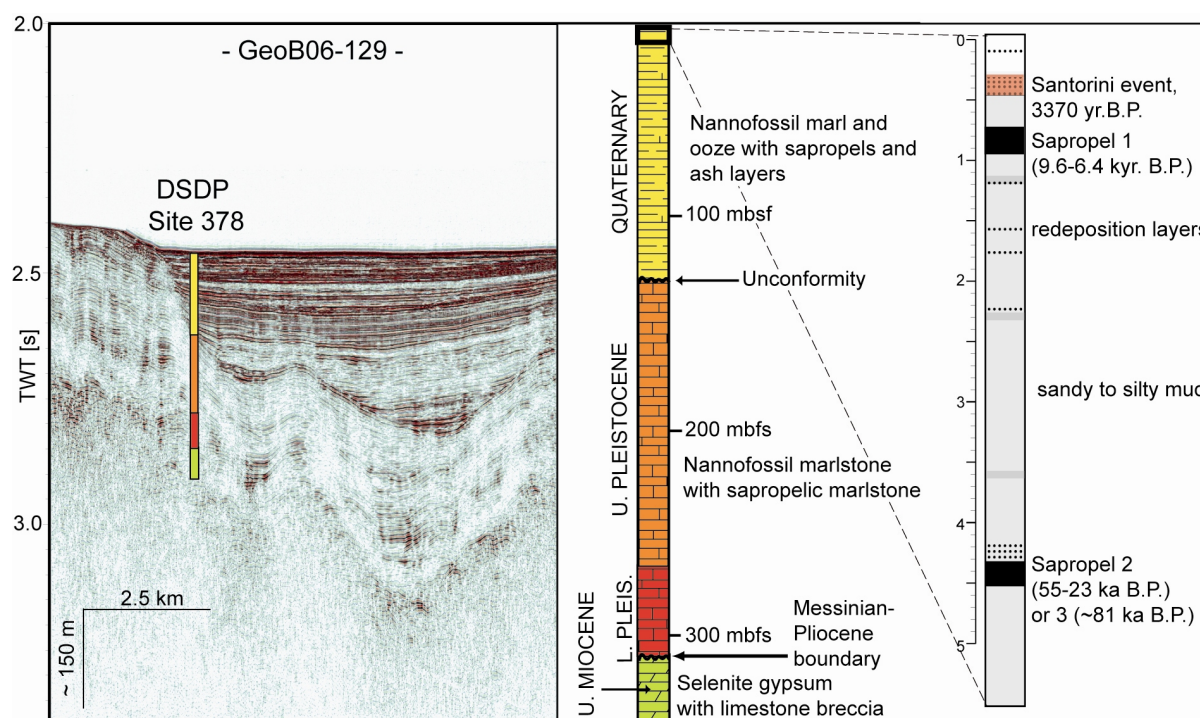


Fig. 9) Generalized lithostratigraphic setup (centre) recovered at DSDP core Site 378 in the central Cretan Sea (Hsü et al., 1978), projected to seismic profile GeoB-129 (left) recorded during P336 at the DSDP location, Heraklion Basin (for location see Fig. 4), and a standardized gravity core log recovered during P336 (Kopf et al., 2006; right) similar to other studies on the youngest northern Cretan margin lithostratigraphy (e.g., Aksu et al., 1995; Giresse et al., 2003).

What is known today about the sedimentary system and its evolution on the northern margin of Crete and in the southern to central Cretan Sea basin is based on gravity core sampling of the uppermost meters of sedimentary succession (e.g., Aksu et al., 1995; Geraga et al., 2000; Giresse et al., 2003; Chronis et al., 2000a, b; Kopf et al., 2006). The deeper lithostratigraphy is only marginally known from single DSDP cores in the Heraklion Basin in central Cretan Sea (Hsü et al., 1976; Fig. 9). Studies on the intact near-surface sediments have shown that the shelf region is dominated by coarse-grained clastics of terrigenous origin, while the slope and the deeper parts of the basin are dominated by finer hemipelagic lithology of biogenic origin (e.g., Chronis et al., 2000). Several sapropels and ashes are interbedded in those sequences of yellowish to brown- and grey-coloured, mud-rich sediments and were identified throughout slope as well as basin sediments (Aksu et al., 1995; Giresse et al., 2003; Fig. 9). Sapropel 1, mostly found in 0.5 to 1.5 meter below seafloor (meter below seafloor; 9.6-6.8 ka B.P.; Giresse et al., 2003 and references therein; Fig. 8), is an often used marker horizon (e.g., Aksu et al., 1995). Sapropel 2 (55-23 ka B.P.) and 3 (~81 ka B.P.) are partially present in approximately 4-5.5 mbsf (e.g. Muerdter et al., 1984; Giresse et al., 2003; Fig. 9). Ash-layers were detected and also used as marker horizons, whereof the layer according to the Z-2-Santorini event (3370 years B.P.; Pichler and Friedrich, 1976; Keller et al., 1978; Fig. 9) often occurs in 0.2 to 1.0 mbsf, and the X-1 Hellenic volcanic event (~80 ka B.P.; Keller et al., 1978) in about 5.0 mbsf (e.g., Kopf et al., 2006). Thereof back-calculated sediment accumulation rates are in the order of 7-20 cm/ ka for the Cretan margin as well as the Cretan Sea sub-basins (Hsü et al., 1976; Geraga et al., 2000; Giresse et al., 2003). Hence,

shallower gravity cores represent the sedimentary record of the last ten- to hundred thousands of years (e.g., Kopf et al., 2006; 2007). Furthermore, geotechnical tests on the physical and mechanical attributes of this mean sediment column were already performed by e.g. Chronis et al. (2000) and Kopf et al. (2006; 2007), indicating a high, undrained shear strength and high- to over-consolidation.

As already mentioned, the deeper Cretan Sea lithology was recovered at DSDP Site survey 378 in the Heraklion Basin (Hsü et al., 1976), where basin sediments were drilled up to 343.5 mbsf (Fig. 9). These cores showed (i) Quaternary nanofossil marls with sapropelic and marl conglomerate interlayers up to 64 mbsf, and nanofossil marls with interbedded sapropelic marls up to 131.5 mbsf, (ii) Late Pleistocene nanofossil marlstones and sapropelic marlstones up to 286 mbsf, (iii) Early Pliocene lithology of almost same composition up to 308 mbsf, and (iv) ‘selenite gypsum with minor limestone breccia’ below the prominent Messinian-Pliocene boundary in 308-343.5 mbsf (Hsü et al., 1976; Fig. 9). The interpretation of the shallower DSDP core lithostratigraphy in ≤ 130 mbsf indicates an almost consistent sediment composition (Hsü et al., 1976) that is almost consistent with that obtained for the uppermost meters at the northern Cretan slope (e.g., Giresse et al., 2003; Chronis et al., 2000; Kopf et al., 2006). As already suggested by Mascle and Martin (1990) also the seismic characteristics of this sediment column in the Cretan Sea sub-basins as well as in the southern Aegean Sea are similar to those along the Cretan margin, whereas their distribution and total thickness are strongly related to the differing structural characteristics of those regions (e.g., Jongsma et al., 1977).



3. Applied methods

With respect to the major targets of this Ph.D. project (see Chapter 1.3), an investigation, interpretation, and analyses of different data types as well as a combination of these multi-methodological approaches were carried out. A brief description of the data basis, the required preparation and interpretation techniques, as well as data merging strategies is given in the following. Note that details on the data acquisition techniques and already available data and results utilized in this study are given in Chapters 4-7 as well as in the P336 cruise report (Kopf et al., 2006).

3.1 Preparation and application of acoustic data

Different types of geophysical acoustic data are used as the basis for a detailed interpretation, measuring and analyses of seafloor and sub-seafloor features. Acoustic data acquisition during P-336 comprised a multibeam echosounder system, used for a continuous mapping of the seafloor, a conventional 3.5 kHz system for imaging the uppermost part of the sedimentary section, and a high-resolution multi-channel reflection seismic system to image the deeper sub-surface sedimentary and tectonic structures down to the acoustic basement (see also Kopf et al. (2006) and e.g. section 4.4). In this study, bathymetric charts that were created from multibeam echosounder data and processed multi-channel reflection seismic profiles are utilized for lateral tracking and interpretation of surface and sub-surface features, respectively.

Onboard pre-stacked seismic profiles, provided by Prof. Dr. Sebastian Krastel (IFM-GEOMAR) and Kopf et al. (2006), were used for a first screening of available data. Distinct sets of profiles and thus the closer areas of interest were selected (Chapters 4-6; Fig. 9). An accurate data preparation and processing of seismic data was carried out with Vista (Seismic Image Software Ltd.) to obtain high-resolution imaging of sedimentary and tectonic features. The data processing also reduced the range of uncertainty in lateral and vertical measures of seismic unit (see Chapters 4, 5, and 6). For a detailed description of seismic data processing working steps see Chapters 4.4 and 5.4. In a next step, seismic profiles were imported into commercial seismic interpretation software (Kingdom Suite; Seismic Micro-Technology Inc.). A detailed identification, tracing, and description of the dominant sedimentary units in terms of seismic character, e.g. amplitude, continuity, and reflection configuration were carried out (see Chapters 4 and 5). As this data examination focused on deposits from gravitational mass-transport (MTDs), generally characterized by a higher deformation of the sediment (e.g. Lee et al., 2007; Shanmugam, 2009), the respective chaotic to transparent conditions of seismic reflection patterns was used for an identification (see e.g. 4.5.2.1). Hence, MTDs can be traced in vertical and lateral direction using their pronounced sharp boundary to the surrounding, well-stratified pattern of intact slope and basin sediments (see e.g. 4.5.2.2 and 5.4.2). Further, prominent reflector off-sets in this background sediment pattern enabled the identification of (main) faults (e.g.

Figs. 4.5 and 5.4), as well as their lateral interpreted throughout cross-profiles (e.g. 5.4.2.1 and 4.5.2.2).

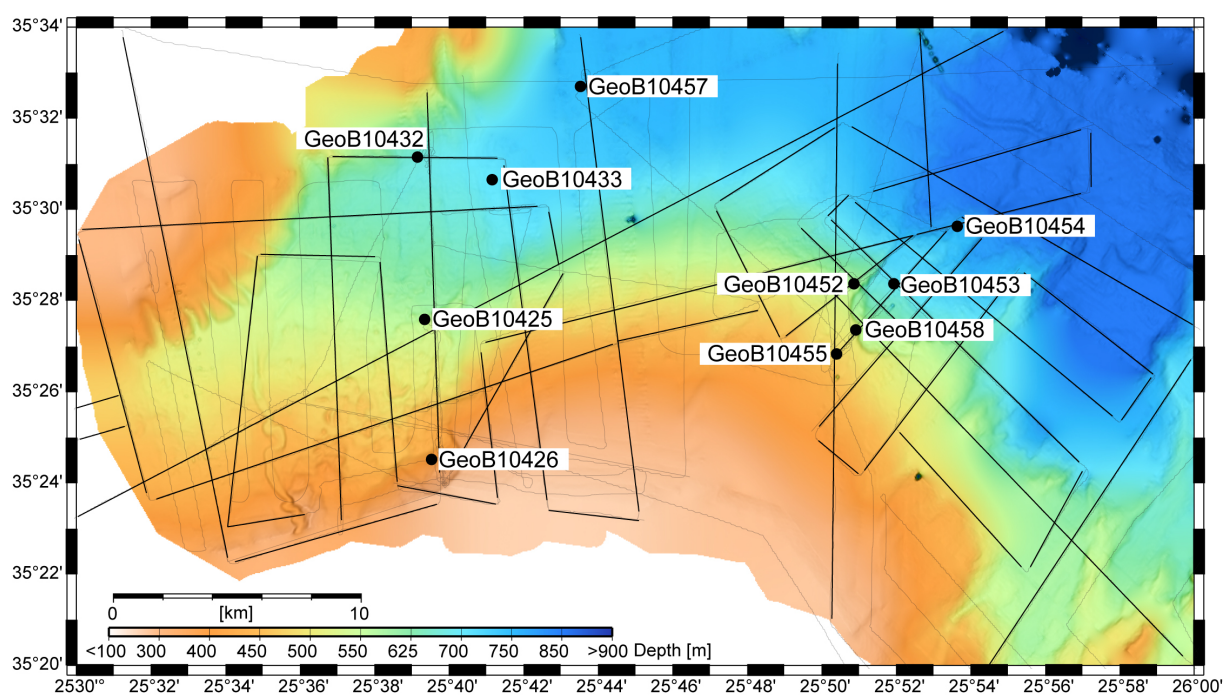


Fig. 10) Bathymetric chart of the investigated slope area compiled from echosounder data recovered during the P336 cruise (see section 1.2). The cruise tracks are marked as thin black lines and comprise the here investigated seismic reflection profiles (thick black lines). Further, 10 of the in total 11 coring stations utilized for this thesis are marked as black dots (after Kopf et al., 2006).

Bathymetric charts were used to investigate morphological seafloor features and the lateral extent of topographic elements (see e.g., Figs. 4.3A and 5.2A). As the onboard P336 used multibeam echosounder system was highly susceptible to sea conditions, as well as the quality of data generally decreases with increasing water depths (see e.g., Fig. 5.2A), data preparation in terms of single beam editing had to be carried out using MBSYSTEM (Caress and Chayes, 2006). After data editing, different visualization techniques provided by GMT (Generic Mapping Tool; Wessel and Smith, 1998), e.g. shaded relief plots (e.g. Fig. 4.3A) and slope gradient plots (Fig. 4.3B), were used to image the bathymetry charts (e.g., Fig. 10) and interpret small- and large-scale seafloor architecture (e.g. Figs. 5.2A and B). Further, the bathymetric charts were combined with seismic data for additional lateral interpretation of near-surface seismic units merged to surface features, e.g. MTDs (e.g., Fig. 5.2B), volumetric proportions of MTD source scars (Fig. 4.9), or major fault tracking depending on their offsets as relief structures and fault-scarps (e.g., Fig. 5.7). Publicly available bathymetric charts of much lower resolution (GEBCO data set (General Bathymetric Chart of the Ocean), provided by the British Oceanographic Data Centre (BODC)), were used to trace major relief elements and large topographic features throughout the limits of the high-resolution P336 bathymetric data (e.g. Fig. 5.1B).

3.2 Sediment attributes and slope stability assessment

To gain insight into (i) the regional lithological framework, (ii) sediment accumulation rates, (iii) the ages and recurrence rates of landslides, and (iv) the mechanical attributes of the slope sediment, lithological descriptions and geotechnical measurements from eleven P336 gravity cores (Fig. 10 and Fig. 6.2) provided by the P336 cruise-report (Kopf et al., 2006) were examined for this study.

In a first step, the already interpreted marker horizons (i.e. Sapropel 1, Z2 Santorini Event; Kopf et al., 2006; see chapter 2.1.2) were confirmed by ^{14}C -age dating, measured at Poznań Radiocarbon Laboratory, Poland (see 4.5.3 and Table 4.1). An interpretation of characteristic microfossil assemblages in additional cores (see 6.3.2 and 6.4.1.2) was carried out. The identification of planktonic microfossils was provided by courtesy of Dr. Barbara Donner (MARUM). Marker horizon ages were then combined to their stratigraphic depth in cores (e.g. section 4.5.3), enabling a back-calculation of mean accumulation rates for the study sites (see 4.6.2 and 6.4.1.2). Additionally, information on the deeper lithostratigraphic framework was adopted from the DSDP Site survey 378 in the Heraklion Basin (Fig. 9), provided by Hsü et al. (1978; see also section 2.1.3; Fig. 9) (for location see Fig. 4).

Results of geotechnical measuring on P336 cores, provided by Annika Förster (MARUM) and Kopf et al. (2006; 2007; see section 6.4.1.1), were used for a characterization of physical and mechanical attributes of the topmost Cretan slope sediment cover (see section 6.4.2). The utilized measurements comprised undrained shear strength (S_u) and mean bulk densities from a Multi-Sensor Core Logger (MSCL; see section 6.3.2.). Geotechnical characteristics as well as geometrical measurements from seismic data were combined and implemented into infinite, 1-D slope models to back-analyze slope stability and instability scenarios (see section 6.3.4) as well as to determine the required seismic trigger for sediment failure initiation (see section 6.4.2).

3.3 Design and performances of numerical models

For this study, the commercial software PFC2D was used to (i) design granular, bonded materials of specific micro-properties simulating the macro-behaviour of standardized natural sediments using biaxial-cell test simulations (see section 7.2.2; Fig. 7.1) and (ii) design two different models of large assemblages of these designed materials and deform them to critically inclined slopes due to normal on one hand and reverse master-fault off-sets on the other hand (see section 7.2.1; Fig. 7.3).

Several test runs for both the material design (i.e. cohesive and non-cohesive sediment) and the slope model configurations (i.e. extensional and compressional setting) were performed to adjust (i) the physical and mechanical behaviour of materials according to natural sediments (see section 7.2.2) and (ii) to achieve 2-D model that represent the proportions, off-sets, off-set velocities, and master-fault propagations comparable to natural slopes, their deformation, and mass-movement development (see section 7.2.3). After model runs, different data analysis and visualization strategies (see section 7.2.4;

Fig. 7.3) were carried out for an interpretation of fault patterns and dislocation of mparticle assemblages (i.e. mass movements; see section 7.3; Figs. 7.4 and 7.5). These strategies enabled a combined interpretation of faults and near-surface mass movements to conceptual models of the long-term slope evolution and development with respect to the mechanical behaviour of different sediment types (see 7.4; Fig.7.7). Furthermore, explicit model configurations that simulate mass-movement development due to extensional basin flank movement were used to compare with the situation observed on the northern Cretan margin as well as on other basin flanks (see section 8.5.4).

4. New evidence for massive gravitational mass-transport deposits in the southern Cretan Sea, eastern Mediterranean

Published as: Frank Strozyk¹, Katrin Huhn¹, Michael Strasser¹, Sebastian Krastel², Ingo Kock¹ & Achim Kopf¹, 2009. New evidence for massive gravitational mass-transport deposits in the southern Cretan Sea, eastern Mediterranean, *Marine Geology* 263, 97-107

¹ MARUM, Centre for Marine Environmental Sciences - Cluster of Excellence: The Ocean in the Earth System, University of Bremen, P.O. Box 33 04 40, D-28359 Bremen, Germany

² IFM-GEOMAR, Leibniz Institute of Marine Sciences, Cluster of Excellence: The Future Ocean, Christian-Albrecht-University Kiel, D-24148 Kiel, Germany

Abstract:

Newly acquired bathymetric and seismic reflection data have revealed mass transport deposits (MTDs) on the northeastern Cretan margin in the active Hellenic subduction zone. These include a stack of two submarine landslides within the Malia Basin with a total volume of approximately 4.6 km³ covering an area of about 135 km². These two MTDs have different geometry, internal deformations and transport structures. The older and stratigraphic lower MTD is interpreted as a debris that fills a large part of the Malia Basin, while the second, younger MTD, with an age of at least 12.6 cal. ka B.P., indicates a thick, lens-shaped, partially translational landslide. This MTD comprises multiple slide masses with internal structure varying from highly deformed to nearly undeformed. The reconstructed source-area of the older MTD is located in the westernmost Malia Basin. The source area of the younger MTD is identified in multiple headwalls at the slope-basin-transition in 450 m water depth. Numerous faults with an orientation almost parallel to the southwest-northeast-trending basin axis occur along the northern and southern boundaries of the Malia Basin, and have caused a partial steepening of the slope-basin-transition. The possible triggers for slope failure and mass wasting include (i) seismicity and (ii) movement of the uplifting island of Crete from neotectonics of the Hellenic subduction zone, and (iii) slip of clay-mineral-rich or ash-bearing layers during fluid involvement.

4.1. Introduction:

Submarine landslides are commonly observed at continental margins worldwide. Many studies (e.g. Locat and Lee, 2002; Sultan et al., 2004; Canals et al., 2004; Masson et al., 2006) have shown that earthquake activity and oversteepening of slopes, as well as wave activity, sealevel changes, and rapidly increasing sediment load are some of the most common trigger mechanisms for slope failure. In addition, gas hydrate dissociation may play an important role for slope destabilization (e.g. Gunn et al. 2002; Mienert et al., 2003; Vendeville & Gaullier, 2003). Pore pressure increase is a common cause of low effective stresses, and may hence be another potential generator of slope instability (Bromhead, 1992; Sultan et al., 2004), for instance by liquefaction of ash-layers (Carey, 1997; Kutterolf et al.,

2008). Submarine landslides are commonly initiated by transient pore-pressure conditions associated with the variety of above-mentioned geological processes (see summary in Hampton et al., 1996, and Locat & Lee, 2002).

One region that concentrates several of these geological processes is the tectonically active Hellenic subduction zone in the eastern Mediterranean with the Island of Crete in its centre (Fig. 4.1). Various data sets (e.g. Mascle & Martin, 1990; Fassoulas, 2000; Manakou & Tsapanos, 2000) indicate earthquake activity and active faults in the vicinity of Crete. Thereby, the accretionary prism and its continental crust backstop south of Crete are tectonically more active (Chaumillon & Mascle, 1996; Polonia et al., 2002; Kopf et al., 2003; Chamot-Rooke et al., 2005), indicating a generally higher potential for slope destabilization, demonstrated by large-scaled landslides identified along the southern margin of Crete, e.g. the Lithion Slide (Huson and Fortuin, 1985). Along the northern Cretan slope submarine landslides have rarely been studied. This area is characterized by high sedimentation rates of 8-22 cm ka⁻¹ (Chronis et al., 2000b) and by fine-grained mixed hemipelagic and terrigenous sediments with several interbedded sapropels and volcanic ashes in shallow and mid-slope regions (Chronis et al., 2000a; Kopf et al., 2007). Consequently, potentially unstable slope areas and large landslide events are expected also for the northern Cretan slope. Chronis et al. (2000b) already provided evidence for gravitational mass transport on the northern Cretan mid-slope. However, detailed studies are not available at present.

We collected a dense grid of bathymetric data and multi-channel reflection seismic profiles from the southern Cretan Sea sub-basins and along the northern Cretan slope in water depths of 150 m to 2800 m during R/V-Poseidon Cruise P-336 “CRESTS” (Cretan Sea Tectonics and Sedimentology; Fig. 4.1). Main objectives of the CRESTS cruise were to study slope instability and related geohazards at the northern Cretan Margin, and to acquire site survey for potential future scientific drilling (see also Kopf et al., 2006; 2007). In addition to the acoustic data, 30 gravity cores of 1 m to 5.7 m length were recovered along transects on seismic lines.

In this study, we (i) identify and characterize MTDs in an area off shore the Cretan town of Malia, (ii) reconstruct the sediment source areas, and (iii) propose a conceptual model for sediment transport mechanisms and possible triggers.

4.2. Geological setting along the Hellenic subduction zone

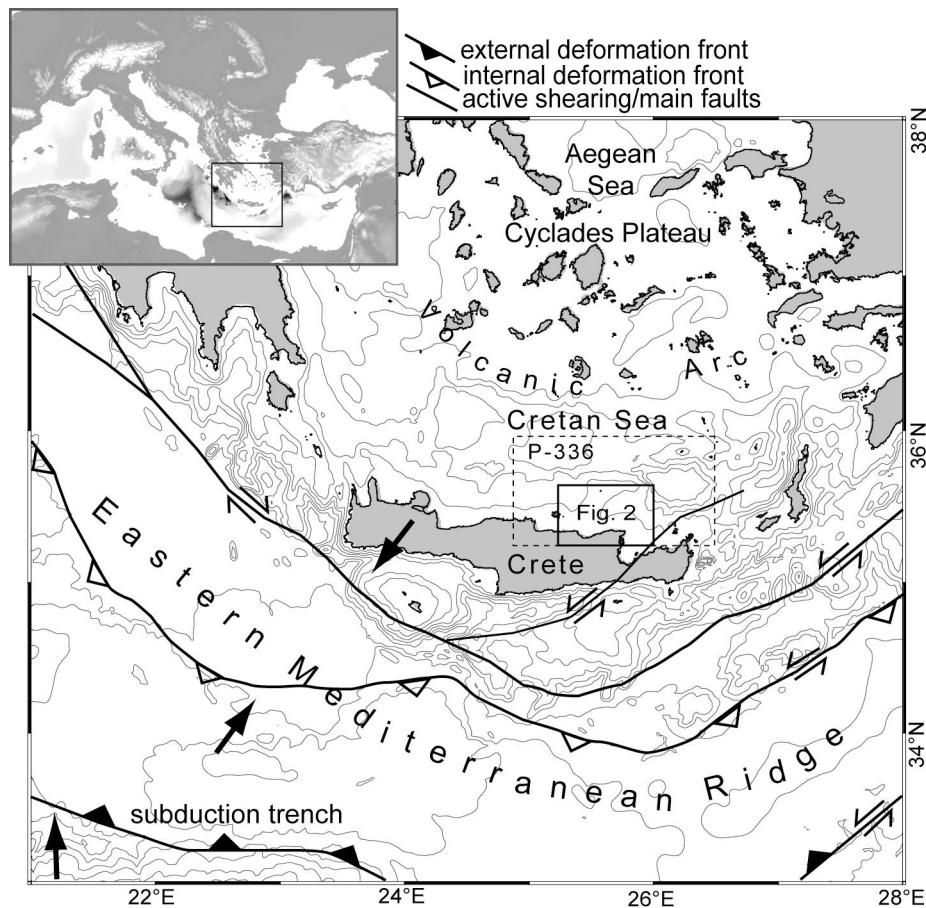


Fig. 4.1) Schematic illustration of the tectonic setting along the Eastern Mediterranean subduction zone and surrounding landmasses. The black dotted box shows the entire area surveyed during Poseidon cruise 336; the black box shows the area of Fig. 4.2 Thick black arrows indicate general direction of plate movement. The bathymetric chart is based on the GEBCO-dataset with a contour interval of 500 m.

The east-west-trending, 1500 km long and 200 km wide Mediterranean Ridge is a major structure of the convergent margin between the African and Eurasian plate (Fig. 4.1). It is bordered to the south by the subduction trench and to the north by the island of Crete, which represents an exhumed forearc-high acting as a backstop for the accreted strata (e.g. Le Pichon et al., 2002; Polonia et al., 2002; Kopf et al., 2003). Continuous uplift of Crete combined with fast sediment accretion along the Mediterranean Ridge results in a high neotectonic activity, associated with numerous generations of faults and active fluid venting from depth (e.g. Camerlenghi et al., 1992; Dylle & Kopf, 2001). Various datasets by e.g. Papazachos (1990), Manakou & Tsapanos (2000), and Meier et al. (2004) confirm numerous earthquakes occurring along the Mediterranean Ridge mainly at the Aegean-African plate boundary, along arc-parallel trenches, in the central to western Cretan deeper lithosphere, and along the volcanic arc to the north.

Crete has been exhumed and continuously uplifted about 30 km as a result of a detachment of the subducting slab (Bonneau, 1984; Fassoulas, 2000; Pirazzoli, 2005). As a consequence, the area is currently characterized by north-south and east-west-extension (Mascle & Martin, 1990; Peterek & Schwarze, 2004; Casten & Snopek, 2006).

To the north, Crete is bordered by the Cretan Sea (Fig. 4.1). This extensional fore-arc-type basin comprises various topographic lows or sub-basins, separated by ridges of variable elevation and strike (Angelier et al., 1981; Mascle & Martin, 1990). Main sub-basins are the Heraklion Basin, the Kamilonisi Basin (Fig. 4.2A) and the north-south-elongated Karpathos Basin.

The uplift of Crete combined with subsidence of the Cretan Basins caused a local steepening of the northern Cretan slope associated with the generation of numerous faults. Thereby, the main fault system of the south-eastern Cretan Sea is developed parallel to the main southwest-northeast-trending Herapetra Fault (Fig. 4.2A; Angelier et al., 1981; Mascle & Martin, 1990; Fassoulas, 2000). This fault system is made of half graben and subordinated horst and graben structures (Fig. 4.2B). In addition, faults with northeast-southwest, north-south and northwest-southeast trends compose a tectonically complex system of tilted blocks and half grabens. Their trends are perpendicular to the main structural direction of the plate boundary southwest of Crete and therefore an expression of the regional plate convergence vector, parallel to the trench system southeast of Crete (Figs. 4.1 and 4.2A; Mascle & Martin, 1990).

To the north, the Cretan Basin is bounded by the Aegean volcanic arc at the boundary to the Aegean Sea backarc basin, representing the northernmost part of the Hellenic subduction zone (Fig. 4.1; Le Pichon 1979; Angelier et al., 1981). Volcanic activity in this region generated several ash-layers, such as the Z2 Santorini Event about 3750 cal. years B.P., which is also detected in the Cretan Sea (Giresse et al., 2003, and references therein). Another remarkable feature of Cretan Sea sediments is the occurrence of several sapropel layers, whereof Sapropel 1 with an age of 9.6 - 6.4 ka BP is a common well-described marker horizon in shallow cores of the Cretan Sea (Aksu et al., 1995; Giresse et al., 2003).

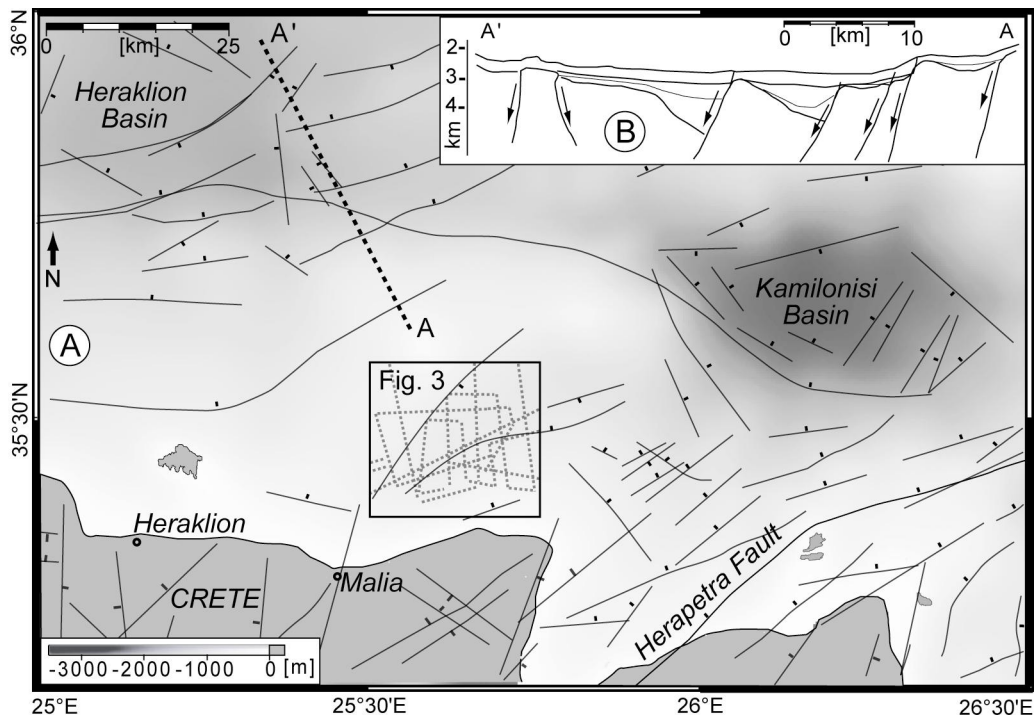


Fig. 4.2) 2A: Bathymetric map of the south-east Cretan Sea and its sub-basins in the vicinity of the study area based on the GEBCO-dataset (for location see Fig. 4.1). Land masses are presented in monochrome grey. The black box shows the location of the survey area of this study (Fig. 4.3); dotted grey lines show seismic profiles of the surveyed area. Black lines indicate major faults compiled after ten Veen et al. (2004), Fassoulas (2000) and Mascle & Martin (1990); 2B: Profile along line A-A' after Mascle and Martin (1990), showing the typical tilted blocks and half graben systems in the southern Cretan sea.

4.3. Methods

The geophysical data acquisition of Cruise P-336 included a dense grid of swath bathymetric data recorded with an ELAC SEABEAM 1050. This system is operated at 12 kHz with a maximum angular coverage of 150° corresponding to a swath width of up to 7.5 times the water depth. Bathymetric data were processed using MB-System (Caress & Chayes, 2006) and gridded with a resolution of 20 m cell-size using GMT (Generic Mapping Tool; Wessel & Smith, 1998). The bathymetry of the investigated area covers approximately 625 km².

Nearly 1400 km of reflection seismic profiles were recorded during P-336 using a Mini-GI-Gun (2 x 0.25 l, 50-500 Hz, operated at 140-150 bar) and an 100 m-long 16-group streamer with 8 hydrophones per group and a group distance of 6.25 m. The shooting rate was 8 s, ship speed was about 4 kn and the resulting shot-point distance is about 17 m. 13 seismic lines in E-W-direction and 10 lines in N-S-direction with a spacing of 2-5 km and a total length of 250 km were collected in the area relevant for this paper. We used Vista software (Seismic Image Software Ltd.) to carry out standard processing, including trace editing, Common-Mid-Point (CMP) sorting, static and delay corrections, normal moveout corrections, bandpass frequency filtering (frequency content: 55/110 – 600/800 kHz), stacking and water velocity migration (1500 m s⁻¹). A CMP spacing of 10 m was applied throughout. A constant velocity of 1500 m/s was used for NMO-correction and migration because no velocity

analysis was done due to the short streamer length. Interpretation on prominent reflectors and faults was carried out using KINGDOM Suite (Seismic Micro-Technology Inc.).

Sediment cores were collected with a standard gravity corer. Accelerated Mass Spectrometry (AMS) ^{14}C -age dating on three samples of core GeoB-10426 (location in Fig. 4.3A) was applied by the Poznań Radiocarbon Laboratory, Poland. ^{14}C ages were calibrated using CALIB5.0.1 (Stuiver and Reimer, 1986) and the Marine 04.14C dataset (Hughen et al., 2004) assuming a conservative reservoir age of 400 years (DeMenocal et al., 2000). More details of data acquisition and methodology are listed in the P-336 cruise report (Kopf et al., 2006).

4.4. Observations & Results

4.4.1 Bathymetric data

The area surveyed is occupied by an elongated basin of about 25 km in length and up to 15 km in width with a southwest-northeast-trending axis that smoothly dips to the northwest towards the Kamilonisi Basin (Fig. 4.2A). Water depth ranges from 170 m to 730 m (Fig. 4.3A). Owing to its proximity to the city of Malia at the Cretan coast, we name it the Malia Basin (Fig. 4.2A).

The Malia Basin is bordered to the south by the continental slope of Crete (Fig. 4.3). To the northwest a morphological high (“Northern High”) rises 350 m above the basin floor. The seafloor of the Malia Basin is flat and smooth in the southwestern, northwestern and southeastern part of the map area (Seafloor Texture A, Fig. 4.3A). In contrast, we identify an irregular seafloor morphology within the south-central portion of the map area, causing positive relieve locally up to 40 m above the flat basin floor (Seafloor Texture B; Figs. 4.3A and B). The Seafloor Texture B is located at the transition from the narrow northeast-southwest-trending portion of the slope to the Malia Basin. In particular, a hummocky morphology throughout this seafloor texture is also identified from a gradient plot (Fig. 4.3B). A third Seafloor Texture C is traced from the southwestern area towards the northeastern part of the Malia Basin and forms a gently arcuated band along the edge of the northern high (Fig. 4.3A). It exhibits a rougher morphology compared to Seafloor Texture A, but is smoother than Seafloor Texture B. Several scattered mounds are present on this texture close to the northern edge of Seafloor Texture B (Fig. 4.3B).

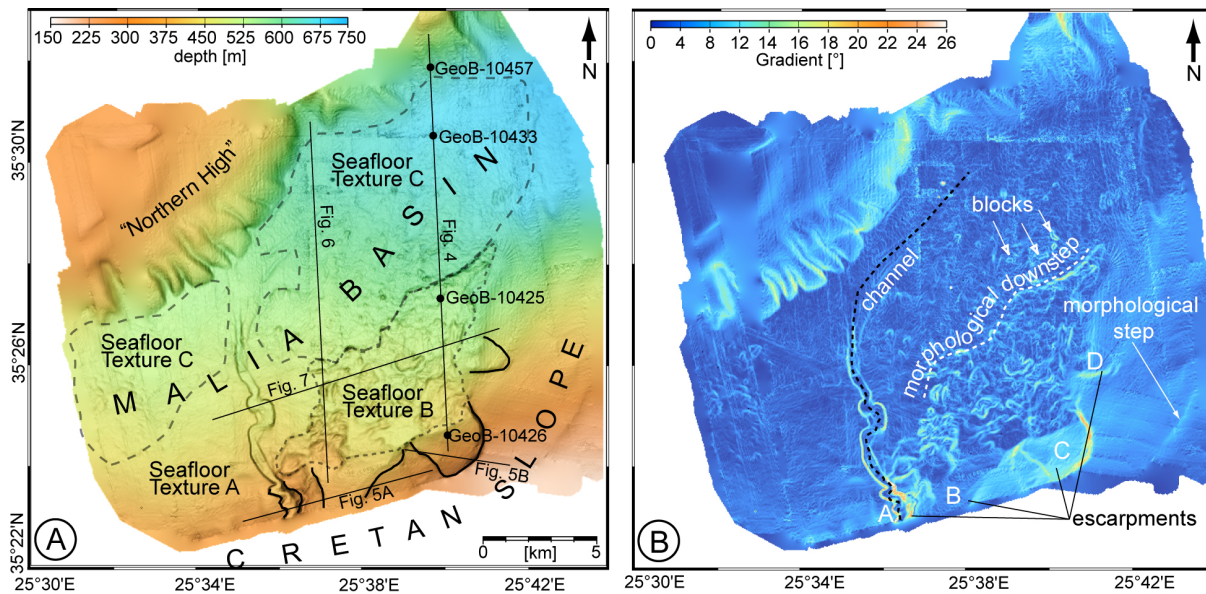


Fig. 4.3) A: Measured bathymetric map of the survey area. Black lines indicate the locations of seismic profiles shown in this study. Dotted lines indicate possible boundaries of Seafloor Textures B and C. All non-marked areas belong to Seafloor Texture A. Thick black lines represent escarpment walls. Black dots show positions of gravity coring stations of P-336; B: Map showing slope gradients calculated from the data of 4.3A. Escarpments are annotated with A-D. White dotted line shows a morphological step between seafloor textures B and C. The black dotted line traces a channel.

A remarkable morphological element is a meandering channel that runs smoothly from the continental slope northward into the Malia Basin towards northeast with orientation nearly parallel to the basin gradient (Fig. 4.3B). The channel has a mean depth of 25 m and a width of 400-800 m. On either side of the channel a levee of 25 m height and up to 2 km width traces the channels pathway.

Similar to the “Northern High”, the Cretan slope in the southern and southeastern study area shows a generally smooth surface morphology with an inclination of 2°- 4°. The smooth slope is interrupted by a narrow area with an irregular topography and partially higher inclinations of up to 22° south and southeast of Seafloor Texture B. The highest slope angles correspond to the four escarpments in this area (Escarpments A-D; Fig. 4.3B). Escarpments A and B occur as pairs of opposite-dipping walls. In contrast, the eastern Escarpments C and D show concave and continuous wall geometries heading towards the basin. The height of these escarpments ranges between 10 and 60 m.

4.4.2 Seismic reflection data:

4.4.2.1 Description of seismic units:

We identify three seismic units¹ on the basis of seismic character such as amplitude, continuity, and reflection configuration.

Seismic Unit 1 comprises an elongated, up to 30 m-thick sediment package that occupies a large part of the Malia Basin. An example of this unit is shown in Figure 4.4 Unit 1 is characterized by a

¹ A “seismic unit” is not used in terms of seismic sequence stratigraphy, but to distinguish and classify distinct sedimentary bodies and background strata.

transparent to chaotic reflection pattern. Scattered blocks on top of Unit 1 rising above the basin seafloor are identified especially in the eastern Malia Basin (Fig. 4.4A and B).

Unit 2 is a lens-shaped up to 85 m-thick body with an irregular surface morphology but the scattered blocks observed for Unit 1 are absent (Figs. 4.4A and B). The reflection pattern is highly chaotic and transparent contrasting with the flat and continuous reflectors of undisturbed basin sediments (see below; Fig. 4.4A). Unit 2 also includes some laminated packages especially in its upper part, e.g. in the southern part of this unit on Fig. 4.4 In general, transparency dominates in the lower part of this unit, while the upper part is characterized by a chaotic reflection pattern. Unit 2 is exposed at the sea floor and major parts of this unit rise up to 45 m above the surrounding seafloor.

Seismic Unit 3 is defined as “background unit” (see Figs. 4.4B, 4.5B, 4.6B and 4.7). This unit is up to 300 m-thick and drapes the acoustic basement. Major parts of seismic Unit 3 are characterized by well-stratified, continuous and parallel reflectors (e.g. Figs. 4.4 and 4.6). Faults within Unit 3 constitute a system of northwest and southeast dipping normal faults at the slope area and in basin-transition respectively (eastern part in Fig. 4.7). In the southern part of the study area along the Cretan Margin slope, the four major escarpments found on the bathymetric chart can also be seen in seismic profiles (Fig. 4.5A and B). The escarpments occur in association with well-defined fault patterns (Fig. 4.5A). We define this constricted area of Unit 3 as faulted and disturbed background sediments. Occasionally, smaller wedge- to lens-shaped bodies with a chaotic-to-transparent reflection pattern occur within the acoustically well-stratified succession of seismic Unit 3 (Figs. 4.6 and 4.7).

4.4.2.2 Lateral distribution of seismic units:

Unit 1 is found in water depths from 350 m to almost 700 m, covering an area of about 100 km² as an east-west-elongated, 10 to 30 m thick body (Fig. 4.8) that principally occupies the central axis of the Malia Basin. Surface roughness and thickness slightly increase to the west (Fig. 4.3A). At its northern, southern and eastern boundaries, this unit onlaps the raising slopes (Figs. 4.4 and 4.6).

Unit 2 occurs in water depths of 400 m to 660 m within an area of 35 km² in the southern part of the Malia Basin (Fig. 4.8). Its western border is defined by the channel levee system (Figs. 4.7 and 4.8) and the northern border is indicated by a pronounced downstep of seafloor morphology (Figs. 4.3B and 4.4). To the south and south-east there is a sharp, almost vertical contact to seismic Unit 3 (Figs. 4.7 and 4.8). The generally lens-shaped Unit 2 thins westward, and forms an elongated sediment accumulation of up to 30 m thickness, close to its western boundary defined by the levee system (Fig. 4.6). In this area Unit 2 does not cut into underlying strata. It is important to note that the north-western part of Unit 2 overlays Unit 1 and smoothly pinches out towards the northwest (Fig. 4.6). A comparison of seismic profiles GeoB-164 (Fig. 4.4B) and GeoB-170 (Fig. 4.6B) shows that the unit's surface roughness and irregularity increases to the west, except for the central basin area where it covers Unit 1. Here Unit 2 shows a smooth morphology (central part of GeoB-170; Fig. 4.6B).

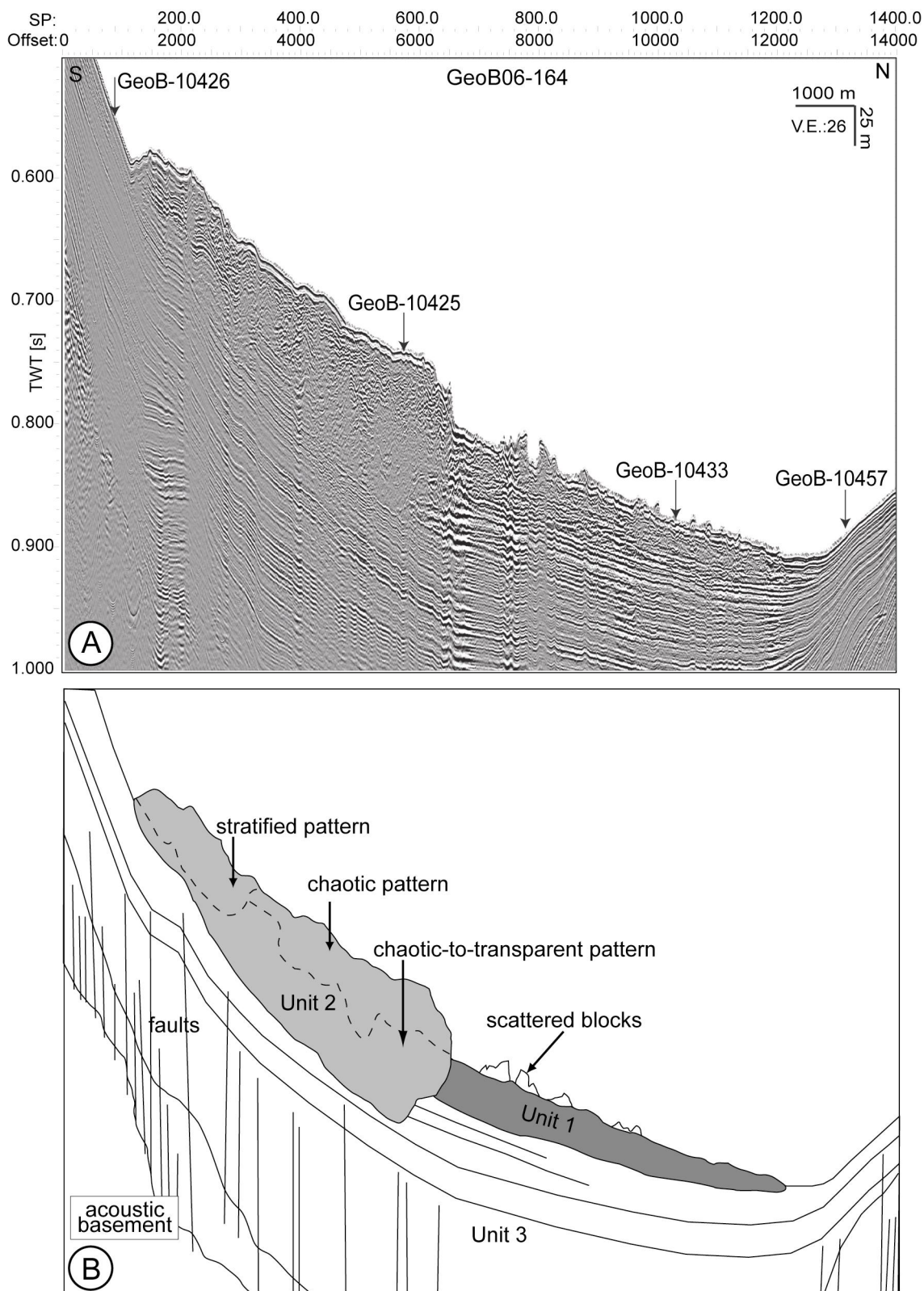


Fig. 4.4 A: N-S seismic profile GeoB06-164 (vertical exaggeration (V.E.) 26) with locations of gravity cores recovered during P-336; B: Interpretation Figure showing Unit 1 (dark grey), Unit 2 (light grey) and Unit 3 within the eastern Malia Basin. Dotted lines within Unit 2 represent boundaries between mostly stratified, chaotic and transparent reflection pattern. For location of seismic line see Figure 4.3A.

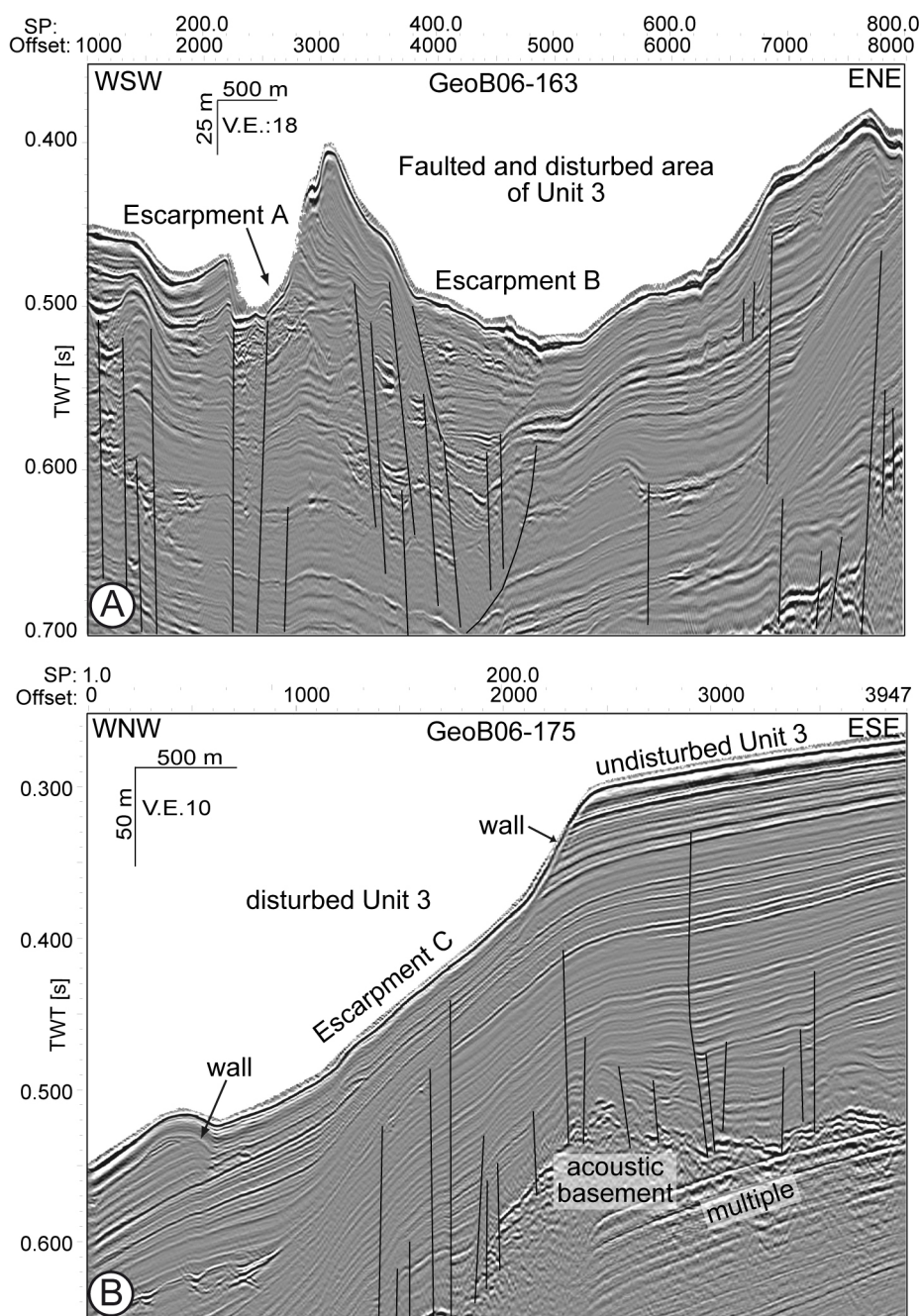


Fig. 4.5 A: SW-NE seismic profile GeoB06-163 showing Escarpments A and B in the area of dense faulted Unit 3 (V.E.18); B: SE-NW profile GeoB06-175 (V.E.10) of the southern study area along the Cretan slope, crossing Escarpments C. For location see Figure 4.3A.

Unit 3 is found on all seismic profiles of the Malia Basin and along the Cretan slope (Fig. 4.8). Thickness of strata varies strongly with morphology, while the thickest portion occurs at the northern border of the Malia Basin and the thinnest at the southern flank of the “Northern High”. The area of seismic Unit 3 that is characterized by steeply dipping faults and associated with Escarpments A - D occurs along the transition from the Cretan slope to the southern Malia Basin (Fig. 4.8). This part of Unit 3 covers an area in the range of 20 km² and its outer limits to west and east nearly coincide with those of Unit 2. Hence, it is bordered by the channel-levee-complex to the west and by Escarpment D

to the east/northeast. All escarpments are found in the narrow area of concentrated normal faulting at the slope-basin-transition.

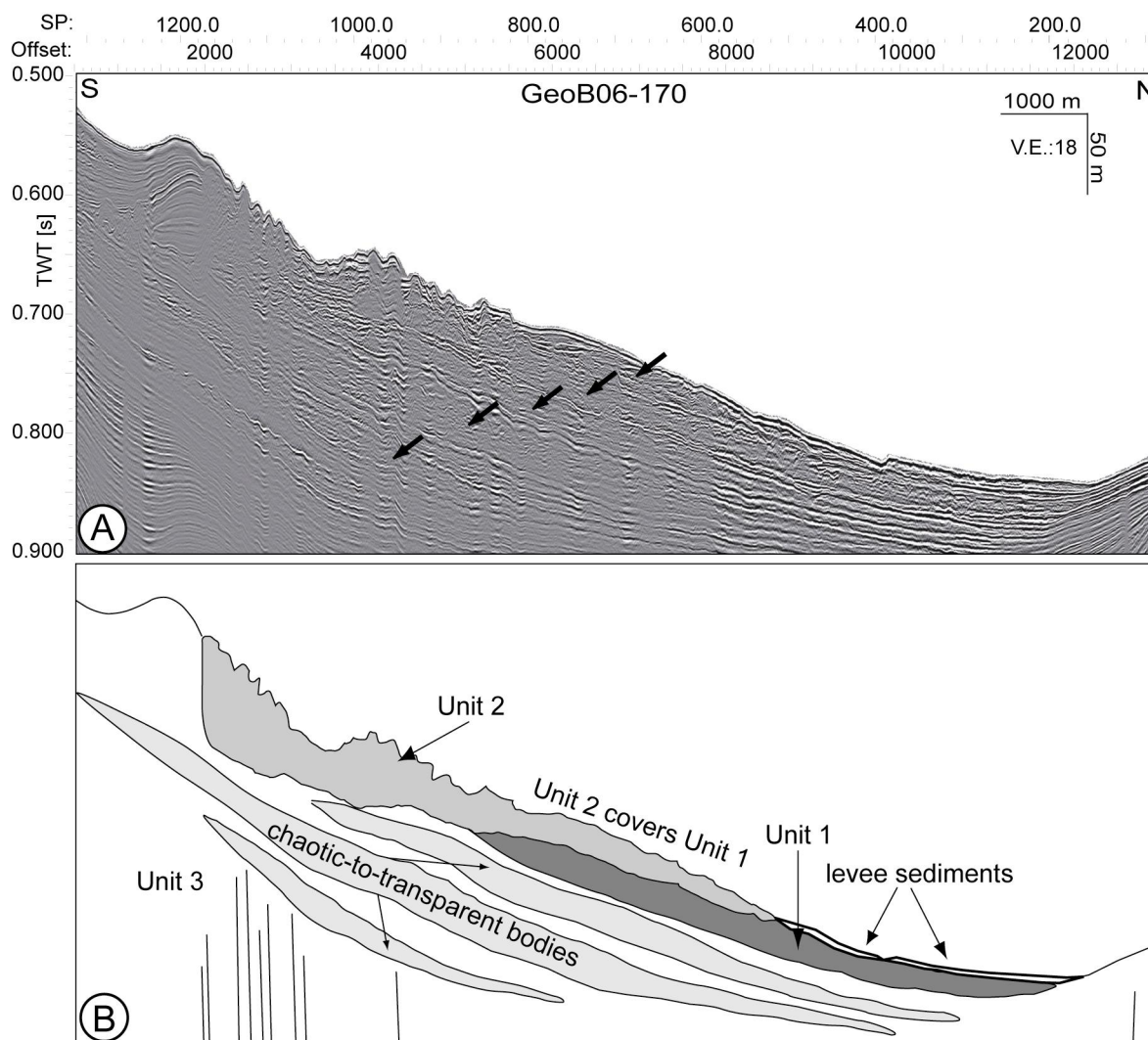


Fig. 4.6 **A:** N-S seismic profile GeoB06-170 (V.E.18); **B:** interpretation Figure tracing Units 1, 2 (upper two black arrows) and 3 about 5 km west of profile GeoB06-164 (Fig. 4.3). Light grey drawings beneath Unit 1 and 2 represent lens- to wedge-shaped units with chaotic to transparent reflection, also marked with the lower three black arrows in 4.6A. For location of seismic line see Fig. 4.3A.

The areal tracking of faults is based on the structural interpretation of Mascle and Martin (1990) in combination to traceable continuity of some major faults throughout seismic profiles and their spatial impression on seafloor morphology, e.g. as a northeast-trending morphological step in the southeastern map area (Fig. 4.3B). Smaller, sub-ordinated faults are interpreted parallel to major faults, and therefore to the generally southwest-northeast-trending axis of the Malia Basin (Fig. 4.8). Faults along the slope in the southeastern map area show mainly northwest-dipping. An additional fault-set dipping southeast is identified along the southern edge of the “Northern High” and represents the northern boundary of the basin.

The buried chaotic to transparent bodies identified in some seismic profiles (Figs. 4.6 and 4.7) only occur in the basin at stratigraphic levels below seismic Units 1 and 2. Seismic data do not allow us to accurately define their lateral extension.

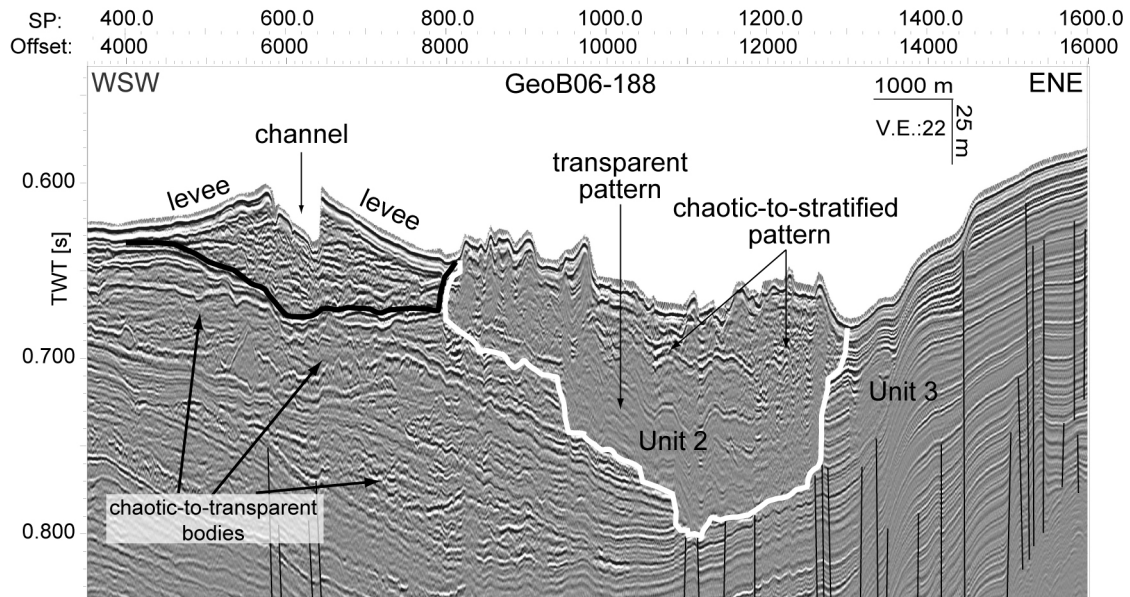


Fig. 4.7) WSW-ENE seismic profile GeoB06-188 (V.E. 22) tracing Unit 2 (white line) and Unit 3 (non-marked areas). The NE-leading channel with the levee (black line) occurs in the western part of the profile. Chaotic-to-transparent bodies are identified within deeper stratigraphic levels of Unit 3 (see also Fig. 4.6). For location of seismic line see Fig. 4.3A.

4.4.3 Core data

In order to obtain age control on the shallower subsurface, we examined four gravity cores of 1.3 to 4.45 m length (Fig. 4.9) recovered along seismic profile GeoB-164 (see Figs. 4.3A and 4.4A for location). Sediments comprise pelagic oozes with varying amounts of clay, thin layers of volcanic ash, fine-grained terrigenous grains in deeper sections, organic material and, occasionally, carbonaceous clasts and nodules (Kopf et al., 2007). The prominent marker horizons are interpreted to correspond to the Z2-Santorini ash layer and Sapropel S1 and can be correlated among all cores. However, because core GeoB-10426 is located within Escarpment C (Fig. 4.3A) and reveals higher sand and silt contents in its lower part, this core was analyzed for AMS ^{14}C -dating to confirm the inferred age model. Measured and calibrated ages of samples at 1.28, 1.77, and 1.94 mbsf (meter below seafloor) are shown in Table 4.1. Results confirm that the observed sapropel coincides with the age-range of about 9.6-6.4 ka BP of Sapropel 1 in the southern Cretan Sea.

Table 4.1) AMS ^{14}C and calibrated ages of samples of GeoB-10426

Depth	Age ^{14}C	Cal. ages
1.27 -1.29 mbsf	6380 ± 40 B.P.	6850 ± 115 B.P.
1.76 -1.78 mbsf	9370 ± 60 B.P.	10211 ± 61.5 B.P.
1.93 -1.95 mbsf	11070 ± 50 B.P.	12748.5 ± 50.5 B.P.

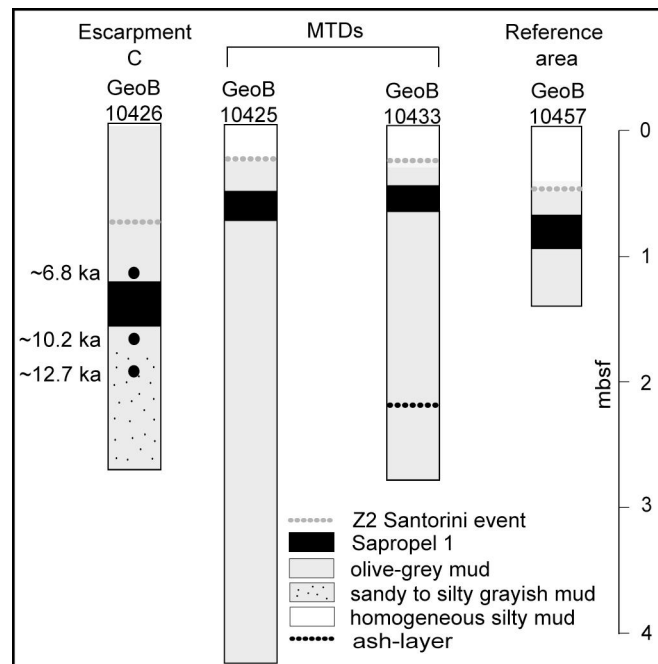


Fig. 4.8) Schematic illustration of sediment cores GeoB-10426, -10425, -10433, and -10457, retrieved during P-336 along seismic profile GeoB-164 (Fig. 4.4.). Black dots in core GeoB-10426 indicate the positions of AMS ^{14}C -age dating samples in 1.28, 1.77 and 1.94 mbsf with the resulting calibrated calendaric ages.

4.5. Interpretations

4.5.1 Seismic units and seafloor textures

Based on structures identified from seismic data in correlation with surface analysis of bathymetry data, seismic Units 1 and 2 are interpreted as mass-transport deposits (MTDs) of two mass-movement events.

Unit 1 is identified as MTD, because the degree of deformation of the reflection pattern is high, which suggests deposition of chaotic masses and sediment amalgamation. The areal distribution of this MTD 1 mostly coincides with the rough Seafloor Texture C, which is consistent with interpretation of Unit 1 as a deposit of gravitational mass transport (see data in McAdoo et al., 2000). Further, surface Texture C is partially correlated to the channel levee system, which masks Unit 1 in the central basin area (compare Fig. 4.3A and Fig. 4.8). The thin, widespread and chaotic MTD that strictly traces the basin morphology can be defined as a debrite according to Hampton et al. (1996) and Lee et al. (2007). The slight trend of decreasing thickness towards the east and the well-defined pinch-out geometry at its northern, southern and eastern boundaries, clearly reveal an eastward mass-transport direction. The onlap geometry in the northeastern map area indicates that further eastward transport to the Kamilonisi Basin was prevented by a decrease in seafloor inclination. Due to lack of data coverage, the source area to the west could not be mapped. A volume calculation, using the mean thickness and areal extent of seismic Unit 1 in combination with the lateral distribution of Seafloor Texture C, reveals that about 2.5 km³ of the total masses of MTD 1 are found in the surveyed area.

The acoustic pattern of seismic Unit 2 and its correlation to the rough to blocky Seafloor Texture B, except in the central basin area, where Unit 2 is correlated to Seafloor Texture C, supports the interpretation of seismic Unit 2 also as MTD. Because Unit 2 overlies Unit 1 in the central basin area (Figs. 4.6 and 4.8), the described MTDs represent two distinct mass-movement events.

Owing to the morphological break that clearly defines the northern boundary and the lower deformation degree in the southern part, which includes acoustically-laminated packages interpreted as slide blocks, we infer a northward-directed, partially translational sliding of masses (see similar data in Hampton et al., 1996, and Lee et al., 2007). With increasing depth and increasing distance from the slope-basin-transition, the intermediate and deeper parts of the MTD are increasingly deformed. This is interpreted as a result from higher internal deformation during transport. In addition, the base of the highly deformed sediments partially cuts into basin strata at its northern edge indicating that a certain amount of erosion occurred during mass transport (Figs. 4.4 and 4.7). A calculation of the volume of Unit 2, also using its mean thickness and areal extension, results in 2.1 km³.

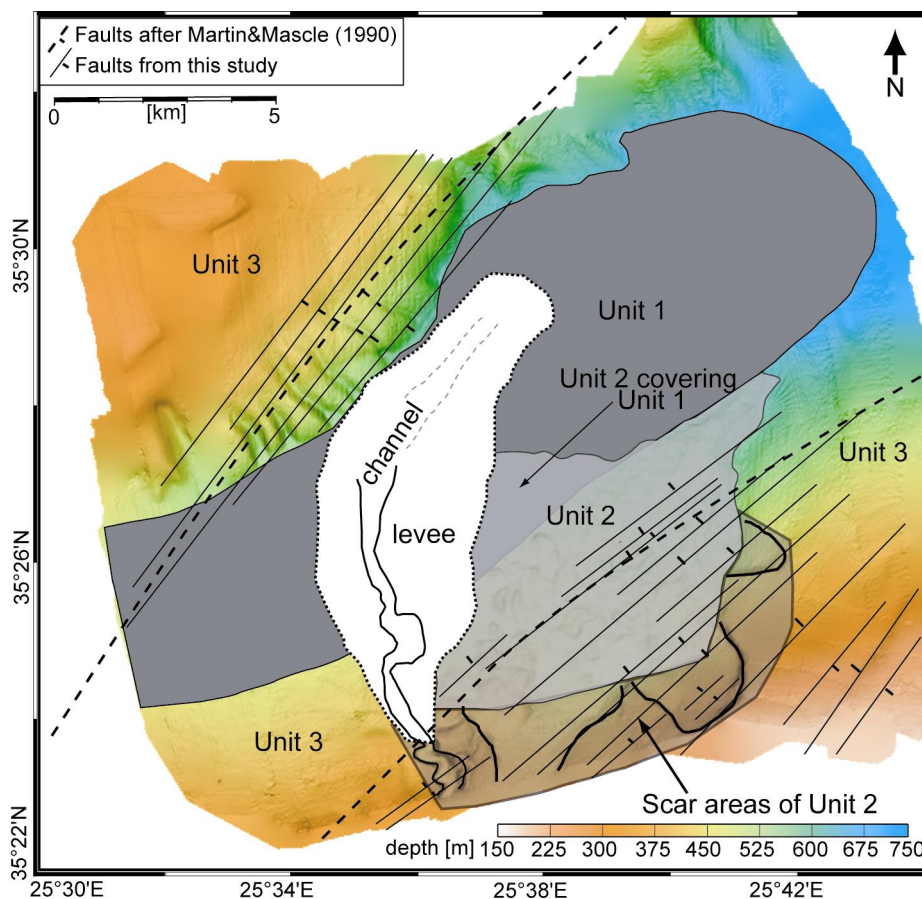


Fig. 4.9) Schematic illustration of lateral distribution of interpreted seismic units. Unit 3 is present in most map areas. The outline of Unit 1 (dark grey) and 2 (light grey) is based on seismic interpretation, partially combined with lateral contribution of Seafloor Textures B and C. The disturbed and faulted part of Unit 3 is identified as the scar areas of Unit 2 and defined by the extension of escarpments (transparent grey). Black lines mark lateral tracking of interpreted, traceable faults, while dotted lines with dip-markers represent main faults after Mascle & Martin (1990).

The slide scar of MTD 2 is identified in the amphitheatre-like geometry, basin-ward orientation and depletion of sediment masses of escarpments B-D along the slope (Fig. 4.8). Due to its vicinity to and its orientation towards the channel system, Escarpment A is inferred to be related to mass-wasting in the channel head (Fig. 4.8). Escarpment B only shows sidewall geometries suggesting that the headwall is located to the south off the area covered by our data.

In order to associate the volume proportions of MTD 2 that correspond to the different escarpments, we reconstruct a pre-failure slope across the escarpments. The result for Escarpments C and D reveals a displaced volume in the order of 0.25 km³. The eroded volume within that part of Escarpment B that lies within the range of our data is reconstructed to almost 0.275 km³. To estimate the total volume sourced from Escarpment B, we compare eroded volume reconstructions from the areas covered by data to the total volume of MTD 2. Our calculations reveal that at least 2 km³ have been mobilized from Escarpment B and its unknown upslope counterpart. This shows that the biggest portion of MTD 2 is associated with an upslope part of Escarpment B that lies outside of the range covered by our multibeam and seismic data. An alternative interpretation of the unbalanced volume proportion is entrainment of background sediments during movement of the slide masses, which would result in a significant smaller volume of the displaced material in the scar areas.

4.5.2 Age control from core and seismic data

Sediment core analysis reveals that the seismically imaged slide deposits are covered by at least 4.45 m of younger background sediment, as indicated by the absence of gravitational mass transport deposits and the coherent presence of stratigraphic marker horizons (Fig. 4.9). ¹⁴C age dating from core GeoB-10426, which was retrieved within Escarpment C, evidences that the age of both MTDs is older than 12.6 ka B.P. Further, it indicates accumulation rates of 15-20 cm ka⁻¹ for the study site. The 4.45 m continuous stratigraphic succession of background sediment therefore reveals an age of 22-30 ka B.P. for the base of the core. Because we would be able to detect a drape thicker than 5 m from seismic data, which is not the case for either MTDs, a maximum drape of 5 m thickness results in a possible maximum age of 25-33 ka B.P. for the base of the drape on top of MTDs.

4.6. Discussion

4.6.1 Conceptual model

The interpretation of the two gravitational mass-movement events in the Malia Basin is based on the deposits' variations in surface roughness, geometry, thickness and degree of internal deformation yielding different transport mechanisms and erosional behaviours. Because there is neither an evidence for background sedimentation nor for erosion between the two MTDs, we assume that their emplacement took place within a short time lapse, whose sedimentary record is thinner than the vertical seismic resolution.

Older MTDs, however, are inferred from the occurrence of wedge- to lens-shaped, acoustically chaotic-to-transparent bodies intercalated between well-stratified background sediment in the lower part of the Malia Basins' sedimentary succession (Figs. 4.6 and 4.7). Because of their geometries and their distribution in front of the southern slope-basin-transition, a source area along the slope is most likely. Their stacked occurrence indicates frequent slope failure at the study site.

Based on our findings we developed a conceptual model for the two younger mass-transport events (Figs. 4.10A and B): we assume that the emplacement of MTD 1 took place first as a debris flow from a source area to the west of the investigated area (Fig. 4.10A). Massive and continuous levee accumulation of the channel is supposed to have later reworked and covered the debris in the central to western Malia Basin (Fig. 4.10B). As we cannot identify a distinct drape across the channel complex, we suggest that the channel system may be active today. However, due to the dimension and thickness of the levee and its distribution relatively to MTDs, the channel-levee system most likely has been active already prior to the emplacement of MTD 1. High transport and kinetic energy of the debris flow thus may have spilled over and/or partially eroded the existing channel levee complex in this area.

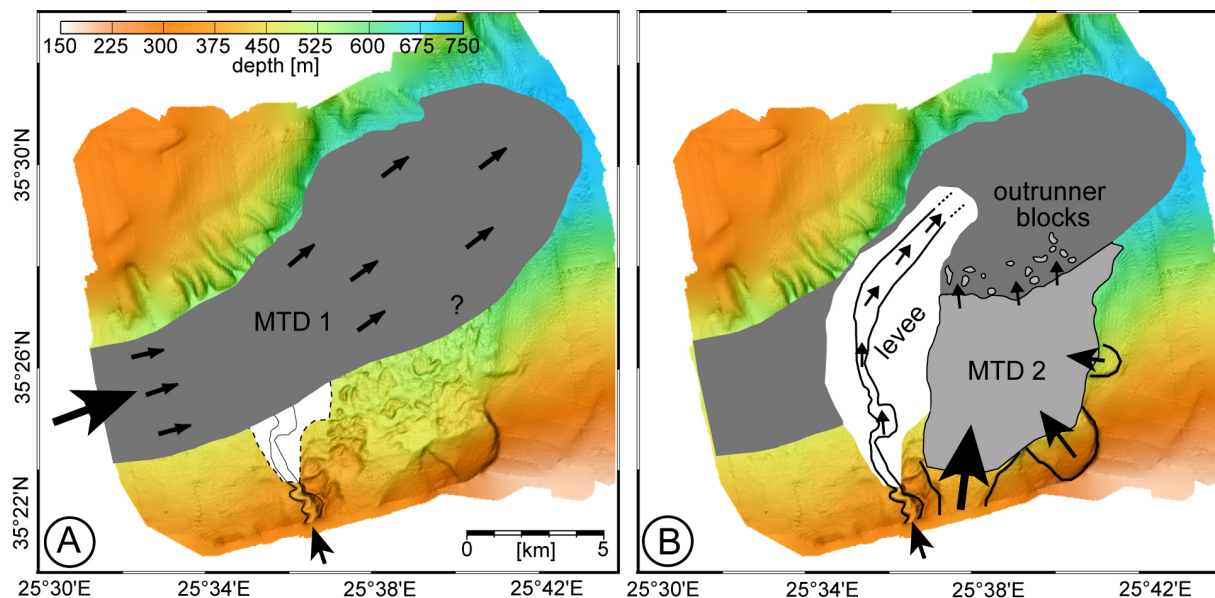


Fig. 4.10) Schematic illustration of a conceptual model for the study area; **A:** masses of the first event are transported as a debris flow from an area west of the Malia Basin into the survey area. The lateral distribution in the southeastern basin is unknown due to consequent emplacement of MTD 2 and its potential reworking of debris deposits; **B:** masses of the second slide event are transported from escarpments B-D to the south-eastern Malia Basin and accumulate as MTD 2. Outrunner blocks deposit in front of MTD 2 on top of MTD 1 (small black arrows). The existence of the channel-levee-complex (white drawing) during emplacement of the slide is highly assumed, but its lateral distribution unknown (indicated by a dotted line); further the post-slide accumulation of channel levee sediments with covering and probably reworking of debris deposits is indicated. In general, arrows indicate assumed transport direction and -paths of gravitational mass movement. Arrow-size shall roughly imply volume-proportion of sediment supply from the different source areas.

Within the next stage, masses of the second slide event were transported from the slope-basin-transition and an area upslope into the southeastern Malia Basin (Fig. 4.10B). The resulting MTD 2 is

interpreted as an aggregation of masses from multiple sources (Escarpments B-D), although individual slide bodies and associated scars cannot be conclusively traced in our data. Because there is no evidence for a temporal interval in between the superimposed masses, we postulate this MTD to be one distinct landslide event. The northwestern portion accumulated on top of the older debrite deposits and the channel levee is assumed to have constituted a western barrier for MTD 2 (Figs. 4.7 and 4.10B). Varying degrees of internal deformation within this MTD are interpreted to result from different transport mechanisms as a function of different transport distances of its masses. A mostly undisturbed reflection pattern within the southeastern portion indicates less internal deformation during transport and short transport distances. This is compatible with translational sliding from the well-defined and relatively small Escarpments C and D. In contrast, the northern to western deposits generally show a higher degree of deformation, which is consistent with a larger transport distance assuming an increase in degree of internal deformation during transport (compare Figs. 4.4 and 4.6 to Fig. 4.8; see also data in Hampton et al., 1996). Hence, these deposits are interpreted to be associated with Escarpment B, the headwall of which is expected further upslope. This may explain the larger transport distances of relevant slide masses.

Although there is no evidence for the source of the scattered blocks that occur on the seafloor in front of MTD2 and on top of MTD1, we interpreted the blocks as outrunner blocks of the second event due to their frontal, arcuated position (Fig. 4.10B).

4.6.2. Trigger mechanisms

Based on our data it is not possible to identify the explicit trigger mechanism, but the occurrence of faults and widespread ash layers, mud-rich sediments and/or sapropel layers allows a comparison of the most likely trigger mechanisms. Because of different transport directions and sources, and due to the chronological arrangement of MTDs based on our data, we identified two independent mass-movement events. The Cretan slope shows a partial increase of inclination at the base of the slope, close to the slope-basin transition (Fig. 4.3B) most probably resulting from ongoing extensional tectonic activity in the Cretan Sea. This indicates (over-) steepening as a likely pre-conditioning factor. In addition, geometries and orientations of the escarpments as well as locations of headwalls reflect the general trends of fault patterns in the area, suggesting a link between the initiation of the landslide and faults (see Fig. 4.8). Further, the presence of ash-layers, sapropels and intervals of mud-rich sediments found within core samples of the investigated area may indicate sediment layers with a potential for mechanical weakening at the level of slide planes (e.g. Huhn et al., 2006; Kutterolf et al., 2008). Based on the observation of several deeper ashes and sapropels from other studies on Cretan Sea sediments (e.g. Emeis et al., 1996; Robertson et al., 1998), we assume that such layers also occur at the level of slide planes of detected mass-wasting processes in the Malia Basin and along the slope. An earthquake and the associated dynamic loading could have produced pore-pressure transients and/or cyclic degradation along such a layer and is considered as a likely ultimate trigger candidate.

Alternatively, we assume that the emplacement of the debris flow into the Malia Basin may have caused spatial reworking and therewith unloading of sediments at the slope-basin-transition (Fig. 4.10A). This unloading could have triggered a destabilization in slope sediments and initialized failure and sliding of the second slide event.

4.7. Summary & Conclusions

The analysis of a dense net of acoustic data in combination with some core data in the Mali Basin north of Crete allows a detailed discussion of mass-wasting in this region for the first time. The main conclusions are:

[1] We identified two stacked MTDs with a total volume about 4.5 km³ over an area of 135 m². The two deposits represent the youngest events of repeating mass-wasting activity in the Malia Basin. A younger, massive MTD is identified as an aggregation of slide masses derived from multiple source areas. This MTD partially covers an older MTD, a large-scaled debrite, that fills the larger part of the Malia Basin and that is reconstructed to originate from the area west of the basin. Several older MTDs are detected beneath the two described bodies and indicate frequent mass wasting along the northern Cretan mid-slope over geological time scales.

[2] The two major MTDs show different source areas and differ in transport distances, mechanics and kinematics. This may also indicate different trigger events.

[3] Ash-layers, mud-rich sediments and sapropels assumed at the depth of slide planes represent layers of potential weakening from one of the common earthquakes in this region. Hence their occurrence is the most important preconditioning factor for slope failure initiation. The increase of slope inclination associated with a dense faulting at the slope-basin-transition further increases the likelihood of mass-wasting processes at study site.

[4] All detected mass transport deposits are older than 12.6 cal. ka B.P. The estimated maximum age of the two uppermost MTDs is about 25 ka B.P.

4.8. Acknowledgments

We thank the whole scientific party and the ship crew of P-336 for faithful and detailed recording of data. We thank all involved scientists at the Hellenic Centre for Marine Research, Greece, for their scientific input and discussions as well as support of the P-336 cruise. We want to thank the MARUM for scientific support and all involved scientists and members for fruitful discussions and outcomes. We thank reviewer Angelo Camerlenghi and a second, unknown reviewer for their dedicative work and thoughtful comments that considerably improved the manuscript. This publication is funded through the DFG-Research Centre / Excellence Cluster „The Ocean in the Earth System“.

References:

- Aksu, A.E., Yasar, D., Mudie, P.J., 1995. Paleoclimatic and paleoceanographic conditions leading to development of sapropel layer S1 in the Aegean Sea. *Palaeogeogr. Palaeoclimatol. Palaeoecol.* 116, 71-101.
- Angelier, J., Lyberis, N., Le Pichon, X., Barrier, E., Huchon, P., 1981. The Tectonic development of the hellenic arc and the sea of Crete: a synthesis. *Tectonophysics* 86, 159-196.
- Bonneau, M., 1984. Correlation of the Hellenide nappes in the south-east Aegean and their tectonic reconstruction. *Geol. Soc., London, Special Publications* 17, 517-527.
- Bromhead, E. N., 1992. *The Stability of Slopes*. Blackie Academic & Professional, Glasgow, UK.
- Canals, M., Lastras, G., Urgeles, R., Casamor, J.L., Miernert, J., Cattaneo, A., De Batist, M., Hafliadon, H., Imbo, Y., Laberg, J.S., Locat, J., Long, D., Longva, O., Masson, D. G., Sultan, N., Trincardi, F., Bryn, P., 2004. Slope failure dynamics and impacts from seafloor and shallow sub-seafloor geophysical data: case studies from the COSTA project. *Mari. Geol.* 213, 9-72.
- Camerlenghi, A., Cita, M.B., Hieke, W., Ricchiuto, T., 1992. Geological evidence for mud diapirism on the Mediterranean Ridge accretionary complex. *Earth and Planet. Sci. Let.* 109, 493-504.
- Caress, D.W., Chayes, D.N., 2006. MB-System: Mapping the Seafloor. <http://www.mbari.org/data/mbsystem>, <http://www.ldeo.columbia.edu/res/pi/MB-System>.
- Carey, S., 1997. Influence of convective sedimentation on the formation of widespread tephra fall layers in the deep sea. *Geology* 25, 839-842.
- Casten, U., Snopek, K., 2006. Gravity modelling of the Hellenic subduction zone - a regional study. *Tectonophysics* 417, 183-200.
- Chamot-Rooke, N., Rabaute, A., Kreemer, C., 2005. Western Mediterranean Ridge mud belt correlates with active shear strain at the prism-backstop geological contact. *Geology*, 33(11), 861-864
- Chaumillon, E., Mascle, J., 1996. From foreland to forearc domains: Mew multichannel seismic reflection survey of the Mediterranean ridge accretionary complex (Eastern Mediterranean). *Mar. Geol.* 138, 237-259.
- Chronis, G., Lykousis, V., Georgopoulos, D., Poulos, M., Zervakis, V., Stavrakakis, S., 2000a. Suspended particular matter and nepheloid layers in the southern margin of the Cretan Sea (NE Mediterranean): seasonal distribution and dynamics. *Progr. Oceanogr.* 46, 163-185.
- Chronis, G., Lykousis, V., Anagnostos, C., Karageorgis, A., Stavrakakis, S., Poulos, S., 2000b. Sedimentological processes in the southern margin of the Crete Sea (NE Mediterranean). *Progr. Oceanogr.* 46, 143-160.
- DeMenocal, P.B., Ortiz, J., Guilderson, T., Sarnthein, M., 2000. Coherent high- and low-latitude climate variability during the Holocene warm period. *Science* 288, 2198-2202.
- Deyhle, A., Kopf, A., 2001. Deep fluids and ancient pore waters at the backstop: Stable isotope systematics (C, B, O) of mud volcano deposits on the Mediterranean Ridge accretionary wedge. *Geology*, 29/11, 1031-1034.
- Emeis, K.-C., Robertson, A.H.F., Richter, C., et al., 1996. *Proc. ODP, Init. Repts.*, 160: College Station, TX (Ocean Drilling Program).
- Fassoulas, C., 2000. The tectonic development of a Neogene basin at the leading edge of the active European margin: the Heraklion basin, Crete, Greece. *J. Geodyn.* 31, 49-70.
- Giresse, P., Buscail, R., Charriere, B., 2003. Late Holocene multisource material input into the Aegean Sea: depositional and post-depositional processes. *Oceanol. Acta.* 26, 657-672.
- Gunn, D.A., Nelder, L.M., Rochelle, C. A., Bateman, K., Jackson, P.D., Lovell, M.A., Hobbs, P.R.N., Long, D., Rees, J. G., Schultheiss, P., Roberts, J., Francis, T., 2002. Towards improved ground models for slope instability evaluations through better characterization of sediment-hosted gas-hydrates. *Terra Nova* 14, 443-450.
- Hampton, M.A., Lee, H.J., Locat, J., 1996. Submarine landslides. *Rev. Geophys.* 34, 33-59.
- Hughen, K.A., Baillie, M.G.L., Bard, E., Beck, J.W., Bertrand, C.J.H., Blackwell, P.G., Buck, C.E., Burr, G.S., Cutler, K.B., Damon, P.E., Edwards, R.L., Fairbanks, R.G., Friedrich, M., Guilderson, T.P., Kromer, B., McCormac, G., Manning, S., Ramsey, C.B., Reimer, P.J., Reimer, R.W., Remmele, S., Southon, J.R., Stuiver, M., Talamo, S., Taylor, F.W., van der

- Plicht, J., Weyhenmeyer, C.E., 2004. Marine04 Marine Radiocarbon Age Calibration, 0–26 Cal Kyr BP. *Radiocarbon* 46, 1059–1086.
- Huhn, K., Kock, I., Kopf, A., 2006. Comparative numerical and analogue shear box experiments and their implications for the mechanics along the failure plane of landslides, *Norw. J. Geol.*, 86(3), 209-220.
- Huson, W.J., Fortuin, A.R., 1985. The Lithion Slide: A large submarine slide in the South Cretan Trough, eastern Mediterranean. *Mar. Geol.* 65, 103-111.
- Kopf, A., Mascle, J., Klaeschen, D., 2003. The Mediterranean Ridge: A mass balance across the fastest growing accretionary complex on Earth. *J. Geophys.* 108, 2372-2403.
- Kopf, A., Alves, T., Heesamnn, B., Irving, M., Kaul, N.E., Kock, I., Krastel, S., Reichelt, M., Schäfer, R., Stegmann, S., Strasser, M., Thölen, M., 2006. Report and preliminary results of Poseidon cruise P336: CRESTS – Cretan Sea Tectonics and Sedimentation, Heraklion 28.04.-17.05.2006. *Berichte, Fachbereich Geowissenschaften, Universität Bremen*, 253.
- Kopf, A., Stegmann, S., Krastel, S., Förster, A., Strasser, M., Irving, M., 2007. Marine deep-water Free-fall CPT Measurements for landslide characterisation off Crete, Greece (Eastern Mediterranean Sea) - PART 2: Initial data from the western Cretan Sea. In: Lykousis, V., Sakellariou, D., Locat, J. (eds.). *Submarine Mass movements and their consequences. Advances in Natural and Technological Hazards Series*, Springer, 199-208.
- Kutterolf, S., Freundt, A., Schacht, U., Bürk, D., Harders, R., Mörz, T., Pere'z, W., 2008. Pacific offshore record of plinian arc volcanism in Central America: 3. Application to forearc geology. *AGU and the Geochemical Society* 9, Number 2.
- Lee, H.J., Locat, J., Desgagnés, P., Parsons, J.D., McAdoo, B.G., Orange, D.L., Puig, P., Wong, F.L., Dartnell, P., Boulanger, E., 2007. Submarine mass movements on continental margins. In: Nittrouer, C.A., Austin, J.A., Field, M.E., Kravitz, J.H., Syvitski, J.P.M., Wiberg, P.L. (eds.). *Continental Margin Sedimentation: From Sediment Transport to Sequence Stratigraphy*, Wiley-Blackwell, UK, 213-274
- Le Pichon, X., Lallemand, S.J., Chamot-Rooke, N., Lemeur, D., Pascal, G., 2002. The Mediterranean Ridge backstop and the Hellenic nappes. *Mar. Geol.* 186, 111-125.
- Le Pichon, X., 1979. The Hellenic arc and trench system: A key to the neotectonic evolution of the eastern Mediterranean area. *Tectonophysics* 60, 1-42.
- Locat, J., Lee, H.J., 2002. Submarine landslides: advances and challenges. *Can. Geotech. J.* 39, 193-212.
- McAdoo, B.G., Pratson, L.F., Orange, D.L., 2000. Submarine landslide geomorphology, US continental slope. *Mar. Geol.* 169, 103-136.
- Manakou, M. V., Tsapanos, T. M., 2000. Seismicity and seismic hazard parameters evaluation in the island of Crete and the surrounding area inferred from mixed data files. *Tectonophysics* 321, 157-178.
- Mascle, J., Martin, L., 1990. Shallow structure and recent evolution of the Aegean Sea: a synthesis based on continuous reflection profiles. *Mar. Geol.* 94, 271–299.
- Masson, D.G., Harbitz, C.B., Wynn, R.B., Pedersen, G., Løvholt, F., 2006. Submarine landslides: processes, triggers and hazard prediction. *Phil. Trans. R. Soc. A* 364, 2009–2039.
- Meier, T., Rische, M., Endrun, B., Vafidis, A., Harjes, H.-P., 2004. Seismicity of the Hellenic subduction zone in the area of western and central Crete observed by temporary local seismic networks. *Tectonophysics* 383, 149-169.
- Mienert, J., Andreassen, K., Bunz, S., 2003. Gas hydrates at Storegga Slide In: J. Mienert and P. Weaver, Editors, *European Margin Sediment Dynamics: Side-Scan Sonar and Seismic Images*, Springer-Verlag, Berlin Heidelberg, 107–110.
- Papazachos, B.C., 1990. Seismicity of the Aegean and surrounding area. *Tectonophysics* 178, 287–308.
- Pirazzoli, P.A., 2005. A review of possible eustatic, isostatic and tectonic contributions in eight late-Holocene relative sea-level histories from the Mediterranean area. *Quaternary Sci. Rev.* 24, 1989-2001.
- Peterek, A., Schwarze, J., 2004. Architecture and Late Pliocene to recent evolution of outer-arc basins of the Hellenic subduction zone (south-central Crete, Greece). *J. Geodyn.* 38, 19-55.

-
- Polonia, A., Camerlenghi, A., Davey, F., Storti, F., 2002. Accretion, structural style and syn-contractonal sedimentation in the Eastern Mediterranean Sea. *Mar. Geol.* 186, 127-144.
- Robertson, A.H.F., Emeis, K.-C., Richter, C., and Camerlenghi, A. (Eds.), 1998. *Proc. ODP, Sci. Results, 160*: College Station, TX (Ocean Drilling Program).
- Stuiver, M., Reimer P.J., 1986. A computer program for radiocarbon age calculation. *Radiocarbon* 28, 1022-1030.
- Sultan, N., Cochonat, P., canals, M., Cattaneo, A., Dennielou, B., Halifladson, H., Laberg, J.S., Long, D., Mienert, J., Trincardi, F., 2004. Triggering mechanisms of slope instability processes and sediment failure on continental margins: a geotechnical approach. *Mar. Geol.* 213, 291-321.
- Wessel, P., Smith, W. H. F., 1998. New, improved version of Generic Mapping Tools released. *EOS Trans. Amer. Geophys. U.* 79, pp. 579.
- Vendeville, B. C., Gaullier, V., 2003. Role of pore-fluid pressure and slope angle in triggering submarine mass movements: natural examples and pilot experimental models. *Submarine Mass Movements and Their Consequences, 1st International Symposium*, 137-144.



5. Reconstruction of retreating mass wasting in response to progressive slope steepening of the northeastern Cretan margin, eastern Mediterranean

Submitted to *Marine Geology* as: Frank Strozyk¹, Michael Strasser¹, Sebastian Krastel², Mathias Meyer² & Katrin Huhn¹. Reconstruction of retreating mass wasting from progressive slope steepening of the northeastern Cretan margin, eastern Mediterranean

¹ MARUM, Centrum for Marine Environmental Sciences - Cluster of Excellence: The Ocean in the Earth System, University of Bremen, P.O. Box 33 04 40, D-28359 Bremen, Germany

² IFM-GEOMAR, Leibniz Institute of Marine Sciences, Cluster of Excellence: The Future Ocean, Christian-Albrecht-University Kiel, D-24148 Kiel, Germany

Abstract

In this study we aim on a reconstruction of mechanisms and kinematics of slope-failure and mass-movement processes along the northeastern slope of Crete in the Hellenic forearc, eastern Mediterranean. Here, subsidence of the forearc basin and the uplift of the island of Crete cause ongoing steepening of the slope in-between, emphasising the high level of neotectonic activity in this region, and are expected to exert a key role in slope-failure development. Newly acquired reflection seismic data from the upper slope region reveal an intact sediment cover while the lower slope is devoid of both intact strata and mass transport deposits (MTDs). In a mid-slope position, however, we found evidence for a 4-km³-sized landslide complex that comprises several MTDs from translational transport of coherent sediment bodies over short distances. Morphometric analysis of these MTDs and their source scars indicates that this part of the northeast Cretan slope can be characterised as a cohesive slope. Furthermore, we reconstruct retrogressive development for this complex and determine a critical slope angle for both pre-conditioning of sediment failure and subsequent landslide deposition. Consequently, data imply that the investigated shallower slope is stable due to lower angles of $\leq 3^\circ$, whereas the $\leq 5^\circ$ -inclined mid-slope favours both slope destabilization and landslide deposition. Failed mid-slope parts are also dominated by sediment truncations from faults. Hence, we suggest that these cohesive landslides and MTDs can only be generated and preserved, respectively, in these critical slope regions. If once generated, cohesive landslides reach the lower slope further downslope that exceeds the threshold gradient for MTD deposition, they are transported all the way down to the foot of the slope while they disintegrate to mass flows. From these results we deduce that the mass-wasting history of the investigated Cretan slope area over a longer period of time is characterized by repeated sediment erosion and transport into the deeper Cretan Sea basin. The relocation of the critical slope portion and therefore recurrence of mass-wasting events is thereby likely controlled by the progressive steepening of the slope. This mechanism and restriction of sediment failures to a narrow, critically inclined slope area likely explains how such an active margin

setting can exhibit only scarce findings of landslide deposits on the slope despite the expected extensive and widespread mass wasting.

5.1. Introduction

It is generally accepted that repeated mass movements can erode a significant amount of submarine slope sediment through time and thus strongly affect slope morphology (e.g., Leeder, 1999; Canals et al., 2004; Haflidason et al., 2004; Urgeles et al., 2006). The mechanical behaviour of sediments and slope geometry thereby exert key roles in failure development and also have a high impact on the mass-movement transport mechanisms, which can occur either in a cohesive or disintegrative fashion (e.g., Locat and Lee, 2002; McAdoo et al., 2000). McAdoo et al. (2000; 2004) have shown that mass movements along active margin slopes bearing cohesive sediments often consist of compact landslides or slumps of low recurrence as these slopes can be of high resistance against shearing. Such cohesive landslides are of relatively small volumes and can have short runouts (e.g., Hampton et al. (1996) and Lee et al. (2007)). Disintegration of landslides during longer runout as well as failure in sediments of non- or less-cohesive character can result in mass-flows (e.g., Gee et al., 1999; Masson et al., 2006; Lee et al., 2007). Morphometric analyses of mass-transport deposits (MTDs), source scars and the adjacent slopes of cohesive landslides compared to mass-flows indicate that they can strongly differ in scar geometry, headwall height and gradient, the gradient of the adjacent slope, as well as the mass-movement size and runout distance (McAdoo et al., 2000; Haflidason et al., 2003). Therefore, morphometric measurements on scars and MTDs can be used to reconstruct failure and transport kinematics as well as the mechanical behaviour of sediment during failure and transport (McAdoo et al. (2000)).

The northeastern margin of Crete represents the southern border of the Cretan Sea submarine basin (Fig. 1A) and is an example that evidences only some scattered landslide scars and MTDs on an active margin slope. The detected pattern of MTDs on the slope comprises slides as well as debrites with volumes in the order of ≤ 0.5 to ≥ 2.0 km³ (e.g., Chronis et al., 2000; Kopf et al., 2006; Kopf et al., 2007; Strozyk et al., 2009). Seismic data presented by Kopf et al. (2006) suggest the presence of stacked MTDs also in the deeper Cretan Sea sub-basins (i.e. the Kamilonisi and Heraklion Basin). However, the scarce findings of MTDs along this slope contrast the expectation of a diffuse and extensive mass-movement pattern depending on the region's high neotectonic activity (e.g. earthquakes and tectonic movement), as characteristic for active margin settings. The high shear resistance of the cohesive, consolidated Cretan slope sediment is proposed being the responsible mechanism restricting a higher frequency of slope collapse (Chronis et al., 2000; Kopf et al., 2006; 2007).

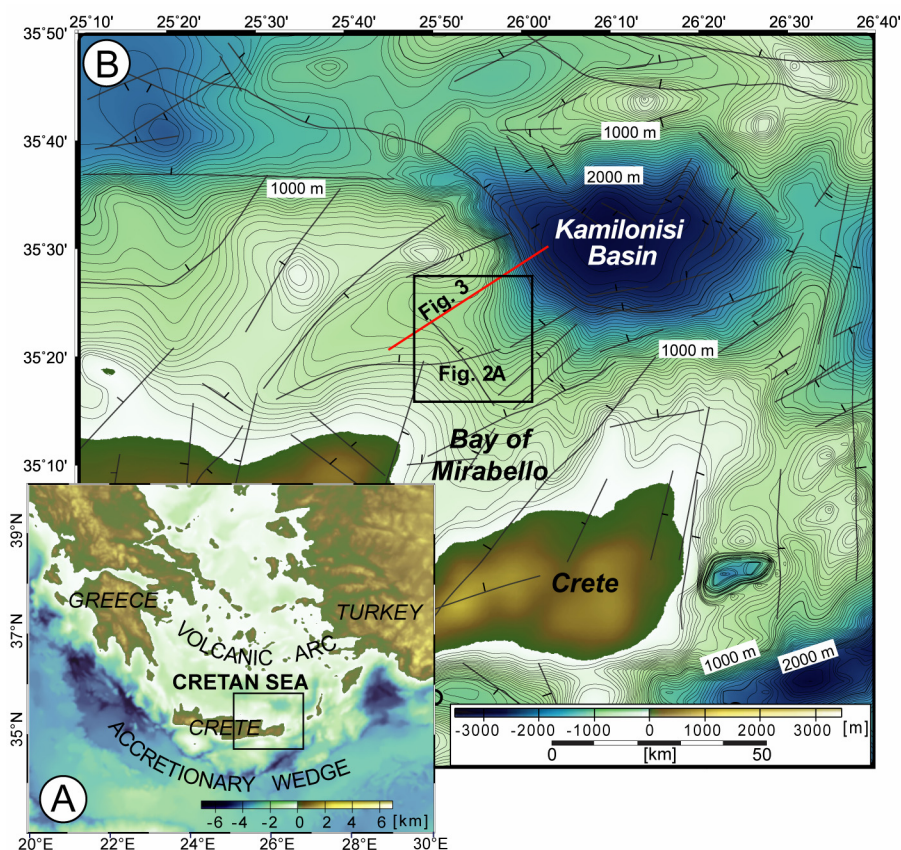


Fig. 5.1) A: Bathymetry map of the eastern Mediterranean active margin. The black box indicates the location of the study site and surroundings in the southern Cretan Sea (Fig. 5.1B); **B:** bathymetry map of the study site and surroundings on the northeastern margin of Crete, north of the Bay of Mirabello and southwest of the Kamilonisi Basin. Thin lines represent relief counter lines in 50-m intervals. Thick black lines indicate major faults in the southern Cretan Sea interpreted and compiled after Mascle and Martin (1990) and Angelier et al. (1982). The red line indicates the location of seismic profile GeoB06-133, the black box outlines the study site in the mid-slope region (Fig. 5.2).

The aim of this study is (i) a detailed description of a cluster of MTDs on the northeastern Cretan slope, (ii) to measure proportions of MTDs, their source scars and the adjacent intact slope supported by a morphometric analysis of these features, (iii) a determination of mass-movement types, runout distances and transport mechanisms, and (iv) to evaluate critical slope angles for sediment stability and pre-conditioning of its destabilization. Our study is based on the interpretation of multi-channel reflection seismic profiles and bathymetric data recorded during the 2006 CRESTS (Cretan Sea Tectonics and Sedimentology) cruise aboard R/V Poseidon. We also compare our findings to the concept of morphometric analysis of slope failures, and discuss the results in terms of slope morphology and tectonic movement representing pre-conditioning factors for mass wasting in such active margin environments.

5.2. Regional settings

The Cretan Sea basin represents the large forearc basin of the Hellenic subduction zone (McKenzie, 1978; Le Pichon and Angelier, 1979; Fig. 5.1A). This elongated, east-west-trending, almost north-

south-extensional forearc depression is bordered to the north by the volcanic arc and to the south by the island of Crete (Fig. 5.1A and B), which is an exhumed horst structure and still being uplifted (Bonneau, 1984). Extension and subsidence of the basin is reconstructed to a last main creation phase during the Late Miocene and Pliocene, while it is proposed to have decreased since that time (Meulenkamp et al., 1988; Mascle and Martin, 1990). However, several surveys indicated recent fault activity and micro-seismicity in the southern Cretan Sea and have confirmed that the tectonic system is still active today (e.g. Lykousis et al., 1995; Perissoratis and Papadopoulos, 1999). Subsidence rates in the forearc region increase from the west to the east, associated to an increase of the dip of the African slab subduction to the east (e.g. Angelier et al., 1982; Meier et al., 2004). The resulting tectonic deformation and high subsidence rates caused the formation of several large sub-basins, of which the Kamilonisi Basin is the deepest with up to 2500 m water depth (Fig. 5.1B; e.g. Stavrakakis et al., 2000). Major faults associated with these sub-basins trend approximately northeast-southwest (Angelier et al., 1979; Mascle and Martin, 1990). A second system of smaller, more scattered faults trends almost perpendicular southeast-northwest (Fig. 5.1B; Mascle and Martin, 1990). Owing to the extension in the forearc, the Cretan Sea sub-basin subsidence, and the countering uplift of the island of Crete, the northern Cretan slope in-between is of steep and irregular topography (Chronis et al., 2000; Kopf et al., 2006; Strozyk et al., 2009).

5.3. Data and methods

5.3.1. Multibeam bathymetric data

A bathymetric mapping of the northeastern Cretan margin slope and the adjacent deeper Cretan basin was carried out continuously during the CRESTS cruise with an ELAC SeaBeam 1050 multibeam echo-sounder. This system was operated at 12 kHz with an auto-adjusting, maximum angular coverage of 150° corresponding to a swath width of up to 7.5 times the water depth. Bathymetric data of the investigated area (25°47'E-26°03'E/ 35°22'N-35°36'N) occupies about 700 m² of the northeastern Cretan slope in water depths of <200 to >1200 m. The data were processed with MB-System (Caress & Chayes, 1996) and gridded with resolutions of 10 and 20 m cell-sizes using GMT (Generic Mapping Tool; Wessel & Smith, 1998). Shaded relief plots of the bathymetric grid were used to identify, describe, and measure topographic and morphological seafloor features.

5.3.2. Seismic data

Reflection seismic profiles were recorded using a Mini-GI-Gun (2 x 0.25 l, 100-500 Hz, operated at 140-150 bars) and a 100 m-long 16-channel streamer with 8 hydrophones per channel and a group distance of 6.25 m. The shooting rate was 8 s, ship speed was about 4 kn and the resulting shot-point distance is about 17 m. Twenty-three seismic lines of northeast- southwest- and southeast-northwest-orientation in 3-5 km spacing were acquired (Fig. 5.2) and processed. Additional details on acquisition techniques are given in the P-336 cruise report (Kopf et al., 2006). We use Vista software

(Seismic Image Software Ltd.) for standard processing of data, including trace editing, Common-Mid-Point (CMP) sorting, static and delay corrections, normal moveout corrections, bandpass frequency filtering (frequency content: 55/110–600/800 kHz), stacking, and migration (1500 m s^{-1}). A CMP spacing of 10 m is applied throughout. The Kingdom Suite (Seismic Micro-Technology Inc) was used for seismic data visualization and interpretation.

5.3.3 Morphometric analysis

According to the morphometric analysis of slope failure sensu McAdoo et al. (2000), we use seismic and bathymetry data to measure the (mean) gradient of the undisturbed slope adjacent to landslide scars, the height and slope of headwalls, the areas of seafloor affected by failure, the failure depths (in between slide planes and pre-failure seafloor), the eroded sediment volumes (surface \times mean thickness), and the runout distance of slid masses where identifiable. In the next step, we compare measured headwall heights vs. runout distances, the slope gradient adjacent to failure vs. headwall slopes, headwall heights, slope gradient, failure depths, and failure areas to the compilation of ‘cohesive’ and ‘disintegrative’ slope failures presented in McAdoo et al. (2000).

5.4. Observations from acoustic data

5.4.1. Relief and seafloor morphology from bathymetric data

In the study area northeast off the Bay of Mirabello, the Cretan shelf drops down towards the increasingly inclined slope ($1\text{--}8^\circ$) and the steep southwestern flank of the Kamilonisi Basin ($\geq 8^\circ$; Figs. 5.1B and 5.2A). The southwestern part of the investigated slope area shows a smooth seafloor morphology and topography of the upper slope region ($\leq 3^\circ$; Fig. 5.2A). Towards the northeast further down the slope, the relief of the slope is more irregular and composed of small, northeast-southwest-trending topographic highs and lows (Fig. 5.2A). In the mid-slope region, which is of $3\text{--}5^\circ$ mean inclination, the seafloor drops off to the lower slope and the southwestern flank of the Kamilonisi Basin (Fig. 5.2A). The central part of the investigated area is dominated by a downslope-concave scarp heading northeast (Fig. 5.2B). The seafloor morphology within the scarp as well as in an area further downslope northeast is irregular and hummocky (Figs. 5.2B). In closer inspection, a narrow area of ‘en echelon’ topography is identified along the head region of the scarp (Fig. 5.2B). Additionally, a large block associated to the intact slope apron can be traced from the western boundary to the central part of the scarp (Fig. 5.2B).

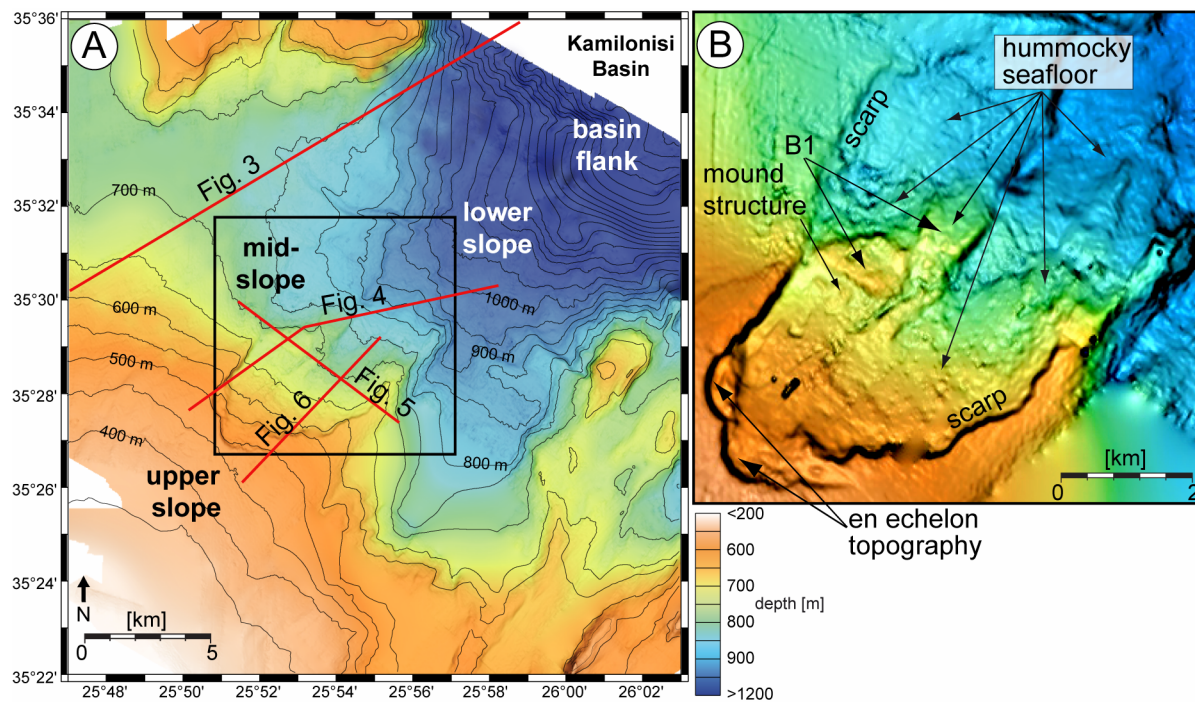


Fig. 5.2) A: The newly recovered bathymetric chart (shaded relief + colour) of the investigated area. Thin lines represent relief counter lines in 50-m intervals. Red lines indicate locations of seismic profiles shown in subsequent figures; **B:** close-up of the scar-structure in the central study site, showing steep outer walls, a hummocky seafloor morphology within the structure and an en echelon topography along the southwestern-most boundary. Note the block ('B1') of smooth morphology within the scar.

5.4.2. Seismic characterization of sediments

In this study, we define seismic units in terms of deposits from gravitational mass-transport in contrast to undisturbed strata using seismic reflection pattern attributes, such as amplitude, continuity and configuration. As reasoned below, we identify three types of sedimentary features: (1) undisturbed sediment as a background unit U1 (Figs. 5.3-5.6), (2) scars as source areas of MTDs (SC1-3; Figs. 5.4-5.6), and (3) deposits from gravitational mass movement (MTD1-3; Figs. 5.4-5.6).

5.4.2.1 Background sediments (U1, B1, drape)

The background unit U1 is characterized by a parallel- to sub-parallel-, well-stratified reflector pattern that represents regularly accumulated sediment on top of a gently inclined acoustic basement (Figs. 5.3, 5.4, 5.5, and 5.6), which most likely correlates to the Messinian-Pleistocene boundary (Masclé and Martin, 1990). Hence, the up to 250 m-thick sediment cover investigated in this study represents an age of between 4 and 5 Ma. In shallower water depths (i.e. <800 m), the slope shows a mostly undisturbed, continuous U1 pattern, except for reflector off-sets at faults (e.g., Figs. 5.4, 5.5, and 5.6) and for those places where the regular pattern has been affected by erosional scars (see section 5.4.2.2). The steeper slope in >800 m water depths is almost devoid of the U1 pattern (e.g., Fig. 5.3). Measured values of mean U1-reflector inclination and approximated U1 thicknesses above the acoustic basement are presented in Table 5.1.

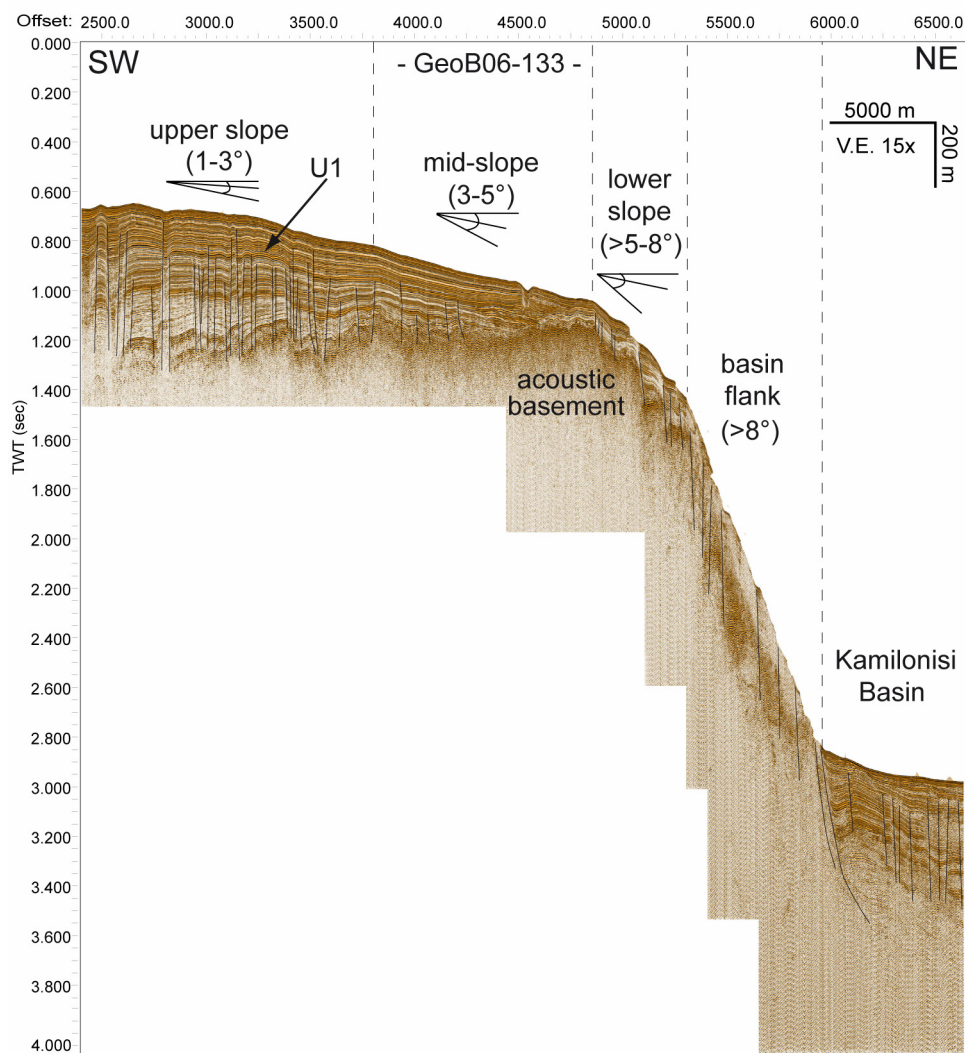


Fig. 5.3) Southwest-northeast seismic profile GeoB06-133 (for location see Figs. 5.1 and 5.2), showing the approximated positions of the upper, middle, and lower slope, transposed from the study site to this profile, as well as the Kamilonisi Basin flank and the foot region of the slope (Fig. 5.2). Note that the well-stratified U1 background sediment can be traced throughout the upper and mid-slope, while it is missing at the lower slope and the basin flank. Further note that slope angles as well as the slope part boundaries are projected from the closer study site (Fig. 5.2).

Faults

Faults are identified from offsets of seismic reflectors and mostly occur as straight to listric lineaments of various scales. We interpret two major trends of faults in the investigated area. The first and dominant pattern can be traced in approximately northeast-southwest-direction (e.g., Figs. 5.5A, 5.7) and the second occurs almost perpendicular trending approximately slope-parallel southeast-northwest (Figs. 5.3, 5.4, 5.6, 5.7). Larger normal faults with high offsets in the southern and southeastern study area (e.g., right hand side Fig. 5.5) can be traced down to the acoustic basement and are mostly associated to the northeast-southwest-trending fault system. Some of these faults can also be traced along relief structures in the bathymetric chart (Fig. 5.7). Hence, these faults follow main structural elements of topographic highs and lows, and are thus associated to the almost north-south-trending Cretan Sea basin extension and half graben formation. The perpendicular, second system comprises mainly smaller and more scattered faults that often assemble in areas of

pronounced changes in slope inclination, e.g. the slope breaks from the lower to the mid-slope and from the mid-slope to the upper slope (e.g. Fig. 5.3). Here, they often occur pairwise as small-scaled graben structures, while younger sediments above and older below are often not affected (e.g., Fig. 5.4 left hand side). Hence, these faults may correlate to phases of active tectonic movement (slope steepening) and thus activity of large normal faults further downslope at the Kamilonisi Basin flank (Fig. 3).

Stable block (B1)

A 2-km²-sized block of intact U1-stratification that occurs at the northwestern sidewall of SC2 (see section 5.4.2.2) is referred to as “B1”. As we are able to extrapolate the B1 reflection pattern continuously to U1 upslope SC2, this structure is interpreted to represent a stable block of unmoved U1-succession within MTD2 (see section 5.4.2.3; Fig. 5.7). Furthermore, the northeastern part of this block is covered by a MTD (MTD2b; Figs. 5.4B and 5.7). Geometrical proportions of B1 are presented in Table 5.1.

Drape

Also as part of U1, a uniform (post-failure) drape is interpreted on scars (5.4.2.2) and on top of MTDs (Figs. 5.4, 5.5, and 5.6). Measured drape thicknesses are of between 10 and 20 m (± 2.5 m). Drape thicknesses less than 5 m expected along steeper, exposed relief parts are barely identifiable according to the resolution of seismic data (i.e. 5 ± 2.5 m). In contrast to the large well- and parallel-stratified portion of the drape sediments, those on top of (at least) MTD2 show a blocky, slightly rotational segmentation indicated by some low-angle reflector off-sets (Figs. 5.4, 5.5, and 5.6). As these off-sets are not correlatable to U1 fault off-sets (see Fig. 5.4A), they are inferred to originate from a deformation of the MTD after deposition. Furthermore, we identify several smaller capered structures of almost transparent reflection attributes within the MTD’s drape (Fig. 5.4A). Below, within the MTD2, they occur as higher reflection amplitudes compared to the MTD (Fig. 5.4A). Some of these structures further reach the topmost drape reflectors and raise above the seafloor (Figs. 5.3B and 5.4A).

Table 5.1.) Geometrical measures of scars (SCs), MTDs (1-3), and background units (U1, B1)

	Surface [km ²]	Thickness [m]	Gradient [°]	Volume [km ³]	Water depth [m]
SC1	>7	60 ^[1]	25	>1.0 ^[3]	>900
SC2	~40	50 - 70 ^[1]	16-23	~2.6 ^[3]	500-800
SC3	~6	40 ^[1]	20	~0.4 ^[3]	730-800
MTD1	>20	40 ^[2]	5-8	>0.8 ^[4]	>920
MTD2	>50	50 ^[2]	5	~2.0 ^[4]	~520 - 1000
MTD2b	3	<25 ^[2]	3	~0.1 ^[4]	~750 - 780
MTD3	>12	25-30 ^[2]	4-5	~0.4 ^[4]	~750 - 900

U1	-	<100 - >250	<1.4 - 8	-	<200 - 1050
B1	~2	75 ¹	2.5-3	-	~720

[1] Maximum height of headwall

[2] Thickness in-between slide place reflector and reconstructed pre-failure seafloor

[3] Eroded volume, back-calculated from the reconstructed pre-failure sediment thicknesses to the lateral extent of scars

[4] Volumes are calculated from extents and thicknesses of MTDs available in data

5.4.2.2 Scars

We generally define ‘scars’ as volumetric features in between head- and sidewalls down to slide planes, which equal the volumes of eroded sediments prior to slope failure and mass movement. Head- and sidewalls are deep truncations of U1, indicating its erosion and indicated by slope gradient increases to 15-25° (Figs. 5.4A, 5.5, and 5.6). Scars are therefore interpreted to originate from displacement of eroded U1-sediment and are correlated to mass wasting (Fig. 5.7). Further, we observe that trends of side- and headwalls are of same trend and orientation as U1 truncations by faults, with headwalls and sidewalls tracing slope-parallel and the major northeast-southwest-trending fault system, respectively (Figs. 5.4B, 5.5, and 5.7). Geometrical measures of all scars are presented in Table 5.1.

“SC1” (Figs. 5.4 and 5.7) is the northeastern-most scar detected in our data with a large and steep headwall (Figs. 5.4), while this scar do not indicate the presence of pronounced sidewalls. Although we don’t have full control on this scar’s geometry and total extension due to less seismic data in this area, we can measure its headwall height and gradient as well as the gradient of the interpreted slide plane in front.

The second scar, “SC2” (Figs. 5.4, 5.5, 5.6, and 5.7), is present approximately 5 km upslope southwest of SC1 and imaged as a prominent structure in seismics as well as in bathymetry (see section 5.4.1). SC2 consists of pronounced head- and sidewalls (e.g. Figs. 5.4 and 5.5), whereas the spacing between sidewalls is limited by the B1 block and therefore decreases with increasing water depth (Fig. 5.7). The scar shows en echelon blocks of almost intact U1-stratification with small, but identifiable vertical and lateral off-set along its headwall (Fig. 5.6A and B). The blocks’ displacement results in the en echelon topography identified in the bathymetric chart (compare Figs. 5.2 and 5.7; see also section 5.4.1).

The third detected scar “SC3” is located at the northwestern boundary of SC2 (Fig. 5.7; see sidewalls in Fig. 5.5) and is of similar geometry and orientation as SC2, but much smaller in lateral extent and depth (Fig. 5.5; see also Table 5.1). Note that the northwestern sidewall of SC3 occurs as an extension of the northern sidewall of SC2 (see Fig. 5.7), while its head- and southeastern sidewall trace the steep flanks of the B1 block (Fig. 5.5; see also section 5.4.2.4).

5.4.2.3. MTDs

Three MTDs are identified as confined bodies of a chaotic to almost transparent reflection pattern, indicating high deformation of U1 sediment during erosion and transport, thus strongly contrasting

intact U1 (e.g. Figs. 5.4 and 5.6). Measured geometrical proportions of all MTDs and gradients of slide plane reflectors below are comprised in Table 5.1.

MTD1 occurs frontal northeast and downslope of SC1 (Figs. 5.4 and 5.6). As scars SC2 and SC3 cannot explain the volume of this MTD1 as well as it is overlain by MTD2, we interpreted SC1 being its source scar (Fig. 5.7). The MTD is of varying thicknesses, resulting in an irregular contact with the overlying, draping U1-sediments (Fig. 5.4A and B). Note that the basis of this MTD can be traced almost consistently plane-parallel on top of intact seismic reflectors (dashed line in Fig. 5.4B).

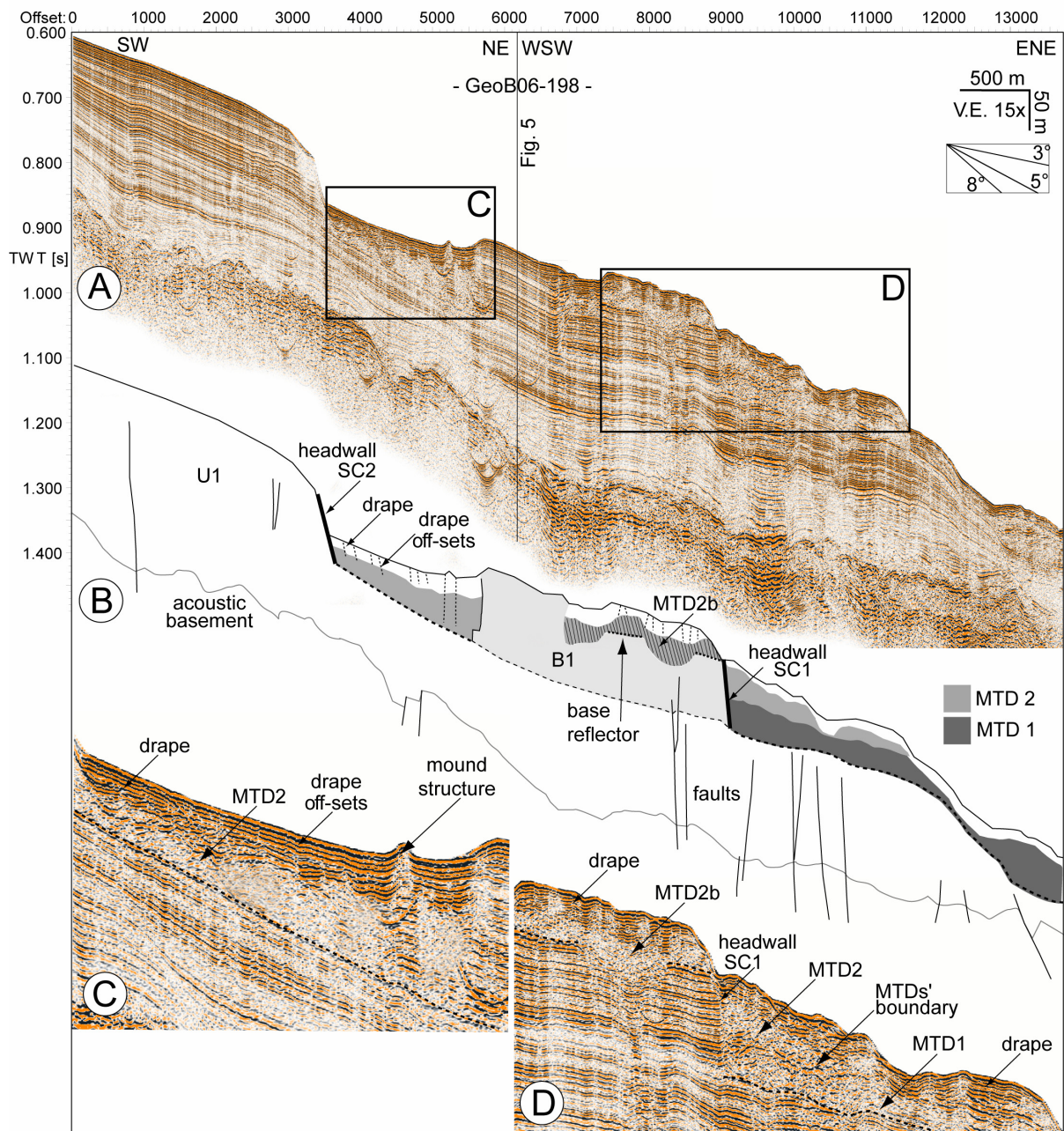


Fig. 5.4 A: Southwest-northeast seismic profile GeoB06-198 slicing the northern and central portion of the prominent scar, turning from a SW-NE-trend to a WSW-ENE-trend at the height of the 'B1'-block (for location see Fig. 2); B: sketch of the interpreted seismic unit MTD1 (dark grey), 2 (grey) and 2b (grey with lines), their scars SC1 and SC2 (headwalls thick, black lines), and the background units U1 (white) and 'B1' (light grey). Faults are marked as black lines, whereas small off-sets in the drape on top of MTDs are marked as thin, dotted, black lines; C: close up of the as MTD2 interpreted seismic unit in front of the interpreted headwall of SC2. Note that the MTD basis (dotted line) is almost parallel to the background sediment pattern below; D: close up of the interpreted MTD2-sub-unit

MTD2b on top of the 'B1' block (left) and the superposition of MTD2 on top of MTD1 in front of the SC1 headwall (right). The slope strata-parallel MTD bases are marked as thin dotted lines.

MTD2 (Figs. 5.4, 5.5, 5.6, and 5.7) is mostly present within SC2 in front of the headwall (Figs. 5.4B and 5.6) and between sidewalls (Fig. 5.6), which is thus identified as its source scar. The downslope increasingly chaotic pattern of MTD2 is almost plane-parallel bedded on top of intact seismic reflectors, which correlate to the stratigraphically depth of the base of MTD1 (Fig. 5.4B). Further, seismic data reveal that a portion of MTD2 covers MTD1 in front of SC1 (Figs. 5.4B and 5.7). The boundary between both MTDs is indicated by some less-deformed reflectors patches at the top of MTD1 contrasting the nearly transparent reflection at the bottom side of MTD2 (Fig. 5.4B). Since these less-deformed reflector patches do not occur further downslope northeast in our data, we interpret them representing less deformed slid sediment at the top of MTD1.

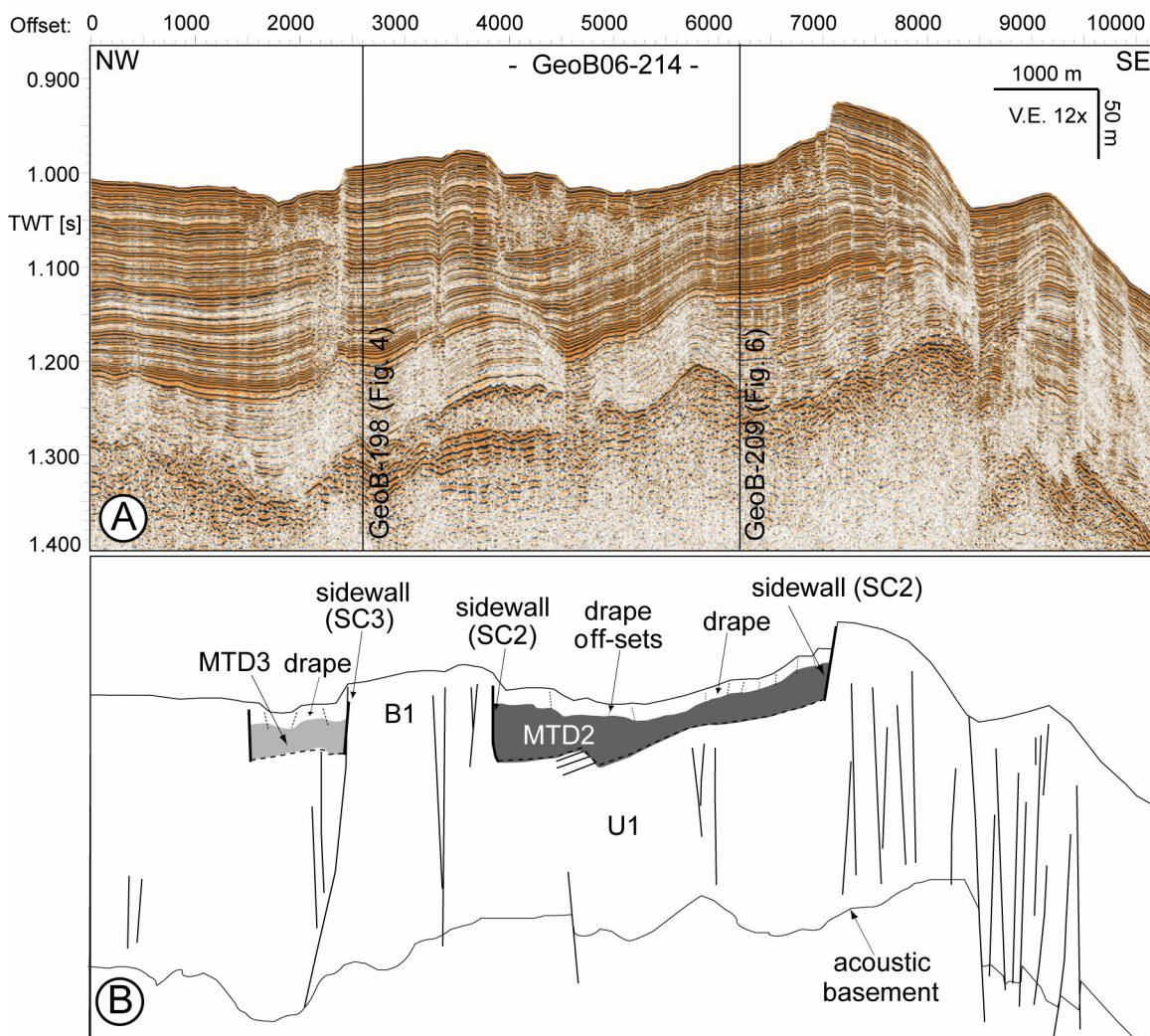


Fig. 5.5 A: Northwest-southeast seismic profile GeoB06-214 (for location see Fig. 5.2), slicing the prominent scar (Fig. 5.2B) slop-parallel and perpendicular to the transport-direction of mass-movements; B: interpretation Figure of MTD2 (grey), sidewalls of SC2, the stable block B1 and MTD3 (light grey) as well as sidewalls of SC3. Black lines indicate interpreted faults, dotted line below MTDs the interpreted almost U1 pattern-parallel MTD basis.

Another portion of MTD2 is referred to as the sub-unit MTD2b, identified as a relatively thin, chaotic, and irregular slide deposit on top of the northeastern extension of B1 (Fig. 5.4B; see also section 5.4.2.1). The genetic linkage of this slide deposit to MTD2 is based on the stratigraphic depth of its basis, which correlates with a seismic reflector representing the seafloor at the time of MTD2 emplacement (Fig. 5.4A and B).

MTD3 is, compared to MTD1 and MTD2, a small landslide deposit (see Table 5.1) and located almost completely within its source scar SC3 (Figs. 5.5 and 5.7). This MTD also occurs plane-parallel-bedded on top of a pronounced seismic reflector that was found in stratigraphically shallower depth compared to those of MTD1 and MTD2 (Fig. 5.5).

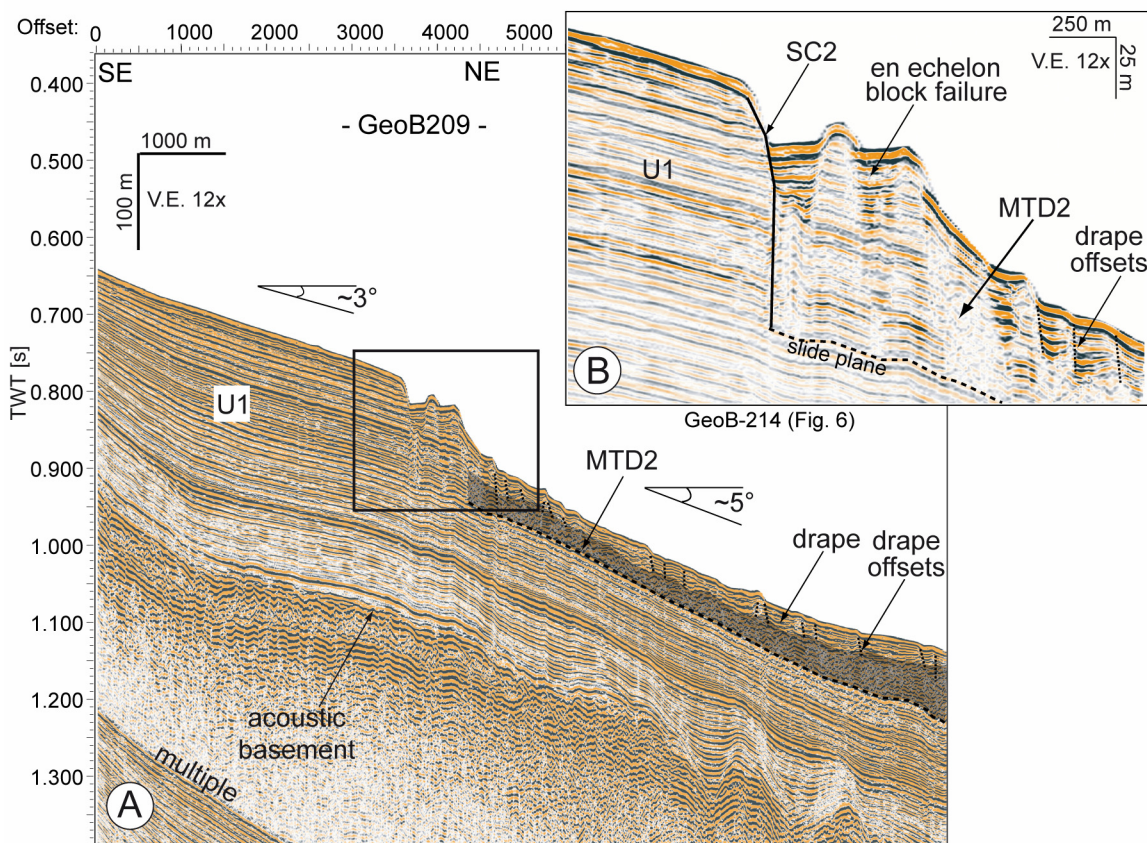


Fig. 5.6 **A:** Southwest-northeast seismic profile GeoB06-209 (for location see Fig. 5.2), slicing MTD2 (grey) in transport direction and the background unit U1. The black box represents a close-up of the headwall area shown in Fig. 5.6B; **B:** close-up on the headwall area of SC2 indicating failure of intact blocks along the wall that build up en echelon topography, and the MTD2 in front with typical, small off-sets in the drape above

5.5. Interpretations

5.5.1 Timing and evolution of slope failure and mass-movements

Based on our observation of sizes, locations and a sequencing of MTDs as well as sizes and locations of their source scars, we here compile a conceptual model of slope-failure development. We focus on mass-movement transport paths and runout distances as well as the relative arrangement of MTDs to

reconstruct a relative timing of single failure events. As a basis for our model, we use a pre-failure slope geometry (Fig. 5.8A) reconstructed from (i) a transposed, intact seismic reflector from depth (e.g., Fig. 5.4B), (ii) measurements of intact slope geometry from bathymetric and seismic data adjacent to the failed slope (e.g., Figs. 5.2 and 5.3), and (iii) the deposition reflector of MTD2b (Fig. 5.4B).

5.5.1.1 Initial failure phase

Our reconstruction of an initial phase of slope destabilization is based upon the stratigraphic arrangement of MTD2 on top of MTD1 (section 5.4.2.3) indicating that MTD1 emplaced prior to MTD2. We assume that an external trigger mechanism, e.g. an earthquake (as proposed by Chronis et al. (2000) and Kopf et al. (2006; 2007)) is responsible for initializing sediment destabilization at the steeper slope (i.e. 5°) along the headwall of SC1 (Figs. 5.8A and B). Consequently, downslope movement of an up to 60-m-thick sediment package along an inclined slide plane towards the northeast occurred (Fig. 5.8B). According to the strong increase in slope angle ($\geq 8^\circ$) further northeast, we infer that one portion of this landslide could have been transported further down the steeper slope out of data range, whereas the larger portion accumulated in front of the headwall. This depletion of sediment at SC1 is suggested to have acted, however, as a pre-conditioning factor for a destabilization of sediments upslope.

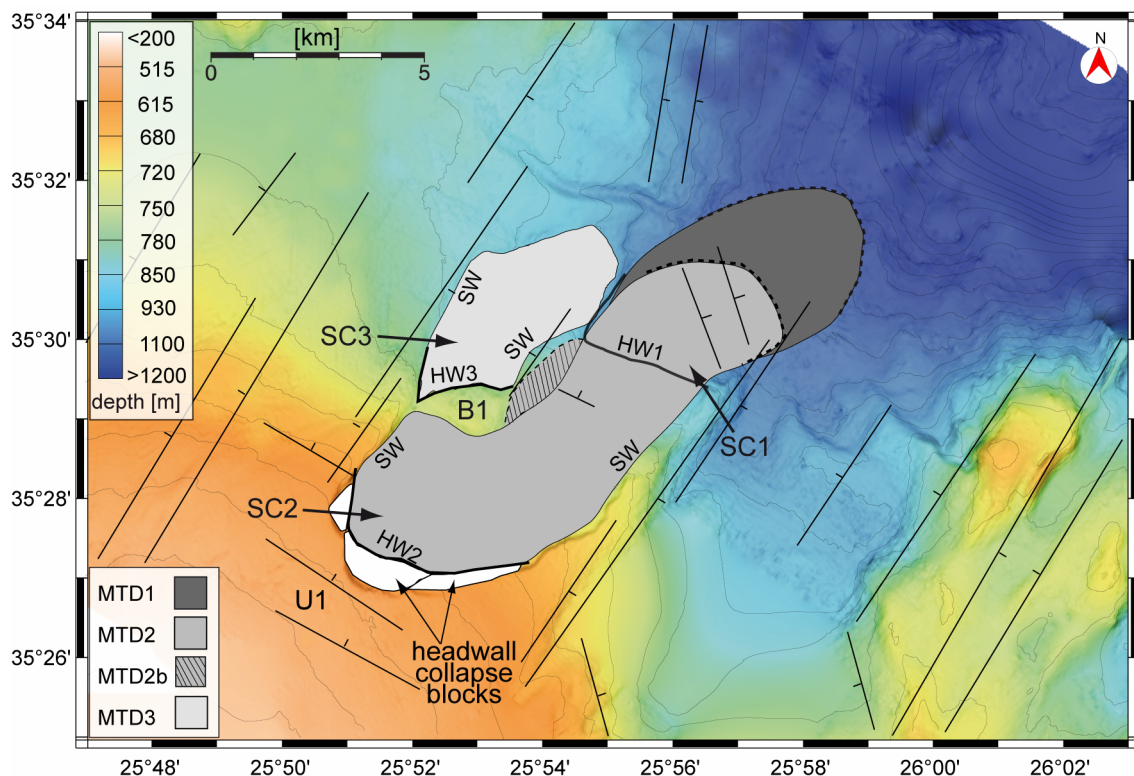


Fig. 5.7) Bathymetry map-plot of the investigated area with interpreted (dashed lines = assumed) lateral extents of MTD 1, 2, 2b, 3, SC1, 2, 3, and B1. All non-marked areas primarily belong to the background unit U1. Interpreted main faults are marked as black lines and dips; SW: sidewall; HW: headwall.

5.5.1.2 Retreating failure phase

We reconstruct this (at least) second phase of slope destabilization in terms of sediment failure retreating upslope towards the southwest (see section 5.5.2.2). We interpret that sediments were destabilized in the back of SC1, have overridden the headwall, and accumulated as one portion of MTD2 on top of MTD1 (Fig. 5.8C).

As we see here some analogies in scar and MTD geometry to well-documented studies on retreating landslide complexes (see data in e.g. Kvalstad et al. (2004) and L'Heureux et al. (2007)), we combine the described MTDs and their scars to a single landslide-complex.

It is difficult to assess whether all masses of MTD2 failed simultaneously or with small intervening time-periods. However, as seismic data do not indicate several, individual slide bodies within MTD2, this MTD may originate from a single as well as several phases of sediment destabilization in a short time-period upslope towards the southwest. With respect to the resolution of the seismic data (i.e., 5 ± 2.5 m vertical resolution), we admit maximum possible intervening periods in the order of 25 - 70 ka based on the sediment accumulation rate range of 7 - 20 cm ka⁻¹ (e.g., Giresse et al., 2003).

Furthermore, the presence of the stable B1-block in the area of SC2 suggests that the northeastern landslide portion was destabilized in upslope direction forming the narrowing passage in between B1 and the southeastern sidewall of SC1 (Fig. 5.8C-D). Here, the slide plane of the MTD2-landslide is present at the same stratigraphic level as the top of the previously accumulated MTD1 (see Fig. 5.8C). We further interpret that the depth of failure stepped down to the pronounced slide plane reflector during the failure retreating somewhat further upslope in the back of SC1 (Fig. 5.8C to D). This implies the presence of a mechanically weak sediment layer in depth, which is held responsible for this preferred depth of sediment failure as well as translational sliding of masses. Coevally, the destabilized sediments spilled across some remaining, intact U1-strata in the back of SC1, then have overridden the headwall of SC1 and finally accumulated on top of MTD1 (Fig. 5.8D).

Another portion of these sliding masses is reconstructed to have been transported along the northwestern sidewall of SC2 and to have overridden the southeastern flank of B1 (Fig. 5.8D). While B1 remained stable during the complex evolution, this small slide portion accumulated on the top of its northeastern extension as MTD2b (Fig. 5.8D).

As a result from this slope failure development, the larger volume of the MTD2-landslide is found in front of the head- and in-between the sidewalls of its source scar. However, it is likely that the northeastern-most portion also of this landslide experienced longer runout downslope out of data range.

In a final stage of the complex evolution, coherent, triangular blocks of almost intact U1-stratification failed along the SC2-headwall and built-up the en echelon topography detected in both seismic and bathymetry data (Figs. 5.2B, 5.6B, and 5.8D). We suggest that the most proximal part of MTD2

restricts further downslope movements of these blocks. This ‘headwall collapse’ traces the slope break that is also characterized by faults and separates the mid-slope (5°) and upper slope region (3°). Hence, we deduce that this sagging of blocks along slope-parallel faults at this particular slope break position finally uncoupled the sediment failure upslope towards the southwest (Fig. 5.8D).

5.5.1.3 MTD3

The failure of masses deposited as MTD3 cannot be arranged in stratigraphic order to the other MTDs. As this landslide shows a very short runout, no sequenced bedding and thus no chronology relative to other MTDs can be determined. However, the drape thickness on top of MTD3 is almost identical to that of the entire complex, thus indicating a roughly similar age and allowing us to propose this event to have occurred coevally to the development of this landslide complex (Fig. 5.8C-D).

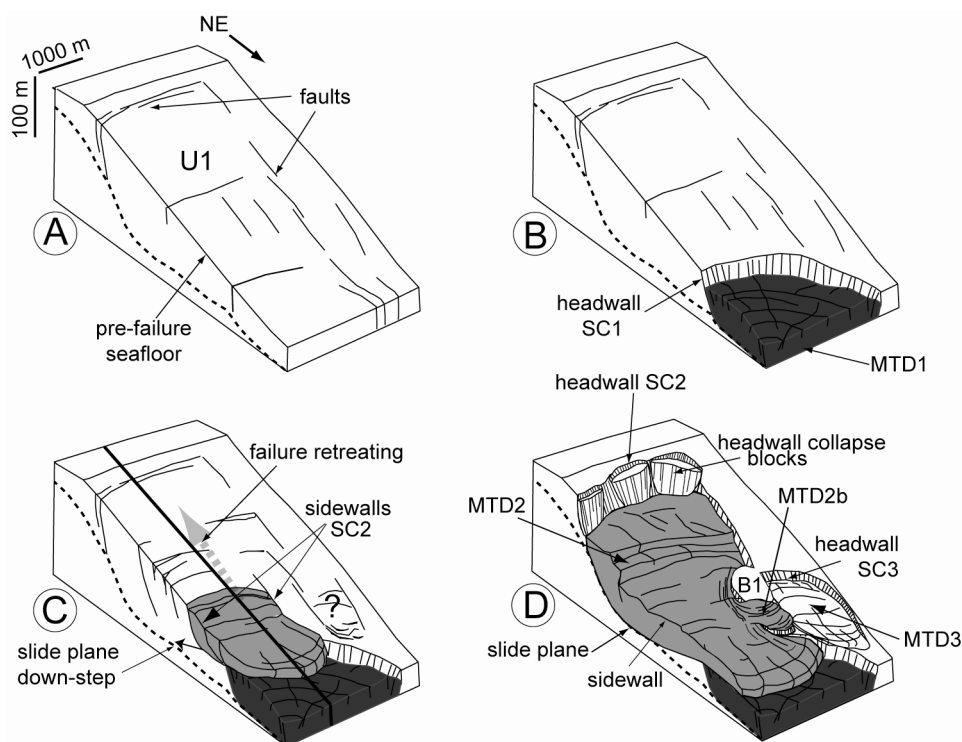


Fig. 5.8) Time series of 3D-sketches showing the landslide complex evolution: **A:** reconstructed pre-failure setup; **B:** initial failure along SC1 and deposition of MTD1; **C:** failure retreating upslope towards the southwest, maybe also failure of masses within SC3; **D:** emplacement of MTD2 and possibly MTD3; uncoupling of failure along minor slope-parallel faults resulting in the headwall of SC2.

5.5.1.4 Post-slide phase

Since the emplacement of the MTDs, constant draping of sediments to the currently detectable 10-20 m thick background sediment on top of MTDs occurred. Short distant creeping is deduced for at least MTD2, as indicated from the rotational deformation of the drape on top of the MTD in downslope direction (Fig. 5.4). This deformation is interpreted to coincide with a de-watering of at least MTD2 to the drape, resulting also in some fluid-escapes at the seafloor. The observed acoustically-

transparent, capered structures in e.g. seismic profile GeoB-198 (Fig. 5.4) and bathymetry data (Fig. 5.2B) support this interpretation of fluid-escape features, as similar structures have been related to such processes in other settings (e.g., Moernaut et al., 2009). These processes likely indicate that at least MTD2 has not been consistently of steady state since its emplacement at the mid-slope. Furthermore this may indicate ongoing tectonic movement and some further steepening of this slope area after the MTD's emplacement.

5.5.2 Identification of mass-movement types

Our interpretation of failure and transport mechanisms of mass movement at the study site is based on the general landslide nomenclature by Hampton et al. (1996) and Lee et al. (2007). Interpreted source scars (SC1-3) and slide planes as well as MTD geometries, internal deformation patterns, transport paths, and runout distances are considered for their classification.

All landslides and MTDs at the study site have been released and moved or have accumulated, respectively, along more or less distinct slide planes as indicated by almost intact seismic reflectors along MTD bases (see section 5.4.2.4). We hence interpret translational sliding along those planar surfaces to be the dominant transport mechanism. The high degree of internal deformation of MTDs implies relatively high transport dynamics and thus slow movement is unlikely despite short runout distances of MTDs detected on the slope. This is in line with a rough comparison of scar and MTD volumes implying that the larger portions of MTDs is found within or close to their source scars.

Nevertheless, the volumetric comparisons as well as the downslope increasing slope gradient ($>5^\circ$) may also imply that not the entire eroded masses deposited after short runout. Hence, we infer movement of destabilized sediments also down the steeper lower slope towards northeast. Strozzyk et al. (2009) found evidence of both landslide and mass-flow deposits along the northeastern Crete slope, and thus propose that larger runout can cause disintegration of landslides to mass flows on the northeastern Cretan margin. Based on that, we suggest that a similar behaviour may also apply to former landslides generated at this study site if their transport down to the steeper lower slope has led to an increase in transport dynamics. This is seen to also have caused disintegration of primary cohesive landslides and enabled their further movement as debris or mass flows all the way down to the slope foot region. This interpretation is in line with seismic data showing multiple stacked MTDs in the Kamilonisi Basin (Kopf et al., 2006).

5.6. Discussion and Conclusions

We have shown that the multiple MTDs found in a mid-slope position on the northeastern Cretan margin originate from the deposition of coherent sediment masses after short distant sliding along well-defined slide planes close to their source scars. A first event was possibly triggered by an earthquake and caused the destabilization of sediment packages further upslope. We observe that neither stable background sediments, nor MTDs can be found on the examined portion of the steeply

inclined lower slope and Kamilonisi Basin flank further downslope this first MTD (Fig. 5.3). Opposite, background sediment of the shallower, lower inclined slope is intact and still stable in the study area (e.g., Figs. 5.2, 5.3, 5.4; see also Kopf et al. (2006; 2007)). A structural interpretation of fault patterns at and adjacent to the landslide scars shows that the sum of fault offsets in downslope direction is higher within scar areas than in the stable slope apron. This is in line with our measurements of the MTD base-reflectors gradient, which thus show higher values in the order of 5° within the scars (Table 1). Hence, fault off-sets are held responsible for the 5° slide plane gradient which is inferred to be a critical threshold for sediment destabilization scenarios.

In terms of mass wasting producing landslides at the size of observed MTDs, the investigated slope area can consequently be subdivided into (1) a stable upper slope, (2) a partially critical inclined mid-slope, and (3) an over-critical lower slope (Figs. 5.3 and 5.9). Initiation of landsliding at the critical mid-slope as well as uncoupling of failure at the break from the mid-slope to the upper slope may further indicate a restriction of such slope collapses to the well-defined critical slope region. We therefore deduce that slope geometry of breaks in slope angle is an important pre-conditioning factor for repeated sediment destabilization (see Fig. 5.9).

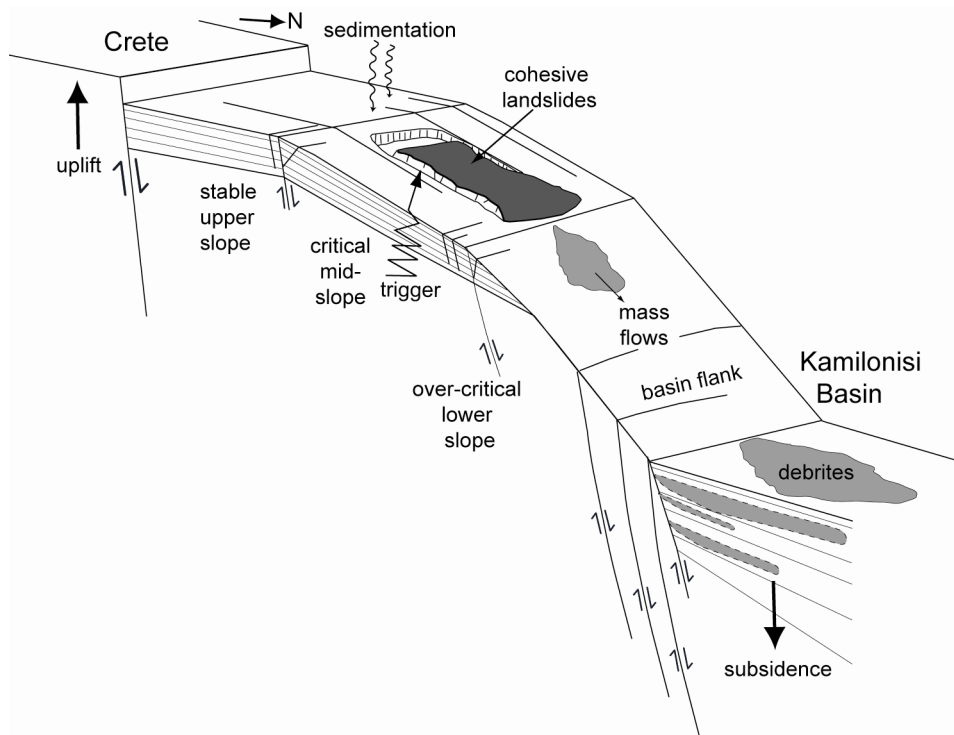


Fig. 5.9.) Sketch showing the assumed, long-term mass-movement development on the investigated northeastern Cretan slope (not to scale). Note that we infer an external stimulus (e.g., earthquake trigger) to release landslides in the critical mid-slope region. These landslides can deposit in the critical mid-slope region or being transported further downslope immediately or after reactivation, disintegrate into mass-flows, and finally deposit as debrites in the Kamilonisi Basin if they reach the steeper lower slope. Thereby, both the critical and over-critical slope portions are suggested to have relocated in upslope direction through time due to basin subsidence and the countering uplift of Crete. This entire mechanism is seen to already have eroded and may continue to erode the Cretan slope sediment load.

On closer inspection, our measurements of source scars show some morphometric analogies to 'cohesive failures' described in the literature (McAdoo et al., 2000). These analogies include small failure areas (12 - 50 km²), while headwalls are steep (15 - 25°) and the failure depths are high (~ 60 m). Also the landslide deposits show similarities to the morphometric characteristics of 'cohesive slides' (after McAdoo et al., 2000) as they are of short runout (<1 - 5 km) compared to the heights of their headwalls, and deposited as compact, coherent MTDs (≤ 2 km³). This at first high coherency of destabilized masses is held responsible for their short runout and deposition of MTDs close to scars, thus characterizing this portion of the northeastern Cretan slope as a 'cohesive slope'.

On the other hand, important differences to settings often characterized as 'cohesive slopes', e.g. forearc slopes at accretionary margins (McAdoo et al., 2000), are attributed to the Cretan margin tectono-sedimentary setting that is dominated by hemipelagic sedimentation on an extensional basin slope. Thus, the slope-parallel sediment bedding is held responsible to favour translational mass-movement along well-defined slide planes of 5° inclination, which is below typical values for 'cohesive slope failure'-examples that often occur as deeply incised slumps (McAdoo et al., 2000). McAdoo et al. (2000) further propose that typical 'cohesive failures' tend to make a slope steeper whereas mass wasting at the northern Cretan margin indicates that the taper can also be adjusted by translational mass movements. Also, if Cretan slope landslides reach the steeper, lower slope that exceeds the threshold gradient for their deposition, runout distances can be large and cause a disintegration of the coherent landslides into mass flows.

In conclusion, our study suggests that northeast Cretan slope mass-wasting events at the scale of observed scars and MTDs typically occur in narrow, critically steepened slope portions. The youngest events can thus be found in a mid-slope position (Fig. 5.9). On longer time-scales, an upslope relocation of this critical area to its current position may have occurred. This relocation was most likely controlled by the progressive steepening of the slope, caused by the uplift of Crete and a counter movement from high subsidence of the Kamilonisi Basin (Stavrakakis et al., 2000; Fig. 5.9). High subsidence rates in the Cretan basin caused the over-critical inclination of the lower slope and basin flank, and imply an upward extension of slope areas critical for mass-wasting over longer time-scales. We hence deduce that this mechanism may have also caused further transport of former landslides or a reactivation of their MTDs down to the slope foot region (Fig. 5.9). Consequently, evidence for larger mass-wasting in post-Messinian sediments on this slope portion is only present in scattered, youngest mid-slope MTDs and their associated scars, tracing the narrow, critically inclined and densely faulted slope portions. This conceptual model may likely explain how such active margin settings can exhibit only scarce findings of MTDs on the slope while evidences for an extensive and widespread mass wasting is generally expected due to the high neotectonic activity.

Acknowledgements:

We thank the whole scientific party and the ship crew of P-336 for faithful and detailed recording of data. We thank all involved scientists at the Hellenic Centre for Marine Research, Greece, for their scientific input and discussions as well as support of the P-336 cruise. We thank the MARUM for scientific support and involved scientists for fruitful discussions. This publication is funded through the DFG-Research Centre/ Cluster of Excellence „The Ocean in the Earth System“.

References

- Angelier, J., Lyberis, N., Le Pichon, X., Barrier, E., Huchon, P., 1982. The Tectonic development of the Hellenic arc and the sea of Crete: a synthesis. *Tectonophysics* 86, 159-196.
- Bonneau, M., 1984. Correlation of the Hellenide nappes in the south-east Aegean and their tectonic reconstruction. *Geological Society, London, Special Publications* 17, 517-527.
- Canals, M., Lastras, G., Urgeles, R., Casamor, J.L., Mienert, J., Cattaneo, A., De Batist, M., Haflidason, H., Imbo, Y., Laberg, J.S., Locat, J., Long, D., Longva, O., Masson, D. G., Sultan, N., Trincardi, F., Bryn, P., 2004. Slope failure dynamics and impacts from seafloor and shallow sub-seafloor geophysical data: case studies from the COSTA project. *Marine Geology* 213, 9-72.
- Caress, D. W., and D. N. Chayes, 1996. Improved processing of Hydrosweep DS multibeam data on the R/V Maurice Ewing. *Marine Geophysical Research*, 18, 631-650.
- Chronis, G., Lykousis, V., Anagnostos, C., Karageorgis, A., Stavrakakis, S., Poulos, S., 2000. Sedimentological processes in the southern margin of the Crete Sea (NE Mediterranean). *Progress in Oceanography* 46, 143-160.
- Gee, M.J.R., Masson, D.G., Watts, A.B., Allen, P.A., 1999. The Saharan debris flow: an insight into the mechanics of long runout submarine debris flows. *Sedimentology* 46, 317-335.
- Giresse, P., Buscaill, R., Charriere, B., 2003. Late Holocene multisource material input into the Aegean Sea: depositional and post-depositional processes. *Oceanologica Acta* 26, 657-672.
- Haflidason, H., Sejrup, H.P., Nygård, A., Mienert, J., Bryn, P., Lien, R., Forsberg, C.F., Berg, K., Masson, D., 2004. The Storegga Slide: architecture, geometry and slide development. *Marine Geology* 213, 201-234.
- Haflidason, H., Sejrup, H.P., Berstad, I.M., Nygård, A., Richter, T., Bryn, P., Lien, R., Berg, K., 2003. A weak layer feature on the Northern Storegga Slide escarpment. In: Mienert, J., Weaver, P. (Eds.), *European Margin Sediment Dynamic - Side-Scan Sonar and Seismic Images*. Springer, Berlin, 55-62.
- Hampton, M.A., Lee, H.J., Locat, J., 1996. Submarine landslides. *Reviews of Geophysics* 34, 33-59.
- Kopf, A., Alves, T., Heesamnn, B., Irving, M., Kaul, N.E., Kock, I., Krastel, S., Reichelt, M., Schäfer, R., Stegmann, S., Strasser, M., Thölen, M., 2006. Report and preliminary results of Poseidon cruise P336: CRESTS – Cretan Sea Tectonics and Sedimentation, Heraklion 28.04.-17.05.2006. *Berichte, Fachbereich Geowissenschaften, Universität Bremen*, 253
- Kopf, A., Stegmann, S., Krastel, S., Förster, A., Strasser, M., Irving, M., 2007. Marine deep-water Free-fall CPT Measurements for landslide characterisation off Crete, Greece (Eastern Mediterranean Sea) --- PART 2: Initial data from the western Cretan Sea. In: Lykousis, V., Sakellariou, D., Locat, J. (eds.). *Submarine mass movements and their consequences*. *Advances in Natural and Technological Hazards Series*, Springer, 199-208
- Kvalstad, T. J., Andresen, L., Forsberg, C. F., Berg, K., Bryn, P., Wangen, M., 2004. The Storegga Slide: evaluation of triggering sources and slide mechanics, *Marine and Petroleum Geology* 22, 245-256.
- Lee, H.J., Locat, J., Desgagnes, P., Parsons, J.D., McAdoo, B.G., Orange, D.L., Puig, P., Wong, F.L., Dartnell, P., Boulanger, E., 2007. Submarine mass movements on continental margins. In: Nittroer, C.A., Austin, J.A., Field, M.E., Kravitz, J.H., Syvitki, J.P.M., Wiberg, P.L. (eds.), *Continental Margin Sedimentation*, Blackwell Publishing, UK, 213-274.
- Leeder, M., 1999. *Sedimentology and Sedimentary Basins – from Turbulences to Tectonics*. Blackwell Publishing, UK.
- Le Pichon, X., Angelier, J., 1979. The Hellenic Arc and Trench system: a key to neotectonic evolution of the Eastern Mediterranean area. *Tectonophysics* 6, 1-42.

- L'Heureux, J.-S., Longva, O., Hansen, L., Vingerhagen, G., 2007. The 1990 submarine slide outside the Nidelv River mouth, Trondheim, Norway. In: Lykousis, V., Sakellariou, D., Locat, J. (eds.). *Submarine Mass movements and their consequences*. Advances in Natural and Technological Hazards Series, Springer, 199-208.
- Locat, J., Lee, H.J., 2002. Submarine landslides: advances and challenges. *Canadian Geotechnical Journal* 39, 193-212.
- Lykousis, V., Roussakis, G., Alexandri, M., Pavlakis, P., Papoulia, I., 2002. Sliding and regional slope stability in active margins : North Aegean Trough (Mediterranean). *Marine Geology* 186, 281-298.
- Lykousis, V., Anagnostou, C., Anastasakis, G., Pavlakis, P., Roussakis, G., Alexandri, M., 1995. Quaternary sedimentary history and neotectonic evolution of the eastern part of Central Aegean Sea. *Marine Geology* 186, 281-298
- Masson, D.G., Harbitz, C.B., Wynn, R.B., Pedersen, G., Løvholt, F., 2006. Submarine landslides: processes, triggers and hazard prediction. *Philosophical Transaction of the Royal Society A* 364, 2009-2039.
- Masclé, J., Martin, L., 1990. Shallow structure and recent evolution of the Aegean Sea: a synthesis based on continuous reflection profiles. *Marine Geology* 94, 271-299.
- McAdoo, B.G., Pratson, L.F., Orange, D.L., 2000. Submarine landslide geomorphology, US continental slope. *Marine Geology* 169, 103-136.
- McAdoo, B.G., Capone, M.K., Minder, J., 2004. Seafloor geomorphology of convergent margins: Implications for Cascadia seismic hazard. *Tectonics* 23.
- McKenzie, P.D. (1978): Active tectonics of the Alpine-Himalayan belt: the Aegean Sea and surrounding regions. *Geophysical Journal of the Royal Astronomical Society* 55, 217-254.
- Meier, T., Rische, M., Endrun, B., Vafidis, A., Harjes, H.-P., 2004. Seismicity of the Hellenic subduction zone in the area of western and central Crete observed by temporary local seismic networks. *Tectonophysics* 383, 149-169.
- Meulenkamp, J.E., Wortel, M.J.R., van Wamel, W.A., Spakman, W., Hoogerduyn Strating, E., 1988. On the Hellenic subduction zone and the geodynamic evolution of Crete since the late Middle Miocene. *Tectonophysics* 146, 203-215
- Moernaut, J., De Batist, M., Heirman, K., Van Daele, M., Pino, M., Brümmer, R., Urrutia, R., 2009. Fluidization of buried mass-wasting deposits in lake sediments and its relevance for paleoseismology: Results from a reflection seismic study of lakes Villarrica and Calafquén (South-Central Chile). *Sedimentary Geology* 213, 121-135.
- Perissoratis, C., Papadopoulos, G., 1999. Sediment instability and slumping in the southern Aegean Sea and the case history of the 1956 tsunami. *Marine Geology* 161, 287-305.
- Stavrakakis, C., Chronis, G., Tselepidis, A., Heussner, S., Monaco, A., Abbasi, A., 2000. Downward fluxes of settling particles in the deep Cretan Sea (NE Mediterranean). *Progress in Oceanography* 46, 217-240.
- Strozyk, F., Huhn, K., Strasser, M., Krastel, S., Kock, I., Kopf, A., 2009. New evidence for massive gravitational mass-transport deposits in the southern Cretan Sea, eastern Mediterranean. *Marine Geology* 263, 97-107.
- Urgeles, R., Leynaud, D., Lastras, G., Canals, M., Mienert, J., 2006: Back-analysis and failure mechanisms of a large submarine slide on the ebro slope, NW Mediterranean. *Marine Geology* 226, 185-206.
- Wessel, P., Smith, W. H. F., 1998. New, improved version of the Generic Mapping Tools Released, *EOS Trans. AGU* 79, 579.

6. Slope failure repetition in active margin environments – constraints from submarine landslides in the Hellenic forearc, eastern Mediterranean

Submitted to *JGR - solid earth* as: Frank Strozyk¹, Michael Strasser¹, Annika Förster¹, Achim Kopf¹ & Katrin Huhn¹. Slope failure repetition in active margin environments – constraints from submarine landslides in the Hellenic forearc, eastern Mediterranean.

¹ MARUM, Centre for Marine Environmental Sciences - Cluster of Excellence: The Ocean in the Earth System, University of Bremen, P.O. Box 33 04 40, D-28334 Bremen, Germany

Abstract

It has been shown that submarine landslides can occur less frequently at subduction zone forearcs despite the general expectation of extensive slope failures from high neotectonic activity in active margin settings. The Hellenic subduction zone, Greece, represents such an example where modern evidence for slope failure is scarce. Taking the deeper parts of the forearc basin into account, however, a sequence of massive landslide deposits are found at recurrence intervals of approximately $250 \text{ ka} \pm 70 \text{ ka}$. Given neotectonic movements and local seismicity in the area, this rate of slope failure recurrence is low. In order to improve our understanding on the relationship between landslide recurrence rates and required trigger mechanisms, we here assess the mechanical behaviour of the slope sediment cover during instability scenarios. Seismic profiles and geotechnical measurements from cores of midsize landslides on the northern Cretan mid-slope are used to back-analyze slope destabilization in one-dimensional, infinite slope models for static conditions as well as for the case of seismic loading. High shear strength values of the slope sediment require peak ground accelerations (PGA) of $> 29 \text{ \%g}$, most likely in the order of 42 \%g for large-scale slope failure. Based on data from regional earthquake hazard catalogs, such PGAs critical for failure initiation are expected to occur at frequencies similar to those estimated for larger slope collapses from seismic reflection profiles and age models in cores. Overall, our findings lead us to propose that (i) only infrequent large-magnitude earthquakes generate stresses sufficient for major landsliding of the shear-resistant Cretan margin sediment, and that (ii) results are consistent with data and observations from other active margins (e.g. western North America). The study implies that permanent taper adjustment and dynamic compaction favour larger resistance to small and intermediate seismic loads and other potential triggers in such active margin settings.

6.1. Introduction

Gravitational mass movements are of significant interest as they are leading agents for submarine landscape development [e.g., *O'Grady*, 2001; *Hutton and Syvitski*, 2003] and the stratigraphic

evolution of sedimentary systems in different environmental settings [e.g., *Cochonat et al.*, 2002; *Shanmugam*, 2009]. As subaquatic mass movements can involve large volumes of wasted material, both the flow itself and the possible tsunami triggered by it are of high societal concern regarding their geohazardous impact on on- and offshore infrastructure [e.g., *Bardet et al.*, 2003]. Numerous mass movements of different types, scales, triggers (e.g. earthquakes), and consequences (e.g. tsunamis) were imaged in active margin settings [e.g., *Canals et al.*, 2004; *Camerlenghi et al.*, 2009]. Active margin systems are known to commonly produce $M_s > 8$ earthquakes, thus linked to a high probability for frequent, extensive mass wasting because of the earthquake-induced high ground acceleration and induced shear stresses and pore water pressures [e.g., *Locat and Lee*, 2002; *Canals et al.*, 2004; *Strasser et al.*, 2006, *Lee et al.*, 2007]. Recurrences rates of mass movements are therefore often used to reconstruct paleo-seismicity and its impact on slope stability in active margin systems [e.g., *Goldfinger et al.*, 2003; *McAdoo and Watts*, 2004] as well as other environmental settings [e.g., *Strasser et al.*, 2007].

In contrast, active margin case studies have shown that earthquake recurrence-times may differ significantly from those of mass movement in the same region [e.g., *McAdoo et al.*, 2000, 2004]. Although these settings often show a frequent recurrence of large PGAs, their slopes appear to remain stable for long periods of time. This resistance is explained by high mechanical sediment strength [e.g., *Sultan et al.*, 2004, 2008] or high consolidation state, as it may naturally result from exhumation of older sediment in accretionary complexes [e.g., *McAdoo et al.*, 2004; *McAdoo and Watts*, 2004]. To date, a number of questions remain open concerning the importance of pre-conditioning factors, trigger requirements, and the temporal relationship between trigger and mass movement [*Locat and Mienert*, 2003]. Pre-conditioning factors such as steep slopes, rapid sediment accumulation, the presence of gas or meteoric water, gas-hydrate destabilization or deep-seated fluid flow can influence slope stability as well as timing, scale and type of submarine landslides [*Locat and Lee*, 2002; *Sultan et al.*, 2004; *Masson et al.*, 2006; *Sultan et al.*, 2008].

The Cretan Sea, the forearc basin of the Hellenic subduction zone in the Eastern Mediterranean, is situated in a tectonically highly active setting (Fig. 6.1), where scattered mass movements of maximum cubic-kilometre-scale were recently observed [e.g., *Chronis et al.*, 2000; *Kopf et al.*, 2006; 2007; *Strozyk et al.*, 2009]. Conversely, the irregular steep relief [*Chronis et al.*, 2000], a complex system of faults [e.g., *Angelier et al.*, 1982; Fig. 6.2] and regional seismicity [e.g., *Meier et al.*, 2004; Fig. 6.2] provide a framework for high frequency extensive mass wasting. To improve our conceptual understanding of recurrence times of submarine landslides of different scales as well as their trigger and pre-conditioning requirements, we use multi-channel seismic reflection profiles, bathymetry charts and gravity cores from the northeastern mid-slope of Crete and the adjacent Kamilonisi Basin, representing the toe region of the slope.

Based on the more accurate data from landslides of cubic-kilometer-scale (‘midsize’) in a mid-slope position [see also *Kopf et al.*, 2006; 2007], we compare our results from one-dimensional, infinite slope models for static and pseudo-static conditions of midsize landslides with the seismicity of the Hellenic forearc. We consequently focus on constraints for a required seismic trigger in terms of mechanical sediment attributes and the recurrence of ground acceleration in place. We then discuss our findings in terms of recurrence and trigger requirements for some larger scaled mass-transport deposits in the Kamilonisi Basin, associated with major slope collapses, also in a more general context of causes for infrequent submarine mass movement events in such particularly active margin environments.

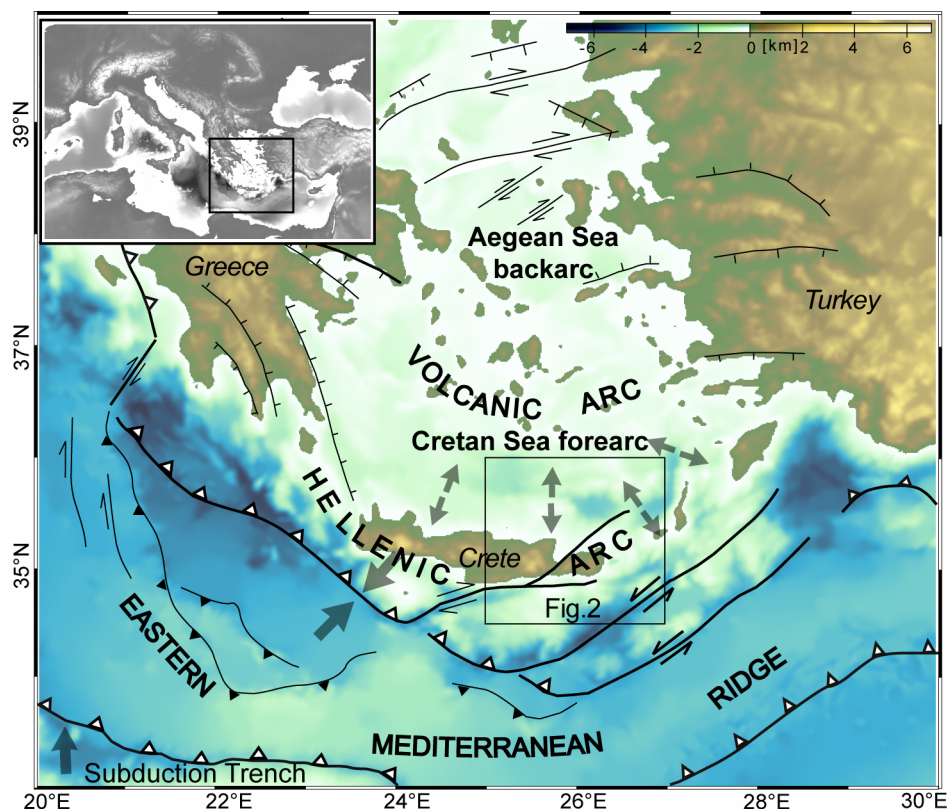


Fig. 6.1) Principal setup of the Hellenic subduction zone, eastern Mediterranean, and main tectono-sedimentary settings, comprising the eastern Mediterranean Ridge accretionary complex, the Hellenic arc, the Cretan Sea forearc basin, the volcanic arc, and the Aegean backarc basin. Arrows indicate direction of plate convergence in the south, backstop of the eastern Mediterranean Ridge south of Crete, and forearc basin extension further north (compiled after *Angelier et al.* [1982], *Masclé and Martin* [1990], and *Ganas and Parsons* [2009]).

6.2. Tectonical setting

The island of Crete is located in the centre of the active convergent margin of the African and Eurasian lithospheric plate collision zone in the eastern Mediterranean (Fig. 6.1). The convergence between these two plates results in subduction of the African plate to the north beneath the Aegean region and forms the Hellenic Arc [e.g., *Meulenkamp et al.*, 1988; Fig. 6.1]. Rooted on a deep-seated detachment fault, Crete was exhumed approximately 19 Ma ago and now presents a topographic high that is still being uplifted [*Bonneau*, 1984]. The island has acted as a backstop to the eastern

Mediterranean Ridge (Fig. 6.1), a large accretionary complex south of Crete [*Polonia et al.*, 2002; *Kopf et al.*, 2003]. North of Crete, the Cretan Sea represents a large, N-S- as well as E-W-extensional forearc basin, bordered to the north by the volcanic arc, which is followed further north by the Aegean Sea backarc (Fig. 6.1). With respect to the arcuate shape of the entire Hellenic arc and the orthogonal to oblique subduction (Fig. 6.1) trends of the Cretan Sea extension and subsidence rates strongly vary from the west to the east [*Angelier et al.*, 1982; *Masclé and Martin*, 1990; see arrows in Fig. 6.1]. This results in the formation of several sub-basins, e.g. the Heraklion Basin and the Kamilonisi Basin, which increase in depth from the west to the east [e.g., *Angelier et al.*, 1982; *Chamot-Rooke et al.*, 2005; Fig. 6.2]. Ongoing forearc extension during the incremental curvature of the subduction system (see Fig. 6.1) affects the Cretan Sea half-graben system [*Masclé and Martin*, 1990; Fig. 6.2B] as well as the regional pattern of multiple fault-sets [*Angelier et al.*, 1982; Fig. 6.2], whose dominant pattern is linked to forearc basin extension and follows the general structural trend of the Hellenic arc. Sets of minor faults in various orientations are genetically linked to neotectonic movement at variable subsidence rates [*Angelier et al.*, 1982]. *Masclé and Martin* [1990] reconstructed the last basin creation phase in the Cretan Sea to have occurred during the Late Miocene and Pliocene, and propose that extension may have decreased afterwards. However, major faults in the basin have been seismically active in recent times, for instance the prominent, southwest-northeast-trending Hera-Petra Fault [e.g., *Lykousis et al.*, 1995; Fig. 6.2].

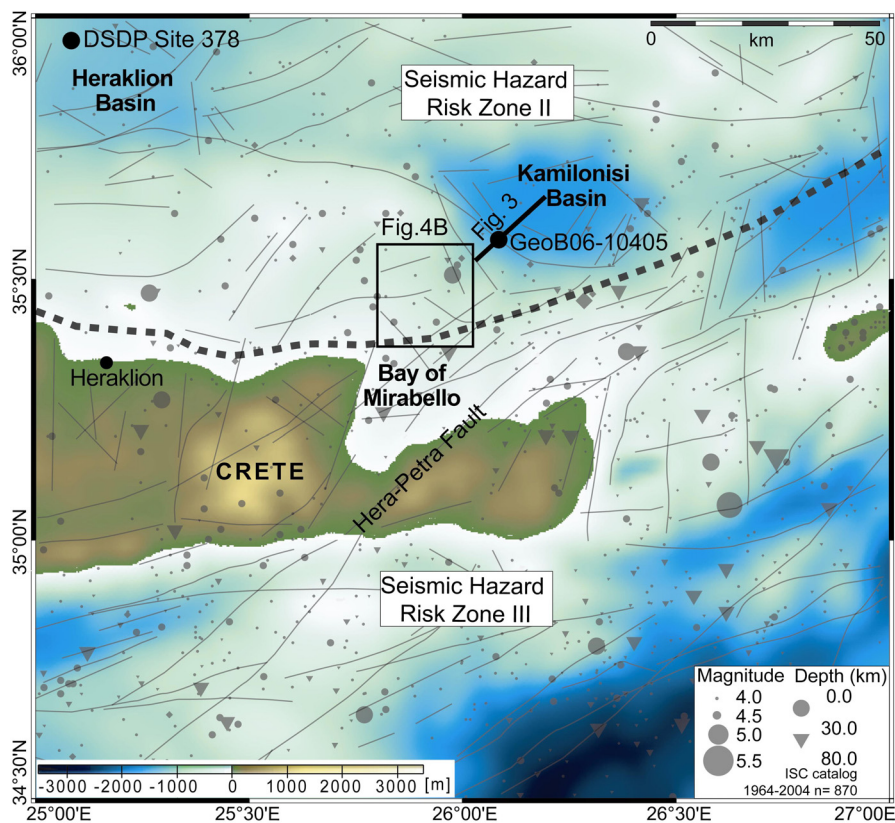


Fig. 6.2) Bathymetry map of the northeastern Cretan margin and the adjacent region. Faults (thin black lines) are compiled from *Masclé & Martin* (1990) and *Angelier et al.* (1982). Earthquakes (grey symbols) are obtained from the ISC catalog 1964 - 2004

(<http://www.eri.u-tokyo.ac.jp>). The dotted line indicates the boundary between the EPPO (1992) seismic hazard risk zones II to III.

Largest recent earthquakes at the Hellenic Arc plate boundary was recorded with $M_s = 7.3$ [Ambraseys, 2001], whereas historical and archeological studies suggest that earthquakes of $M_s > 8$ may have occurred [e.g., Guidoboni and Comastri, 1997; Stiros, 2001]. A maximum magnitude calculated from ISC catalog data (International Seismological Centre, UK) suggests $M_s = 7.8 \pm 0.4$ [Hamouda, 2006]. Subduction thrusting and large-scale neotectonic movements are responsible for this high seismicity being recorded by a network of seismic recording stations throughout the Hellenic forearc region (ISC catalogue [e.g., Engdhal and Villaseñor, 2002]). Earthquake source-mechanisms correspond to the Cretan island block uplift tectonics and E-W- as well as N-S-extension in the forearc [Meier et al., 2004]. These mechanisms, in addition to deep-seated N-S-directed plate-interface seismicity, lead to a clustered distribution of earthquake epicentres and variation in seismic hazard risk [e.g., Manakou and Tsapanos, 2000].

The EPPO (Earthquake Planning and Projection Organization of Greece; e.g., Moratto et al., 2007) defined four seismic hazard risk zones from the more than 4000 earthquakes of $M_s \geq 4$ recorded and localized since 1964 (Fig. 6.2). This risk zone classification provides most probable maximum values of peak ground acceleration (PGA) as a function of the mean repeat time (T_m). The southern Cretan Sea in Zone II is characterized by a ‘moderate risk’ (Fig. 6.2), whereas the northern margin of Crete traces the boundary between Zone II and Zone III, thus indicating higher risk (dashed line in Fig. 6.2). Maximum constraints provided by the EPPO catalog from the currently available earthquake records indicate that T_m for 22 %g PGA in Zone II and 29 %g for Zone III is expected not to exceed 500 years.

6.3. Data and methods

6.3.1 Acoustic data

Methodological details of acoustic data acquisition techniques are given in the P-336 cruise report [Kopf et al., 2006]. For further details of data processing and imaging strategy we also refer to Strozzyk et al. [2009].

6.3.2 Sediment physical properties data

Gravity cores of 1.5 to 4.6 m length and 10 cm diameter were recovered during P-336 with a standard gravity corer of approximately 1.5 tons weight (core locations in Figs. 6.2 and 6.3 (GeoB-10405) as well as 6.4A (GeoB-10452, -53, -54, -55, -58)). Cores were analyzed immediately on their sediment composition and physical properties. Bulk density was derived from a Multi-Sensor Core Logger (MSCL). The geotechnical measurements (additional methodological detail and core data acquisition techniques are given in the P-336 cruise report [Kopf et al., 2006] and in Kopf et al. [2007]) include the determination of the undrained shear strength (S_u) with a Wykeham-Farrance cone penetrometer on the intact split gravity core surfaces [Wood, 1985]. Additionally, the SHANSEP approach (‘Stress

History and Normalized Soil Engineering Properties' [Ladd *et al.*, 1977]) was used to obtain 'normalized shear strength' values from the S_u -vs.-overburden pressure-ratio (S_u / σ_v'), where σ_v' is the effective vertical stress, derived from σ_v (vertical stress [kPa]) – u (pore pressure [kPa]). For comparison, we also use *in situ* shear strength and pore-pressure data from P-336 Cone Penetration Tests (CPT) published in Stegmann *et al.* [2007] and Kopf *et al.* [2007].

Furthermore, the sediment's total carbonate content was determined using the HCl-digestion method after Heinrichs & Herrmann [1990]. The core sampling strategy for the carbonate content determination is based on the results from the MSCL runs, S_u -values, and core description. To identify marker horizons selected intervals from cores were analyzed for microfossil assemblages (i.e. Globigerinoides ruber and Globorotalia inflata due to their distinct stratigraphic distribution in uppermost Cretan slope strata; e.g., Geraga *et al.* [2005]).

6.3.3 One-dimensional, undrained, infinite slope stability analysis

Slope failure may be triggered either by an increase of loading forces, a decrease of resisting forces, or a combination of both (see summary by Lee *et al.* [2007]). In the limit equilibrium approach, a slope is classified as stable until one or more effects trigger the resisting-to-loading-force ratio to a critical Factor of Safety (FS). To evaluate the FS for distinct stable and destabilized slope portions at the Cretan Margin, we implement results from geotechnical experiments into one-dimensional, undrained, infinite slope stability analysis (SSA; after Morgenstern and Price [1965]). Almost linear trends of measured undrained shear strength are extrapolated to the depth of the inferred shear plane. Initial resisting forces of the sediment correspond to S_u values measured on the intact gravity cores. Loading forces under static conditions are calculated from the gravitational shear stress in the sediment column, derived from the effective normal stress (σ_n') acting on a shear plane. Additional shear forces from seismic loading (T_s) are implemented using a pseudo-static acceleration based on peak ground acceleration (PGA) generated by an earthquake. Our analysis assumes that the earthquake acceleration is applied over a significantly long period of time so that the induced stress can be considered constant [e.g., Hampton *et al.* [1996]]. This may lead to some minor uncertainties in slope stability analysis due to dynamic behaviour of the sediment, e.g. accumulation of plastic strain or shear-induced excess pore water pressures with increasing number of loading cycles [e.g., Sultan *et al.*, 2004; Biscontin, and Pestana, 2006]. However, as this simplified approach was successfully applied in other studies [e.g., Urgeles *et al.*, 2006; Strasser *et al.*, 2007], we adopt it here to gain insights on trigger quantity requirements and constraints. Our back-analysis assumes failure occurs if $FS \leq 1$ for both the static (i.e. ground acceleration $k = 0$) and pseudo-static case (i.e. $k > 0$), comparing undrained shear strength to the sum of static and pseudo-static shear forces:

$$FS = S_u' / (\gamma' h (\sin(\alpha) \cos(\alpha) + k (\gamma / \gamma') \cos^2(\alpha))) [6.1]$$

, whereof Su^* is the undrained shear strength in failure depth (kPa), γ' the submerged unit weight (kN/m³), γ the bulk saturated unit weight (kN/m³), k the ratio of the peak horizontal ground acceleration to gravitational acceleration (%g), α the slope inclination to horizontal (°), and h the depth of slide surface below seabed (m).

6.4. Results

6.4.1 Geophysics, lithology, and geotechnical testing

6.4.1.1. Geophysical data base

The starting point for this study was the discovery of thick, widespread, seismically incoherent sequences interbedded between layered deposits from background sedimentation of the Kamilonisi Basin. In general, seismic reflection profiles show different sedimentary units defined by seismic reflection pattern attributes such as amplitude, continuity and configuration. High-amplitude, layered units are smooth, undisturbed slope and basin background sediments (Figs. 6.3 and 6.4B) whereas less coherent, fuzzy packages are interpreted as mass-transport deposits ('MTDs'; Figs. 6.3 and 6.4B).

In the southwestern to central portion of the Kamilonisi Basin, a sequence of at least three, up to 50-m thick MTDs is found within the younger background sediment-succession (Fig. 6.3). These MTDs are interbedded by 15 - 25 m-thick (mean thickness: 20 m) background sediment packages, while the stratigraphically youngest MTD is draped by approximately 15 - 20 m of background sediment. Reconstructed geometries for these wedge-shaped MTDs to the southwestern basin flank as well as only little erosion for mass wasting along the northeastern basin flank imply that their source areas are likely located in the southwest. Since the massive MTD series in the Kamilonisi Basin was not fully mapped out owing to time constraints during the cruise, we used publicly available bathymetric charts (Fig. 6.2) and extrapolated symmetrically over the locally restricted Kamilonisi Basin. When using such an almost basin-wide extent (approximately 600km²) and keeping the sediment thickness of the MTDs at an average of 30 - 50 m, a first order volume of 30 - 50 ± 10 km³ can be estimated for each event.

Within the inferred provenance area of these MTDs in the southwest (Fig. 4A), we do not observe prominent scars along the margin that would account for the large MTD volumes in the basin. In contrast, mid-sized landslides and their source scars with 0.5 to 2 km³ volumes are present (see Fig. 6.4A and B) and were previously reported by *Kopf et al.* [2006; 2007]. On the other hand, they reflect similar lithologies to the missing MTDs as they are exposed close to source areas of Kamilonisi Basin MTDs and are thus assessed to have had a comparable evolution regarding sediment mechanics, failure site geometry and trigger requirements. Therefore, we here utilize slope instability back-analyses for the mid-slope study area (500 - 900 m water depth) to constrain a conceptual relationship of sediment mechanics and respective trigger requirements for the northeastern Cretan slope. Geometrical proportions of stable slope sediment cover as well as eroded material (i.e. failure depths)

of these mid-slope landslides (see Fig. 6.4B) were measured from a reconstruction of the pre-failure sediment thicknesses above a detected, pronounced slide plane reflector (dashed line Fig. 6.4B). We measure 3° and 5° gradients and 75 m and 60 m pre-failure thicknesses for the intact slope apron and failed slope portions, respectively (Fig. 6.4B).

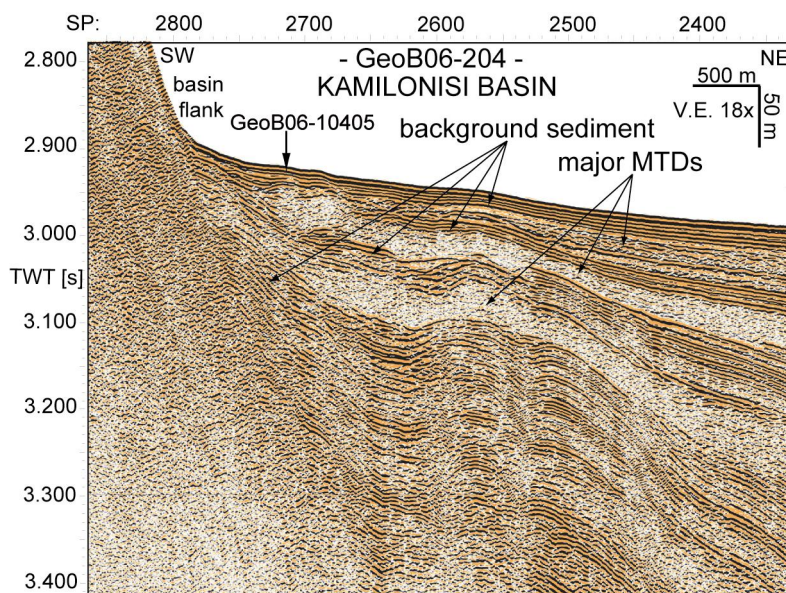


Fig. 6.3) Southwest-northeast seismic profile GeoB06-204 (for location see Fig. 6.2) slices the southwestern Kamilonisi Basin and the basin flank and shows three sequenced, large-scaled MTDs in the basin sediment succession, and shows the projected location of P-336 core GeoB-10405.

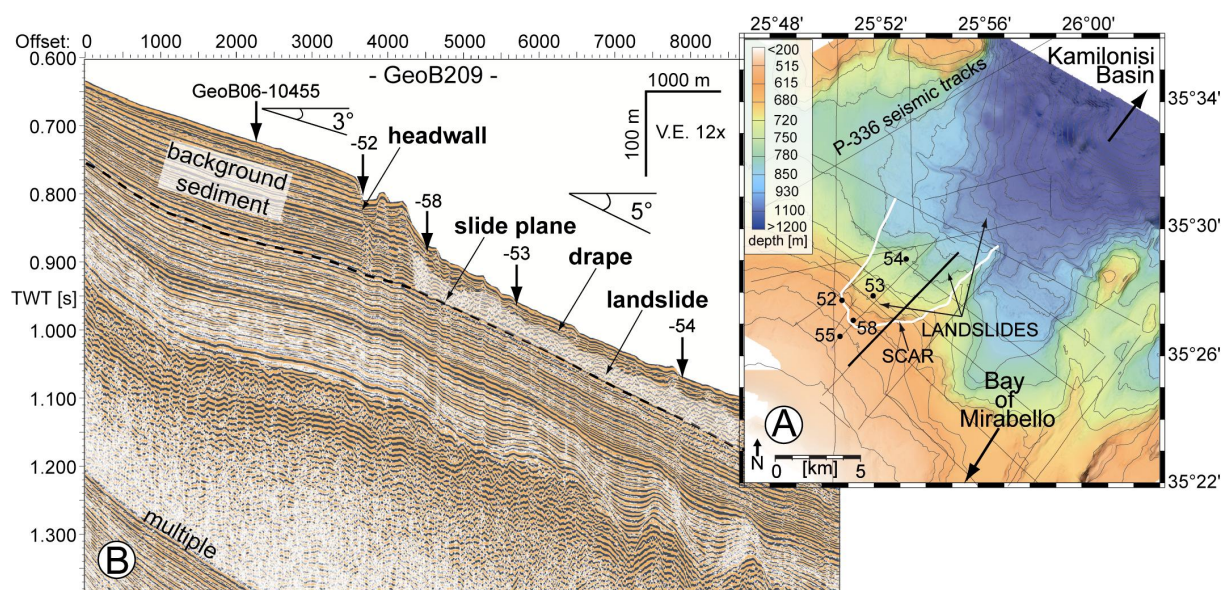


Fig. 6.4) A: Bathymetric chart of the mid-slope study site north of the Bay of Mirabello (for location see Fig. 6.2). Note the prominent scar and interpreted landslides in the central part. Black dots indicate P-336 coring locations, the thick black line the location of GeoB06-209 (Fig. 6.4B). **B:** Southwest-northeast seismic profile GeoB06-207 (see Fig. 6.4A for location) slices undisturbed background sediments (i.e. lefthandside up to the headwall and below landslide), one of the mid-slope landslides, and the associated headwall in transport direction of the slide. It further shows projected P-336 mid-slope core locations (see Fig. 6.4B for location).

6.4.1.2 Sediment composition, lithostratigraphy and accumulation rates

Sediment composition and lithostratigraphy

Five cores from the mid-slope study site (Fig. 6.4A; see projected location on Fig. 6.4B) and one core from the Kamilonisi Basin were analysed (Fig. 6.2; see projected location on Fig. 6.3). Cores were recovered from the undisturbed slope (GeoB-10455), from headwall-drape (-52, -58), from the drape on top of mid-slope MTDs (-53 and -54), and from the drape overlying the stratigraphic youngest MTD in the Kamilonisi basin (-05). For all cores, the main lithofacies is a mud-rich, sandy to silty sediment [Kopf *et al.*, 2006; Fig. 6.5]. It is interrupted by a sapropel at 0.45 - 0.8 mbsf (meters below seafloor), except core GeoB-10458, where the sapropel occurs at 1.5 - 1.85 mbsf (Fig. 6.5). Based on colour, grain size distribution, sediment composition and organic material content, the dominantly hemipelagic lithologies assign to the existing stratigraphic framework of the northern Cretan margin mid-slope sediments [Aksu *et al.*, 1995; Giresse *et al.*, 2003]. Analysis of planktonic microfossil species (see section 6.3.2) below and above the sapropel reveals an assemblage that is characteristic for the sapropel 'S1' [Geraga *et al.*, 2005]. This reinforces the stratigraphic correlation of the sapropel to S1, which is dated to 9.6 - 6.4 ka B.P. [Giresse *et al.*, 2003; Strozyk *et al.*, 2009]. Furthermore a pronounced ash layer recovered in all cores, except the headwall core GeoB-10452, is correlated to the Z2-Santorini event (3370 B.P. [Pichler and Friederich, 1976]), providing a second robust time-marker for the age model of drape overlying MTDs.

The single gravity core in the Kamilonisi Basin shows a similar sediment succession including S1 and Z2 (Fig. 6.7). In contrast to the mid-slope cores, however, it is characterised by a larger number of redepositional events. While the five cores recovered at the mid-slope scar and surroundings have in average ca. 0.5 events m^{-1} (~ 12.8 ka) and accordingly one event per ~ 25 ka, core GeoB10405 exhibits 4 events m^{-1} core length and accordingly one event per ~ 3 ka. This implies that mass-wasting efficiency is enhanced in the exposed lower slope and basin flank areas where gradients are steeper (Figs. 6.2, 6.3 and 6.4A).

In order to get a more solid data base, we considered a DSDP (*Deep Sea Drilling Project*) core recovered from Site 378 in the Heraklion Basin [Hsü *et al.*, 1978; for location see Fig. 6.2]. The 343.5-m-deep boring recovered Quaternary, late Pleistocene, early Pleistocene, and late Miocene lithologies. The upper 64 meters comprise Quaternary nanofossil marl with cm- to dm-scaled interlayers of sapropelic marl and marl conglomerates, with the latter being interpreted as sedimentary slump conglomerates. Core data for 64 - 131.5 mbsf show Quaternary nanofossil marl and ooze with interlayered sapropelic marls [Hsü *et al.*, 1978]. As this Quaternary sediment composition correlates with our findings in the shallow P-336 cores, we assume that this sedimentary succession can be applied also to the deeper strata at the northeastern Cretan mid-slope as well as the southwestern Kamilonisi Basin.

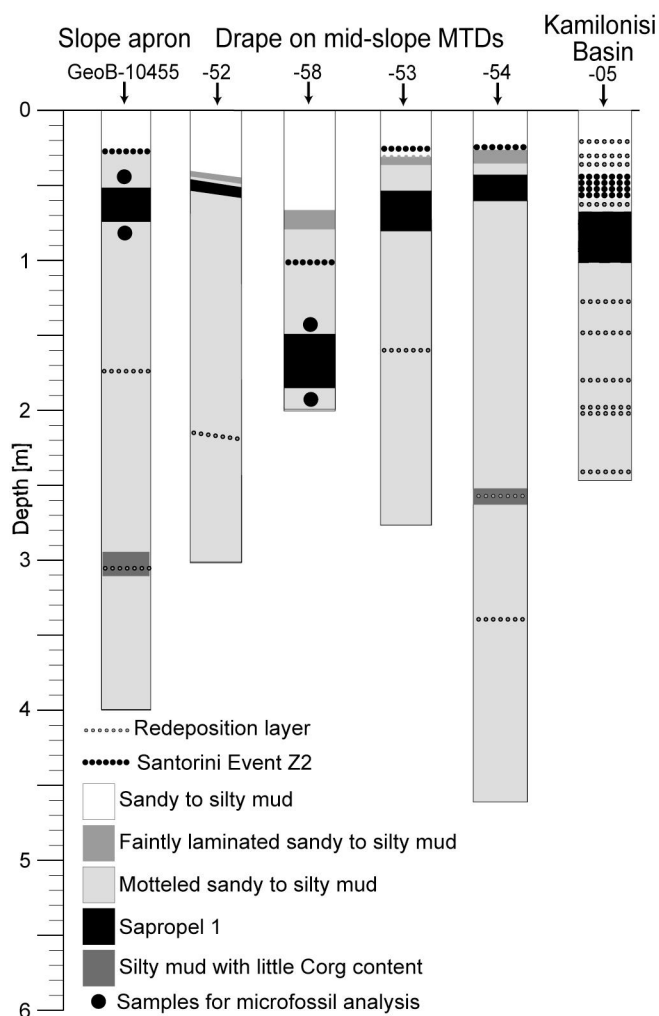


Fig. 6.5) Gravity core logs from the mid-slope (see Figs. 6.4A and B for locations) and one core from the Kamilonisi Basin (see Figs. 6.2 and 6.3 for location) showing the lithostratigraphic framework. Black points above and below Sapropel 1 in cores GeoB-10455 and -58 mark positions of microfossil content sampling.

Sediment accumulation rate estimates

We use the age constraints identified from cores GeoB-10453, -54, and -55 to determine an accumulation rate of 7.8 cm ka^{-1} (range of uncertainty: $7.0 - 8.5 \text{ cm ka}^{-1}$) for the topmost meters of intact drape recovered above the mid-slope MTDs and scars. Cores GeoB-10452 and -58 from the headwall region were neglected as higher sediment accumulation rates at the foot of the headwall are biased by talus. This interpretation is reinforced by high concentration of mussel shell fragments in core -58 and evidence for erosion in core -52 from the upper part of the headwall (i.e. missing Z2-marker layer and condensed S1; Fig. 6.7). For the Kamilonisi Basin, the age model of the uppermost part of core GeoB10405 consistently reveals sediment accumulation rates of 7.8 cm ka^{-1} .

For the deeper portion of the drape, there are no age-tie points available in core data and no information of ‘pre-S1’ sedimentation rates along the southern Cretan sea mid-slope region and the Kamilonisi Basin is documented in the literature. We therefore can only assume constant

sedimentation rates, as also proposed for the upper 120 m of the sediment column in the Heraklion Basin from DSDP Leg 42 [Hsü *et al.*, 1978] Site 378 core interpretation. Accordingly, we use their accumulation rate estimates of 7.7 cm ka^{-1} for the Heraklion Basin (see Fig. 6.2), apply it to the Kamilonisi Basin and extrapolate to depth.

Timing and evolution of MTDs

As reasoned above, both cores and seismic profiles independently indicate a continuous background sediment accumulation since the emplacement of mid-slope MTDs. Also the sediment accumulation rates from gravity core data in the mid-slope and those inferred for the Kamilonisi Basin as well as those from the Heraklion Basin (DSDP Site 378 [Hsü *et al.*, 1978]) are almost the same. These data show mean MTD drape thicknesses of 15 m in the mid-slope, which corresponds to a landslide age of about 192 ka B.P. (range of uncertainty when using min. and max. accumulation rates and $\pm 2.5 \text{ m}$ drape thickness according to the resolution of the seismic system: 250 - 147 ka B.P.). The 15 - 20 m thick drape from same accumulation rates on top of the youngest MTD in the Kamilonisi Basin results in an age-range of 192 - 250 ka B.P. (range of uncertainty: 320 - 147 ka B.P.). Given the equal spacing of the transparent MTD layers in the seismic data (Fig. 6.3), the recurrence time of the described three youngest events identified may be back-calculated (see below).

Although error bars on our estimates are quite large, the estimated age for the mid-slope MTDs is comparable to that of the youngest MTD in the Kamilonisi Basin according to similar accumulation rates and drape thicknesses. Therefore, we interpret that the Kamilonisi Basin records the history of large-scale slope failures along the adjacent Cretan slope, with the mid-slope landslides possibly being a remnant of the youngest event. When using thicknesses of only the background sediments between the individual Kamilonisi Basin MTDs, recurrence time can be back-calculated to be approximately 250 ka (range of uncertainty: 200 - 320 ka).

6.4.1.3. Geotechnical tests

Physical and mechanical sediment properties were measured regularly along all six cores of both study sites. MSCL bulk densities range in between $1.7 - 2.0 \text{ g cm}^{-3}$. Undrained shear strength (S_u) is found to be more variable, with 10 - 15 kPa close to the seafloor and a steady increase with depth to 160 kPa at the maximum terminal depth of 4.5 mbsf (see Fig. 6.6A). According to the SANSHEP approach (see section 6.3.2), Ladd *et al.* [1977] propose a normal consolidation state for S_u -vs.-overburden pressure-ratios of 0.1 - 0.4. Calculated values of these values for our core data show 0.48 - 1.4 and indicate an apparent sediment over-consolidation [e.g., Sultan *et al.*, 2004]. Elevated calcite concentrations of 40 - 55 Vol.-% were monitored for the upper two core meters, which may indicate cementation processes that increase shear strength. However, all cores show approximately linear increases of S_u vs. depth. As a sediment column is generally assumed to fail along the weakest units, the minimum S_u -vs.-depth-

gradient 5 kPa m^{-1} is primarily favoured for a Su -vs.-depths correlation, whereas the ‘best-fit’-gradient for measured data is 8.75 kPa m^{-1} (Fig. 6.6A).

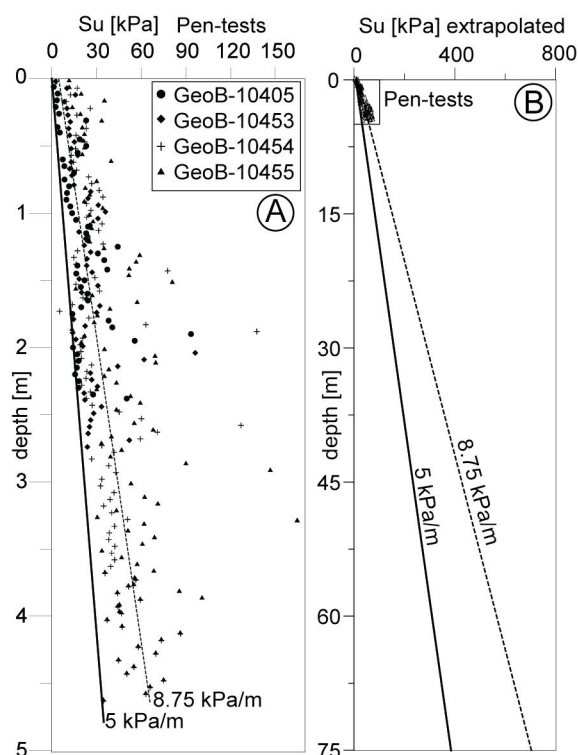


Fig. 6.6) A: Results from Wykeham-Farrance cone penetrometer measurements on undrained shear strengths along sediment cores GeoB-10405, -53, -54, and -55 in up to ~ 4.6 mbsf. The minimum S_u -vs.-depth-gradient ($\sim 5 \text{ kPa m}^{-1}$) is marked as solid line, the ‘best-fit’ gradient ($\sim 8.75 \text{ kPa m}^{-1}$) as dotted line; **B:** 5 and 8.75 kPa m^{-1} S_u -vs.-depth-gradients obtained from the PEN (falling cone penetrometer) tests extrapolated to the slide plane depths of 60 and 75 mbsf observed for mid-slope landslides.

When compared to the review paper on shear strengths-vs.-depths trends in ODP (Ocean Drilling Program) cores, the minimum gradient obtained here is much higher than the average 1 kPa m^{-1} for deeper drillholes, but also suggests a linear increase of S_u with depth [Bartetzko and Kopf, 2007]. Again, the superficial ‘apparent’ over-consolidation processes and calcareous cements may serve as an explanation. Accordingly, our S_u -vs.-depth-model does not account for maximum peaks of measured S_u -values (i.e. all values above the S_u -vs.-depth-gradient of $> 8.75 \text{ kPa m}^{-1}$), as they may derive from an occasionally occurrence of carbonaceous clasts and nodules in cores. However, the relatively high trends given by core data are also supported by S_u derived from *in situ* CPT deployments using a shallow-water probe in a landslide complex in the upper slope [Kopf et al., 2007].

6.4.2. Slope stability analyses and trigger evaluation

Our interpretation of a dominant MTD-pattern with large slope failure events having a 250-ka recurrence interval challenges the expectation of an extensive, high-frequency mass-movement pattern

being characteristic of such active margin environments. In fact, only very few midsize landslides and scars were found [e.g., *Strozyk et al.*, 2009; *Kopf et al.*, 2006; 2007], and the dominant mechanism seems to be massive mobilisation involving volumes of 30 - 50 km³ and frequent, very small-scale (i.e. cm- to dm-sizes) sediment failures along exposed steep slopes (e.g. GeoB-10405, Fig. 6.5). To get quantitative control on trigger requirements for this pattern dominated by large-scale mass movements, we utilise our measures from seismic profiles and geotechnical tests for the mid-slope landslides to back-analyze sediment stability and instability under static (see section 6.4.2.1) and pseudo-static conditions (see section 6.4.2.2).

The scenarios of mid-slope failure and stability are sketched in Figure 7A. The measured slope gradients and pre-failure sediment thicknesses are used as a bracket for the assessment (see section 6.4.1.1; Fig. 6.7A). For both types of failure conditions, a uniform sediment column of the hemipelagic, mud-rich sediment (see section 6.4.1.2) was assumed with a mean bulk density of 1.90 g cm⁻³ and *Su*-vs.-depth-gradients of either 5.0 or 8.75 kPa m⁻¹ with a linear increase to failure depths (see Fig. 6.6B; see also Table 6.1).

Table 6.1) Geometrical slope proportions and according geotechnical sediment characterizations as incorporated to slope stability analysis (α = gradient; σ_n' = effective normal stress; T = static shear stress). Note that all values address the critical depths ('c.d.'^[1]) of 60 m and 75 m.

	α	c.d. ^[1]	σ_n' [kPa]	T (kPa)	<i>Su</i> -vs.-depth gradient 5 kPa m ⁻¹	<i>Su</i> -vs.-depth gradient 8.75 kPa m ⁻¹
Failed sites	5°	60 m	512.25	44.81	280 kPa in c.d.	510 kPa in c.d.
Stable sites	3°	75 m	643.45	33.72	347.5 kPa in c.d.	633.75 kPa in c.d.

1 depth in between the interpreted slide plane reflector and the reconstructed pre-failure seafloor

6.4.2.1. Slope stability under static conditions

From slope stability analysis (SSA) under static conditions, which incorporates the *Su* against shear stress from the sediment load ($k = 0$, see equation 6.1; Table 6.1), the resulting Factor of Safety (*FS*) exceeds 4 in all cases (Fig. 6.7B) and suggests a stable slope (given $FS \leq 1$ represents slope failure). Additional tests using higher slope gradients up to 10° and sediment thickness-variations of ± 25 m result in $FS \geq 2.5$, and thus also favour a stable slope. This indicates that the slope gradients and sediment load thicknesses cannot explain the observed slope failures under static conditions. However, slope geometry is seen as an important pre-conditioning factor although its relative importance to the ultimate trigger is low. To give also a test on the average gradient for deeper ODP drillholes [*Bartetzko and Kopf*, 2007], the lower trends of 1 kPa m⁻¹ extrapolated to failure depths at the study site result in $FS < 0.9$, thus not sufficient to assume stability of the intact slope apron along the northern margin of Crete under static conditions.

6.4.2.2. Slope stability under pseudo-static conditions

Since we anticipate earthquake-induced peak ground acceleration (PGA) as a possible trigger, we use a pseudo-static approach to back-analyze slope instability under earthquake loading conditions. Scenarios for the stable and failed slope portions (Fig. 6.7A), each with the 5 kPa m⁻¹ and the 8.75 kPa m⁻¹ *Su*-vs.-depth gradient, were applied. Results show that PGAs in the order of 24 %g and 42 %g for the 5 kPa m⁻¹ and the 8.75 kPa m⁻¹ gradient, respectively, are required for failure (Fig. 6.7B). Similarly, we achieve an upper limitation of PGA to 26 %g and 44 %g, respectively (Fig. 6.7B), depending on the geometrical variation in slope architecture (Figs. 6.4B and 6.7A).

In contrast, PGAs about 24 %g, using the 5 kPa m⁻¹ *Su*-vs.-depth-gradient, would cause a mean slope failure recurrence time in the order of 500 years because PGAs in the order of 22 - 29 %g can be expected with $T_m \sim 500$ years at the study site [EPPO, 1992]. Thus, they cannot be viewed as a likely trigger for at least the mid-slope landslides. Owing to the much lower recurrence of slope failure (i.e. no midsize or large-scale mid-slope failure for the last 147 ka (see section 6.4.1.2)) as well as a restriction of slope failure to the steeper-inclined slope portions (i.e. 5°), we assess that (i) PGAs of > 29 %g are required for landslide triggering and (ii) the 5 kPa m⁻¹ gradient underestimates the sediment strength at depth.

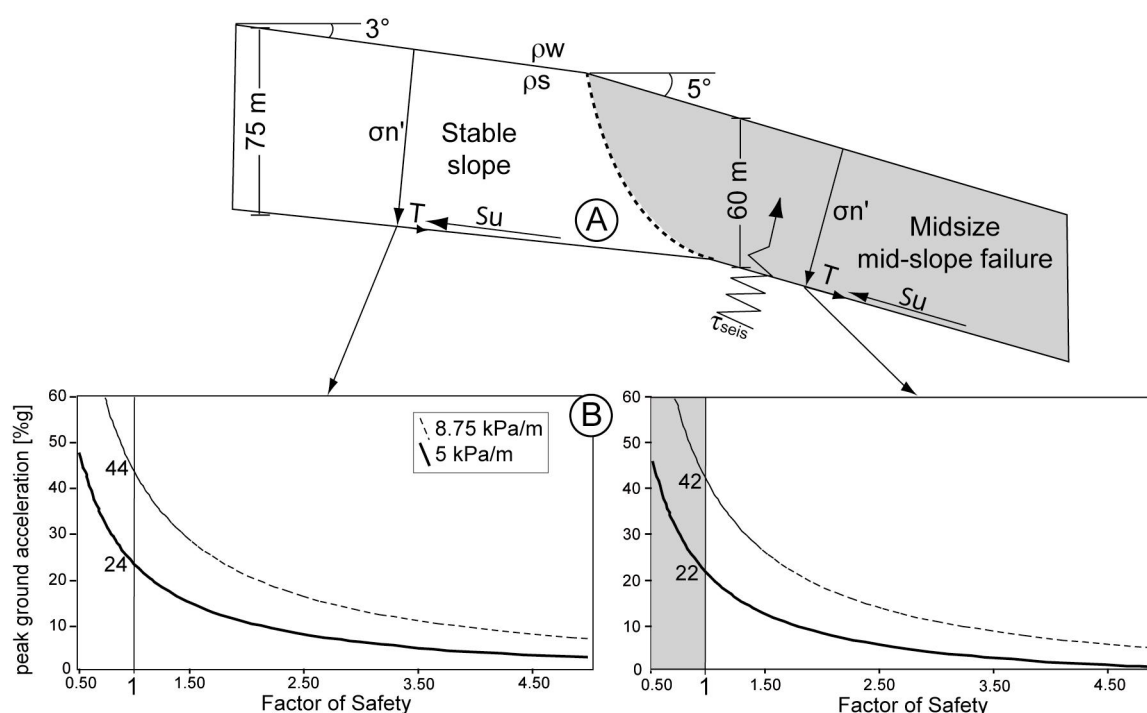


Fig. 6.7 A: Sketch of geometrical setups and acting forces (see Table 6.1) as pre-defined for failed and already stable sediment portions in the mid-slope, and used for slope stability analyses; B: results of slope stability analyses for the intact slope apron (left chart) and midsize landslides (right chart), incorporating the *Su*-vs.-depth-gradients 5.0 and 8.75 kPa m⁻¹ as a function of the Factor of Safety (*FS*) against peak ground acceleration. The intersection points of the two resulting trends with *FS* = 1 = failure (grey shaded area) indicates PGAs that are required for sediment destabilization depending on the shear strength.

6.5. Conclusions and general implications

We have shown that the investigated slope in the southernmost Hellenic forearc basin was only infrequently destabilized. Large-scale mass movements of 30 - 50 km³ that disintegrate during larger

runout and accumulate in the deeper Kamlinosi Basin as debrites are dominant process of slope sediment erosion. Midsized landslides (i.e. 0.5 - 2 km³) as well as small-scale (i.e. cm to dm thicknesses) movements are only a marginal contingent.

From results of slope stability analyses we deduce that the high shear-resistance of the slope sediment cover is responsible for high, long-term slope stability. Although background seismicity prevails in the Hellenic forearc, maximum PGAs (22 – 29 %g) that occur with higher recurrences ($T_m \sim 500$ years) are not sufficient for critical acceleration leading to slope collapse. Consequently, an earthquake trigger that produces $\gg 29$ %g in place is the prerequisites to cause failure. SSA has further shown that sediment shear strengths represented by a ≤ 5 kPa m⁻¹ *Su*-vs.-depth-gradient are insufficient for the long-term slope stability. We suggest that a >5 kPa m⁻¹ gradient and thus most likely the ‘best-fit’ *Su*-vs.-depth-gradient of 8.75 kPa m⁻¹ is required to maintain the observed stability of the Cretan slope.

To get control on the trigger requirements for major landslide events, for instance the large-scale MTDs in the Kamilonisi Basin, we confront their repetition-time to recurrence rates of required PGAs in the surveyed area. Extrapolation of the Eppo catalogue data suggests that PGAs in the order of 42 %g can be expected with $T_m \sim 250$ ka, thus almost in-line with the recurrence rate of major MTD emplacement in the Kamilonisi Basin. This PGA is favoured by our results from SSA indicating 42 %g as potential trigger for a sediment column bearing the ‘best-fit’ *Su*-vs.-depth-trend ~ 8.75 kPa m⁻¹. We consequently deduce that PGAs of this magnitude exert seismic triggers for major sediment collapses mobilising volumes of 30 - 50 km³ per event. We recommend a nearby (< 30 km) $M_s > 7$ earthquake providing such PGAs as shown by similar M_s -PGA-relations that triggered landslides in the Aegean backarc (e.g., Perissoratis and Papadopoulos, 1999).

As the relative importance of slope gradients and sediment thicknesses to the seismic trigger is low, no mass movement of intermediate scale and recurrence is observed, at least if locally very confined small-size events along exposed steep slope parts are disregarded here. This also implies that the local tremor of PGAs below critical threshold values for larger failure may only cause this small, near-surface sediment remobilization (Fig. 6.7B) as it was already shown by *Chronis et al.* [2000]. Consequently, no frequent mass wasting interferes with undisturbed sediment accumulation about longer periods of time on the northeastern Cretan slope.

When comparing the low recurrence rate of the large earthquake-triggered landslides to other areas, similar conclusions were drawn from studies investigating submarine landslides along active subduction zones [e.g., *McAdoo et al.*, 2004; *McAdoo and Watts*, 2004; *Camerlenghi*, 2009]. Here, forearc slopes at accretionary and erosive margins also show large infrequent landslides because of tectonically exhumed sediments that tend to be over-consolidated, therefore bearing a high shear resistance and requiring large earthquakes as triggers [*McAdoo et al.*, 2004]. The low repetition time of trigger conditions for landslides in the southern Hellenic forearc basin thus shows analogies to the

„cohesive slope failure“-model *sensu McAdoo et al.* [2000], while the sediment history of the younger basin flank cover differs from the accretionary margin examples. We deduce that an additional consolidation and strengthening of the Cretan slope sediment occurs. As the regional seismic tremor provides frequent PGAs below critical threshold values for landslide initiation (see above), this may rather strengthen the sediment column through development of excess pore-water pressures and subsequent drainage, resulting in a densification during the intervening periods [e.g., *Locat and Lee, 2002; Lee et al., 2007*].

We conclude that the causal relationship of high neotectonic activity in active margin settings to infrequent large-scale slope collapses is controlled by a high strength of the sediment. The strength of the sediment cover then requires large PGAs which in turn are reached at low recurrence times. We suggest that only infrequent, nearby earthquakes of large magnitudes produce such PGAs, whereas low to intermediate magnitudes do not affect the slope catastrophically. Overall, our findings imply that only infrequent large magnitude earthquakes generate stresses sufficient for major sediment collapse along active margin slopes bearing cohesive, consolidated sediments. Permanent taper adjustment and dynamic compaction from seismic tremor favour the sediment's large resistance to the seismic tremor or other potential triggers.

Acknowledgements

We thank the scientific party and the ship crew of P-336 for faithful and detailed recording of data. We thank all involved scientists at the Hellenic Centre for Marine Research, Greece, for their scientific input and discussions as well as support of the P-336 cruise. We thank the MARUM for scientific support and all involved scientists and members for fruitful discussions and outcomes, especially Dr. Barbara Donner for microfossil species identification. We thank reviewers Brian G. McAdoo and Homa J. Lee for their constructive comments and suggestions that highly improved this paper. This publication is funded through the DFG-Research Centre/ Excellence Cluster „The Ocean in the Earth System“

References

- Aksu, A.E., D. Yasar, and P.J. Mudie (1995), Paleoclimatic and paleoceanographic conditions leading to development of sapropel layer S1 in the Aegean Sea, *Palaeogeogr. Palaeoclimat. Palaeoecol.*, 116, 71-101.
- Ambraseys, N. N. (2001), Far-field effects of eastern Mediterranean earthquakes in lower Egypt, *J. Seismol.*, 5, 263 – 268, doi:10.1023/A:1011476718680.
- Angelier, J., N. Lyberis, X. Le Pichon, E. Barrier, and P. Huchon (1982), The Tectonic development of the Hellenic arc and the sea of Crete: a synthesis, *Tectonophysics*, 86, 159-196.
- Bardet, J.-P., C.E. Synolakis, H.L. Davies, F. Imamura, and E.A. Okal (2003), Landslide Tsunamis: Recent Findings and Research Directions, *Pure appl. geophys.*, 160, 1793–1809.
- Bartetzko, A., and A.J. Kopf (2007), The relationship of undrained shear strength and porosity with depth in shallow (<50 m) marine sediments, *Sed. Geol.*, 196, 235-249.

- Biscontin, G., and J.M. Pestana (2006), Factors affecting seismic response of submarine slopes, *Natural Hazards and Earth System Sciences*, 6, 97-107.
- Bonneau, M. (1984), Correlation of the Hellenide nappes in the south-east Aegean and their tectonic reconstruction, *Geol. Soc., London, Special Publications* 17, 517-527.
- Camerlenghi, A., Urgeles, R., and L. Fantoni (2009), A database on submarine landslides of the Mediterranean Sea. In: *Submarine Mass Movements and Their Consequences IV*, edited by D.C. Mosher, C. Shipp, L. Moscardelli, J. Chaytor, C. Baxter, H. Lee, and R. Urgeles, Fourth International Symposium on Submarine mass movements and their consequences, November 8-11, 2009, Austin, Texas, *Advances in Natural and Technological Hazards Research*, in press.
- Canals, M., G. Lastras, R. Urgeles, J.L. Casamor, J. Miernert, A. Cattaneo, M. De Batist, H. Haflidason, Y. Imbo, J.S. Laberg, J. Locat, D. Long, O. Longva, D. G. Masson, N. Sultan, F. Trincardi, and P. Bryn (2004), Slope failure dynamics and impacts from seafloor and shallow sub-seafloor geophysical data: case studies from the COSTA project, *Mar. Geol.*, 213, 9-72.
- Caress, D.W., and D.N. Chayes (2006), MB-System: Mapping the Seafloor, <http://www.mbari.org/data/mbsystem>, <http://www.ldeo.columbia.edu/res/pi/MB-System>.
- Chamot-Rooke, N., A. Rabaute, and C. Kreemer (2005), Western Mediterranean Ridge mud belt correlates with active shear strain at the prismbackstop geological contact, *Geology*, 33, 861 – 864, doi:10.1130/G21469.1.
- Chronis, G., V. Lykousis, C. Anagnostus, A. Karageorgis, S. Stavrakakis, and S. Poulus (2000), Sedimentological processes in the southern margin of the Crete Sea (NE Mediterranean), *Progr. Oceanogr.*, 46, 143-160.
- Cochonat, P., J.P. Cadet, S.J. Lallemand, S. Mazzotti, H. Nouze, C. Fouchet, and J.P. Foucher (2002), Slope instabilities and gravity processes in fluid migration and tectonically active environment in the eastern Nankai accretionary wedge (KAIKO-Tokai'96 cruise), *Mar. Geol.*, 187, 193-202.
- Engdahl, E.R., and A. Villaseñor (2002), Global Seismicity: 1900–1999. In: Lee, W.H.K., Kanamori, H., Jennings, P.C., Kisslinger, C. (Eds.), *International Handbook of Earthquake and Engineering Seismology, Part A*, Ch. 41 Academic Press, San Diego, 665–690.
- EPPO (Earthquake Planning and Projection Organization of Greece) (1992), Appendix to the new building code of Greece.
- Ganas, A., and T. Parsons (2009), Three-dimensional model of Hellenic Arc deformation and origin of the Cretan uplift, *J. Geophys. Res.*, 114, B06404, doi:10.1029/2008JB005599
- Geraga, M., S. Tsaila-Monopolis, C. Ioakim, G. Papatheodorou, and G. Ferentinos (2005), Short-term climate changes in the southern Aegean Sea over the last 48,000 years, *Palaeogeol., Palaeoclim., Palaeoeco.*, 220, 311-332.
- Giresse, P., R. Buscail, and B. Charriere (2003), Late Holocene multisource material input into the Aegean Sea: depositional and post-depositional processes, *Oceanol. Acta*, 26, 657-672.
- Goldfinger, C., C.H. Nelson, and J.E. Johnson (2003), Holocene earthquake records from the Cascadia subduction zone and northern San Andreas Fault on precise dating of offshore turbidites, *Annu. Rev. Earth Planet. Sci.*, 31, 555-577.
- Guidoboni, E., and A. Comastri (1997), The large earthquake of 8 August 1303 in Crete: Seismic scenario and tsunami in the Mediterranean area, *J. Seismol.*, 1, 55– 72, doi:10.1023/A:1009737632542.
- Hamouda, A. Z. (2006), Seismic hazard of the eastern Mediterranean, *Acta Geophys.*, 54, 165–176, doi:10.2478/s11600-006-0013-z.
- Hampton, M., H. Lee, and J. Locat (1996), Submarine Landslides, *Rev. Geophys.*, 34, 33-59.
- Heinrichs, H., and A.G. Hermann (1990), *Praktikum der Analytischen Geochemie*, 357-361. Springer, Heidelberg.
- Hutton, E.W.H., J.P.M. Syvitski (2003), Advances in the numerical modeling of sediment failure during the development of a continental margin, *Mar. Geol.*, 203, 367-380.
- Hsü, K.J., L. Montadert, D. Bernouilli, G. Bizon, M. Cita, A. Erickson, F. Fabricius, R.E. Garrison, R.B. Kido, F. Mellieres, C. Muller, and R.C Wright (1978), Site 378: Cretan Basin. *Init. Rep. Deep-Sea Drill. Proj.*, 42, 321-257, doi:10.2973/dsdp.proc.42-1.108.1978.
- Kopf A., J. Mascle, and D. Klaeschen (2003), The Mediterranean Ridge: A mass balance across the fastest growing accretionary complex on Earth, *J. Geophys. Res.*, 108, 23-72, doi:10.1029/2001JB000473.2003

- Kopf, A., T. Alves, B. Heesamnn, M. Irving, N.E. Kaul, I. Kock, S. Krastel, M. Reichelt, R. Schäfer, S. Stegmann, M. Strasser, and M., Thölen (2006), Report and preliminary results of Poseidon cruise P336: CRESTS – Cretan Sea Tectonics and Sedimentation, Heraklion 28.04.-17.05.2006, Berichte, Fachbereich Geowissenschaften, Universität Bremen, 253.
- Kopf, A., S. Stegmann, S. Krastel, A. Förster, M. Strasser, and M. Irving (2007), Marine deep-water Free-fall CPT Measurements for landslide characterisation off Crete, Greece (Eastern Mediterranean Sea) --- PART 2: Initial data from the western Cretan Sea. In: Lykousis, V., Sakellariou, D., Locat, J. (eds.), Submarine Mass movements and their consequences, Advances in Natural and Technological Hazards Series, Springer, 199-208.
- Ladd, C. C., R. Foott, K. Ishihara, F. Schlosser, and H. G Poulos (1977), Stress-deformation and strength characteristics, State of the art report, Proceedings, 9th International Conference on Soil Mechanics and Foundation Engineering, 2, 421-494.
- Lee, H.J., J. Locat, P. Desgagnes, J.D. Parsons, B.G. McAdoo, D.L. Orange, P. Puig, F.L. Wong, P. Dartnell, and E. Boulanger (2007), Submarine mass movements on continental margins. In: Nittrouer, C.A., Austin, J.A., Field, M.E., Kravitz, J.H., Syvitki, J.P.M., Wiberg, P.L. (eds.), Continental Margin Sedimentation, Blackwell Publishing, UK, 213-274.
- Locat, J., and H.J., Lee (2002), Submarine landslides: advances and challenges. *Can. Geotech. J.*, 39, 193-212.
- Locat, J., and J. Mienert (2003), Submarine mass movements and their consequences, *Advances in natural and technological hazards research* 19, Kluwer, Dordrecht, 540 pp.
- Lykousis, V., C. Anagnostou, G. Anastasakis, P. Pavlakis, G. Roussakis, and M. Alexandri (1995), Quaternary sedimentary history and neotectonic evolution of the eastern part of Central Aegean Sea, *Mar. Geol.*, 186, 281-298.
- Manakou, M.V., and T.M. Tsapanos (2000), Seismicity and seismic hazard parameters evaluation in the island of Crete and the surrounding area inferred from mixed data files, *Tectonophysics*, 321, 157-178.
- Masclé, J., and L. Martin (1990), Shallow structure and recent evolution of the Aegean Sea: a synthesis based on continuous reflection profiles, *Mar. Geol.*, 94, 271-299.
- McAdoo, B.G., L.F. Pratson, and D.L. Orange (2000), Submarine landslide geomorphology, US continental slope, *Mar. Geol.*, 169, 103-136.
- McAdoo B. G., M. K. Capone, and J. Minder (2004), Seafloor geomorphology of convergent margins: Implications for Cascadia seismic hazard, *Tectonics*, 23, TC6008, doi:10.1029/2003TC001570.
- McAdoo, B.G., and P. Watts (2004), Tsunami hazard from submarine landslides on the Oregon continental slope, *Mar. Geol.*, 203, 235-245.
- Meier, T., M. Rische, B. Endrun, A. Vafidis, H.-P. Harjes (2004), Seismicity of the Hellenic subduction zone in the area of western and central Crete observed by temporary local seismic networks, *Tectonophysics*, 383, 149-169.
- Meulenkamp, J.E., M.J.R. Wortel, W.A. van Wamel, W. Spakman, and E. Hoogerduyn Strating (1988), On the Hellenic subduction zone and the geodynamic evolution of Crete since the late Middle Miocene, *Tectonophysics*, 146, 203-215.
- Moratto, L., B. Orlecka-Sikora, G. Costa, P. Suhadolc, C. Papaioannou, and C.B. Papazachos (200), A deterministic seismic hazard analysis for shallow earthquakes in Greece, *Tectonophysics*, 442, 66-82.
- Morgenstern, N.R., and V.E. Price (1965), Analysis of stability of general slip surfaces, *Geotechnique*, 15, 79-93.
- O'Grady, D.B. (2001), Sedimentary Geomorphology of siliciclastic continental slopes, Ph.D. thesis Faculty of the Graduate School of the University of Colorado.
- Perissoratis, C., and G. Papadopoulos (1999), Sediment instability and slumping in the southern Aegean Sea and the case history of the 1956 tsunami, *Mar. Geol.*, 161, 287-305.
- Pichler, H., and W. Friedrich (1976), Radiocarbon-dates of Santorini Volcanics, *Nature*, 262, 373-374.
- Polonia, A., A. Camerlenghi, F. Davey, and F. Storti (2002), Accretion, structural style and syn-contractional sedimentation in the Eastern Mediterranean Sea, *Mar. Geol.*, 186, 127-144.
- Shanmugam, G. (2009), Slides, Slumps, Debris Flows, and Turbidity Currents, *Encyclopedia of Ocean Sciences*, 4509-4529, Elsevier.

- Stegmann S., M. Strasser, F. Anselmetti, and A. Kopf (2007), Geotechnical in situ characterization of subaquatic slopes: The role of pore pressure transients versus frictional strength in landslide initiation, *Geophys. Res. Lett.*, 34, L07607, doi:10.1029/2006GL029122.
- Stiros, S. C. (2001), The AD 365 Crete earthquake and possible seismic clustering during the fourth to sixth centuries AD in the eastern Mediterranean: A review of historical and archaeological data, *J. Struct. Geol.*, 23, 545– 562, doi:10.1016/S0191-8141(00)00118-8.
- Strasser, M., S. Stegmann, F. Bussmann, F.S. Anselmetti, B. Rick, and A. Kopf (2007), Quantifying subaqueous slope stability during seismic shaking: Lake Lucerne, Central Switzerland, as model for ocean margins, *Mar. Geol.*, 240, 77-97.
- Strasser, M., F.S. Anselmetti, D. Fäh, D. Giardini, and M., Schnellmann (2006), Magnitudes and source areas of large prehistoric northern Alpine earthquakes revealed by slope failures in lakes, *Geology*, 34, 1005-1008.
- Strozyk, F., K. Huhn, M. Strasser, S. Krastel, I. Kock, and A. Kopf (2009), New evidence for massive gravitational mass-transport deposits in the southern Cretan Sea, eastern Mediterranean, *Mar. Geol.*, 263, 97–107.
- Sultan, N., P. Cochonat, M. Canals, A. Cattaneo, B. Dennielou, H. Halifladson, J.S. Laberg, D. Long, J. Mienert, and F. Trincardi (2004), Triggering mechanisms of slope instability processes and sediment failure on continental margins: a geotechnical approach, *Mar. Geol.*, 213, 291-321.
- Sultan N., A. Cattaneo, R. Urgeles, H. Lee, J. Locat, F. Trincardi, S. Berne, M. Canals, and S. Lafuerza (2008), A geomechanical approach for the genesis of sediment undulations on the Adriatic shelf, *Geochem. Geophys. Geosyst.*, 9, Q04R03, doi:10.1029/2007GC001822.
- Wessel, P., and W. H. F. Smith (1998), New, improved version of Generic Mapping Tools released, *EOS Trans, Amer. Geophys. U.*, 79, pp. 579.
- Wood, D.M. (1985), Some fall-cone tests, *Géotechnique*, 35, 64-68.

7. Oversteepening as a key factor for gravitational mass movement comparing cohesive and non-cohesive slopes utilizing Discrete-Element models

In preparation for *Structural Geology* as: Oversteepening as a key factor for gravitational mass movement comparing cohesive and non-cohesive slopes utilizing Discrete-Element models, Frank Strozyk, Katrin Huhn, and Ingo Kock

Abstract:

In this study we investigate how progressive oversteepening and fault kinematics impact on mass failure development along extensional basin flanks covered with different types of sediments. We use numerical models of large assemblages of granular particles that are bonded to simulate the mechanical behaviour of cohesive (muddy) and non-cohesive (sandy) sediments. After high basin subsidence produces steep slopes of both materials, we observe that cohesive sediments deform restrictedly along major faults producing a cascaded topography and a stable slope in the long-term. Mass failures of cohesive sediments occur as large, compact slides of short runout. In contrast, the non-cohesive slope cover deforms diffusely with faults being much smaller in scale and sediment failure is higher in frequency immediately balancing critically inclined slope portions. The resulting slope topography is smoother and laterally more elongated compared to the compact and steep cohesive slope geometry. We deduce that these differences in mass movements and slope architecture are governed by (i) characteristic fault patterns, which are a function of the materials' cohesion and are instrumental in failure initiation, at least on cohesive slopes, (ii) repeated oversteepening of the lower slope during ongoing basin subsidence, which is an important prerequisite for failure initiation on non-cohesive slopes. We conclude that the distribution, dimension, failure and transport mechanics, as well as the recurrence rate of gravitational mass movements record the deformational character of sediment types over longer periods of time.

7.1. Introduction

The evolution of sedimentary basins is often associated with slope failure events occurring along steepening basin flanks resulting from ongoing basin subsidence under subaquatic conditions (e.g. Leeder, 1999). Hence, tectonic oversteepening and associated fault activity is an important control on the recurrence rate, type, and dimension of gravitational mass movements (Booth et al., 1993; Hampton et al., 1996). Sediment collapses can strongly affect slope evolution through time (Hutton and Syvitski, 2003), suggesting basin architecture is a unique record of the tectonic deformation history in different tectono-sedimentary environments (e.g. O'Grady et al., 2001; Hutton and Syvitski, 2003; Lyså et al., 2008).

Although other trigger mechanisms, e.g. transients in excess pore pressure (e.g. Stegmann et al., 2007) or seismic loading (e.g. Biscontin and Pestana, 2006) are generally proposed to cause sediment slope failure besides tectonic movement and deformation (e.g. Bryn et al., 2000; Solheim et al., 2005; Crescenzo and Santo, 2005), at least a small inclination is required for sediment destabilisation. Therefore, failure will occur if driving stresses caused by critical inclination exceed the mechanical strength of the slope sediments (e.g., Morgenstern and Price, 1965). Accordingly, the critical inclination depends on mechanical sediment attributes (e.g. Morgenstern, 1967; Lambe & Whitman, 1969; Lee and Edwards, 1986; Takahashi, 1991; Mohrig et al., 1999).

Owing to the broad spectrum of slope sediment types found in various basin environments, a wide range of recurrence rates, dimensions, and types of gravitational mass movements can be observed in nature (e.g. McAdoo et al., 2000; Cochonat et al., 2007; Shanmugam, 2009). Thereof, typical cohesive slopes can produce deep-seated landslides and slumps that occur in lower repetition due to the long-term stability of the sediments (e.g. Hampton et al., 1978; McAdoo et al., 2000). This contrasts with pure sandy, non-cohesive slopes which tend to have a higher frequency of sediment failure that is often characterized by mass-flows and (subaquatic) turbidites (e.g. Morgenstern, 1967; Shanmugam, 2000).

It is generally accepted that tectonic oversteepening often plays a major role in failure pre-condition and that sediment physics exert the most important constraint on slope failure development (e.g. Lee et al., 2007). Therefore, principal approaches on such sediment destabilization scenarios regarding shear stresses from critical inclination through time are considered. But the relationship between these aspects and slope deformation in time and space, and dynamic processes like fault activity and slope topography evolution over longer periods of time and in larger scale, are not captured for most cases and hence are still not fully understood.

The major aim of this study is to highlight the key role that sediment physical behaviour plays in slope deformation and failure development along subsidence induced steepening flanks. Therefore, we compare two representative end-members of sediment type – muddy, cohesive and sandy, non-cohesive slope sediments, and analyze their characteristic deformation behaviour in terms of slope taper, fault evolution and kinematics, as well as the resulting dimension, geometry and recurrence rates of slope failure events. Results will be discussed in terms of linking large-scale tectonic deformation over longer times to mass-movement patterns in different sediment types.

To achieve this, we utilize a numerical particle based simulation technique – the Discrete Element Method. This approach was successfully used to simulate large-scaled geodynamic processes of the brittle upper crust under extensional conditions over long-time periods, e.g. the evolution of graben systems (Seyferth & Henk, 2003) as well as the activation and reactivation of basement faults on different scales (Saltzer and Pollard, 1992). Additionally, this technique is well-suited to investigate

localized deformation with sediment-physical material behaviour and geotechnical aspects, e.g. soil deformation, and failure mechanisms (e.g., Mustoe et al., 1987; Chang, 1992; Sitharam and Nimbkar, 1997; Huhn et al., 2006) and gravitational near-surface slope failure events (e.g., Morgan, 2006).

7.2. Methods

7.2.1 The Discrete Element Method

7.2.1 The Discrete Element Method

The Discrete Element Method (DEM) is a numerical simulation technique based on the description of granular materials (Cundall and Strack, 1978). In this study, we use the commercial Particle Flow Code *PFC2D* in 2-dimensions (Itasca, Inc. ® (Itasca 2004)) which utilizes the theory by Cundall and Strack (1978).

The numerical ‘sediments’ are simulated by an assemblages of discrete, frictionally coupled, spherical particles which interact as common contact points in accordance to simple physical contact laws (for more details see e.g. Cundall and Strack, 1978; Fig. 7.1A). Micro-properties of each particle, notably each particles’ coefficient of friction (μ_p) and the shear and normal stiffnesses (k_s , k_n), control the macro-properties of the particle package, e.g. the overall coefficient of friction of the ‘sediment’ layer (μ_s), and therewith the overall sediment-physical behaviour of the material (e.g. Morgan & Boettcher, 1999; Mitchell and Soga, 2005; Kock and Huhn, 2007a, b).

We utilize a Mohr-Coulomb rheology

$$(1) \quad \tau_{crit} = \mu_C \sigma_N + C$$

where σ_N is normal stress, μ_C is the coefficient of friction, and C is cohesion, as natural slope sediments obey this material behaviour (e.g. Marone et al., 1998; Lohrmann et al., 2003; Mitchell and Soga, 2005). The critical shear stress (σ_{crit}) is the shear stress at the failure plane and is equivalent to F_{Smax} :

$$(2) \quad F_{Smax} = \mu_C \sigma_N + C$$

Hence, the maximum shear force at each contact point (F_{Smax}) is limited to the critical shear force. So, progressive breaking of contacts along discrete planes reproduces fracture and fault propagation in nature (e.g. Strayer and Suppe, 2002).

Cohesion is simulated by bonding of each particle contact. Therefore, each bond is modelled with a linear spring in the contact normal direction (normal bond stiffness sn ; Fig. 7.1A) and a linear spring in the contact tangential direction (shear bond stiffness ss ; Fig. 7.1A). In addition, the E_C parameter,

which is comparable to the Young's modulus in nature, has to be defined for each bond. Consequently, the interplay of E_C , normal and shear stiffnesses generate the overall cohesion of the 'sediment' package (Fig. 7.1A). In case of breakage of a contact bond, the particle's coefficient of friction (μ_p) applies (ITASCA, 2004).

As a detailed numerical and mathematical description of this approach would exceed the scope of this paper, we refer to Cundall and Strack (1978, 1979, 1983), Cundall (1989), and Itasca (2004). Short reviews are also given e.g. in Antonellini and Pollard (1995), Morgan and Boettcher (1999) and Kock and Huhn (2007a, b).

7.2.2 Model configuration - 2D numerical biaxial tests

Besides numerical direct shear tests (e.g. Morgan, 1999; Kock and Huhn, 2007a, b), we utilize 2-D biaxial shear tests to calibrate micro-properties of the particle assemblage to reproduce the deformation behaviour as well as overall macro-scopic cohesion, strength, and coefficient of friction in accordance to natural slope materials (e.g., Schellart, 2000). Calibration is done by adjusting microproperties of the particles to reproduce the desired deformation behaviour.

These 2-D biaxial cells exhibit a size of 100 m x 200 m (Fig. 7.1B). Initially, particles are generated randomly inside this cell. A gaussian particle size with a unimodal diameter arrangement between 1-3 m is used to simulate natural deformational behaviour (e.g. Saltzer and Pollad, 1992). After force equilibrium of the particle assemblage is reached, contact-bonds are assigned to each particle-particle contact to generate a cohesive material (Fig. 7.1A). Next, the material is loaded in biaxial compression (Fig. 7.1B) starting with a uniform confining pressure of $\sigma_1 = \sigma_3 = 1$ kPa. Afterwards, each test comprises eight loading steps with confined lateral pressures $\sigma_3 =$ of 10, 50, 100, 200, 300, 500 and 700 kPa.

A numerical algorithm prescribes the motion of boundary walls so that lateral stress remains constant. The biaxial tests are performed with a wall velocity of 0.01 cm s^{-1} until the material 'cracks' (Fig. 7.1C). This velocity is calibrated to maintain quasi-static conditions.

Based on the ratio of confining pressure to crack-initializing peak stress (Fig. 7.1C), micro-parameters of the particle-particle contact bonds are defined to obtain material strengths of the DEM particle assemblages almost similar to natural sediments.

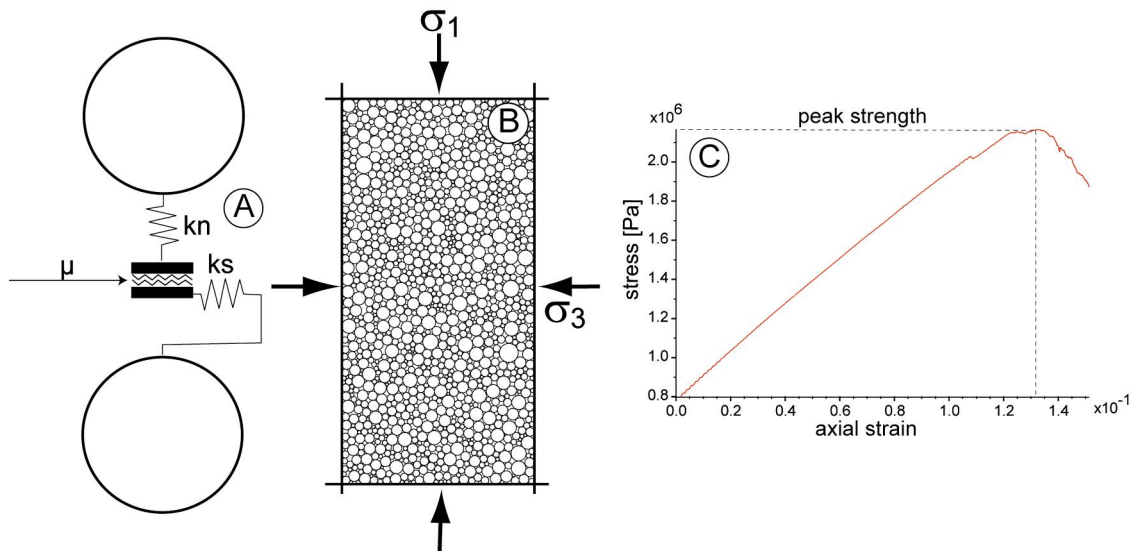


Fig. 7.1 A: bonds at particle-particle contacts are used to simulate cohesion and friction of the natural sediments with kN (normal stiffness), kS (shear stiffness) and μ (friction coefficient); B: confined biaxial-cell test models are performed to translate the micro- in macro-properties of the granular, bonded material; C: example of stress-strain-development during a confined biaxial-test with a confined pressure of 700 kPa, specifying the required peak strength to initiate cracking of the particle assemblage

As we aim on a comparison of two material end-members in accordance to the broad spectra of slope sediment types, we designed two numerical materials: (A) mud-rich ‘sediment’ and (B) sandy ‘sediment’. The physical and mechanical behaviour of material-A simulates typical cohesive, muddy slope sediments with lower friction, whereas material B resembles nearly cohesion-less, coarser, terrigenous clastics with higher friction and only a small apparent cohesion (e.g. Schellart, 2000). These material properties were chosen in accordance to field observations, e.g. along the northwest U.S. Eel margin (Walsh and Nittrouer, 1999) and the northern margin of Crete (Chronis et al., 2000; Kopf et al., 2006; 2007; Strozzyk et al., 2009). There, mud-rich, cohesive sediments (e.g. $C_{\text{Crete}} = 25 - 40$ kPa; pers. comments A. Förster) are observed. Conversely, slopes dominated by non-cohesive, sandy sediments were mapped e.g. along the shelf-brake in the northern Gulf of Mexico (e.g., Coleman, 1988; Balsam and Beeson, 2003) or along large parts of the slope offshore Norway (e.g. Jackson et al., 2008).

The micro-properties and respective input parameters as well as macro-properties of both materials A and B are listed in Table 7.1.

Table 7.1) Biaxial test input parameters utilized from natural sediment examples, the output parameters after biaxial-cell tests, and the resulting input parameters for the slope models of material A and B.

Input Parameters	Sediment A ('mud'):	Sediment B ('sand'):
Density ρ [kg/m ³]	1800.0	2200.0
Coefficient of particle friction μ_p	0.4	0.52
Normal stiffness k_N [N/m ²]	1.0×10^{10}	1.0×10^{10}
Shear stiffness k_S [N/m ²]	1.0×10^{10}	1.0×10^{10}
Normal bond stiffness s_N [N/m ²]	1.25×10^5	1×10^3
Shear bond stiffness s_S [N/m ²]	1.25×10^5	1×10^3
E-modulus E_C [Pa]	1×10^7	5×10^8
Wall stiffness $k_N; k_S$ [N/m ²]	1×10^9	1×10^9
Coefficient of wall friction μ_{wall}	0.4	0.4
Output Parameters from biaxial-cell tests	Material A ('mud'):	Material B ('sand'):
Density ρ [kg/m ³]	1800.0	2200.0
Coefficient of material friction μ_s	0.37	0.63
Cohesion C [Pa]	$49,8 \times 10^3$	4.64×10^3

7.2.3 Model configuration - extensional basin flank

Initially, we generate a rectangular fixed box model of 2000 m length and 200 m height to simulate a flat basin (Fig. 7.2A). All walls are defined as impermeable and stiff boundaries (Tab. 7.1). Approximately 22.000 particles with a gaussian particle size distribution and diameters between 1-3 m are generated in the entire box. These particles settle down under gravity generating the undeformed basin 'sediment' layer on top of the fixed box bottom (see Fig. 7.2A). Afterwards, the topmost particles are deleted to obtain always an identical 150-m-thick smooth and flat initial surface topography (Fig. 7.2A). Finally, particle frictions (μ_s) and stiffnesses are assigned and particles are bonded to generate a cohesive material (see section 7.2.2).

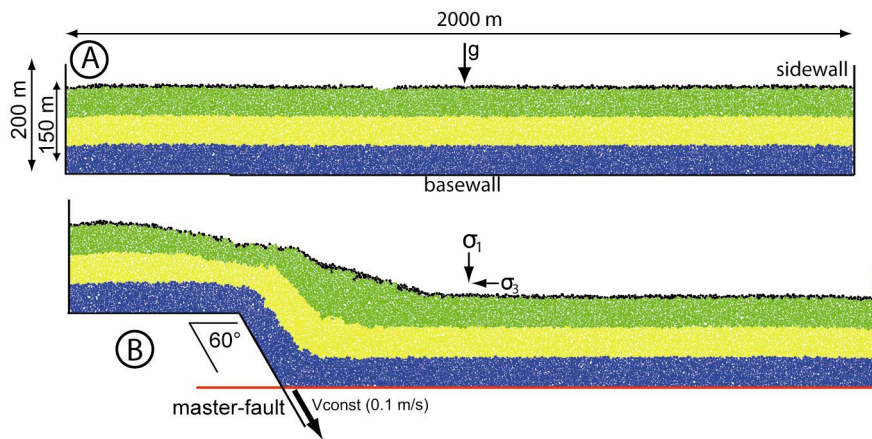


Fig. 7.2) Basic model setup used to generate an inclined slope from basin subsidence along a 60° master-fault. Models are performed with 0.1 m/s base-wall off-set until the total vertical displacement equals the 150-m-thickness of the particle assemblage. Moving walls are marked in red, static walls are black.

We are running two model suites with the two different ‘sediment’ types which obey a Mohr-Coulomb rheology (see chapter 2.1): (A) a cohesive, muddy and (B) a nearly cohesion-less, sandy slope cover (Tab. 7.1). This enables us to simultaneously investigate large-scaled slope deformation processes, e.g. fault evolution and kinematics, but also to observe near-surface gravitational mass movements of smaller scales can be observed simultaneously. Therefore, the ‘sediment’ thickness and particle resolution are chosen to enable modelling of slide events of meter to several tens meters thickness as they are widely observed in nature (e.g., Canals et al, 2004; Lee et al., 2007; Shanmugam, 2009). Besides, this configuration requires a reasonable amount of computer time ranging from a couple of days up to a week calculation time. Increasing spatial resolution would require an increase in particle number and therewith an exponential increase in calculation time.

Basin subsidence is performed by a continuous downward motion of two thirds of the box bottom wall along a 60° inclined master-fault (Fig. 7.2B). Movement along this master-fault simulates slope evolution and subsequent basin flank oversteepening under extension. The angle of master-fault inclination to the direction of main stress σ_1 was chosen as it represents the average orientation of brittle material failure in nature (e.g., Ramsey & Huber, 1987; Twiss & Moores, 1992; Bos, 2000). The basin wall subsides with a constant velocity of 0.1 ms^{-1} until the total vertical off-set equals the initial material thickness of 150 m (Fig. 7.2B). We are aware that this is an artificially high velocity, but we are simulating a dry Mohr-Coulomb material for which material behaviour is time-independent. In addition, we ensure a force and momentum equilibrium at each calculation time and that a disturbance of a given particle only propagates to its immediate neighbors as it is requested by the Discrete Element Method (Cundall and Strack, 1978; Haff and Anderson, 1993). Furthermore, low strain rates were ensured, and inertial forces within the quasi-static system remained small.

Limitation and capabilities of this model

As our modelling targets on the effect of tectonic deformation and mass failure only depending on fundamental sediment mechanics, several simplifications were made, e.g. the major fault dip was held constant and fluid flow and fluid pressures were not considered in the experiments. Furthermore, our models disregard lithological variances and stratified sediment bedding as well as sediment accumulation through time. Nevertheless, we can simulate the natural sediment deformation behaviour gaining a general understanding of fault mechanics and kinematics (e.g. Buitter and Schreurs, 2006). Specifically, we can map out the distribution, position, geometry, and temporal activation and reactivation of faults and slope tapers as well as mass failure and movement distribution as a function of slope sediment type. A quantification and comparison of these measurable parameters between different experiments (A and B) permits us to evaluate the influence of, for example, sediment cohesion and friction, on the evolution of an increasingly inclined slope and the distribution, dimension, mechanical behaviour, and recurrence rate of gravitational mass movements.

7.2.4. Interpretation techniques

During each model run, particle configuration as well as shear and normal forces at each particle contact are saved in regular calculation steps (i.e. 10.000 ‘cycles’). This correlates with approximately 0.7-1 m subsidence according to variations in material strength of the different ‘sediments’ (A, B). These data are used for post-processing to translate the numerical model output, e.g. particle displacements and contact forces, into geological interpretable data, e.g. fault zones, fault kinematics and mass transfer pattern, utilizing the Generic Mapping Tool (GMT (Wessel and Smith, 1999); Fig. 7.3).

Initially, horizontal layers were coloured because offsets of these marker layers enable a simple visualisation of fault zones (Fig. 7.2). However, detailed information about particle positions at each time step enable a highly resolved visualisation of fault evolution, re-activation and kinematics in space and time (e.g. Morgan and Boettcher, 1999; Huhn et al., 2006). Therefore, we designed colour plots to show the absolute displacement of each particle in between two time steps (Fig. 7.3B). This displacement field monitors areas of high and low particle movement to identify the position of localized deformation or the location of shear zones (e.g. Guo and Morgan, 2004; Kock and Huhn, 2007a, b). We define that a near-surface particle assemblage that is displaced more relative to the surrounding particles in a down-slope direction indicates the position of gravitational mass transport (orange to red colours in e.g. Fig. 7.3B). Note that we cannot interpret distinct slide planes in most cases as the large displacement of particles that are assigned to a mass movement affect surrounding particles (yellowish coloured particles in the vicinity of the mass movement in Fig. 7.3B). Additional information about the sense of shear along discrete failure zones can be extracted from gradient plots comparing relative displacements between neighbouring particles (e.g. Morgan, 1999; Fig. 7.3C).

We interpreted the relative gradient displacement fields over subsidence intervals of 20 m to investigate deformation processes, slope topography, and fault evolution over long-time periods. In addition, absolute displacement fields were analyzed to identify gravitational mass movements both in short- as well as long-term periods (Figs. 7.4 and 7.5).

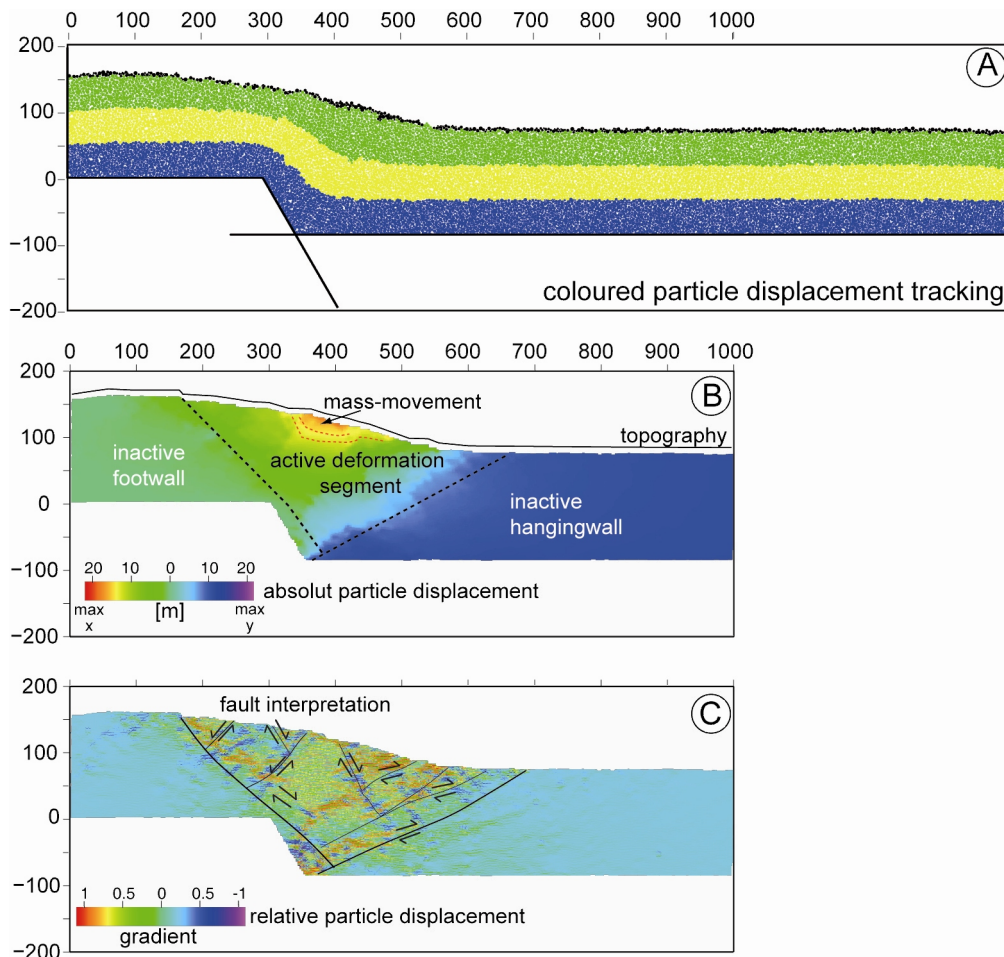


Fig. 7.3) Example of data visualization styles used for different types of interpretation: the numerical model of the entire particle assemblage for single particle tracing (A), the thereupon generated particle displacement plot (absolute displacement) to identify and quantify mass-movement (B), and gradient plots of the relative particle displacement (C) utilised for fault interpretation.

7.3. Model results

In both experiments - the cohesive (A) and the non-cohesive model (B), slope ‘sediments’ deformed as a consequence of basin subsidence. In both settings, numerous fault zones evolve, basin slope flanks overstep and gravitational mass movements occur. Besides, we can identify inactive, with respect to fault evolution and degree of internal deformation, foot- and hangingwall segments as well as an active deformation segment (Fig. 7.3B). The latter is always characterized by its position that correlates with the inclined slope as well as faulting and gravitational near-surface mass movement (Fig. 7.3B).

However, (i) lateral distribution of these segments, (ii) number and distribution of faults, (iii) slope inclination and topography, as well as (iv) geometry, dimension, and position of mass movement differ with the slope 'sediment' type (see following chapter).

7.3.1 Cohesive slope 'sediments' - model A

- *Evolution of deformation segments and fault system*

The active deformation segment evolves immediately after initiation of basin subsidence with a width of approximately 400 m at the surface (Fig. 7.4A-1). With increasing subsidence, an increase in lateral segment width to almost 600 m could be observed (>100-m subsidence; Fig. 7.4A-5 to A-7). This extension of the active segment is mostly caused by a basin-ward migration of the outer segment boundary - the so-called deformation front, whereas its boundary to the footwall is nearly fixed relative to the master fault (Fig. 7.4A).

This active segment is always bordered to the footwall by a large normal fault which simultaneously governs the continuous detachment from the inactive footwall segment (e.g. Fig. 7.4A-7). The position and dip angle ($\alpha = 40^\circ$) of this major normal fault does not correlate with the master fault throughout the entire experiment. In addition, the position of the currently active major fault migrates away from the master fault with increasing subsidence (Fig. 7.4A-7).

The segment border in the direction of the hangingwall block is defined by large-scale, antithetic thrust faults which extend towards the foot region of the developing slope (Fig. 7.4A-5). Simultaneously, these thrusts detach the active deformation segment from the inactive hanging wall (Figs. 7.4A-2 to A-7).

The normal faults, which are active for longer time-periods, and often produce steep fault scarps at the surface, primarily control the internal deformation of this active segment. Sub-ordinated, mostly antithetic, minor faults occur only for short periods of time (Figs. 7.4A-1 and A-2). Hence, extensional behaviour is dominant in the earliest subsidence stages (Fig. 7.4A1-3). Accordingly, extensional sub-segments of the active deformation segment with lateral extents of about 10 - 50 m evolve (Fig. 7.4A). Compression is only observed at the basin-side of the active segment where slope material is overthrusting the undeformed hanging wall (Fig. 7.4A-7). This indicates that once generated major faults accommodate most of the deformation in the cohesive material A, while internal deformation of the sub-segments in-between these faults is low.

- *Slope topography*

As a result of basin subsidence, a typical tripartite of the deformed basin 'sediment' layer evolve consisting of two nearly flat areas on top of the hanging- and footwall segments as well as a steeper slope (Fig. 7.4A). The position of this inclined slope correlates with the active deformation segment.

Hence, the slope is bordered by the major normal as well as the outermost thrust faults. Slope angles increase continuously throughout the entire experiment. However, a typical segmentation of the slope into a gently dipping upper slope ($\alpha_{\text{upper}} = 4\text{-}8^\circ$, disregarding the much steeper fault scarps) and a steeper lower slope ($\alpha_{\text{lower}} = 15\text{-}28^\circ$) could be identified after approximately 90 m subsidence (Fig. 7.4A-4). This upper slope correlates with that part of the active segment which is dominated by extensional deformation whereas the latter is continuously tilted by basin subsidence. Here, no compensation of slope angle by normal fault offsets occurs. This results in a hinge marked by a high change in slope angle. Furthermore, the hinge moves continuously towards the subsiding basin simultaneously to master-fault offset.

We further observe that the upper slope portion is characterized by an alternation of smoother topography due to long-term activity of major normal faults and high stability of the small-scaled extensional sub-segments (Fig. 7.4A-4). Here, areas with the highest slope gradient correlate with fault scarps ($\sim 35^\circ$; e.g., Fig. 7.4A-6). Thus, the outcropping scarps of major faults lead to a steep, cascaded topography and an irregular shape ('morphology') of the upper, extension-dominated slope segment (e.g. Figs. 7.5A-2 to A-4).

- *Mass movement*

Caused by the ongoing basin subsidence and the resulting progressive steepening of the slope, slope destabilizations occur as soon as total basin subsidence reaches approximately 80 - 90 m offset. The occurrence of gravitational mass movement is thereby limited to the hinge region between upper and lower slope (Fig. 7.4A-4 to A-7). Here, absence of normal fault activity cause an oversteepening of the lower slope front up to critical slope angles with respect to material attributes. Headwalls of destabilized masses occur in the upper, lower-inclined slope and correlate with steep normal fault scarps (Fig. 7.6A). Hence, destabilized particle assemblages occur as deep-seated, wedge-shaped, compact bodies with partially downward concave shear planes with a mean inclination of 25° (disregarding the pre-defined inclination of the headwall) in-between normal faults and the oversteepened front of the lower slope (e.g., Figs. 7.4A-4 and 6A). Consequently, mass movements are dominated by a rotational material displacement with less internal deformation and a short runout leading to deposition at the slope hinge. Further, we observe that the fault surfaces preparing headwalls of these repeated mass movements make the slope continuously steeper in place as they are steeper than the adjacent slope.

However, these large scale mass movements show a recurrence with at maximum one event per 20-m subsidence interval. Hence, they alternate with time periods of stable, further steepening slopes (Fig. 7.4A-7 and 5A-1 to A-4). Both the active normal faults and the ongoing basin subsidence producing a steepening of the lower slope are then necessary prerequisites for failure initiation. We measure

gradients of up to 28° for those slope portions that tend to destabilize immediately afterwards (Fig. 7.4A-4 to A-7).

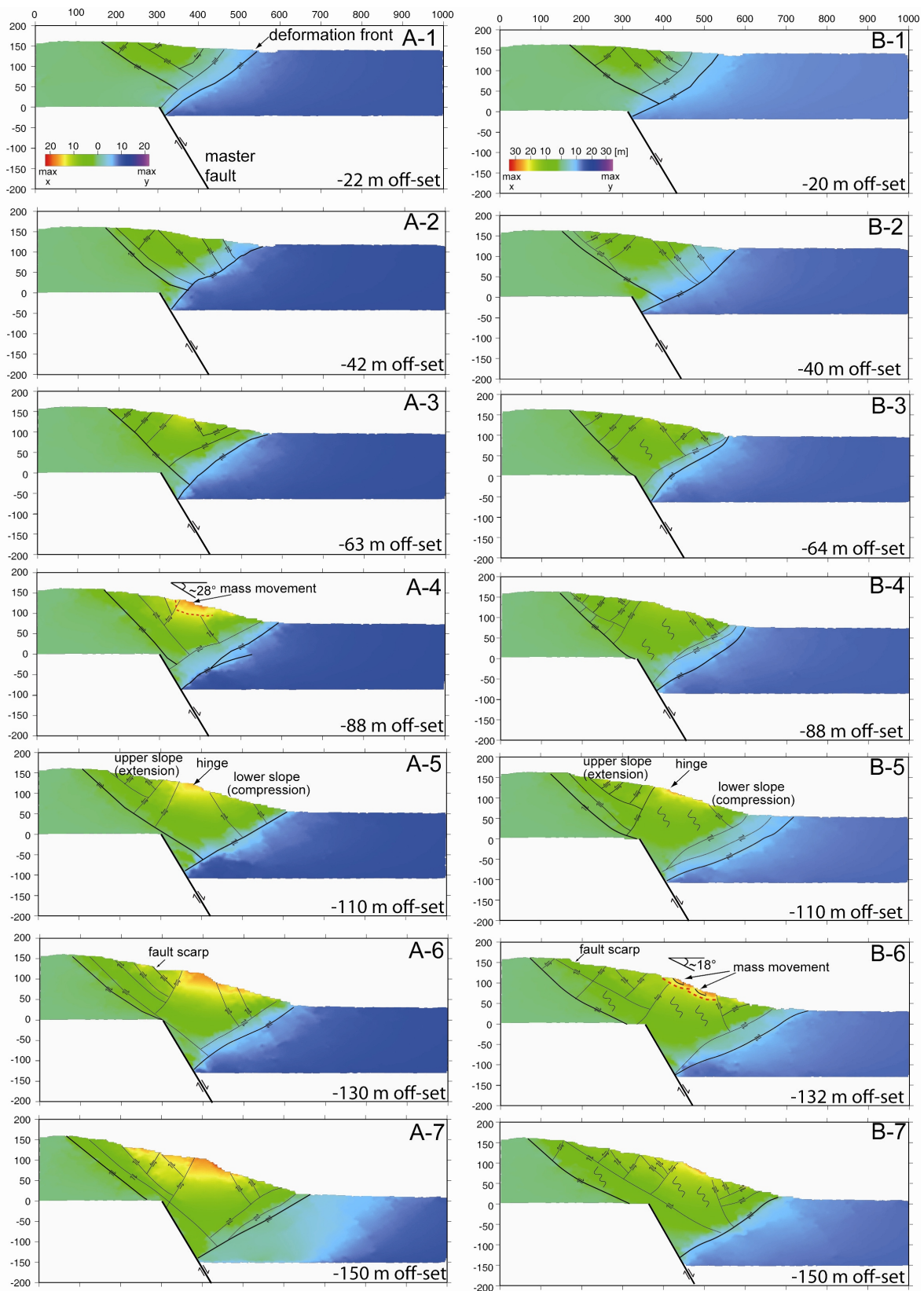


Fig. 7.4) Time series of incremental displacement plots from 20-m off-set intervals in between 10 m to 150 m basin subsidence for the cohesive model A (A1-7) and the non-cohesive model B (B1-7). Arrows indicate fault off-sets, thick

lines major faults along active segment boundaries, thin lines sub-ordinated faults within the active segments. Wavy lines in model B represent chaotic deformation patterns not assignable to distinct faults. Yellow to orange colours indicate the occurrence of near-surface mass movement.

In addition, we observe that the dimension of the described mass movements is linked to the stage of slope development and thus basin subsidence (Fig. 7.4A-3 to A-7). As headwalls of slope failures migrates simultaneously to the activation of younger normal faults outward in footwall direction, the dimension of masses that fail in between these new headwalls and the almost static slope front increases. Consequently, the largest slope failure event of > 200 m width and about 50 m in thickness can be observed in the final model stages at approximately 150 m subsidence (Fig. 7.4A-7). Hence, we deduce that the dimensions of destabilised masses increase with ongoing basin subsidence, the growing size of the active deformation segment, and the number of normal faults.

7.3.2. Non-cohesive slope 'sediments' - model B

- *Evolution of deformation segments and fault system*

The active deformation segment of the non-cohesive model B establishes immediately after master-fault off-set initiation with a lateral surface width of approximately 400 m (Figs. 7.4B1 to B4). Already 100 m basin subsidence in the order of 100 m, the segment reaches its largest extent of about 650 m (Figs. 7.4B5 to B7). Simultaneously, the advancement of the segment is especially in the later model stages much larger towards the subsiding basin than towards the inactive footwall (e.g. Fig. 7.4A-7).

We observe major, long-term active normal faults ($\alpha \sim 40-50^\circ$; Fig. 7.4B-2 to B-7) that develop towards the inactive footwall. Coevally, thrust faults ($\alpha \sim 20-30^\circ$; Fig. 7.4B-2 to B-7) establish towards the inactive hanging wall almost perpendicular to the master-fault. Hence, both fault types continuously prepare the outer limits of the active segment in accordance to model A. While the activation of major normal-fault migrates towards the inactive footwall (see Fig. 7.4B-5 to B-7), thrust faults are more or less static in position (compare Figs. 7.4B-4 to B-7). In accordance with model A, we also observe a segmentation of the active segment into an upper, lower inclined and a lower, steeper slope for the model B (e.g., Fig. 7.4B-7).

In contrast to major faulting along the outer limits of the active segment, its internal deformation is controlled by the almost non-cohesive material attributes leading to dense sets of short-term active normal and thrust faults in a diffuse distribution. These sub-ordinated minor normal faults prepare complex, brittle deformation almost parallel as well as antithetic to major faults due to extension in the upper slope. The various smaller thrusts occur in parallel to major thrusts in the lower slope portion towards the slope foot region due to an increase in compression during slope advancement basinwards (compare Figs. 7.5A-1 to A-4 with 7.5B-1 to B-4). This overall diffuse brittle deformation,

especially in the segment's central portion (~300 - 500 m model length; e.g., Figs. 7.4B-5 and B-7), strongly contrasts the large, long-term stable sub-segments assembling the active segment in model A.

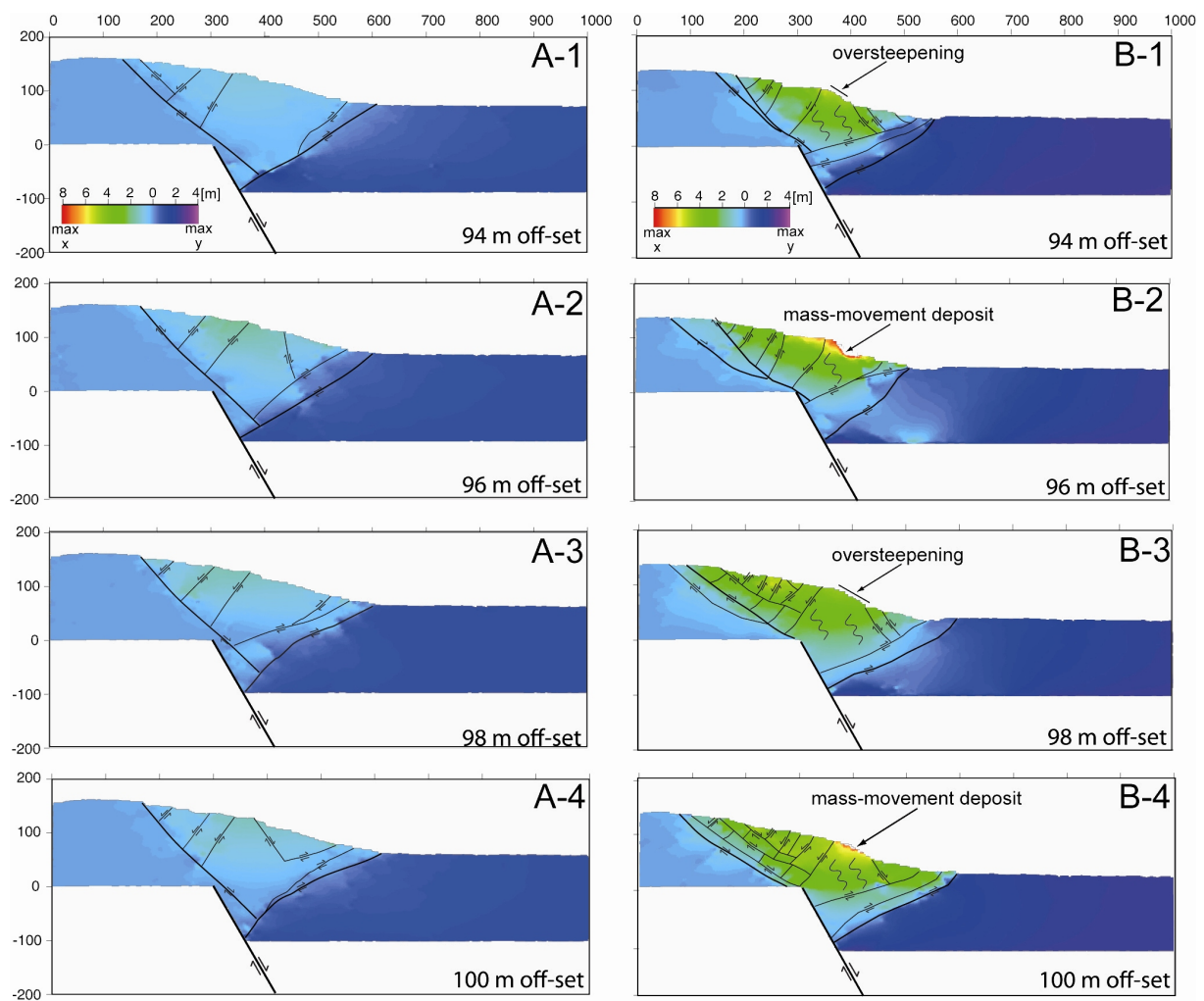


Fig. 7.5) Time series of 2 m subsidence intervals in between approximately 94-100 m total basin subsidence for material A (A1-4) and material B (B1-4). In these plots of higher time-interval resolution, material B reveals its typical complex faulting and the resulting changes in the fault-pattern as well as the higher number in near-surface mass-movement events compared to model A. Model A indicates the more static and larger-scaled faulting of material A and does not evidence pronounced gravitational mass movement within this short time-period.

- *Slope topography*

The flat surface topography of the inactive foot- and hangingwall segments consistently contrasts with the irregular and partially steep topography of the active segment (compare e.g. Figs. 7.4A-7 and 4B-7). Already after ~100 m basin subsidence, the active slope segment exhibits a further separation into a lower-inclined ($\alpha_{\text{upper}} = 6 - 8^\circ$ at maximum), extension-dominated upper slope and a steeper ($\alpha_{\text{lower}} = 14 - 20^\circ$), compression-dominated lower slope (Fig. 7.4B-7). Although both slope parts are of significantly different mean inclination, a well-defined hinge analogous to model A cannot be observed continuously (e.g., Fig. 7.4B-4 to B-6). Also slope angle transitions at both active-inactive-segment boundaries are smooth, especially in the slope-foot region (e.g. Fig. 7.4B-6). Hence, the entire slope maintains a smoother topography and also 'morphology' compared to model A.

Nevertheless, the upper slope also periodically shows fault scarps resulting from ongoing normal fault activation (e.g., Fig. 7.4B-6) analogous to the structures observed in model A (e.g., Fig. 7.4A-7), while these features are barely observed in model stages with >100 m subsidence (see changes from Figs. 7.5B1-3 to 5B-4).

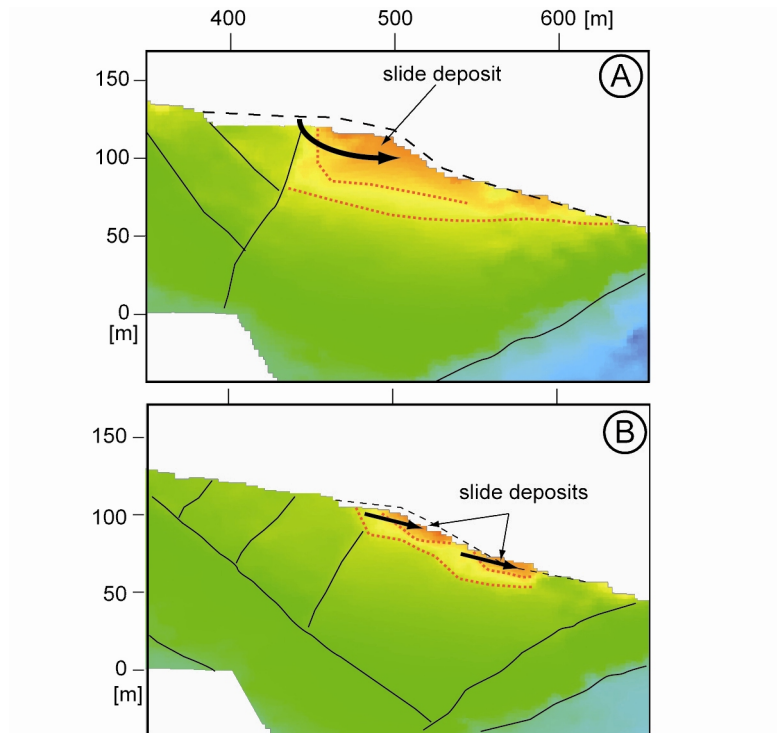


Fig. 7.6) Examples of mass movements that typically occur in the “cohesive” (A) and the “non-cohesive” (B) material at approximately same stages of basin subsidence (~130 m). As can be seen, the slope of cohesive material (A) produces a single, large, deep-seated slide, whereas the slope bearing the non-cohesive material (B) comprises (at least) two smaller landslides of shallower, almost plane-parallel failure geometry. Note that such failure events are of much lower repetition for material-A (max. 1 event per >20 m subsidence) than for material-B (in mean 1-3 events per 2-4 m subsidence intervals).

- *Mass movement*

After approximately 100 m basin subsidence, mass movements occur frequently in model B (Fig. 7.4B-5 to B-7). These mass failures are restricted to the near-surface material in the upper portion of the lower slope close to the hinge region (e.g., Figs. 7.4B-6; 7.5B-4, and 7.6B). Here, we detect almost slope-parallel sliding of masses in those slope portions where the inclination reaches 18-20° immediately before the failure occurs (e.g., Fig. 7.4B-6 and 5B-4). Furthermore, some of the detected events correlate to a temporary activation of minor low-angle normal faults directly at the slope hinge similar to model A (e.g., Fig. 7.5B-2), while most failures are restricted to the steeper front of the lower slope.

The major difference to model A is that the mass movements are smaller and measured to 10 - 20 m thickness and 20 - 50 m in length (e.g., Fig. 7.6B). Their mean recurrence rate is much higher with about 1-2 events during 4-m subsidence intervals (Fig. 7.4B-5 to B-7; Fig. 7.5B-2, B-4). High resolution plots of 2-m subsidence intervals (Fig. 7.5B-1 to B-4) reveal that the size of single events decreases, while their number increases. We infer that most mass-movement events observed in lower resolution plots consist of such multiple smaller events (compare Figs. 7.4B-5 to 7.5B-2 and 7.5B4).

When examining those locations where mass failures frequently occur, we observe that progressive oversteepening of the lower slope occurs frequently and is always immediately balanced by a mass movement event (e.g. Figs. 5B-3 to 5B-4). This contrasts with the long-term stability and only occasional slope failures that occur in model A (compare Figs. 5A and 5B). Further, model B mass movements are of larger runout and they deposit on the lower slope where gradients are below those measured for initiation of sediment transport (i.e. 18 - 20°). However, on the lower slope their deposition repeatedly caused over-steepening (Fig. 7.5B-2) and thus was destabilized (Fig. 7.5B-3) again until the activated and reactivated masses reach the slope foot (e.g. Figs. 7.4B-6 and 7.6B). Compared to model A, this process is held responsible for the smoother, more elongated slope foot taper and its advancement towards the inactive hangingwall segment.

7.4. Interpretation & Discussion

The cohesive and the non-cohesive model show similarities in the strict segmentation into inactive foot- and hangingwall segments as well as an active, deformed segment in-between (Fig. 7.7A and B). The active segments are further partitioned into an upper, extension-dominated and lower, compression-dominated slope (Fig. 7.7A and B). The detachment of the inactive segments from the active segment is associated to major faults, which are slope-parallel normal faults from extension in the upper slope and thrust faults from compression in the lower slope (Fig. 7.7C). However, kinematics of the active segments in both models strictly differ. We observe long-term active, large normal and thrust faults dominant in model A contrasting with diffuse patterns of smaller, short-term active normal and thrust faults as well as chaotic deformation in-between in model B (see 7.3.1 and 7.3.2). Consequently, the overall active segment deformation in model A results in a compact slope geometry with a relatively steep, cascaded topography. This slope configuration shows many analogies to the behaviour of the natural submarine slope from which the physical attributes of the cohesive sediment type were adopted (e.g., Kopf et al., 2006; 2007; Strozyk et al., 2009). In contrast, the diffuse deformation patterns in model B lead to a generally lower inclined and smoother topography of the laterally more elongated slope. This also corresponds well with natural examples representing kinematics of non-cohesive sediments (e.g., parts of the submarine slope offshore Norway (Jackson et al., 2007)). We conclude that the overall basin flank development of cohesive and non-cohesive slope sediment covers can show analogies in several stages of basin subsidence, while

the ongoing tilting and the kinematically differing responses of the two materials lead to more and more variation in the subsequent slope architecture evolution.

Upon closer inspection of the way slope kinematics impact on failure initiation in cohesive, muddy material, we deduce that major normal fault activity and the resulting steep fault-scarps at the surface are an important factor (section 7.3.1). The high cohesion of the material is responsible for high sub-segment stability, while traces of initially cracked particle contact-bonds prepare major faults due to a strong weakening of the material. In terms of oversteepening of the lower slope (i.e. $\sim 28^\circ$), large masses in front of slope-parallel normal faults in the upper slope are destabilized (Fig. 7.6A). The resulting mass failures prepare compact slide bodies with a short lateral transport along deep-seated, almost planar to slightly concave-shaped slide planes (Fig. 7.6A; see also Fig. 7.7A and section 3.1). Based on this geometry, the failures do not produce large downslope transport of the material, while they bias oversteepening in the slope hinge region. This slope failure and transport mechanism correlates to mass movements generally classified as cohesive slides or even slumps that often occur along natural slopes bearing cohesive sediments (e.g. Sawicki and Leśniewska, 1991; McAdoo et al., 2000). Further, the fault patterns and the restriction of deformation along these faults as well as high stability of the sediment between faults are similar to analogue ‘sandbox’ experiments with cohesive materials (e.g., van Gent et al., 2009). We observe that these mass movements (i) are restricted to the break (‘hinge’) from the upper to the lower slope, (ii) are associated with normal faults which prepare headwalls according to their mechanical weakness from the material fraction, (iii) occur in front of faults and fault-scarps that make the slope steeper because the remaining headwalls are steeper than the slope, and (iv) are associated with the activation of new faults in the back of prior events which also leads to a retreating of headwalls in an upslope direction. These observations are almost consistent to slope failure development and the resulting slope architecture e.g. along the western US submarine Eel margin (Walsh and Nittrouer, 1999; McAdoo et al., 2000) and the northeastern margin of Crete (Kopf et al., 2006; 2007; Strozyk et al., 2009).

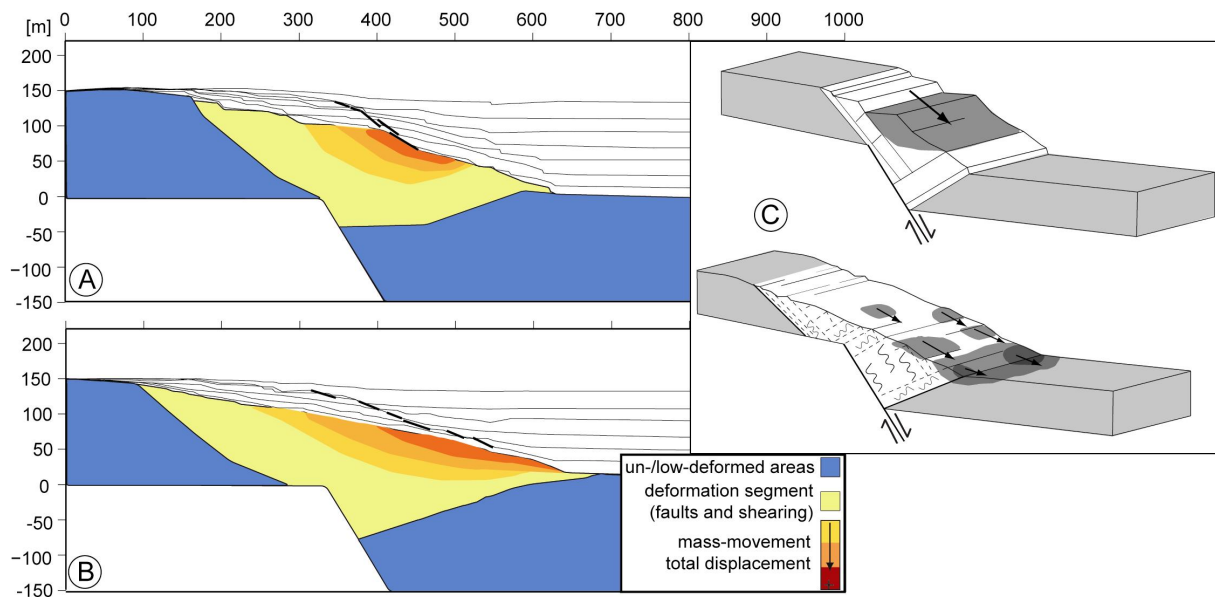


Fig. 7.7 A and B: Plots showing the total lateral particle displacement that occurs from 150 m basin subsidence in the cohesive model (7A) and in the non-cohesive model (7B). The high increases of particle displacement to the active segments (yellow) top regions (orange to red colours) indicate the final position of most particles that assigned to mass movement during the entire model performances. Slope topography evolution is shown in 20-m subsidence intervals. Thick black markings indicate locations where oversteepening could be observed; 7C: Conceptual 3-D sketches for extensional basin slopes bearing cohesive (top) and non-cohesive (bottom) sediments as implied from results of the numerical models.

In contrast, the non-cohesive, sandy slope cover of model B reveals a higher frequency of failure and thus a higher number of mass movements (see 7.3.2). The large number and smaller size of events are interpreted to correlate to frequent oversteepening of the lower slope front. The many single mass movements then occur as almost plane-parallel near-surface slides with shear planes almost parallel to the slope angle of the uppermost lower slope (i.e. 18 - 20°; e.g., Fig. 7.6B). Further, the slid masses are repeatedly reactivated after their emplacement due to local oversteepening from this additional sediment deposition, until they reach the slope foot region. This permanent material transport all the way down the slope occurs as recently as the slope is oversteepened for the first time. Afterwards, this sediment transport downslope produces the smooth taper at the slope foot, similar to natural slopes (e.g., Bromhead, 1978; O’Grady, 2001). Compared to cohesive sediment slopes, slopes bearing almost non-cohesive sediment covers are dominated by a high, diffuse sediment export in terms of many small slide events to the slope-foot region (Fig. 7.7B; see section 7.3.2). This relative arrangement and frequency of mass movement shows many analogies to natural slopes bearing dominantly non-cohesive sediments, e.g. the northern subaquatic slope in the Gulf of Mexico, which also has a high percentage of its steeper surface area covered with smaller failures from multiple slides (e.g., McAdoo et al., 2000). Such natural examples have shown that non-cohesive slope covers are characterized by a diffuse distribution of mass failure on the steeper slope front (i.e. the lower slope) resulting in multiple smaller slides and mass-flows (maybe also turbidites) providing an efficient sediment transport down to the slope foot.

7.5. Conclusion

In this study we have shown that the deformation of a sedimentary slope cover, the associated mass movements, and the resulting long-term evolution of the slope architecture along extensional basin flanks is strongly predisposed by the mechanical behaviour (i.e. cohesion) of the inherent sediment type. Comparing our observations and interpretations for both materials, we conclude that

(1) Mass movement on a slope bearing dominantly cohesive sediment can be governed by both the occurrence of normal faults preparing pre-defined headwalls and the oversteepening of the slope in front due to ongoing basin subsidence. Hence, permanently acting stresses from the tectonic movement are accommodated by single major faults while the slope is stable about long periods of time, and only occasional collapses occur;

(2) Mass movement on a slope bearing less or non-cohesive sediment is governed by a frequent slope front instability due to oversteepening while deformation in lower-inclined slope parts is accommodated by a diffuse faulting;

The models imply that fault kinematics and mass movements of the cohesive and non-cohesive slope do not produce significant differences in the overall slope architectures during initial as well as some intermediated stages of basin subsidence. Hence, both can appear in similar shapes regarding slope geometry and topography. However, the long-term effects of the characteristic fault patterns as well as repeated impacts of mass movements in different scales, types, and recurrence rates produce the characterised differences in topography, morphology, and the lateral extent of the deformed slope during time. It was already suggested that slope sediment types are subjected to the shown attributes of cohesive vs. non-cohesive slope topography, morphology, and mass movements (e.g., Moriya, 1972; McAdoo et al., 2000). But in addition, the results of our modeling imply that this linkage strongly depends on the current stage of slope evolution and the impact of long-term dynamic processes, e.g. most recent active faults and the prior occurrence of mass movements;

We conclude that the distribution, dimension, number, and the mechanics of slope failure events, as well as the resulting evolution in slope architecture, record sediment characteristics in terms of sediment cohesion. The results further imply that a 'static' investigation of such slopes may lead to uncertainties in kinematical interpretations if most dynamic processes regarding longer periods of time and larger scales are disregarded. Consequently, the relative importance of a slope's kinematical behaviour against the many others suggested triggers for sediment instability can be determined using (1) physical sediment properties, e.g. provided by deeper drillings of slope sediment covers and in-situ geotechnical measurements, (2) a detailed analysis of slope architecture from mapping of slope

topography and morphology, and (3) a reconstruction of slope evolution during time, e.g. fault interpretation and back-stripping of tectonic movements, are evident.

Acknowledgements

We thank Dr. Michael Strasser and Dr. Ed Hathorne for thoughtful comments and suggestions. We thank the MARUM for scientific support and involved scientists for fruitful discussions. This publication is funded through the DFG-Research Centre/ Cluster of Excellence „The Ocean in the Earth System“.

References

- Antonellini, M.A., Pollard, D.D., David D., 1995. Distinct element modelling of deformation bands in sandstone. *Journal of Structural Geology* 17, 1165–1182.
- Balsam, W.L., Beeson, J.P., 2003. Sea-floor sediment distribution in the Gulf of Mexico, *Deep-Sea Res.* 50, 1421–1444.
- Biscontin, G., Pestana, J.M., 2006. Factors affecting seismic response of submarine slopes. *Natural Hazards and Earth System Sciences* 6, 97-107.
- Booth, J.S., O'Leary, D.W., Popenoe, P., Danforth, W.W., 1993. U.S. Atlantic continental slope landslides: Their distribution, general attributes, and implications, in *Submarine Landslides. Selected Studies in the U.S. Exclusive Economic Zone*, edited by Schwab, W. C., Lee, H. J., Twichell, D.C., U.S. Geol. Surv. Bull., 2002, 14-23.
- Bos, B., 2000. Faults, Fluids and Friction. *Geologica Ultraiectina*, 197.pp.157.
- Bromhead, E. N., 1986. *The Stability of Slopes*. Surrey University Press.
- Buiter, S.J.H., Schreurs, G., (eds.) 2006. *Analogue and numerical modelling of crustal-scale processes*. Geological Society.
- Bryn, P., Solheim, A., Berg, K., Lien, R., Forsberg, C.F., Haflidason, H., Ottesen, D., Rise, L., 2002. The Storegga Slide complex; repeated large scale sliding in response to climatic cyclicity. In: Locat, J., Mienert, J. (Eds.), *Submarine Mass Movements and Their Consequences*. Kluwer Academic Publishers, The Netherlands, 215-222.
- Canals, M., Lastras, G., Urgeles, R., Casamor, J.L., Mienert, J., Cattaneo, A., De Batist, M., Haflidason, H., Imbo, Y., Laberg, J.S., Locat, J., Long, D., Longva, O., Masson, D. G., Sultan, N., Trincardi, F., Bryn, P., 2004. Slope failure dynamics and impacts from seafloor and shallow sub-seafloor geophysical data: case studies from the COSTA project. *Mar. Geol.* 213, 9-72.
- Chang, C.S., 1992. Discrete element method for slope stability analysis. *J. Geotech. Eng.* 118, 1889– 1905.
- Chronis, G., Lykousis, V., Anagnostos, C., Karageorgis, A., Stavrakakis, S., Poulos, S., 2000. Sedimentological processes in the southern margin of the Crete Sea (NE Mediterranean). *Progr. Oceanogr.* 46, 143-160.
- Cochoat, P., Dürr, S., Herzig, P., Mevel, C., Mienert, J., Schneider, R., Weaver, P.P.E., Winkler, A., 2007. The deep-sea frontier- Science challenges for a sustainable future. European Communities, printed in Belgium, 52.
- Coleman, J. M., Prior, D. B., 1988. Mass wasting on continental margins. *Annu. Rev. Earth Planet. Sci.* 16, 101-119
- Crescenzo, G.D., Santo, A., 2005 Debris slides–rapid earth flows in the carbonate massifs of the Campania region (Southern Italy): morphological and morphometric data for evaluating triggering susceptibility. *Geomorphology* 66, 255–276
- Cundall, P.A., Strack, O.D.L., 1978. BALL e a program to model granular media using the distinct element method. Technical Note. Advanced Technology Group, Dames and Moore, London.
- Cundall, P.A., Strack, O.D.L., 1979. A discrete numerical method for granular assemblies. *Geotechnique* 29, 47–65.
- Cundall, P.A., Strack, O.D.L., 1983. Modeling of microscopic mechanisms in granular material. In: Jenkins, J.T., Satake, M. (Eds.), *Mechanics of Granular Materials: New Models and Constitutive Relations*. Elsevier Science Publishers B.V, Amsterdam.
- Cundall, P.A., 1989. Numerical experiments on localization in frictional materials. *Ingenieur-Archiv* 59, 148-159.

- Dillon, W.P., Risch, J.S., Scanlon, K.M., Valentine, P.C., Huggert, Q.J., 1993. Ancient crustal fractures control the location and size of collapsed blocks at the Blake Escarpment, east of Florida, in *Submarine Landslides: Selected Studies in the U.S. Exclusive Economic Zone*, edited by W. C. Schwab, H. J. Lee, and D.C. Twichell, U.S. Geol. Surv. Bull., 2002, 54-59.
- Guo, Y., Morgan, J.K. 2004. Influence of normal stress and grain shape on granular friction; results of discrete element simulations. *Journal of Geophysical Research* 109; B12, B12305.
- Hampton, M.A., Bouma, A.H., Carlson, P.R., Molnia, B.F., Clukey, E.C., Sangrey, D.A., 1978. Quantitative study of slope instability in the Gulf of Alaska, paper presented at 10th Annual Offshore Technology Conference A, m. Inst. Of Min. and Metal. Eng., Houston, Tex.
- Hampton, M.A., Lee, H.J., Locat, J., 1996. Submarine landslides. *Rev. Geophys.* 34, 33-59.
- Huhn, K., Kock, I., Kopf, A., 2006. Comparative numerical and analogue shear box experiments and their implications for the mechanics along the failure plane of landslides, *Norwegian Journal of Geology* 86, 209-220.
- Hutton, E.W.H., Syvitski, J.P.M., 2003. Advances in the numerical modeling of sediment failure during the development of a continental margin, *Mar. Geol.* 203, 367-380.
- Itasca Consulting Group, 2004. Particle flow code in 2-D (PFC-2D): User's manual. Version 3.0
- Kock, I., Huhn K., 2006. Influence of particle shape on the frictional strength of sediments- a case study, *Sedimentary Geology* 196, 217 - 233, doi:10.1016/j.sedgeo.2006.07.011
- Kock, I., Huhn, K., 2007. Numerical Investigation of localization and micromechanics in a stratified soil specimen. *Journal of Structural Geology* 29, 1679-1694, doi:10.1016/j.jsg.2007.07.013
- Kopf, A., Alves, T., Heesamnn, B., Irving, M., Kaul, N.E., Kock, I., Krastel, S., Reichelt, M., Schäfer, R., Stegmann, S., Strasser, M., Thölen, M., 2006. Report and preliminary results of Poseidon cruise P336: CRESTS – Cretan Sea Tectonics and Sedimentation, Heraklion 28.04.-17.05.2006. *Berichte, Fachbereich Geowissenschaften, Universität Bremen*, 253.
- Kopf, A., Stegmann, S., Krastel, S., Förster, A., Strasser, M., Irving, M., 2007. Marine deep-water Free-fall CPT Measurements for landslide characterisation off Crete, Greece (Eastern Mediterranean Sea) - PART 2: Initial data from the western Cretan Sea. In: Lykousis, V., Sakellariou, D., Locat, J. (eds.). *Submarine Mass movements and their consequences. Advances in Natural and Technological Hazards Series*, Springer, 199-208.
- Lambe, T.W., Whitman, R.V., 1969. *Soil Mechanics*, 553, John Wiley, New York.
- Lee, H. J., Edwards, B.D., 1986. Regional method to assess offshore slope stability, *J. Geotech. Eng.* 112, 489-509
- Lee, H.J., Locat, J., Desgagnes, P., Parsons, J.D., McAdoo, B.G., Orange, D.L., Puig, P., Wong, F.L., Dartnell, P., Boulanger, E., 2007. Submarine mass movements on continental margins. In: Nittrouer, C.A., Austin, J.A., Field, M.E., Kravitz, J.H., Syvitki, J.P.M., Wiberg, P.L. (eds.), *Continental Margin Sedimentation*, Blackwell Publishing, UK, 213-274.
- Leeder, M., 1999. *Sedimentology and Sedimentary Basins – from Turbulences to Tectonics*. Blackwell Publishing, UK.
- Lohrmann, J., Kukowski, N., Adam, J., Oncken, O., 2003. The control of sand wedges by material properties: sensitivity analyses and application to convergent margins. *Structural Geology* 25, 1691-1711.
- Lyså, A., Hansen, L., Christensen, O., L'Heureux, J.L., Longva, O., Olsen, H.A., Sveian, H., 2008. Landscape evolution and slide processes in a glacioisostatic rebound area; a combined marine and terrestrial approach. *Mar. Geol.* 248, 53–73
- Marone, C., 1998. Laboratory-derived friction laws and their application to seismic faulting. *Annual Review of Earth and Planetary Sciences* 26, 643-696.
- McAdoo, B.G., Pratson, L.F., Orange, D.L., 2000. Submarine landslide geomorphology, US continental slope. *Mar. Geol.* 169, 103-136.
- Mustoe, G.G.W., Williams, J.R., Hocking, G., 1987. The discrete element method in geotechnical engineering. In: Banerjee, P.K., Butterfield, R. (Eds.), *Dynamic Behavior of Foundations and Buried Structures. Developments in Soil Mechanics and Foundation Engineering*, vol. 3, pp. 233–263.
- Mitchell, J.K., Soga, K., 2005. *Fundamentals of soil behavior*. Wiley, New Jersey. 577 pp.

- Mohrig, D., Elverhøi, A., Parker, G., 1999. Experiments on the relative mobility of muddy subaqueous and subaerial debris flows, and their capacity to remobilize antecedent deposits *Marine Geology*, Volume 154, Issues 1-4, 2 Pages 117-129
- Morgan, J.K., Boettcher, M.S. 1999. Numerical simulations of granular shear zones using the distinct element method 1. Shear zone kinematics and the micromechanics of localisation. *Journal of Geophysical Research* 104, 703-719.
- Morgan, J.K., 1999. Numerical simulations of granular shear zones using the distinct element method: II. The effect of particle size distribution and interparticle friction on mechanical behavior. *J. Geophys. Res.* 104, 2721–2732.
- Morgan, J.K., 2006. Volcanotectonic interactions between Mauna Loa and Kilauea: Insights from 2-D discrete element simulations. *Journal of Volcanology and Geothermal Research* 151, 109–131
- Morgenstern, N.R., Price, V.E., 1965. Analysis of stability of general slip surfaces. *Geotechnique* 15, 79-93.
- Morgenstern, N.R., 1967. Submarine slumping and the initiation of turbidity currents, in *Marine Geotechnique*, edited by A. F. Richards, 189-210, Univ. of Ill. Press, Urbana.
- Moriya, I., 1972. Slope classifications by failure topographic units and slope development. *Proc. Geograph. Sci. Jpn.* 2, 168–169.
- O’Grady, D.B., 2001. Sedimentary Geomorphology of siliciclastic continental slopes. Ph.D. thesis, Faculty of the Graduate School of the University of Colorado.
- Ramsay, J.G., Huber, M.I., 1987. *The Techniques of Modern Structural Geology: Vol. 2, Folds and Fractures*.
- Saltzer, S.D., Pollard, D.D., 1992. Distinct element modeling of structures formed in sedimentary overburden by extensional reactivation of basement normal faults. *Tectonics* 11, 165– 174.
- Sawicki, A., Leśniewska, D., 1991. Stability of fabric reinforced cohesive soil slopes. Pub by Elsevier Ltd. doi:10.1016/0266-1144(91)90025-R
- Schellart, W.P., 2000. Shear test results for cohesion and friction coefficients for different granular materials: scaling implications for their usage in analogue modelling, *Tectonophysics* 324, 1–16
- Seyforth, M., Henk, A., 2003. Coupling of PFC2D and ANSYS— concepts to combine the best of two worlds for improved geodynamic models. In: Konietzky, H. (Ed.), *Numerical Modeling in Micromechanics via Particle Methods*. A.A. Balkema Publishers, Lisse, 283–290.
- Sitharam, T.G., Nimbkar, M.S., 1997. Numerical modelling of the micromechanical behavior of granular media by discrete element method. *Geotech. Eng. Bull.* 6, 261– 283.
- Shanmugam, G., 2000. 50 years of the turbidite paradigm (1950s–1990s): deep-water processes and facies models - a critical perspective. *Marine and Petroleum Geology* 17
- Shanmugam, G., 2009. Slides, Slumps, Debris Flows, and Turbidity Currents, in: *Encyclopedia of Ocean Sciences*, 4509-4529, Elsevier.
- Solheim, A., Bryn, P., Sejrup, H.P., Mienert, J., Berg, K., 2005. Ormen Lange - An integrated study for the safe development of a deep-water gas field within the Storegga Slide complex, NE Atlantic continental margin; executive summary. *Marine and Petroleum Geology*, 22(1-2), 1-9.
- Stegmann S., Strasser, M., Anselmetti, F., Kopf, A., 2007. Geotechnical in situ characterization of subaquatic slopes: The role of pore pressure transients versus frictional strength in landslide initiation, *Geophys. Res. Lett.*, 34, L07607, doi:10.1029/2006GL029122.
- Strayer, L.M., Suppé, J. 2002. Out-of-plane motion of a thrust sheet during along-strike propagation of a thrust ramp; a distinct-element approach. *Journal of Structural Geology* 24, 637-650.
- Strozyk, F., et al., 2009. New evidence for massive gravitational mass-transport deposits in the southern Cretan Sea, eastern Mediterranean, *Mar. Geol.* 263, 97–107.
- Takahashi, T., 1991. *Debris Flows*. Balkema, Rotterdam, 165 pp.
- Twiss, R.J., Moores, E.M., 1992. *Structural Geology*. Freeman, 415pp.
- Walsh, J. P., Nittrouer, C. A., 1999. Observations of sediment flux to the Eel continental slope, northern California. *Mar. Geol.* 154, 55-68
- Wessel, P., Smith, W.H.F., 1991. Free software helps map and display data. *EOS Trans. AGU*, 72, 441.

Van Gent, H. W., Holland, M., Urai, J. L., Loosveld, R., 2009. Evolution of fault zones in carbonates with mechanical stratigraphy – Insights from scale models using layered cohesive powder. *Struct. Geol.* (in press), doi: 10.1016/j.jsg.2009.05.006



8. Synthesis: Conclusions and outlook

In this chapter, a summary of conclusions obtained from the single studies in chapters 4-7 are compiled to a synthesis about the mass-wasting activity and development on the northeastern Cretan margin as well as its exertion on more general research targets regarding active margin mass movement. Note that some further key aspects that emerged during this compilation, although not emphasised in the single chapters, are also mentioned.

8.1. The northeast Cretan margin mass-movement patterns

[1] As a first solid result, distinct patterns of mass-transport deposits (MTDs) are identified and described on the northeast Cretan margin as well as in the deeper parts of the southern Cretan Sea (i.e. the Kamilonisi Basin) for the first time (Chapters 4-6). It was shown that these MTDs are restricted to mid-slope positions (i.e. in the eastern study site near the Bay of Mirabello) on one hand, and to the foot regions of steeper slopes (i.e. the Malia and the Kamilonisi Basin) on the other hand. Largest MTDs of 30-50 km³ volumes were found in the Kamilonisi Basin and represent a pattern of ‘major’ mass-movement events (Chapter 6). MTDs found in mid-slope positions as well as in the Malia Basin represent displaced sediment volumes of 0.5 to 2.5 km³ and present a pattern of ‘midsize’ mass-movement events (Chapters 5 and 6). A third pattern of MTDs consists of centimetre- to decimetre-thick sediment dislocations locally restricted to foot regions of steeper slope parts (e.g., chapter 6). As no deposits of mass-movement activity with intermediate scales can be observed, the investigated data suggests that the dominant portion of northeast Cretan margin mass wasting is recorded in these three patterns. Thereof, major MTDs in the Kamilonisi Basin assemble the largest contingent of sediment volume and are seen to be the most important process of Cretan slope sediment erosion.

[2] Based on the back-calculation of mean accumulation rates of younger sediment drape on top of MTDs, it is possible to assess their ages as well as the recurrence times of landslide events, estimated from the thicknesses of interbedded background sediment packages (Chapters 4 and 6). Ages of 33-25 ka B.P. are back-calculated for the youngest “midsize” MTDs in the Malia Basin and 250-147 ka B.P. for the MTDs of the eastern mid-slope landslide complex. A frequency for these events is estimated to at least 34 ka for the sequenced Malia Basin MTDs (total range of uncertainty is 34-125 ka due to the possible range of 8-22 cm/ka accumulation rate), whereas no older events are detected for the landslide complex in the eastern study site with an age of about 192 ka B.P. (range of uncertainty: 250-147 ka B.P.). The age of the youngest major MTD in the Kamlinois Basin is back-calculated to 192- 250 ka B.P. (range of uncertainty: 320-147 ka B.P.), and a recurrence-time of ~250 ka (\pm 70 ka) is estimated for the single major events below. For the third pattern of small events, intervals of approximately 3-25 ka are identified in core data. Comparing the dimension and the recurrence rates of mass movements, a major outcome is that the temporal occurrence of mass-movement events

correlates to their sizes. Hence, smallest events are of highest and major events of lowest frequency. This also coincides with the total number of detected events compiled to the three patterns.

[3] Slope angle threshold values sufficient for both sediment destabilization and transport about only short distances are determined to 5° (Chapters 5 and 6). As this gradient is only measured along the mid-slope (approx. 400-900 m water depth), findings of MTDs and their source scars on the slope are restricted to this area (Chapter 5). This restriction of landslide distribution as well as only scarce findings and the low recurrences of landslides primary indicate the NE Cretan margin to be a ‘cohesive slope’ *sensu* McAdoo et al. (2000). Also morphometric measurements of MTDs and their scars on the slope, as well as the surrounding intact slope geometry classify a generally ‘cohesive failure’ mechanism and according ‘cohesive landslides’ for the Cretan margin sediment cover *sensu* McAdoo et al. (2000). Consequently, at least this portion of the Cretan slope is classified regarding its behaviour of sediment instability and landslide activity. This is proven by the measured high shear strengths of the sediment (Chapter 6). Opposite, the slope-parallel sediment bedding and the resulting translational transport of the ‘cohesive slides’ force their disintegration to mass flows if they reach the over-critical ($\geq 8^\circ$) lower slope. After the larger runout they finally accumulate as debrites at the slope foots (i.e. in the Kamlioiisi and Malia Basin; Chapters 4-6). From a reconstruction of the long-term evolution of the Cretan slope architecture (Chapter 5) it could be shown that this failure and transport mechanism leads to infrequent, but efficient slope sediment erosion and export into the deeper Cretan Sea sub-basin.

8.2. Triggers and pre-conditioning factors

[1] The infrequent occurrence of landslides indicates that the Cretan slope sediment requires a high external stimulus for its destabilization despite the slope is attributed to permanent steepening (Chapters 5 and 6). Owing to the high seismicity in the Hellenic forearc, an earthquake trigger is deduced to prepare additional loading forces required for sediment instability. Back-analyses of slope stability scenarios show that also the 5° -inclined slope sediment is highly stable under low to moderate seismic loading conditions (Chapter 6). The high shear strength of the sediment (>5 kPa/m up to 8.75 kPa/m *Su*-vs.-depth gradients) thereby highly exceeds shear stresses frequently provided by the seismic background tremor that prevails in the Hellenic forearc. Consequently, very high peak ground accelerations (PGA) of $>29\%$ g, most likely in the order of 42% g, represent triggers sufficient for midsize and major sediment failure (Chapter 6). High-magnitude earthquakes in the closer proximity are hypothesized to infrequently provide such high PGAs in place. Based on an extrapolation of seismic hazard risk data, the high PGAs and also the associated earthquakes are expected to occur as infrequent as at least major landslides. The frequent background tremor only provides PGAs much below these critical threshold values that do not affect the slope catastrophically and is suggested to

cause only the small-scaled sediment dislocations along steepest slope parts (Chapter 6), as well as it may induce creeping and de-watering of mid-slope MTDs (Chapter 5).

[2] Based on a structural interpretation of the seismic data (Chapters 4-6) as well as numerical models, simulating the long-term deformation and the resulting sediment failures in cohesive sediments on active basin flanks (Chapter 7) such as the northeast Cretan margin, most important pre-conditioning factors for sediment failure initiation can be summarized by the following: (1) The distribution of slope parts of gradient increases leading to sediment oversteepening is limited to particular slope portions; (2) Sediment truncations and offsets from faults depend on the cohesive attributes of the slope sediment and prepare a localized, critical steepening as well as faults pre-define head- and sidewalls of landslide scars; (3) The bedding of strata almost parallel to the slope gradient (Chapters 5 and 7) enables translational sediment sliding and a reduction of the critical slope angle, which is here lower than typical for cohesive slopes (McAdoo et al., 2000). Overall, factors that are seen to favour slope stability and those that favour instability in the investigated areas are compiled in Table 4.

Table 4) Compilation of factors and processes that are identified or suggested being important for either northeast Cretan slope stability or instability

Effects favouring slope stability	Effects favouring slope instability
High cohesion and consolidation state of slope sediment resulting in a high shear strength ('cohesive slope')	Slope-parallel sediment bedding provides downslope inclination of slide planes (translational transport mechanism); the critical slope angle is 5° in terms of seismic triggering, and thus low for a cohesive slope
Smooth sediment accumulation and moderate build-up of the sediment load. The occasional mass wasting prepares taper adjustment.	Slope architecture: expansion of the critically steepened slope region (see above) and the over-critical lower slope controlled by Cretan margin steepening and high fault activity
Frequent PGAs of the seismic background tremor are below critical threshold values for sediment destabilization	Occasional recurrence of PGAs in the order of threshold values critical for slope instability
Additional strengthening of the sediment in response to cyclic loading of PGAs below values critical for failure initiation is suggested (<i>sensu</i> Locat and Lee, 2000)	No indication for a pronounced degradation of the mud-rich sediment in response to cyclic loadings (<i>sensu</i> Pestana et al., 2000)
No indications for further mechanisms that may play a significant role in landslide initiation besides or instead the seismic loading and slope architecture	Plane-parallel sediment sliding along preferred seismic reflectors suggests the occurrence of sedimentary units with a potential for mechanical weakening ('weak layers'), e.g. clayey layers or ashes

[3] The northern Cretan slope lithology shows up several sedimentary units that bear a potential for mechanical weaken during stress involvement. These are the detected ash-layers (chapters 4 and 6)

that may weaken in terms of liquefaction during excess pore pressure built-up (e.g. Harders et al., 2007). Seed and Idriss (1971) already emphasized this effect of liquefaction on the stability of sediment deposits as several large landslides are known to have occurred in material susceptible to liquefaction, particularly during earthquakes. Also Hampton et al. (1989) reported considerable cyclic strength degradation in ash-rich sediments and their vulnerability to liquefaction type failures. Furthermore, clayey layers, which can be found in Cretan slope stratigraphy, are known to preferentially shear during stress involvement (Loseth, 1999; Huhn et al., 2006). In contrast, the well-known sapropels (chapters 4 and 6) are not expected to prepare weak layers, as e.g. Kopf et al. (1998) described a positive correlation between the abundance of organic carbon and sediment strength to depth in this region. Although the role of mechanically weak layers in slope failure development is not resolved for the northeast Cretan slope, the plane-parallel slipping of landslides interpreted in these studies may, however, indicate well-defined slide planes in depth (chapters 4 and 5). Consequently, mechanically weak layers at failure depths of Cretan margin landslides are likely, while such layers may not considerably reduce the extrapolated, calculated shear strengths of sediments in critical depths (chapter 6). Overall, factors favouring slope stability and those favouring instability along the northeastern Cretan margin are compiled in Table 3.

8.3 General implications

According to the open questions in a more general context of submarine landslide research (see Chapter 1.1) the key results of this study imply that

[1] an infrequent occurrence of landslides along active margin slopes can be governed by (i) a high shear strength of the sediment cover which may be additionally strengthened from cyclic seismic loads leading to higher consolidation (Chapter 6), (ii) the only occasional occurrence of nearby earthquakes that may generate shear stresses sufficient for instability in the sediments (Chapter 6) (iii) large and longterm tectonic movements and associated fault kinematics leading to progressive steepening of a slope, thus controlling a restricted occurrence of a pre-conditioning setup sufficient for sediment collapses (Chapters 5 and 7).

[2] The state of cohesion of sediment governs the kinematics of long-term slope deformation and the resulting slope architecture (Chapter 7). This particular kinematic behaviour then pre-defines failure initiation and transport conditions of the only occasional landslide events (Chapter 6), which in turn significantly affect the further slope evolution through time (Chapter 5).

[3] not only tectonically exhumed, over-consolidated sediments along accretionary margins provide a high, long-term stability of submarine active margin slopes (see McAdoo et al., 2000; 2004). Hence, the northeast Cretan margin case implies that a similar situation can also occur along e.g. forearc basin

flanks covered by much younger, plane-parallel bedded, hemipelagic, and mud-rich sediments. An additional strengthening of these cohesive sediments may then result in a resistance against seismic triggers similar to the accretionary margins examples (Chapter 6).

[4] in accordance to short runout distances of many cohesive landslides (e.g., Chapters 4 and 5), active margin slopes bearing dominantly cohesive sediments can be of relatively low landslide-tsunami risk (personal communication Dr. S. Tinti, EGU 2009, Vienna; see also 8.4.3). On the other hand, transport dynamics of major landslide events in terms of a large runout may result in sufficient tsunami initiation, while high-magnitude earthquakes triggering major landslides may also trigger tsunamis. However, a low recurrence rate of tsunamogenic landslides along cohesive active margin slopes may reduce the general landslide-to-tsunami risk.

8.4 Future perspectives & outlook

[1] In this study, it was repeatedly shown that the data recovered during the P336 cruise provides a well-suited framework for an investigation, interpretation, and reconstruction of the landslide activity along the northeast Cretan slope (Chapters 4-6). But there some areas not covered by (any) data or of only low quality data with large gaps in between seismic lines and/or in the bathymetric charts (e.g. the source area of the “Malia Basin debrite” (see section 4.7.1) and bad-quality data at the lower slope towards the Kamilonisi Basin (see section 5.4.2.3)). Consequently, additional acoustic data that may be recorded during the upcoming research cruise SACRE (Slide activity along the northern Cretan margin) back to the study sites in 2010 may enable filling these gaps.

[2] The open question about the presence of mechanically weak layers, as already suggested in this (section 8.2.3) and other studies (Kopf et al., 2006; 2007), is not resolved for the northeast Cretan margin landslide activity. During the upcoming SACRE cruise (see above), the newly designed MeBo drill rig (MARUM) is planed to recover sediment cores of ≤ 70 mbsf and thus sediments from the depths of slide planes reconstructed for Cretan margin midsize landslides. Several of these cores are planned, e.g. at the undisturbed slope, at headwalls, and at described landslide deposits in the Malia Basin, and the mid-slope slide complex next to the Bay of Mirabello. Such deeper core data may then provide a geotechnical characterisation of slide plane material. Depending on the prosperity of the SCACRE cruise, this may also reduce uncertainties in measures of mechanical sediment properties in depths as well as landslide ages and recurrence times due to more accurate dating and sediment accumulation rate determination.

[3] Current research on landslide-to-tsunami activity has shown that such proposes for the Cretan margin would require proper information from seismology, marine geology, geotechnical engineering and hydrodynamics, which is not given by the data sets currently available. However, Bradshaw et al.

(2007; and references therein) and Tinti et al. (1994; 2007) have shown that landslide kinematics and sediment attributes (sections 8.1-8.3) can be utilized for basic approaches on landslide-to-tsunami models and thus may be also used for an first estimate on the regional landslide tsunami risk.

Dr. Stefano Tinti rated the midsize MTDs at the Cretan mid-slope (see section 8.1.1) to be of relatively low tsunamogenic potential by reason that they are of short runout and moderate volumes (personal communication, EGU 2009, Vienna). In contrast, the large Kamilonisi Basin debrites (chapter 6; section 8.1.1) were speculated to be of much higher tsunamogenic potential, as they are larger in size ('large enough') to initiate a tsunami as well as they may have occurred as high dynamic mass-movement events of large runout (see analogies of results in Chapter 6 to data in Tinti and Maramai (1999) and Bardet et al. (2003)). Overall, the landslide-tsunami potential for at least the described major slope failure events is likely, but remains speculative for now. In closer inspection of tsunami residues described in literature from potential target areas of tsunamis sourced from the northern Cretan margin (i.e. the Cretan coast, the volcanic arc islands, and the Cyclades plateau further north), the coastal area adjacent to the study sites was frequently affected by tsunamis (e.g., Papadopoulos and Chalkis, 1984; Papazachos et al., 1986; Dominey-Howes 1996). At least the range of uncertainties in MTD age-models does not allow for a linkage of the reconstructed slope-failure events to known tsunami events or their residues. Furthermore, here, as well as in many other cases, it is difficult to assess whether a landslide may have triggered a tsunami or an earthquake that triggered a landslide (e.g., Mienert, 2007).

However, the fundamental input parameters for numerical models (e.g., Tinti et al., 1994) simulating landslide kinematics (e.g., UBO-BLOCK 1 and 2; TRT, University of Bologna) and resulting probabilities for a tsunami initiation (e.g., UBO-TSUIMP; TRT, University of Bologna) are provided by the major outcomes of this study about the Cretan margin landslide activity. Consequently, numerical models of landslide kinematics, which may be also emphasized by results of the upcoming SACRE cruise, and numerical landslide-to-tsunami finite-element models (e.g. Tinti et al., 2006; 2007) are a feasible goal for future works.

[4] From the outcomes of the different numerical models, the here presented thesis chapter focused on the model configuration of an extensional basin flank in order to gain deeper insights for the Cretan margin case study sites (see e.g., 1.3.4). Consequently, the results from the models simulating compressional slope deformation are suggested to prepare the basis for a future manuscript. The data as well as the interpreted results obtained during the Ph.D. project may then be used for an investigation of the deformation and near-surface mass-movement development of cohesive vs. non-cohesive slope sediments under compressional tectonic movement. Furthermore, these results can also be discussed on their significant differences to the results from the extensional slope experiments presented in this thesis.

9. Acknowledgements and References

Acknowledgements

I am deeply grateful to my advisors Prof. Dr. Katrin Huhn and Prof. Dr. Achim J. Kopf as well as my colleagues, co-authors, advisors, and friends Dr. Michael Strasser, Prof. Dr. Sebastian Krastel, Dr. Ingo Kock, Annika Förster, Mathias Meyer, and Dr. Barabara Donner. I would like to thank all my colleagues at the MARUM, Bremen, especially Xin Li, Melanie Schäfer, Carola Ott, Lutz Torbahn, and Dr. Stephan Steinke. Special thanks to cross-readers Michael ‘the devils advocate’ Strasser, Andre ‘shed light’ Hüpers, and Ed ‘native’ Hathorne. Further, I would like to thank all my colleagues at the Poseidon cruise 2006 (P-342) and the Meteor cruise 2007 (M-73) as well as the shipcrew and scientific staff of P-336 in 2006 for the exhaustive collecting of data I used for my thesis. I thank Vicky for waiving and wating. I thank the DFG for funding this Ph.D. project via the MARUM – Center for Marine Environmental Sciences, Bremen.

References

- Aksu, A.E., Yasar, D., Mudie, P.J., 1995. Paleoclimatic and paleoceanographic conditions leading to development of sapropel layer S1 in the Aegean Sea. *Palaeogeogr. Palaeoclimat. Palaeoecol.*, 116, 71-101.
- Ambraseys, N. N., 2001. Far-field effects of eastern Mediterranean earthquakes in lower Egypt. *J. Seismol.*, 5, 263-268, doi:10.1023/A:1011476718680.
- Angelier, J., Lyberis, N., Le Pichon, X., Barrier, E., Huchon, P., 1981. The Tectonic development of the Hellenic arc and the Sea of Crete: a synthesis. *Tectonophysics*, 86, 159-196.
- Bardet, J.-P., Synolakis, C.E., Davies, H.L., Imamura, F., Okal, E.A., 2003. Landslide Tsunamis: Recent Findings and Research Directions. *Pure appl. geophys.*, 160, 1793-1809.
- Barley, B., 1999. Deepwater problems around the world. *Leading Edge*, 18, 488-494.
- Becker, D., Meier, T., Rische, M., Bohnhoff, M., Harjes, H.-P., 2006. Spatio-temporal microseismicity clustering in the Cretan region. *Tectonophysics*, 423, 1-4, 3-16.
- Behrmann, J. H., Flemings, P.B., John, C.M., 2006. IODP Expedition 308 Scientists: Rapid Sedimentation, Overpressure, and Focused Fluid Flow, Gulf of Mexico Continental Margin. *Scientific Drill*, 3, 12-17.
- Biscontin, G., Pestana, J.M., 2006. Factors affecting seismic response of submarine slopes. *Natural Hazards and Earth System Sciences*, 6, 97-107.
- Biscontin, G., Pestana, J. M., Nadim, F., 2004. Seismic triggering of submarine slides in soft cohesive soil deposits. *Marine Geology*, 203, 341-354.
- Biscontin, G., Pestana, J. M., Nadim, F., Andersen, K. H., 2001. Seismic response of normally consolidated cohesive soils in gently inclined submerged slopes. *Proc. of the 4th International Conference on Recent Advances in Geotechnical Earthquake Engineering and Soil Dynamics*, San Diego, California, San Diego, California.
- Bondevik, S., Løvholt, F., Harbitz, C., Mangerud, J., Dawson, A., Svendsen, J.I., 2005. The Storegga Slide tsunami - comparing field observations with numerical simulations. *Marine and Petroleum Geology*, 22, 1-2, 195-208.
- Bohnhoff, M., Makris, J., Papanikolaou, D., Stavrakakis, G., 2001. Crustal investigation of the Hellenic subduction zone using wide aperture seismic data. *Tectonophysics*, 343, 239-262.
- Bohnhoff, M., Rische, M., Meier, T., Becker, D., Stavrakakis, G., Harjes, H.-P., 2006. Microseismic activity in the Hellenic Volcanic Arc Greece, with emphasis on the seismotectonic setting of the Santorini-Amargos zone. *Tectonophysics*, 423, 17-33.
- Bonneau, M., 1984. Correlation of the Hellenide nappes in the south-east Aegean and their tectonic reconstruction. *Geol. Soc., London, Special Publications*, 17, 517-527.

- Booth, J.S., O'Leary, D. W., Popenoe, P., Danforth, W. W., 1993. U.S. Atlantic continental slope landslides: Their distribution, general attributes, and implications, in *Submarine Landslides. Selected Studies in the U.S. Exclusive Economic Zone*, edited by Schwab, W. C., Lee, H. J., Twichell, D.C., U.S. Geol. Surv. Bull., 2002, 14-23.
- Bradshaw, A.S., Baxter, C.D.P., Taylor, O.-D.S., Grilli, S., 2007. Role of Soil behaviour on the initial kinematics of tsunamogenic slides. In: Lykousis, V., Sakellariou, D., Locat, J. (eds.). *Submarine Mass movements and their consequences. Advances in Natural and Technological Hazards Series*, Springer, 387-394.
- Bryn, P., Solheim, A., Berg, K., Lien, R., Forsberg, C.F., Haflidason, H., Ottesen, D., Rise, L., 2002. The Storegga Slide complex; repeated large scale sliding in response to climatic cyclicity. In: Locat, J., Mienert, J. (Eds.), *Submarine Mass Movements and Their Consequences*. Kluwer Academic Publishers, The Netherlands, 215-222.
- Camerlenghi, A., Cita, M.B., Hieke, W., Ricchiuto, T., 1992. Geological evidence for mud diapirism on the Mediterranean Ridge accretionary complex. *Earth and Planet. Sci. Let.*, 109, 493-504.
- Camerlenghi, A., Urgeles, R., Ercilla, G., Brückman, W., 2007. Scientific Ocean Drilling Behind the Assessment of Geo-Hazards from Submarine Slides. *Scientific Drilling*, 4:45-47.
- Camerlenghi, A., Urgeles, R., Fantoni, L., 2009. A database on submarine landslides of the Mediterranean Sea. In: *Submarine Mass Movements and Their Consequences IV*, edited by Mosher, DC., Shipp, C., Moscardelli, L., Chaytor, J., Baxter, C., Lee, H., and Urgeles, R., Fourth International Symposium on Submarine mass movements and their consequences, November 8-11, 2009, Austin, Texas, *Advances in Natural and Technological Hazards Research*, in press.
- Canals, M., Lastras, G., Urgeles, R., Casamor, J.L., Mienert, J., Cattaneo, A., De Batist, M., Haflidason, H., Imbo, Y., Laberg, J.S., Locat, J., Long, D., Longva, O., Masson, D. G., Sultan, N., Trincardi, F., Bryn, P., 2004. Slope failure dynamics and impacts from seafloor and shallow sub-seafloor geophysical data: case studies from the COSTA project. *Mar. Geol.* 213, 9-72.
- Casas, D., Ercilla, G., Baraza, J., Alonso, B., Manlondono, A., 2003. Recent mass-movement processes on the Ebro continental slope (NW Mediterranean). *Mar. Petrol. Geol.*, 20, 445-457.
- Chaumillon, E., Mascle, J., 1996. From foreland to forearc domains: Mew multichannel seismic reflection survey of the Mediterranean ridge accretionary complex (Eastern Mediterranean). *Mar. Geol.* 138, 237-259.
- Chronis, G., Lykousis, V., Anagnostos, C., Karageorgis, A., Stavrakakis, S., Poulus, S., 2000. Sedimentological processes in the southern margin of the Crete Sea (NE Mediterranean). *Progr. Oceanogr.* 46, 143-160.
- Cochoonat, P., Dürr, S., Herzig, P., Mevel, C., Mienert, J., Schneider, R., Weaver, P.P.E., Winkler, A., 2007. *The deep-sea frontier- Science challenges for a sustainable future*, ISBN 92-79-05266-8, European Communities, printed in Belgium, 52.
- Coleman, J. M., Prior, D. B., 1988. Mass wasting on continental margins, *Annu. Rev. Earth Planet. Sci.*, 16, 101-119.
- Coulomb, C. A., 1776. *Essai sur une application des regles des maximis et minimis a quelques problemes de statique relatifs, a la architecture*. *Mem. Acad. Roy. Div. Sav.*, 7, 343-387.
- Dan G., Sultan, N., Savoye, B., 2007. The 1979 Nice harbour catastrophe revisited: Trigger mechanism inferred from geotechnical measurements and numerical modelling. *Mar. Geol.* 245, 40-64.
- Dilek, Y., 2006. Collision tectonics of the Mediterranean region: causes and consequences. In: Dilek, Y., Pavlides, S. (eds) *Post-collisional Tectonics and Magmatism in the Mediterranean and Asia*, Geological Society of America, Special Papers, 409, 1-13.
- Drooger, C.W. and Meulenkamp, J.E., 1973. Stratigraphic contribution to dynamics in the Mediterranean area: Crete as a case history. *Bull. Geol. Soc. Greece*, 10, 193-200.
- Dominey-Howes, D.T.M., 1996. *The Geomorphology and Sedimentology of five tsunamis in the Aegean Sea Region, Greece*. Unpublished thesis, University of Coventry, UK. 272.
- Dominey-Howes, D., Cundy, A., Croudace, I., 2000. High energy marine flood deposits on Astypalaea Island, Greece: possible evidence for the AD 1956 southern Aegean tsunami. *Marine Geology*, 163, 1-4, 303-315.
- Dugan, B., Flemings, P. B., 2002. Fluid flow and stability of the US continental slope offshore New Jersey from the Pleistocene to the present *Geofluids* 2 (2). 137-146 doi:10.1046/j.1468-8123.2002.00032.x
- Fassoulas, C., Kiliadis, A., Mountrakis, A., 1994. Postnappe stacking extension and exhumation of high pressure/ low-temperature rocks in the island of Crete; Greece. *Tectonics*, 13/1: 127-138.

- Fortuin, A.R., 1978. Late Cenozoic history of Eastern Crete and implications for the geology and geodynamics of the Southern Aegean area. *Geol. Mijnbouw*, 57, 451-464.
- Fortuin, A.R. Peters, J.M., 1984. The Prina Complex in eastern Crete and its relationship to possible Miocene strike-slip tectonics. *J. Struct. Geol.*, 6, 459-476.
- Galanopoulos, A.G., 1960. Tsunamis observed on the coasts of Greece from antiquity to present time. *Annali de Geofisica*, 4, 371-386.
- Ganas, A., Parsons, T., 2009. Three-dimensional model of Hellenic Arc deformation and origin of the Cretan uplift. *J. Geophys. Res.*, 114, 1-14.
- Geraga, M., Tsaila-Monopolis, S., Ioakim, C., Papatheodorou, G., Ferentinos, G., 2000. Evaluation of palaeoenvironmental changes during the last 18,000 years in the Myrtoon basin, SW Aegean Sea. *Palaeogeography, Palaeoclimatology, Palaeoecology*, 156, 1-2, 1-17.
- Garziglia, S., Mignon, S., Ducassou, E., Loncke, L., Mascle, J., 2008. Mass-transport deposits on the Rosetta province (NW Nile deep-sea turbidite system, Egyptian margin): Characteristics, distribution, and potential causal processes. *Mar. Geol.* 250,180-198.
- Giresse, P., Buscail, R., Charriere, B., 2003. Late Holocene multisource material input into the Aegean Sea: depositional and post-depositional processes. *Oceanol. Acta.* 26, 657-672.
- Giresse, P., Buscail, R., Charriere, B., 2003. Late Holocene multisource material input into the Aegean Sea: depositional and post-depositional processes, *Oceanol. Acta*, 26, 657-672.
- GITEC-TWO (Genesis and Impact of Tsunamis on the European Coasts: Tsunami Warning and Observations), 1999. *Final Scientific Report*, University of Bologna.
- Goldfinger, C., Nelson, C.H., Johnson, J.E., 2003. Holocene earthquake records from the Cascadia subduction zone and northern San Andreas Fault on precise dating of offshore turbidites, *Annu. Rev. Earth Planet. Sci.*, 31, 555-577.
- Guidoboni, E., Comastri, A., 1997. The large earthquake of 8 August 1303 in Crete: Seismic scenario and tsunami in the Mediterranean area, *J. Seismol.*, 1, 55-72, doi:10.1023/A:1009737632542.
- Hafliðason, H., Sejrup, H.P., Berstad, I.M., Nygård, A., Richter, T., Bryn, P., Lien, R., Berg, K., 2003. A weak layer feature on the Northern Storegga Slide escarpment. In: Mienert, J., Weaver, P. (Eds.), *European Margin Sediment Dynamic - Side-Scan Sonar and Seismic Images*. Springer, Berlin, 55-62.
- Hamouda, A.Z., 2006. Seismic hazard of the eastern Mediterranean, *Acta Geophys.*, 54, 165-176, doi:10.2478/s11600-006-0013-z.
- Hampton, M.A., 1989. Geotechnical properties of sediment on the Kodiak continental shelf and upper slope, Gulf of Alaska. *Marine Geotechnology*, 8, 159-180.
- Hampton, M.A., Lee, H.J., Locat, J., 1996. Submarine landslides. *Rev. Geophys.* 34, 33-59.
- Harbitz, C.B., 1992. Model simulation of tsunamis generated by the Storegga Slides. *Marine Geology* 105, 1-21.
- Harders, R., Brueckmann, W., Feeser, V., Kutterolf, S., Hensen, C., Moerz T., 2007. Are ash layers the controlling factor on translational sliding offshore Central America? EGU-2007-A-07917, EGU 2007.
- Hatzfeld, D., Karakostas, V., Ziazia, M., Selvaggi, G., Leborgne, S., Berge, C. Makropoulos, M., 1993. The Kozani-Grevena (Greece) earthquake of May 13, 1995, a seismological study. *Journal of Geodynamics*, 26, 2-4, 245-254.
- Heezen, B.C., Ewing, M., 1952. Turbidity currents and submarine slumps, and the 1929 Grand Banks earthquake. *Am. J. Sci.* 250, 849-873.
- Heezen, B.C., Ericson, D.B., Ewing M., 1954. Further evidence for a turbidity current following the 1929 Grand Banks earthquake. *Deep Sea Research* 1,193-202
- Huhn, K., Kock, I., Kopf, A., 2006. Comparative numerical and analogue shear box experiments and their implications for the mechanics along the failure plane of landslides, *Norw. J. Geol.*, 86(3), 209-220.
- Huson, W.J., Fortuin, A.R., 1985. The Lithion Slide: A large submarine slide in the South Cretan Trough, eastern Mediterranean. *Mar. Geol.* 65, 103-111.

- Hsü, K.J., Montadert, L., Bernoulli, D., Bizon, G., Cita, M., Erickson, A., Fabricius, F., Garrison, R.E., Kido, R.B., Mellieres, F., Muller, C., Wright, R.C., 1978. Site 378: Certan Basin. *Init. Rep. Deep-Sea Drill. Proj.*, 42, 321-257.
- Hutton, E.W.H., Syvitski, J.P.M., 2004. Advances in the numerical modeling of sediment failure during the development of a continental margin, *Mar. Geol.*, 203, 367-380.
- ISC, 2001, Earthquake Catalogue (computer file), Intern. Seism. Center, Newbury.
- Jongsma, D., Wissman, G., Hinz, F. and Garde, S., 1977. Seismic studies in the Cretan Sea. The southern Aegean Sea: an extensional marginal basin without sea floor spreading? *Meteor. Forschungsergeb. Geol. Geophys. C*, 27: 3-30.
- Edgers, L., Karlsrud, K., 1982. Soil flows generated by submarine slides: Case studies and consequences. *Nor. Geotech. Inst. Bull.*
- Kayen, R.E. and Lee, H.J., 1991. Pleistocene slope instability of gas hydrate-laden sediment on the Beaufort Sea margin. *Mar. Geotech.*, 10, 125-141.
- Keller, J., Ryan, W.B., Ninkowitch, D., Altherr, R., 1978. Explosive volcanic activity in the Mediterranean over the past 20,000 years as recorded in deep-sea sediments. *Geol. Soc. Am. Bull.*, 89, 591-604
- Kock, I., Huhn, K., 2007. Numerical Investigation of localization and micromechanics in a stratified soil specimen. *Journal of Structural Geology*, 29, 1679-1694.
- Kopf, A., Robertson, A.H.F., Clennel, M.B., Flecker, R., 1998. Mechanisms of mud extrusion on the Mediterranean Ridge Accretionary Prism. *Geo-Marine Letters*, 18, 97-114.
- Kopf, A., Mascle, J., Klaeschen, D., 2003. The Mediterranean Ridge: A mass balance across the fastest growing accretionary complex on Earth. *J. Geophys.* 108, 2372-2403.
- Kopf, A., Alves, T., Heesamnn, B., Irving, M., Kaul, N.E., Kock, I., Krastel, S., Reichelt, M., Schäfer, R., Stegmann, S., Strasser, M., Thölen, M., 2006. Report and preliminary results of Poseidon cruise P336: CRESTS – Cretan Sea Tectonics and Sedimentation, Heraklion 28.04.-17.05.2006. *Berichte, Fachbereich Geowissenschaften, Universität Bremen*, 253.
- Kopf, A., Stegmann, S., Krastel, S., Förster, A., Strasser, M., Irving, M., 2007. Marine deep-water Free-fall CPT Measurements for landslide characterisation off Crete, Greece (Eastern Mediterranean Sea) - PART 2: Initial data from the western Cretan Sea. In: Lykousis, V., Sakellariou, D., Locat, J. (eds.). *Submarine Mass movements and their consequences. Advances in Natural and Technological Hazards Series*, Springer, 199-208.
- Lambe, T.W., Whitman, R.V., 1969. *Soil Mechanics*, 53, John Wiley, New York.
- Lastras, G., Canals, M., Urgeles, R., Hughes-Clarke, J.E., Acosta, J., 2004. Shallow slides and pockmark swarms in the Eivissa Channel Western Mediterranean Sea. *Sedimentology* 51:837-850.
- Lastras, G., Canals, M., Amblas, D., Ivanov, M., Dennielou, B., Droz, L., Akhmetzhanov, A., 2006. Eivissa slides, western Mediterranean Sea: morphology and processes. *Geo-Mar Lett* 26:225-233.
- Le Pichon, X., Angelier, J., 1979. The Hellenic arc and trench system: A key to the neotectonic evolution of the eastern Mediterranean area. *Tectonophysics* 60, 1-42.
- Le Pichon, X., 1983. Land-locked oceanic basins and continental collision: The Eastern Mediterranean as a case example, in *Mountain Building, Processes*, edited by K. J. Hsü, 201- 211, Academic, London.
- Le Pichon, X., Lallemand, S.J., Chamot-Rooke, N., Lemeur, D., Pascal, G., 2002. The Mediterranean Ridge backstop and the Hellenic nappes. *Mar. Geol.* 186, 111-125.
- Lee, H.J., 1985. State of the art: Laboratory determination of the strength of marine soils. In: *Strength Testing of Marine Sediments: Laboratory and In situ Measurements* (Eds R.C. Chaney and K.R. Demars), 181-250, STP 883, American Society for Testing and Materials.
- Lee, H.J., Locat, J., Desgagnes, P., Parsons, J.D., McAdoo, B.G., Orange, D.L., Puig, P., Wong, F.L., Dartnell, P., Boulanger, E., 2007. Submarine mass movements on continental margins. In: Nittroauer, C.A., Austin, J.A., Field, M.E., Kravitz, J.H., Syvitki, J.P.M., Wiberg, P.L. (eds.), *Continental Margin Sedimentation*, Blackwell Publishing, UK, 213-274.
- L'Heureux, J.-S., Longva, O., Hansen, L., Vingerhagen, G., 2007. The 1990 submarine slide outside the Nidelv River mouth, Trondheim, Norway. In: Lykousis, V., Sakellariou, D., Locat, J. (eds.). *Submarine Mass movements and their consequences. Advances in Natural and Technological Hazards Series*, Springer, 199-208.
- Locat, J., Lee, H.J., 2002. Submarine landslides: advances and challenges. *Can. Geotech. J.* 39, 193-212.

- Locat, J., Desgagnés, P., Leroueil, S. and Lee, H.J., 2003. Stability analysis of the Hudson Apron slope, off New Jersey, U.S.A. In: *Submarine Mass Movements and their Consequences* (Eds J. Locat and J. Mienert), 267–280, Kluwer, Dordrecht.
- Locat, J., Mienert, J., 2003. Submarine mass movements and their consequences. *Advances in natural and technological hazards research* 19, Kluwer, Dordrecht, 540.
- Loseth, T., 1999. *Submarine Massflow Sedimentation*, Springer Verlag.
- Manakou, M. V., Tsapanos-Theodoros, M., 2000. Seismicity and seismic hazard parameters evaluation in the island of Crete and the surrounding area inferred from mixed data files. *Tectonophysics*. 321; 1, 157-178.
- Leynaud, D., Mienert, J., Vanneste, M., 2009. Submarine mass movements on glaciated and non-glaciated European continental margins: A review of triggering mechanisms and preconditions to failure. *Mar. Petrol. Geol.*, 26, 618–632.
- Lykousis, V., Roussakis, G., Alexandri, M., Pavlakis, P., Papoulia, I., 2002. Sliding and regional slope stability in active margins : North Aegean Trough (Mediterranean). *Mar. Geol.* 186, 281-298.
- Main, L.G., Burton, P.W., 1989. Seismotectonics and the earthquake frequency-magnitude distribution in the Aegean Area. *Geophys. J.*, 98, 575-586.
- Mascle, J., Martin, L., 1990. Shallow structure and recent evolution of the Aegean Sea: a synthesis based on continuous reflection profiles. *Mar. Geol.* 94, 271–299.
- Masson, D.G., Canals, M., Alonso, B., Urgeles, R., Huhnerbach, C., 1998. The Canary Debris Flow: source area morphology and failure mechanisms. *Sedimentology* 45, 411-432.
- Masson, D.G., Watts, A.B., Gee, M.J.R., Urgeles, R., Mitchell, N.C., Le Bas, T.P., Canals, M., 2002. Slope failures on the flanks of the western Canary Islands. *Earth-Sci. Rev.* 57, 1-35.
- Masson, D.G., Harbitz, C.B., Wynn, R.B., Pedersen, G., Løvholt, F., 2006. Submarine landslides: processes, triggers and hazard prediction. *Phil. Trans. R. Soc. A* 364, 2009–2039.
- McAdoo, B.G., Pratson, L.F., Orange, D.L., 2000. Submarine landslide geomorphology, US continental slope. *Mar. Geol.* 169, 103-136.
- McAdoo, B.G., Capone, M.K., Minder, J., 2004. Seafloor geomorphology of convergent margins: Implications for Cascadia seismic hazard. *Tectonics*, 23.
- McClusky, S., Balassanian, S., Barka, A., Demir, C., Ergintav, S., Georgiev, I., Gurkan, O., Hamburger, M., Hurst, K., Kahle, H., Kastens, K., Kekelidze, G., King, R., Kotzev, V., Lenk, O., Mahmoud, S., Mishin, A., Nadariya, M., Ouzounis, A., Paradissis, D., Peter, Y., Prilepin, M., Reilinger, R., Sanli, I., Seeger, H., Tealeb, A., Toksoz, M.N., Veis, G., 2000. Global positioning system constraints on plate kinematics and dynamics in the eastern Mediterranean and Caucasus. *Journal of Geophysical Research* 105, 5695– 5719.
- McKenzie, P.D., 1978. Active tectonics of the Alpine-Himalayan belt: the Aegean Sea and surrounding regions. *Geophys. J. Roy. Astron. Soc.* 55, 217–254.
- Meier, T., Becker, D., Endrun, B., Rische, M., Bohnhoff, M., Stöckhert, B., Harjes, H.-P., 2007. A model for the Hellenic subduction zone in the area of Crete based on seismological investigations, in *Late Palaeozoic and Mesozoic Ecosystems in SE Asia*, edited by E. Buffetaut, J. Le Loeuff, and V. Suteethorn, *Geol. Soc. Spec. Publ.*, 291, 183-199, doi:10.1144/ SP291.9.
- Meier, T., Rische, M., Endrun, B., Vafidis, A., Harjes, H.-P., 2004. Seismicity of the Hellenic subduction zone in the area of western and central Crete observed by temporary local seismic networks. *Tectonophysics* 383, 149-169.
- Mercier, J.-L., Mouyaris, N., Simeakis, C., Roundoyannis, T., Angelidhis, C., 1979. Intra-plate deformation; aquantitative study of the faults activated by the 1978 Thessaloniki earthquakes. *Nature*. 278; 5699, 45-48.
- Mienert, J., 2004. COSTA – continental slope stability: major aims and topics, *Marine Geology*, 213, 1–7.
- Mienert, J., Vanneste, M., Bünz, S., Andreassen, K., Hafliadason, H., Sejrup, H.P., 2005. Ocean warming and gas hydrate stability on the mid-Norwegian margin at the Storegga Slide. *Marine & Petroleum Geology*, 22: 233-244.
- Mienert, J., 2007. ESONET geohazard working group, Barcelona.
- Mienert, J., 2009. *Methane Hydrate and submarine slides*, Elsevier.
- Morgan, J.K., Silver, E., Camerlenghi, A., Dugan, B., Kirby, S., Shipp, C., Suyehiro, K., 2009. Addressing geohazards through ocean drilling. *Scientific Drilling* 7,15-30.

- Morgan, J.K., Clague, D.A., Borchers, D.C., Davis, A.S., Milliken, K.L., 2007. Mauna Loa's submarine western flank: Landsliding, deep volcanic spreading, and hydrothermal alteration, *Geochem. Geophys. Geosyst.*, 8, Q05002, doi:10.1029/2006GC001420.
- Muerdter, D.R., Kennett, J.P., Thunell, R.C., 1984. Late Quaternary sapropels sediments in the eastern Mediterranean Sea: faunal variations and chronology. *Quart. Res.*, 21, 385-403.
- Mulder, T., Cochonat, P., 1996. Classification of offshore mass movements *Journal of Sedimentary Research* 66; 1; 43-57.
- Mulder, T., Savoye, B., Syvitski, J.P.M., 1997. Numerical modelling of a mid-sized gravity flow: the 1979 Nice turbidity current (dynamics, processes, sediment budget and seafloor impact). *Sedimentology*, 44, 305–326.
- Nittrouer, C.A., 1999. STRATAFORM: overview of its design and synthesis of its results. *Marine Geology*, 154, 3-12.
- O'Grady, D.B., 2001. Sedimentary Geomorphology of siliciclastic continental slopes. Ph.D. thesis, Faculty of the Graduate School of the University of Colorado.
- Okubo, C. H., 2004. Rock mass strength and slope stability of the Hilina slump, Kilauea Volcano, Hawaii. *Journal of Volcanology and Geothermal Research*, 138, 43-76
- Papadopoulos, G.A., Chalkis, B.J., 1984. Tsunami observed in Greece and the surrounding area from antiquity up to present times, *Mar. Geol.* 56, 309–317.
- Papadopoulos, G.A., Fokaefs, A., 2005. Strong tsunamis in the Mediterranean Sea: a re-evaluation. ISET J. Earthquake Technol. Paper 463, 159-170
- Papazachos, B.C., Karakostas, V.G., Papazachos, C.B., Scordilis, E.M., 2000a. The geometry of the Wadati-Benioff zone and lithospheric kinematics in the Hellenic Arc, *Tectonophysics*, 319(4), 275–300.
- Papazachos, C.B., Cominakakis, P.E., Karakaisis, G.F., Karakostas, B.G., Papaioannou, C.A., Scordilis, E.M., 2000b. A catalogue of earthquakes in Greece and surrounding area for the period 550BC– 1999, Publ. 1, 333 pp., *Geophys. Lab., Univ. of Thessaloniki, Thessaloniki, Greece.*
- Papazachos, C.B., Hatzidimitriou, P., Panagiotopoulos, D., Tsokas, G., 1995. Tomography of the crust and upper mantle in southeast Europe. *J. Geophys. Res.*, 100, 405–422.
- Papazachos, B.C., Koutitas, C., Hatzidimitriou P.M., Karacostas, B.G., Papaioannou, C.A., 1986. Tsunami hazard in Greece and the surrounding area. *Ann. Geophys.* 4 (B1), 79–90.
- Pestana, J.M., Biscontin, G., Nadim, F., Andersen, K.H., 2000. Modeling cyclic behaviour of lightly over-consolidated clays in simple shear, *Soil Dynamics and Earthquake Engineering*, 19, 501–519.
- Perissoratis, C., Papadopoulos, G.A., 1999. Sediment instability and slumping in the southern Aegean Sea and the case history of the 1956 tsunami. *Mar. Geol.* 161, 287-305.
- Pichler, H., Friedrich, W., 1976. Radiocarbon-dates of Santorini Volcanics, *Nature*, 262, 373-374.
- Piper, D.J.W., Pirmez, C., Manley, P.L., Long, D., Flood, R.D., Normark, W.R., Showers, W., 1997. Mass transport deposits of the Amazon Fan. In: Flood, R.D., Piper, D.J., Klaus, A., Peterson, L.C. (Eds.), *Proceedings of the Ocean Drilling Program*, vol. 155, Scientific Results, Amazon Fan. Ocean Drilling Program, College Station, TX, pp. 109–146.
- Pirazzoli, P.A., Laborel, J., Stiros, S.C., 1996. Earthquake clustering in the eastern Mediterranean during historical times, *J. Geophys. Res.*, 101(B3), 6083-6097.
- Pirazzoli, P.A., Thommeret, J., Thommeret, Y., Laborel, J., Montag-Gioni, L.F., 1982. Crustal block movements from Holocene shorelines: Crete and Antikythira (Greece), *Tectonophysics*, 86, 27-43.
- Polonia, A., Camerlenghi, A., Davey, F., Storti, F., 2002. Accretion, structural style and syn-contractonal sedimentation in the Eastern Mediterranean Sea, *Mar. Geol.*, 186, 127-144.
- Posamentier, H.W., Vail, P.R., 1988. H.W. Posamentier and P.R. Vail, Eustatic controls on clastic deposition, II. Sequence and systems-tracts models. In: C.K. Wilgus, B.S. Hastings, C.G.St.C. Kendall, H.W. Posamentier, C.A. Ross and J.C. Van Wagoner, Editors, *Sea Level Changes—An Integrated Approach* Soc. Econ. Paleontol. Mineral., Spec. Publ. 42, 125–154.
- Postma, G., Fortuin, A.R. van Wamel, W.A., 1993. Basin patterns controlled by tectonics and climate: the Neogene 'fore-arc' graben of eastern Crete as a case history. *Spec. Publs Int. Ass. Sediment.*, 20, 335-362.

- Reilinger, R., et al., 2006. GPS constraints on continental deformation in the Africa-Arabia-Eurasia continental collision zone and implications for the dynamics of plate interactions, *J. Geophys. Res.*, 111, B05411, doi:10.1029/2005JB004051.
- Ring, U., Brachert, T., Fassoulas, C., 2001. Middle Miocene graben development in Crete and its possible relation to large-scale detachment faults in the southern Aegean. *Terra Nova*, 13, 297-304.
- Robertson, A.H.F., Mountrakis, D., 2006. Tectonic Development of the Eastern Mediterranean Region. Geological Society Special Publication no. 260,717, London, Bath: Geological Society of London
- Salamon, A., Rockwell, T., Ward, S.N., 2007. Tsunami hazard evaluation of the eastern Mediterranean: Historical Analysis and selected modelling. *Bull. Seismol. Soc. Am.* 97, 705-724.
- Sato, T., Kasahara, J., Taymaz, T., Ito, M., Kamimura, A., Hayakawa, T., Tan, O., 2004. A study of microearthquake seismicity and focal mechanisms within the Sea of Marmara (NW Turkey) using ocean bottom seismometers (OBS). *Tectonophysics*, 75, 181–241.
- Savoie, B., Rohais, S., Lopez, S., Dan, G., 2005. Revisiting the 1979 submarine avalanche offshore Nice (French Riviera) : impact on the seafloor, flow reconstruction and modelling. *Proc. ICG Conf. n Submarine Mass Wasting, NGF*, 2, 74.
- Seed, H.B., Seed, R.B., Schlosser, F., Blondeau, F., Juran, I., 1988. The Landslide at the Port of Nice on October 16, 1979. Report No. UCB/EERC-88/10, Earthquake Engineering Research Center, University of California, Berkeley, 68.
- Seed, H.B., Idriss, I.M., 1971. Simplified procedure for evaluating soil liquefaction potential. *J. Soil Mech. Found. Eng. Div., ASCE*, 97, 1249–1273.
- Shanmugam, G., 2000. 49 years of the turbidite paradigm (1950s-1990s): deep-water processes and facies models - a critical perspective, *Marine and Petroleum Geology* 17, 385-242.
- Shanmugam, G., 2009, Slides, Slumps, Debris Flows, and Turbidity Currents, in: *Encyclopedia of Ocean Sciences*, 4509-4529, Elsevier.
- Solheim, A., Bryn, P., Sejrup, H.P., Mienert, J., Berg, K., 2005. Ormen Lange - An integrated study for the safe development of a deep-water gas field within the Storegga Slide complex, NE Atlantic continental margin; executive summary. *Marine and Petroleum Geology*, 22(1-2), 1-9.
- Soloviev, S.L., 1990. Tsunamigenic zones in the Mediterranean Sea, *Natural Hazards*, 3, 183-202.
- Soloviev, S.L., Solovieva O.N., Go C.N., Kim, K.S., Shchetnikov, N. A., 2000. Tsunamis in the Mediterranean Sea 2000 *B.C.–2000 A.D.*, Kluwer Academic Publishers, Dordrecht, 237.
- Stavrakakis, C., Chronis, G., Tselepidis, A., Heussner, S., Monaco, A., Abbasi, A., 2000. Downward fluxes of settling particles in the deep Cretan Sea (NE Mediterranean). *Progr. Oceanogr.* 46, 217-240. Strozyk, F., et al., 2009. New evidence for massive gravitational mass-transport deposits in the southern Cretan Sea, eastern Mediterranean, *Mar. Geol.* 263, 97–107.
- Stegmann S., M. Strasser, F. Anselmetti, Kopf, A., 2007. Geotechnical in situ characterization of subaquatic slopes: The role of pore pressure transients versus frictional strength in landslide initiation, *Geophys. Res. Lett.*, 34, L07607, doi:10.1029/2006GL029122.
- Stiros, S.C., 2001. The AD 365 Crete earthquake and possible seismic clustering during the fourth to sixth centuries AD in the eastern Mediterranean: A review of historical and archaeological data, *J. Struct. Geol.*, 23, 545– 562, doi:10.1016/S0191-8141(00)00118-8.
- Strasser, M., Anselmetti, F.S., Fäh, D., Giardini, D., Schnellmann, M., (2006), Magnitudes and source areas of large prehistoric northern Alpine earthquakes revealed by slope failures in lakes. *Geology*, 34, 1005-1008
- Sultan, N., Cochonat, P., Canals, M., Cattaneo, A., Dennielou, B., Halifladson, H., Laberg, J.S., Long, D., Mienert, J., Trincardi, F., 2004. Triggering mechanisms of slope instability processes and sediment failure on continental margins: a geotechnical approach. *Mar. Geol.* 213, 291-321.
- Synolakis, C.E., Bardet, J.P., Borrero, J.C., Davies, H.L., Okal, E.A., Sweet, S., Tappin, D.R., 2002. The slump origin of the 1998 Papua New Guinea Tsunami. *Proc. R. Soc. London Ser. A* 458, 763.
- Thomson, S.N., Stoekhert, B., Brix, M.A., 1998. Thermochronology of the high-pressure metamorphic rocks of Crete, Greece: Implications for the speed of tectonic processes. *Geology*, 26, 259-262.
- Tinti, S., Gavagni, I., Piatanesi, A., 1994. A finite-element numerical approach for modeling tsunamis. *Annals of Geophysics*, 37, 1009-1026.

- Tinti, S., Maramai, A., 1999. Large Tsunamis and Tsunami Hazard from the New Italian Tsunami Catalog. *Ph_ys. Chem. Earth (A)*, 24, 151-156.
- Tinti, S., Maramai, A., Graciani, L., 2001. A new version of the European tsunami catalogue: updating and revision, *Nat. Hazards Earth Syst. Sci.* 1, 255-262.
- Tinti, S., Pagnoni, G., Zaniboni, F., 2006. The landslides and tsunamis of the 30th of December 2002 in Stromboli analysed through numerical simulations, *Bulletin of Volcanology*, 68, 462-479.
- Tinti, S., Manucci, A., Pagnoni, G., Armigliato, A., Zaniboni, F., 2005. The 30 December 2002 landslide-induced tsunamis in Stromboli: sequence of the events reconstructed from the eyewitness accounts. *Natural Hazards and Earth System Sciences*, 5, 763-775.
- Tinti, S., Zaniboni, F., Armigliato, A., Pagnoni, G., Gallazzi, S., Manucci, A., Brizuela Reyes, B., Bressan, L., Tonini, R., 2007. Tsunamigenic landslides in the western corinth gulf: numerical scenarios. In: Lykousis, V., Sakellariou, D., Locat, J. (eds.). *Submarine Mass movements and their consequences. Advances in Natural and Technological Hazards Series*, Springer, 405-414.
- Urgeles, R., Leynaud, D., Lastras, G., Canals, M., Mienert, J., 2006. Back-analysis and failure mechanisms of a large submarine slide on the ebro slope, NW Mediterranean, *Mar. Geol.* 226, 185-206.
- Vandenberg, L.C. and Lister, G.S., 1996. Structural analysis of basement tectonites from the Aegean metamorphic core complex of Ios, Cyclades, Greece. *J. Struc. Geol.*, 18, 1437-1454.
- Varnes, D.J., 1958. Landslide types and processes. In: *Landslides and Engineering Practice* (Ed. E.D. Eckel), 20-47. Special Report 29, Highway Research Board, Washington, DC.
- Wilson, C.K., Long, D., Bulat, J., Haflidason, H., 2003a. The morphology, setting and processes of the Afen Slide, COSTA. *Continental Slope Stability Workshop 4*, 10-13 Febr. 2003, Bologna, Italy, Abstr., 24.
- Yalciner, A.C., Alpar, B., Altinok, Y., Ozbay, I., Imamura, F., 2002. Tsunamis in the Sea of Marmara; Historical Documents for the Past, Models for the future. *Marine Geology*, 190, 445-463.
- Zitter, T.A.C., Woodside, J.M., Mascle, J., 2003. The Anaximander Mountains: a clue to the tectonics of Southwest Anatolia. *Geol. J.*, 38, 375-394.
- Zitter, T.A.C., Huguen, C. Woodside, J.M., 2005. Geology of mud volcanoes in the eastern Mediterranean from combined side-scan sonar and submersible surveys. *Deep-Sea Res. I*, 52, 457-475.